Electrochemical and Infrared Spectroelectrochemical Methods Applied to the NiFe Hydrogenases of *Ralstonia eutropha*

Juan Liu

Balliol College

University of Oxford

Hilary Term 2012

Acknowledgements

I would like to thank my supervisor Dr. Kylie Vincent for her support in terms of positive thinking, enthusiasm, fruitful discussion, critical and scientific spirits throughout the project. She showed me not only how to run experiments and present the research work including one Shakespeare tutorial, but also how to develop your own way of doing science. She also supported me to go to many conferences and to Berlin for purifying the enzyme. Outside the lab, I learnt drinking alcohol, eating cheese and Thai food from her.

I would like to thank our collaborators Dr. Oliver Lenz and Mr. Lars Lauterbach, of Humboldt University in Berlin, for supplying the protein samples I have used in this Thesis.

I would like to thank the Department of Chemistry and Balliol College for providing me nice places to work and live, and supporting me financially to attend conferences.

I would like to thank all of my colleagues, past and present, for accompanying me on this journey and the loud laughter going through the ICL, pubs and restaurants. Big thanks go to my best Part II Ian McPherson and a summer exchange student Thomas Simler for happy and productive work. Thanks also go to Adam for cooperation in the infrared investigation of the RH and for finishing the food after group dinner. Zul is specially thanked for the discussion on the other half of the SH, cylinder help, and more importantly, Oxford restaurant tours. I would like to thank Phil for proofreading this Thesis and generously contributing an evanescent wave picture. I would also like to thank Holly, not only for helping me format this Thesis but also finding the food for me in Manchester when I was cut off almost all the protein source.

I would like to thank my parents for bringing me a life. Thanks also go to my friends in and outside Oxford: Ying, Hanshi, Candy, Maria and Miroslawa for cheerful conversations. Thanks go to my husband Chunmao (I met him in Louvain-la-Neuve, so thanks again to Kylie for sending me to that summer school) for always supporting me. In the end, thanks go to my strict scholarship for offering me a three-and-half year inspirational life at Oxford.

Electrochemical and Infrared Spectroelectrochemical Methods Applied to the NiFe Hydrogenases of *Ralstonia eutropha*

Juan Liu, Balliol College, University of Oxford

A thesis submitted for the degree of Doctor of Philosophy, Hilary Term 2012

Abstract

Hydrogenases are a class of metalloenzymes which catalyse H_2 oxidation and its reverse reaction, H^+ reduction. There is interest in investigating how H_2 as an energy carrier is cycled in biology. Hydrogenases have also been studied extensively because there are potential applications for them as catalysts for H_2 oxidation in fuel cells or H_2 production via light-driven water splitting. For these applications, the ability for the hydrogenase to work in the presence of O_2 is an important issue. The microorganism *Ralstonia eutropha* is a well-studied model aerobic H_2 oxidiser: it can adopt H_2 as the sole energy source to grow cells in the presence of O_2. It produces at least three distinct O_2-tolerant NiFe hydrogenases: the membrane-bound hydrogenase (MBH), the NAD^+-reducing soluble hydrogenase (SH) and the regulatory hydrogenase (RH). This Thesis employs protein film electrochemistry (PFE) to study the SH and RH. It is found that the SH is able to work in both direction (H_2 oxidation and H^+ reduction) with minimum overpotential, which is critical in coupling $2H^+/H_2$ cycling with the closely spaced NAD^+/NADH potential. Reactions of the SH with O_2 have been investigated, revealing at least two distinct O_2-inactivated states, but consistent with the requirement for the SH to function in air, it can be reactivated in the presence of O_2 at low potentials which could be provided by the NAD^+/NADH pool *in vivo*. The affinity of the RH for H_2 was determined by PFE and found to be slightly higher than that of the SH and MBH. This may provide a way for the microbe to regulate hydrogenase expression in response to the H_2 availability. Carbon monoxide and O_2-inactivated states of the RH have been identified for the first time, confirming that a constricted gas channel is *not* sufficient to explain its O_2 tolerance. Observation of potential dependent reactions in hydrogenases means that it is important to have spectroscopic methods for characterising states triggered by inhibitors *and* potential. An Infrared spectroelectrochemical approach suitable for studying metalloenzymes has been developed and preliminary spectra on RH recorded. This method should provide many opportunities for future studies of redox states of hydrogenases.

Abbreviations

PFE	Protein Film Electrochemistry
PGE	Pyrolytic Graphite ‘Edge’
FTIR	Fourier Transform Infrared Spectroscopy
IRAS	Infrared Reflection-Absorption Spectroscopy
SEIRAS	Surface-Enhanced Infrared Absorption Spectroscopy
EMIRS	Electrochemically Modulated Infrared Spectroscopy
EPR	Electron Paramagnetic Resonance
ENDOR	Electron Nuclear Double Resonance
ESEEM	Electron Spin-Echo Envelope Modulation
XAS	X-ray Absorption Spectroscopy
XANES	X-ray Absorption Near Edge Structure
EXAFS	Extended X-ray Absorption Fine Structure
TXRF	Total Reflection X-ray Fluorescence
ATR-IR SEC	Attenuated Total Reflectance Infrared Spectroelectrochemistry
PEMFCs	Proton Exchange Membrane Fuel Cells
OCP	Open Circuit Potential
Re or ***R. eutropha***	*Ralstonia eutropha*
Aa or ***A. aeolicus***	*Aquifex aeolicus*
E. coli	*Escherichia coli*
Av or ***A. vinosum***	*Allochromatium vinosum*
D. gigas	*Desulfovibrio gigas*
Df or ***D. fructosovorans***	*Desulfovibrio fructosovorans*
***Dv* MF** or ***D. vulgaris* MF**	*Desulfovibrio vulgaris* Miyazaki F
Dm. b or ***Dm. baculatum***	*Desulfomicrobium baculatum*
***D. vulgaris* Hildenborough**	*Desulfovibrio vulgaris* Hildenborough
MBH	Membrane-bound Hydrogenase
SH	Soluble Hydrogenase
RH	Regulatory Hydrogenase
RHstop	A monodimeric derivative HoxBC (RH) via a genetic deletion of a C-terminal peptide of 55 amino acids in HoxB

Table of Contents

Chapter 1

Hydrogenases and their activities

1.1 Biology of H_2 cycling

The reversible heterolytic cleavage of H_2 in biology, shown by eqn [1-1], is catalysed by a class of metalloenzyme known as hydrogenases.[1]

$$\mathrm{H_2} \leftrightarrow \mathrm{H^+} + \mathrm{H^-} \leftrightarrow 2\mathrm{H^+} + 2\mathrm{e^-} \qquad [1\text{-}1]$$

In nature, dihydrogen (H_2) plays an important role in the metabolism of microorganisms, either as an energy source through H_2 oxidation or as the terminal electron acceptor via H^+ reduction. Dihydrogen is a trace gas in air (the H_2 concentration in air is around 0.5 ppm, equivalent to 0.39 nM in aqueous solution)[2] as the biologically and geologically produced H_2 is rapidly consumed by a variety of microorganisms before it enters the atmosphere, as shown in Figure 1-1. Dihydrogen would also easily escape from the lower atmosphere since it is very light. Dinitrogen fixing bacteria in soil or root nodules produce H_2 as a by-product of ammonia (NH_3) formation catalysed by nitrogenases.[3] At the very bottom of submerged wetland soil (O_2-poor), fermentative bacteria such as *Clostridia* use organic substrates as an energy source and excrete H_2 and CO_2 as waste products.[3] Under certain conditions, cyanobacteria and algae can produce H_2 to release the electrons generated by photosynthesis.[4,5] Biologically produced H_2 is then used as reducing power, by other organisms, with its oxidation coupled with the reduction of a variety of inorganic species. In methanogens, the electrons produced by H_2 oxidation are passed to CO_2 which is then reduced to CH_4.[6] Sulphate reducers, such as species of *Desulfovibrio*, use H_2 to reduce SO_4^{2-} to H_2S.[7] The family of Fe^{3+} reducers, such as *Geobacter* species, couples H_2 oxidation with reduction of Fe^{3+} oxides.[8] In denitrifying bacteria, H_2 is consumed as an energy source to reduce NO_3^- to N_2.[9] At the surface of the soil, aerobic organisms, such as *Ralstonia* species[10], exposed to O_2 from the atmosphere, couple H_2 oxidation to O_2 reduction.[11] As H_2 is depleted gradually towards upper levels of soil, the threshold value for H_2 uptake (below which H_2 can no longer be consumed) correspondingly decreases from 10-70 nM to 0.35 nM, i.e., the deeper the microorganism exists in the sediments, the greater the threshold value.[12-14] Recently it has been found that *Streptomyces* exhibit the ability to oxidise atmospheric H_2, indicating very high affinity for H_2 (the K_m value is less than 100 ppm corresponding to 78 nM and the threshold value is less than 0.01 nM).[15]

Near the surface, the conditions become aerobic as the air can penetrate and O_2 can also be produced by cyanobacteria and plants through photosynthesis.[5] The closer the organism is to the surface, the more O_2 is available, and this raises challenges for the microorganisms to produce or utilise H_2 in the presence of O_2. In this Chapter, I will consider the implications of O_2 sensitivity or tolerance in hydrogenases expressed by different organisms.

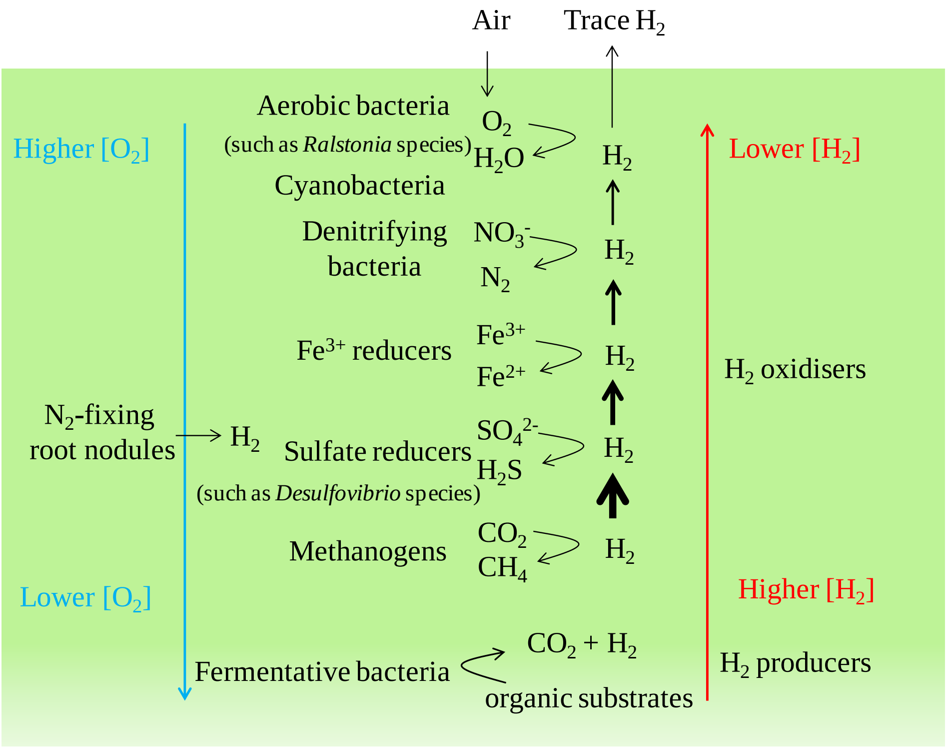

Figure 1-1. Schematic representation of certain redox reactions involved in production and consumption of H_2 in submerged wetland soil. The thickness of the vertical arrows indicates the consumption of H_2. The levels of H_2 and O_2 are indicated by the direction of the red and blue arrow, respectively. Adapted from ref [12].

1.2 Types of hydrogenases

Hydrogenases can be expressed by many organisms, as shown in Figure 1-1, and the physiological function varies depending on the nature of the microorganism, the location of the enzyme in the cell and the *in vivo* redox partner.[1,16] However, according to the metals that are present at the active sites, three types of hydrogenases, the NiFe hydrogenase, the FeFe hydrogenase and the Fe hydrogenase, have been named.[17-19]

Figure 1-2 depicts the coordination chemistry at the active site of the hydrogenases. In the NiFe hydrogenase, a set of biologically unusual ligands (one CO and two CN^-) are coordinated on the Fe ion. Two terminal cysteine ligands are bound to Ni and two extra cysteine ligands are bridging between Ni and Fe.[20] If one of the terminal cysteine ligands coordinated on Ni in NiFe hydrogenases is replaced by a selenocysteine residue, this enzyme is classified as a NiFeSe hydrogenase which is a subclass of the NiFe hydrogenases.[21] In the FeFe hydrogenase, each Fe is ligated by diatomic ligands CO and CN^-. The designation of proximal Fe (Fe^P) and distal Fe (Fe^D) is based on the location in relation to the FeS cluster. Furthermore, one bidentate thiolate ligand is bridging between the two Fe sites.[20] The Fe hydrogenase is slightly different in terms of the single metal content and the replacement of the cyanide with a unidentate *N*-bonded 2-pyridinol ligand.[22] However, it still preserves the feature of the low spin Fe (II) coordinated by two CO ligands and one thiolate from cysteine. The *N*-bonded pyridinol plays a similar role to cyanide (CN^-) which is a stronger σ donor than a π acceptor.[22,23] Although the three types of hydrogenases are phylogenetically unrelated,[24] their active sites share some common features, marked as red in Figure 1-2.

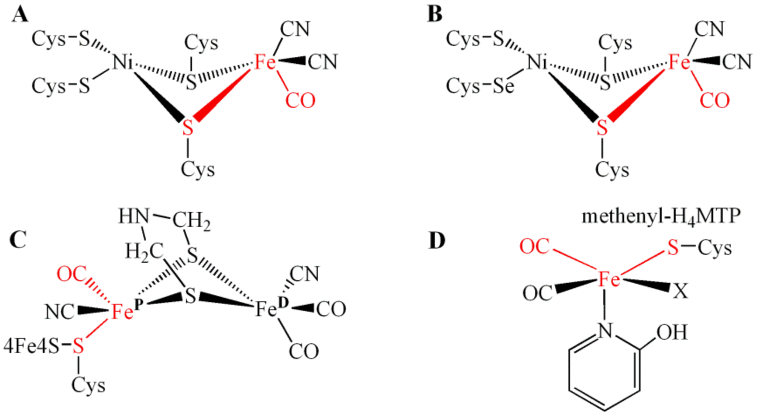

Figure 1-2. Hydrogenase active sites: Panel A: NiFe; Panel B: NiFeSe; Panel C: FeFe and Panel D: Fe hydrogenases. The common features are marked as red.

In this Thesis, I will mainly focus on reviewing the NiFe hydrogenases relevant to this study. All early crystal structures of hydrogenases were for sulphate reducers, organisms found low down in the soil profile and existing in almost entirely anaerobic conditions. These will be used to discuss the general structure of hydrogenases. More recently structures have become available for microaerobic and aerobic organisms, and these will be discussed in **Section 1.10.** In 1995, the crystal structure of the NiFe hydrogenase from *Desulfovibrio gigas (D. gigas)* was first solved.[25] Later, crystal structures of NiFe hydrogenases of other sulphate-reducing bacteria were also solved.

1.3 Crystal structure of *D. gigas* NiFe hydrogenase

Figure 1-3(A) depicts the overall structure of the periplasmic NiFe hydrogenase from *D. gigas* at a resolution of 2.54 Å. The enzyme consists of two polypeptide chains (subunits): a large subunit (purple) with a molecular weight of 60 kDa and a small subunit (green) of 28 kDa. The active site is accommodated in the large subunit. A Ni site was assigned from the electron density map and later on the presence of a Fe ion in the active site was also confirmed based on higher resolution data.[25,26] The distance between the iron and the nickel site is between 2.5 and 2.9 Å depending on the redox state of the enzyme.[26] The small subunit on the other hand houses three iron sulphur clusters: the proximal 4Fe4S, medial 3Fe4S and distal 4Fe4S, named according to their position relative to the active site.

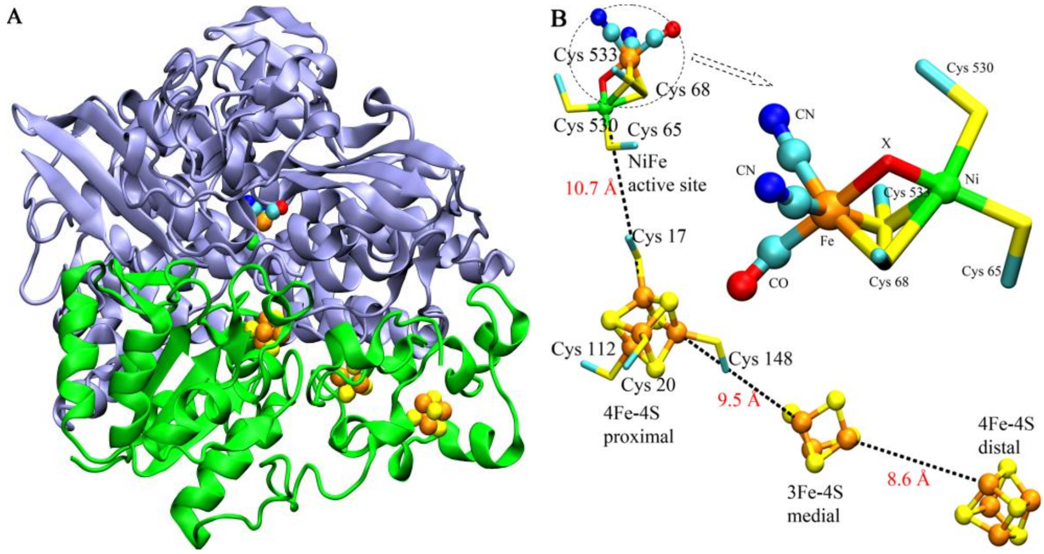

Figure 1-3. Panel A: The overall crystallographic structure of the periplasmic NiFe hydrogenase from *D. gigas* (PDB: 2FRV; solved at a resolution of 2.54 Å).[25] The protein is shown as cartoon and the FeS clusters are shown as spheres. Panel B: The enlargement of the active site and the FeS clusters (yellow: S atom, orange: Fe, green: Ni, cyan: C, red: O, and blue: N).

Figure 1-3(B) shows the enlargement of the NiFe active site and the FeS clusters. It can be seen that the active site is protected by four sulphur-cysteine (C) ligands: C65 and C530 are terminally bound to Ni, and C68 and C533 are bridging the Ni and the Fe. Three diatomic ligands are found to be bound to Fe but the electron density map alone cannot distinguish the small atoms, such as C, N and O. Combined with ^{13}C and ^{15}N labelled infrared spectroscopic data, three biologically unusual ligands (CO and 2 CN^-) were assigned to be coordinated to the Fe site.[27-29]

1.4 Crystal structures of NiFe hydrogenases from other sulphate reducers

Later on, the X-ray crystallographic structures of periplasmic NiFe hydrogenases from sulphate-reducing bacteria *Desulfovibrio vulgaris* Miyazaki F (*Dv* MF, 1.8 Å),[30] *Desulfovibrio fructosovorans* (*Df*, 2.54 Å)[31] and *Desulfovibrio desulfuricans* ATCC 27774 (*Dd* ATCC 27774, 1.8 Å)[32] and one periplasmic NiFeSe hydrogenase from *Desulfomicrobium baculatum* (*Dm. b*, 2.15 Å)[33] were obtained. All of these structures share significant similarities with the NiFe hydrogenase from *D. gigas* as shown in Figure 1-3. They are all composed of two subunits: the large one accommodates the active site and the small subunit houses the FeS clusters. The active site in all the solved structures is composed of a NiFe complex with four sulphur-cysteine ligands coordinated to Ni (two are terminally bound and the other two are bridging the Ni and the Fe; in the *Dm. b* NiFeSe hydrogenase one terminal cysteine is replaced by a selenocysteine[33]), and a standard set of diatomic ligands (1 CO and 2 CN^-) bound to Fe, confirmed in each case by infrared spectroscopy. The electron transfer from the protein surface to the buried active site is through a proximal 4Fe4S, a medial 3Fe4S and a distal 4Fe4S cluster. However, in the *Dm. b* NiFeSe hydrogenase, the medial iron sulphur cluster is a 4Fe4S cluster rather than the 3Fe4S found in *Desulfovibrio* species described above.[33]

1.5 NiFe hydrogenase active site

In the active site of NiFe hydrogenases, as described above in Figure 1-2, the Fe atom is coordinated by one carbonyl (CO) and two cyanide (CN^-) ligands, and it is apparently kept at a +2 oxidation state throughout the process of H_2 cycling, as determined by electron paramagnetic resonance (EPR).[34] As hydrogenases are studied by EPR in a frozen state, it remains possible that the Fe at the active site can access another oxidation state such as Fe (I) as a short-lived, undetected intermediate. On the other hand, the oxidation state of Ni can shuttle during the heterolytic cleavage of H_2 between trivalent (III), divalent (II) and univalent (I).[34] A different assignment of one CO, one CN^- and one SO ligands bound to Fe in the *Dv* MF enzyme was reported based on X-ray crystallography and mass spectrometry,[35] however, FTIR spectroscopic investigations revealed the presence of only CN^- and CO,[36,37] and EPR spectra are essentially the same as those of the NiFe hydrogenases from other sulphate-reducing bacteria.[38] Based on the spectroscopic results, the diatomic ligands bound to Fe were later re-assigned as one CO and two CN^-, the same as in other NiFe hydrogenases.[39]

In Figure 1-4, there is an X ligand bridging the Ni and Fe atoms, depending on the redox state of the enzyme (the nature of the X ligand will be discussed in detail **Section 1.8**). The Fe (II) site has an electron count of 18-electron when the bridging ligand X is an oxygenic species. A transition metal which already houses 18 electrons in the valence shell needs to get rid of a relatively weak existing ligand in order to bind a new ligand.[40]

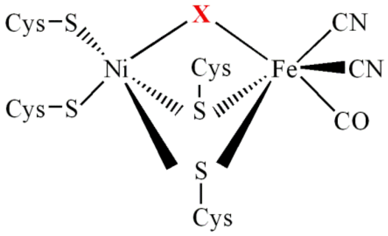

Figure 1-4. The active site of a NiFe hydrogenase. The 'X' is an additional ligand depending on the redox state of the NiFe hydrogenase. It is believed to be a hydroxide (OH^-) group in the inactive form of Ni-B[41,42] and a hydride (H^-) in the active form of Ni-C[43]. The nature of the bridging ligand in Ni-A remains controversial,[44] but it is probably an OOH^- ligand.

1.6 Electron transfer relay in hydrogenases from sulphate reducers

As shown in Figure 1-3, the three FeS clusters are aligned in a linear fashion and the distance between them in this electron relay is within 12 Å, suitable for electron tunnelling.[45,46] Direct electron transfer between the proximal cluster and the distal cluster is unlikely to happen at a significant rate as the distance in-between is *ca.* 20 Å. Therefore, the intramolecular electron transfer from the protein surface to the buried active site (or the reverse) is believed to go through all three FeS clusters.

The electron transfer relay in the NiFe hydrogenases mentioned above (except for the *Dm. b* NiFeSe hydrogenase) is composed of a proximal 4Fe4S, a medial 3Fe4S and a distal 4Fe4S cluster. Notably, the medial 3Fe4S cluster has a relatively positive redox potential (-70 mV) compared to the proximal (-340 mV) and the distal cluster (-290 mV) in the *D. gigas* hydrogenase.[47] Similarly, in the *Df* NiFe hydrogenase, the reduction potentials for the proximal and distal 4Fe4S clusters are both -340 mV whereas the medial 3Fe4S is +65 mV.[48]

In order to further understand the role of the medial iron sulphur cluster, site-directed mutagenesis was performed on the *Df* NiFe hydrogenase by Rousset *et al.* via converting the medial 3Fe4S cluster to 4Fe4S.[48] Proline (P) 238 occupies the position of a potential ligand at the absent fourth Fe site of the 3Fe4S cluster in the wild type protein and is replaced by a cysteine (C) residue for constructing the medial 4Fe4S cluster. The P238C variant results in a 315 mV drop (from +65 to -250 mV) in the midpoint potential. However, no significant changes in the catalytic activity were found in the P238C variant compared to the wild-type enzyme, suggesting that H_2 oxidation is not limited by the electron transfer.[48] Further analysis showed that the variant with a modified medial 4Fe4S cluster in the *Df* NiFe hydrogenase is more O_2-sensitive than the wild-type, implying that the properties of the iron sulphur cluster might be related to the O_2 tolerance.[48] On the other hand, mutagenesis via converting the medial 4Fe4S cluster to 3Fe4S was carried out on the F_{420}-reducing hydrogenase (F_{420}: 8-hydroxy-5-deazaflavin) from *Methanococcus voltae* which has a similar iron sulphur alignment to the *Dm. b* NiFeSe hydrogenase. On converting cysteine 205 to proline, mimicking the situation found in the *Df* NiFe hydrogenase, however, the catalytic activity in the variant (C205P) was almost the same as the wild-type.[49] The role of the medial iron sulphur 3Fe4S cluster in terms of the high midpoint potential is still not clear but believed to be related to control of the intramolecular electron transfer during enzyme turnover. Therefore, Page raised the possibility that the driving force for electron transfer is not always optimized for speed and unfavourable electron tunnelling does happen in NiFe hydrogenases.[45]

To investigate the possible rate-limiting step during hydrogenase turnover, a site-directed variant of the *Df* NiFe hydrogenase was constructed by replacing the histidine ligand of the distal 4Fe4S cluster with a cysteine or a glycine. The composition and reduction potential of the modified FeS cluster is not changed, i.e., it is still a 4Fe4S cluster but with different ligands. However, the enzyme activity for H_2 oxidation with methyl viologen as electron acceptor in the variants is only 1.5 and 3 % respectively of that in the wild-type enzyme, proving that the electron transfer is impaired and the ligation of the distal cluster is important for the electron transfer.[50]

1.7 Hydrogenase activity: H_2 oxidation and H^+ reduction

1.7.1 $2H^+/H_2$ cycling examined by enzyme assays

An enzyme assay is a method for measuring enzyme activity. For hydrogenases, the activity is measured as catalysis of H_2 oxidation shown in eqn [1-2] or H^+ reduction shown in eqn [1-3].[51]

H_2 oxidation:

$$\mathrm{H_2} + \mathrm{A_{ox}} \leftrightarrow 2\mathrm{H^+} + \mathrm{A_{red}} \qquad [1\text{-}2]$$

where A represents an electron acceptor with a relatively high midpoint potential, such as ferricyanide, methylene blue (MB: blue in an oxidising environment and colourless when reduced), methyl viologen (MV: oxidised MV is colourless and reduced MV is blue) or dichloroindophenol (DCPIP).

The concentration of the reduced form of the electron acceptor (A_{red}) can be monitored as an indirect measure of the enzyme activity for H_2 oxidation. A simple spectrophotometric assay with H_2 as electron donor can be carried out by observing the colour change in MB or MV.[52]

H^+ reduction:

$$2\mathrm{H^+} + \mathrm{D_{red}} \leftrightarrow \mathrm{H_2} + \mathrm{D_{ox}} \qquad [1\text{-}3]$$

where D represents an electron donor (a reducing agent) with a moderately low midpoint potential, such as dithionite or mercaptoethanol.

The production of H_2 can be monitored amperometrically using a Clark-type electrode or by measuring the gas pressure by a manometer.[1] The concentration of oxidised form of the electron donor (D_{ox}) can also be monitored as described above.

The soluble hydrogenase from *Ralstonia eutropha* (*Re* SH, formerly *Alcaligenes eutrophus*), is composed of two catalytic moieties: a hydrogenase moiety catalysing $2H^+/H_2$ cycling and a diaphorase moiety catalysing NAD^+/NADH cycling. The enzyme activity (H_2 oxidation or H^+ reduction) can be assayed without using artificial dyes because the $NAD^+ \rightarrow$ NADH reaction can be used to take up electrons from H_2 oxidation or electrons can be provided by the NADH → NAD^+ reaction to reduce H^+. The concentration of NADH can be monitored spectrophotometrically because NADH absorbs at 340 nm in the UV. [53]

1.7.2 $2H^+/H_2$ cycling examined by protein film electrochemistry

Introduction to protein film electrochemistry

In protein film electrochemistry (PFE), an aliquot of a redox protein is adsorbed directly on an electrode to give a monolayer or submonolayer film, as shown schematically in Figure 1-5, and a variety of electrochemical techniques (for example, a linear potential sweep, or potential steps) are applied to investigate the properties of the protein through controlling the electrode potential. The catalytic activity of the film is directly proportional to the current measured. Protein film electrochemistry can therefore monitor changes of the activity triggered by a perturbation in gas composition, temperature or introduction of inhibitors. Various sizes of proteins have been investigated by PFE from relatively simple cytochrome *c* to complex hydrogenases.[54-60] This technique can provide a variety of information on redox proteins: the affinity of the protein for a substrate/inhibitor[61,62], the rate-limiting step in proton-coupled electron transfer[63], potential-dependent inactivation/reactivation of an enzyme[64-66], the limiting step in the electron transfer during turnover[50,67] and kinetic information about gas diffusion inside the enzyme[68,69].

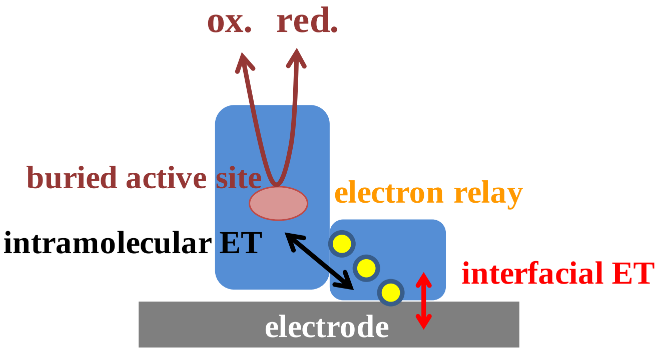

Figure 1-5. Cartoon of an enzyme with a buried active site and a series of electron relay centres adsorbed on an electrode. The interfacial electron transfer is marked in red and intramolecular electron transfer is marked in black. The "ox." and "red." stand for the oxidised and reduced forms of the substrate and their interconversion is catalysed by the active site, driven by the applied potential.

As shown in Figure 1-5, the direction of the catalysis or the interconversion of the oxidised (ox.) and reduced (red.) forms of the substrate is controlled by the applied potential, obeying the Nernst equation. The Nernst equation defines an equilibrium potential or a formal potential E^o under each set of conditions at which there is no net current as the couple (ox. and red.) is in equilibrium. When the applied potential is above E^o, the reaction of oxidation ($\text{red.} \rightarrow \text{ox.} + \text{ne}^-$) occurs at the electrode to re-adjust the ratio of the couple in the electrolyte and electrons flow to the electrode.[70] Take the $2H^+/H_2$ couple for example. Their interconversion, along with the corresponding Nernst equation (more details in Chapter 2) is shown as eqns [1-4] and [1-5].[55]

$$2\text{H}^+(\text{pH } 0) + 2\text{e}^- \leftrightarrow \text{H}_2 \ (1 \text{ bar H}_2), \quad E^o = 0 \text{ V} \qquad [1\text{-}4]$$

$$E = E^o + \frac{2.3\text{RT}}{\text{nF}} \log\{(\alpha\text{H}^+)^2/\rho(\text{H}_2)\} \qquad [1\text{-}5]$$

where αH^+ is the activity of H^+ (where pH = -log αH^+), $\rho(H_2)$ is the H_2 partial pressure, n is number of electrons involved in the electrode reaction (n = 2 for the interconversion of $2H^+/H_2$), F is the Faraday constant, R is the gas constant and T is the absolute temperature.

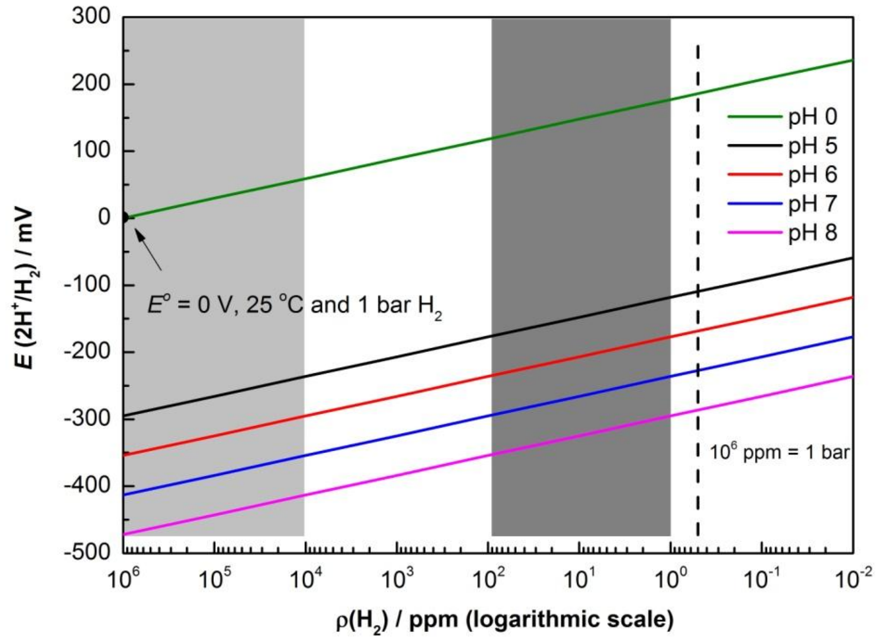

Figure 1-6. Plot showing how *E* ($2H^+/H_2$) is dependent on pH (pH 0 and pH 5-8) and H_2 pressure (0.01 to 10^6 ppm) at 25 °C, based on the Nernst equation. The H_2 partial pressure is in logarithmic scale. The light grey area indicates the H_2 levels usually used in electrochemical experiments,[55] the dark grey part area represents the H_2 levels possibly experienced in the soil as shown in Figure 1-1, and the dashed black line indicates the atmospheric H_2 level (0.5 ppm).

The standard hydrogen electrode (SHE) which is a common reference in electrochemistry represents a potential 0 V, as shown in eqn [1-4], provided by an aqueous solution at pH 0, 25 °C, in equilibrium with 1 bar gaseous H_2. This is also indicated by a black arrow in Figure 1-6. Figure 1-6 shows how the formal potential *E* ($2H^+/H_2$) is dependent on pH and the H_2 partial pressure. According to eqn [1-5], given a certain H_2 partial pressure, *E* ($2H^+/H_2$) decreases as pH increases at a rate of -59.8 mV/pH unit. On the other hand, given a certain pH, *E* ($2H^+/H_2$) increases as the H_2 partial pressure decreases.

The intramolecular electron transfer to and from the buried active site of the enzyme through several electron relay centres can be optimised by minimizing the tunnelling barriers. In NiFe hydrogenases, as discussed above, the distance between pairs of the three FeS clusters (the electron transfer centres) is within 12 Å, suitable for electron tunnelling at rates appropriate to sustain catalysis.[71] Although the medial 3Fe4S cluster has a relatively high reduction potential compared to the other two, the mutagenesis by converting it to a 4Fe4S cluster does not enhance the enzyme activity, implying that H_2 oxidation in the wild-type enzyme is not limited by the intramolecular electron transfer through the FeS cluster centres.[48]

When the interfacial electron transfer between the adsorbed protein and the electrode is fast to meet the Nernst requirement, only minimal overpotential is required to drive the reaction and an observable current occurs in voltammetry very close to E^o of the substrate couple (ox. and red.).[56] On the other hand, when the interfacial electron transfer is not as fast as the intramolecular electron transfer, a sizable overpotential in voltammetry then is required to observe the current. For a NiFe hydrogenase, the distal FeS cluster is expected to be involved in the interfacial electron transfer with the electrode. In order to obtain a fast interfacial electron transfer, the distal FeS cluster should be as close as possible to the electrode, i.e., an effective orientation is required to minimise the tunnelling barrier. However, in reality, a variety of orientations of the enzyme adsorbed on the electrode are expected, causing a dispersion in the interfacial electron transfer rates which contributes to an extended potential dependence in the voltammetry.[72,73] A further study on a variant with a modified distal FeS in *Df* NiFe hydrogenase showed that the enzyme activity was affected due to an impaired electron transfer and a sizable overpotential is required to observe H_2 oxidation. However, adding exogenous imidazole can restore the enzyme activity and minimise the overpotential requirement, implying that the interfacial electron transfer is damaged in the variant.[50]

Provided that the interfacial and intramolecular electron transfers are optimised, the overall catalysis by the enzyme can also be limited by substrate supply or product removal.[55] However, the effect of the mass transport to/from the enzyme film can be minimised by rotating the electrode at high rate. The Levich eqn [1-6] reflects the relationship between the current at a planar rotating disc electrode and the rotation rate.[70]

$$i_{(w)} = 0.62nFAD^{2/3}v^{-1/6}\omega^{1/2}C \qquad [1\text{-}6]$$

where D is the diffusion coefficient of the substrate, v is the kinematic viscosity of the solvent, ω is the electrode rotation speed, C is the concentration of the substrate.

It can be predicted from eqn [1-6] that the current is proportional to the square root of the rotation rate. However, at high rotation rates, current becomes limited by the activity of the enzyme adsorbed on the electrode and the observed current obeys the Koutecky-Levich eqn [1-7],[70]

$$\frac{1}{i_{\lim(\omega)}} = \frac{1}{i_{lim}} + \frac{1}{0.62nFAD^{2/3}v^{-1/6}\omega^{1/2}C} \qquad [1\text{-}7]$$

where $i_{lim(w)}$ is the limiting current at rotation rate ω and i_{lim} is the maximum limiting current extrapolated for infinite rotation rate.

In practice, a rotation speed is applied above which the catalytic current no longer increases significantly as ω is increased. If the active enzyme coverage or activity on the electrode is low, then mass transport control is likely not to exist, and rotation may not be necessary in order to supply sufficient substrate.

Investigation of H_2 cycling by PFE

Protein film electrochemistry has been widely applied to study NiFe and FeFe hydrogenases, such as *Allochromatium vinosum* membrane-bound NiFe hydrogenase (*Av* MBH)[64-66,74-76], *Df* NiFe hydrogenase[50,61,76], *Desulfovibrio Desulfuricans* FeFe hydrogenase[75,77,78], *D. gigas* NiFe hydrogenase[75], *Dv* MF NiFe hydrogenase[79], *Clostridium acetobutylicum* FeFe hydrogenase[76,78,80,81], *Ralstonia eutropha* membrane-bound NiFe hydrogenase (*Re* MBH)[10,76,82,83], *Ralstonia metallidurans* NiFe hydrogenase[76,83], *Salmonella* NiFe hydrogenase[84], *Escherichia coli* membrane-bound NiFe hydrogenase 1 and 2 (*E. coli* Hyd-1, Hyd-2)[85,86], *Aquifex aeolicus* membrane-bound NiFe hydrogenase I (*Aa* MBH I)[87,88], *Dm. b* NiFeSe hydrogenase[89], *Synechocystis sp.* PCC 6803 NiFe hydrogenase[90] and *Chlamydomonas reinhardtii* FeFe hydrogenase[76,78,80,91].

For a hydrogenase immobilised on an electrode, the current measured is directly proportional to the activity or the turnover frequency of the enzyme, providing that interfacial electron transfer and mass transport are not limited. High speed rotation of the electrode is usually required to exclude the diffusion control of the substrate (transport of H_2 or H^+ in this case). The oxidation or reduction current, as the indicator of the reaction catalysed by the enzyme, can easily be measured by scanning or stepping the electrode potential in PFE, as shown in Figure 1-7. Furthermore, information about the overpotential requirement for catalysis of H_2 oxidation or H^+ reduction by a specific hydrogenase can be obtained by comparing the onset potential for these reactions with the thermodynamic E ($2H^+/H_2$) corrected for the experimental condition. This is an important parameter for examining how efficiently the hydrogenase is able to catalyse the reversible reaction $H_2 \leftrightarrow 2H^+ + 2e^-$ *in vivo*. Given the same driving force for H_2 oxidation and H^+ reduction above and below E ($2H^+/H_2$), the catalytic bias of the enzyme can also be measured under a certain set of conditions. Léger *et al.* reported a method to measure the affinity of a hydrogenase for its substrate H_2 using PFE.[61] Since the catalytic current for H_2 oxidation is changing as a function of the concentration of H_2, the current at different concentrations of H_2 fitted to the Michaelis-Menten equation is used to quantify the affinity for H_2. This method can also be used for measuring the inhibition constants for inhibitors such as CO and O_2.[62,68]

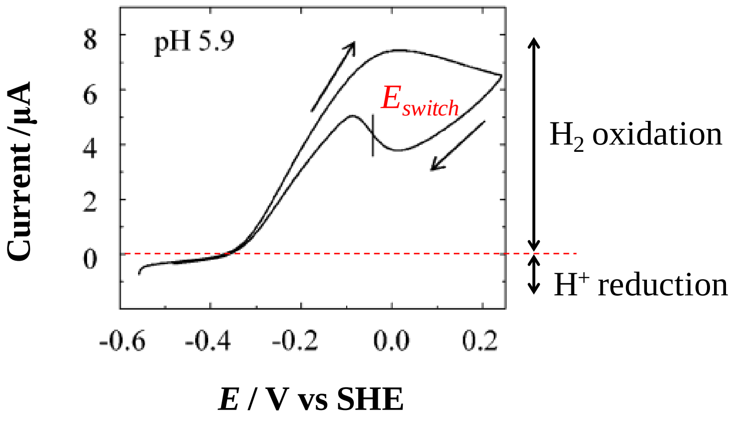

Figure 1-7. A cyclic voltammogram of *Av* MBH adsorbed on a PGE electrode. Other conditions: 1 bar H_2, 0.3 mV/s, electrode rotation rate 2500 rpm and 48 °C. Adapted with permission from reference 64. Copyright 2003 American Chemical Society.

For most NiFe and FeFe hydrogenases, in the presence of substrate, the enzyme will switch off the activity for H_2 oxidation when the potential is scanned to a high value in the oxidative direction. On the reverse scan, it will switch back on again, as shown in Figure 1-7. This is termed reversible anaerobic oxidative inactivation.[64] A switch potential E_{switch} has been defined as the potential of the maximum slope in the reductive activation direction, as shown in Figure 1-7. This is a characteristic parameter for a hydrogenase given that the scan rate is relatively slow compared to the recovery rate, and providing data are collected at the same scan rate E_{switch} can be compared for a set of hydrogenases or for a particular hydrogenase under different conditions. Electrochemical results show that this reductive activation is an e^-/H^+ coupled process.[55,79] Further information on the kinetics of the inactivation and reactivation processes can be achieved by stepping the potential between the active and inactive region and using a semilog plot of the current trace to determine first-order reaction rate. In general, it has been found the oxidative inactivation is slow whereas the reversible reductive reactivation is fast and a clean first-order reaction.[64] In more detail, the anaerobic oxidative inactivation is a chemical/electrochemical (CE) reaction, i.e., a slow chemical step (binding of an OH^-) precedes an electrochemical step (loss of an e^-) whereas the reductive reactivation is an EC reaction in which after receiving one electron (E) a quick removal of a hydroxide ligand (C) occurs.[55,92]

It should be pointed out that the turnover rate measured for H_2 oxidation or H^+ reduction by PFE for *Av* MBH is much higher than that observed in the solution assays.[74] This can be explained by the configuration of the enzyme adsorbed on the electrode which acts as an artificial redox partner. The catalytic activity is not limited by the slow diffusion-controlled electron transfer between the hydrogenase molecule and the dye in the solution assays. Furthermore, the high speed rotation of the working electrode in PFE enables the sufficient substrate (H_2) supply for H_2 oxidation and the removal of the product (H_2) for H^+ reduction. Compared to the solution assays, PFE can provide more information on the hydrogenase activity as it makes it possible to change the thermodynamic driving force by scanning or stepping potential and to easily tune the composition of the electrolyte.

1.8 Reaction of NiFe hydrogenases with O_2

NiFe hydrogenases from sulphate reducers are isolated in a mixture of inactive states referred to as Ni-A/Ni-B (spectroscopically labelled) or Unready/Ready which are kinetically named.[93-95] As shown in Figure 1-7, *Av* MBH, expressed by the microaerobic organism *Allochromatium vinosum*, has also been shown to exist in Ni-A/Ni-B mixtures as isolated.[27,28] This enzyme will be discussed in more detail because it has been widely studied.[27,28,64-66,96,97] Reaction of pre-activated NiFe hydrogenases with dioxygen O_2 also generates a mixture of these states.[98,99] The structure of the 'Ready' Ni-B in NiFe hydrogenases is well-established. Comparison of the calculated geometric data (the distance between Ni and Fe) and magnetic resonance parameter (*g* value) data obtained through DFT (Density Function Theory) calculations with the measured experimental data supports the conclusion that a bridging hydroxo ligand (OH^-) is between the Ni (III) and the Fe (II).[41,42,44] On the other hand, the structure of the 'Unready' Ni-A in NiFe hydrogenases is still controversial. Three structures comprising of a bridging peroxide (OOH^-),[44,65] a bridging hydroxide (OH^-) with a bridging Cys-SO^-[100] and a bridging hydroxide (OH^-) with a terminal Cys-SO^-[101] have been suggested. However, an isotope experiment with labelled ^{17}O did not support the Cys-SO^- related OH^- bridging form properly.[98,102] The 'Unready' Ni-A is assigned to be the OOH^- bridging form in this Thesis. This is consistent with the observations from protein film electrochemistry that the recovery potentials for the Ready and Unready states are very close or indistinguishable, as the hydroxide (OH^-) and peroxide (OOH^-) should exert similar electrostatic interactions with the active site.[55]

1.8.1 EPR investigation of NiFe hydrogenases

Introduction to electron paramagnetic resonance spectroscopy

Magnetic resonance methods including EPR (electron paramagnetic resonance), ENDOR (electron nuclear double resonance) and ESEEM (electron spin-echo envelope modulation) can be used to study metals that have unpaired electron(s) and provide a variety of information, such as the oxidation state and spin state of the metal, the *d*-orbital occupation, the symmetry of the crystal field, the type of ligands, the spin distribution and coupling with other metal centres.[103] On the other hand, a metal centre without any unpaired electrons is EPR-silent.

The active site of the NiFe hydrogenase consists of two transition metals Ni and Fe and different redox levels exist in the FeS clusters. Therefore, EPR and its related advanced techniques are powerful ways to investigate the redox states of the hydrogenase by measuring the electron-electron interaction and the electron-nuclear coupling. Figure 1-8 shows an overall picture of all the observed electron configurations of the Ni and the Fe at the active site of the NiFe hydrogenase during enzyme turnover. An unpaired electron spin adopts one of two orientations (parallel or antiparallel to the applied magnetic field), the '*g*-value' can be obtained by observing the field strength at which the electron resonates. The Fe site remains low spin Fe (II) throughout and is EPR-silent as there is no unpaired electron.[104,105] Therefore, EPR investigation of the NiFe hydrogenases is focused on the Ni site whose valence state shuffles between +1, +2 and +3, as shown in Figure 1-8. There is one unpaired electron in the low spin Ni (III) and Ni (I), therefore, the redox states in NiFe hydrogenases involving Ni (I) and (III) are EPR-active species. On the other hand, the low spin Ni (II) is EPR-silent.

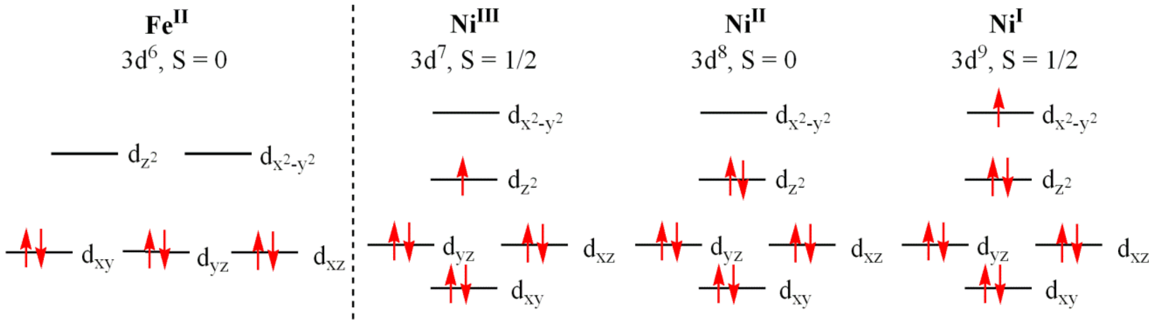

Figure 1-8. The electron configuration of low spin Fe (II), low spin Ni (III), Ni (II) and Ni (I) in the NiFe hydrogenase. For Ni, the *d* orbital splitting is based on the assumption that Ni is in a square pyramidal crystal field. The Fe (II) is assumed to be in an octahedral geometry.

Redox states in the so called ‘O_2-sensitive’ NiFe hydrogenases observed by EPR

O_2-inactivated states investigated by EPR

The NiFe hydrogenases are usually purified in air. The as-isolated enzyme is usually inactive for H_2 oxidation and exists in a mixture of at least two states characterised by different EPR signatures. They are termed Ni-A and Ni-B. It takes hours for the enzyme in the Ni-A state to restore its activity upon incubation with H_2. Therefore, this state has been named the ‘Unready’ state.[52] On the other hand, the enzyme in the Ni-B state only takes minutes or even seconds to be reactivated by H_2 and is therefore called the ‘Ready’ state.[52] The Ni ion in either Ni-A or Ni-B is Ni (III), therefore EPR-active, as depicted in Figure 1-8. Figure 1-9 shows EPR spectra of the Ni-A (Unready) and Ni-B (Ready) states of *Av* MBH. The redox titration analysis on the *D. gigas* NiFe hydrogenase and *Av* MBH showed that one-electron reduction of Ni-A or Ni-B leads to an EPR-silent state. Furthermore, the transition of Ni-A or Ni-B to the corresponding EPR-silent state is pH dependent, proving it is a H^+/e^- coupled process.[93-95]

H_2 splitting at the active site investigated by EPR

Incubation of the NiFe hydrogenase with H_2 leads to a new state Ni-C, observed by EPR, as shown in Figure 1-9. It was proposed that Ni-C in *Dv* MF NiFe hydrogenase is a Ni (III) species with a hydride (H^-) bridging the Ni and Fe sites with a single electron located in the Ni d_{z^2} orbital. However, there was still no direct evidence to clarify the H^- coordination. The advanced ENDOR and ESEEM technique cannot be applied due to the complex spin-spin coupling of the Ni (III) with the reduced proximal iron sulphur cluster ($4Fe4S^{1+}$, EPR-active).[38] The Ni-C split spectrum in Figure 1-9 of *Av* MBH shows the spin-spin interaction with the proximal cluster at lower temperature.[34] A later EPR investigation of the regulatory hydrogenase from *Ralstonia eutropha* (*Re* RH) provided a better way of understanding the coordination chemistry of the hydride in the Ni-C state as the proximal iron sulphur cluster is EPR-silent under reducing conditions. Advanced ENDOR and ESEEM-HYSCORE (hyperfine sublevel correlation) techniques were applied and showed that the electron nuclear double resonance for hydrogen H is different from that for deuterium D. After exchange with D_2O or incubation of the enzyme with D_2, the corresponding H resonance disappears in the H region and a D resonance instead appears in the D region of the spectra, proving that in Ni-C state there is an exchangeable hydride bridging the Ni and Fe sites with a distance of 1.61 Å to the Ni.[43] Redox titration analysis on *D. gigas* NiFe hydrogenase showed that Ni-C is two-electrons more reduced than Ni-B, and that one-electron reduction of Ni-C leads to an EPR-silent state. These transition processes are also pH-dependent.[47,95,106,107]

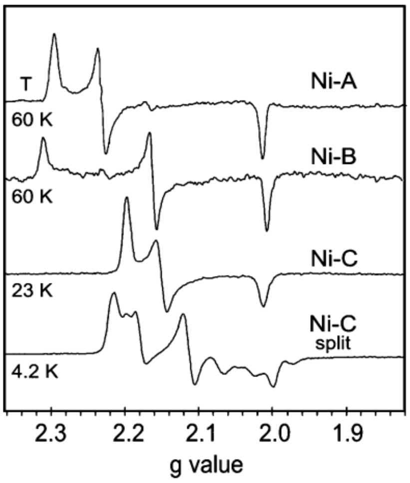

Figure 1-9. EPR spectra of the Ni-A (Unready), Ni-B (Ready) and Ni-C states of *Av* MBH. Adapted with permission from reference 34. Copyright 2007 American Chemical Society.

The splitting of H_2 occurring at the active site of NiFe hydrogenases is believed to proceed through a heterolytic mechanism. A hydride and a proton are first extracted from the molecule H_2. The hydride then bridges the Ni and Fe, as discussed above. The proton is removed by a nearby base, presumably by an amino acid side chain. Then the electrons from the hydride are transferred to FeS clusters and a second proton is produced.[108] Therefore, it requires an active site with a base to balance the H^+ produced, a hydride (H^-) acceptor and an efficient electron relay.

Light-triggered state Ni-L

The formation of an artificial state Ni-L is closely related to Ni-C. At low temperatures, illumination of Ni-C generates a Ni-L state after losing the bridging hydride.[38,43,109,110] Notably, the oxidation state of Ni in Ni-L is believed to be + 1 which is also an EPR-active state with a single electron located in the Ni $d_{x^2-y^2}$ orbital, as shown in Figure 1-8.

In summary, Ni-A (Unready), Ni-B (Ready) and Ni-C (an active state relating to H_2 activation) in the so called 'O_2-sensitive' NiFe hydrogenases are EPR-active species and Ni (III) is in a low spin state. In the Ni-L state, Ni (I) is also an EPR-active species. In the reduced state Ni-SR (reduction of Ni-C), Ni-SI (one electron reduction of Ready state) and Ni-SU (one electron reduction of Unready state) states, Ni (II) is in a low spin state and EPR silent as there is no unpaired electron. The transition process relating to the reduction of Ni-A, Ni-B or Ni-C is pH-dependent, demonstrating an e^-/H^+ coupled process.

1.8.2 A case study by PFE - Reaction of *Av* MBH with O_2

As mentioned above, the so called 'O_2-sensitive' NiFe hydrogenases react with O_2 to generate at least two inactive states, known as Ni-A (Unready) and Ni-B (Ready). It is possible to introduce O_2 during a PFE experiment to study these states providing that O_2 is introduced above 0 V vs. SHE to avoid direct reduction of O_2 at the graphite electrode. At a high potential in the presence of H_2, the activity of *Av* MBH can be monitored after introducing O_2, as shown in Figure 1-10. Clearly, the enzyme activity for H_2 oxidation is immediately diminished after O_2 injection at +214 mV. The activity cannot be restored even after most of the O_2 is removed until a low reductive potential is applied: the current increases immediately after the potential is stepped to -108 mV. Furthermore, this reductive activation process consists of two phases, i.e., a fast reactivation within a few seconds and a slow reactivation within a couple of hundreds of seconds. The clear kinetic difference in the two recovery phases is in line with the findings by EPR, as described above. Therefore, the fast and slow recovery phases observed by PFE correspond to the reactivation process of Ni-B (Ready) and Ni-A (Unready), respectively, as shown in Figure 1-10.[65] Furthermore, by comparing the enzyme activity at the same potential before introducing O_2 and after recovery, the extent of the reactivation can also be examined.[75]

There is a small fraction of activity lost permanently, even when a very long reductive poise is applied.

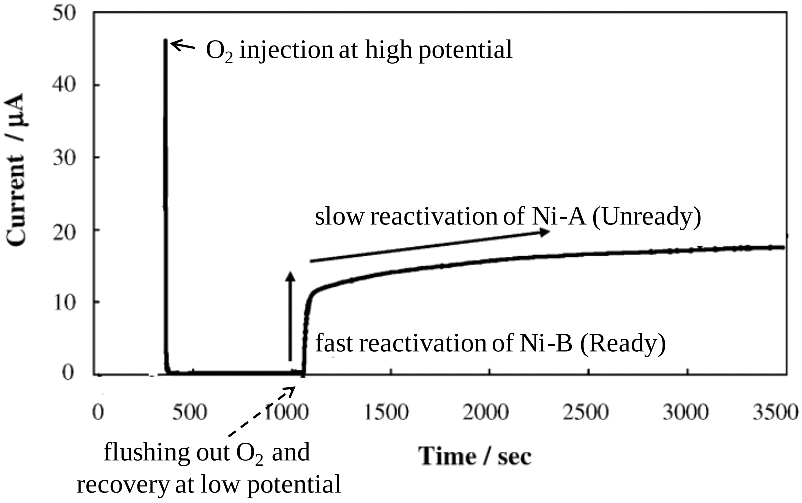

Figure 1-10. Current-time trace showing inactivation by O_2 at high potential and the recovery after flushing out O_2 at low potential on a film of *Av* MBH formed on a PGE electrode under H_2. Two-phase recovery kinetics were observed, with the fast reactivation phase corresponding to reactivation of the Ready (Ni-B) state, and the slow reactivation representing the recovery of the Unready (Ni-A) state. Adapted with permission from reference 65. Copyright 2004 American Chemical Society.

Further experiments under different conditions (the electrolyte pH, O_2 injection potential, the partial pressure of H_2) were performed to examine the environment that favours formation of Ni-A (Unready) or Ni-B (Ready). When the O_2 is injected at a lower potential (electron-rich conditions) or under higher partial pressure of H_2 (H_2 itself is a reducing agent), it favours formation of the Ni-B (Ready). In contrast, exposure to O_2 in the absence of H_2 favours formation of Ni-A, as shown in Figure 1-11.[55,66,92] For the NiFe hydrogenases, anaerobic inactivation at high potentials also generates the Ni-B state, as shown in Figure 1-7.[64] Furthermore, kinetics and potential for reactivation of Ni-B formed by O_2 are indistinguishable from the state generated anaerobically at high potential.

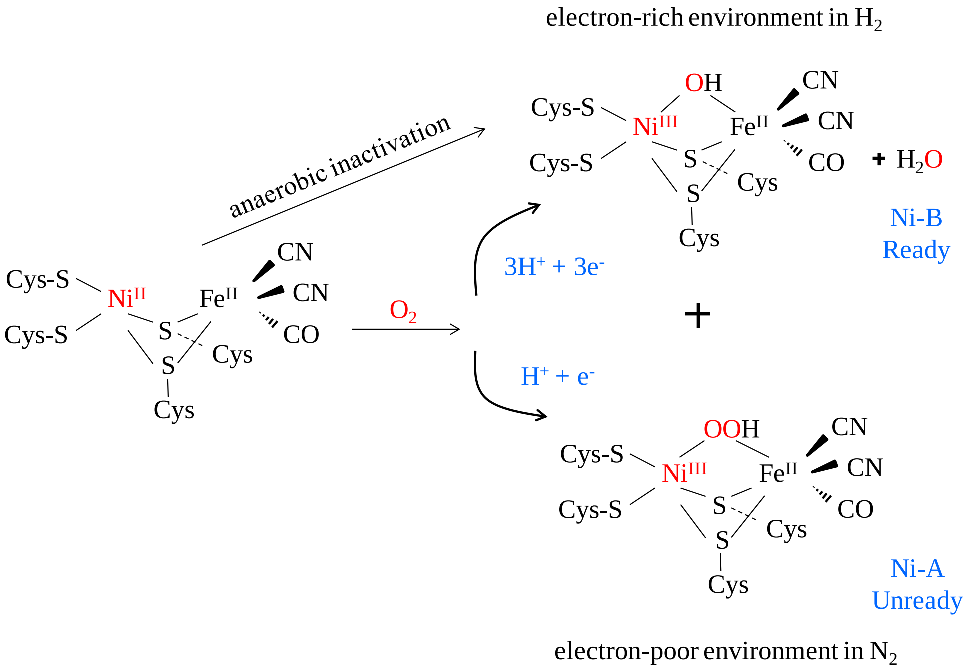

Figure 1-11. A scheme for the reaction of an active 'O_2-sensitive' NiFe hydrogenase with O_2.

1.8.3 Infrared spectroscopic investigation of the 'O_2-sensitive' NiFe hydrogenases

Introduction to Infrared spectroscopy

The ligands CO and CN^- at the active site of hydrogenases provide another important way to investigate the redox states as they give rise to infrared (IR) active vibrations, the frequency of which reflects the electronic environment of the metals at the active site. Furthermore, all states of the hydrogenases show different infrared spectra no matter whether there is an unpaired electron or not, therefore complementing the information obtained from EPR.[23] For the investigation of the active centre of a NiFe hydrogenase, EPR offers useful information on the Ni site whereas IR directly monitors the electronic environment of the Fe site through the vibrational frequencies of the CO and CN^- ligands. Although the Fe site remains formally Fe (II) throughout, it is sensitive to changes in electron density at the Ni or coordination of additional ligands.

Bagley and Albracht *et al.* first applied Fourier Transform Infrared (FTIR) spectroscopy to *Av* (formerly termed *Chromatium vinosum*) MBH and found a set of three absorption bands in the region 2150 ~ 1850 cm^{-1} of the infrared spectrum.[27,28] This study was carried out even before the X-ray crystallographic structure of the *D. gigas* NiFe hydrogenase was published. Later on, Bagley *et al.* cultivated *A. vinosum* cells on ^{13}C or ^{15}N labelled sources so the Fe at the active site was coordinated with the labelled ligands (^{13}CO, $^{13}CN^-$ or CO, $C^{15}N^-$). This confirmed that the low spin Fe (II) in the active site is coordinated with biologically unusual, non-exchangeable and intrinsic ligands, 2 CN^- and 1 CO, complementing the crystallographic information of the three diatomic ligands on Fe as analysis of the electron density map cannot distinguish CO and CN^-.[29] They later used an FTIR instrument equipped with a stopped-flow functionality to gain more detailed kinetic information on the transition of Ni-A/Ni-SU and Ni-B/Ni-SI. It was found that the Ni-A was converted at a very slow rate whereas the transition of Ni-B is rapid, consistent with the EPR and PFE data.[96,99] Figure 1- **12** shows the infrared spectra of the Ni-A, Ni-B and Ni-C states of *D. gigas* NiFe hydrogenase: three absorption peaks corresponding to 2 CN^- and 1 CO ligands can be seen at each state.[111]

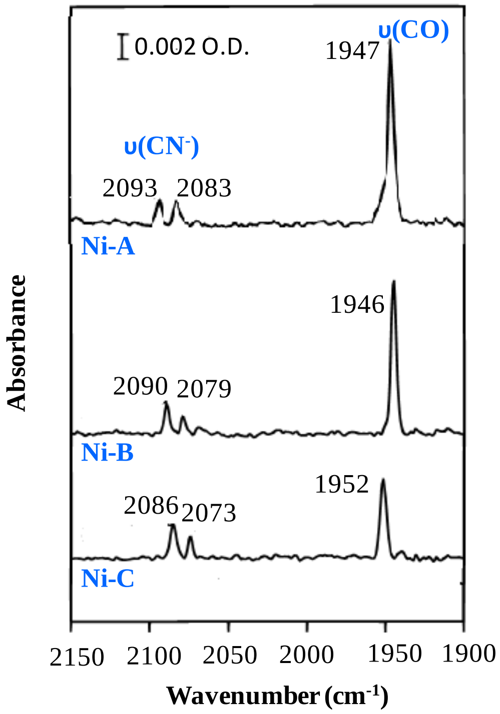

Figure 1- 12. Infrared spectra of *D. gigas* NiFe hydrogenase at Ni-A, Ni-B and Ni-C states. Adapted with permission from reference 111. Copyright 1997 American Chemical Society.

De Lacey *et al.* later applied an infrared spectroelectrochemistry technique based on the Moss transmission cell with few modifications.[111] The hydrogenase enzyme is dispersed in the buffer as a thin layer trapped in the cell, and a redox mediator cocktail which accelerates the electron transfer between the working electrode (Au mesh) and the enzyme is added to speed up the response to a potential step at the working electrode. Most subsequent infrared spectroscopic results on NiFe hydrogenases have been obtained using this technique.[37,112-114] Comparison of the vibrational frequencies of CO and CN^-, the midpoint potentials of transitions, pH-dependence and presence of the EPR-active species (Ni-A, Ni-B and Ni-C) of four so called 'O_2-sensitive' NiFe hydrogenases (*D. gigas*, *D. fructosovorans*, *D. vulgaris* Miyazaki F and *A. vinosum*) showed almost no differences.

Figure 1-13 represents a detailed redox state picture of *Dv* MF NiFe hydrogenase.[39] The as-isolated enzyme lies in a mixture of Ni-A and Ni-B states and is inactive for H_2 oxidation. One-electron reduction of Ni-A leads to formation of Ni-SU. The character "S" here stands for EPR-silent and "U" indicates unready. The midpoint potential for this transition is around -278 mV and this transition is found to be a proton-electron coupled process. Similarily, a one-electron reduction of Ni-B generates a state Ni-SI_I where "I" stands for inactive and this process requires an electron at around -151 mV which is slightly higher than that of the transition Ni-A/Ni-SU, implying that the Ni-B state can be reactivated under relatively mild reducing conditions. The silent ready state exists in two isoelectronic forms Ni-SI_I and Ni-SI_I', and the latter is believed to carry a bridging water instead of a hydroxide ligand between the Ni and Fe sites.[113] After obtaining the Ni-SI_{II} state (losing the bridging water from Ni-SI_I'), a further low potential electron is required to reduce it to Ni-C and this process is again coupled with a proton transfer. The Ni-C state which is obtained is EPR-active as explained above and one-electron reduction of Ni-C leads to a mixture of EPR-silent states Ni-$R_{I,II,III}$ that probably differ in their degree of protonation.[23]

Table 1 summarises the vibrational frequencies of CO and CN^- ligands at the active site of NiFe hydrogenases (*D. gigas, D. fructosovorans, D. vulgaris* MF and *A. vinosum*) for the redox states discussed above. The grey part of Table 1 also lists the vibrational frequencies of CO and CN^- ligands in two ‘O_2-tolerant’ NiFe hydrogenases: *Re* MBH and *Aa* MBH I. In contrast to the ‘O_2-sensitive’ NiFe hydrogenases, the greatest difference lies in the absence of the Unready state Ni-A. This is the common feature for *Re* MBH and *Aa* MBH I, implying that the so called ‘O_2-tolerant’ hydrogenases have a different mechanism to survive when O_2 attacks. More details will be discussed in **Section 1.10.**

This FTIR spectroelectrochemistry technique based on the Moss transmission cell has proved to be informative for studying the pH and potential effects on the transitions between different states, and is suitable for many of the redox states experienced by the enzyme. However, its biggest disadvantage is that the enzyme turnover is limited by the electron supply although mediators are added to accelerate this process. This means that the redox state of the enzyme cannot be controlled accurately under catalytic turnover, where reduction by H_2 competes with oxidation of hydrogenase by oxidised mediators generated at the electrode.

Zebger and co-workers applied a new infrared spectroelectrochemical technique called SEIRA (Surface Enhanced Infrared Reflection Absorption) spectroscopy to investigate NiFe hydrogenases recently.[115-117] Hydrogenase molecules were immobilised on the surface of gold through covalent binding to a functional self-assembled monolayer, and the gold served as the working electrode. The electron transfer between the enzyme and the working electrode should not be limited, therefore in theory the transitions between different redox states during full enzyme turnover can be observed by this method.[116] The observed stretching bands of the CO and CN^- ligands in *Dv* MF NiFe hydrogenase and *Re* MBH by this method are in agreement with those found in solution in the transmission cell.[115,117] However, it should be pointed out that the biggest challenge for this SEIRA technique is the immobilisation of the enzyme onto the gold while keeping the enzyme intact and compatible with the metal surface. It was found that only a small portion of the enzyme seemed to respond rapidly to the electrode potential, suggesting that many molecules were not in good electronic contact with the modified Au electrode.[116]

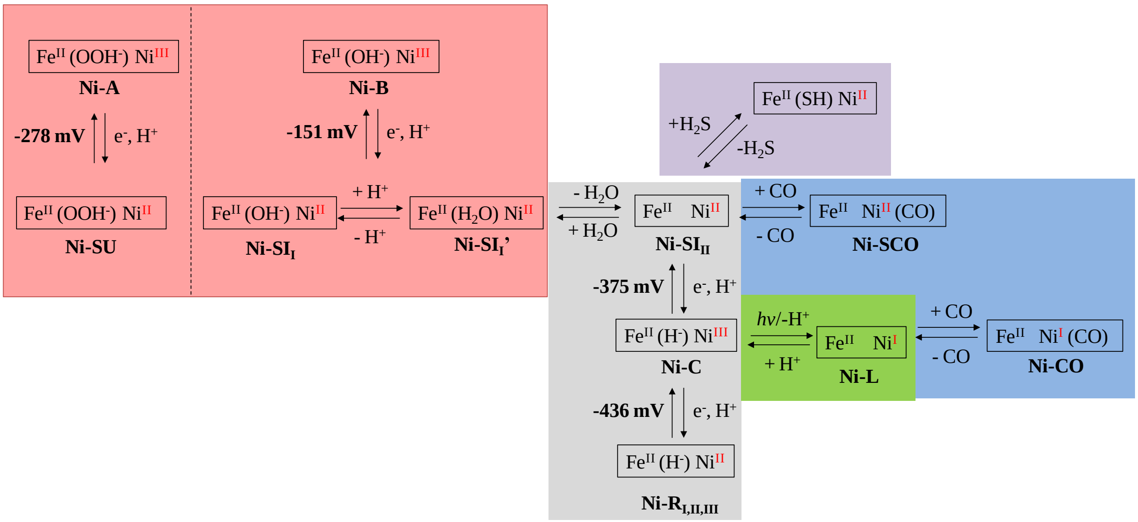

Figure 1-13. Scheme of the different redox states observed for the NiFe hydrogenase from *D. vulgaris* MF.[39,79] It can be divided by several boxes: the pink-red box represents the states related to O_2 exposure, the grey box represents the states involved in H_2 splitting, the blue box indicates CO-inhibited states, the purple box represents a sulphate-inhibited state and the green box represents a light-induced state(s).

1.9 Reactions of NiFe hydrogenases with other inhibitors

1.9.1 CO

Carbon monoxide CO is a meaningful inhibitor for studying the hydrogenases in two aspects. Firstly, it has a similar molecular size to O_2, therefore provides information about the diffusion kinetics of gas access.[68,69] Secondly, it is generally a reversible inhibitor for NiFe hydrogenases and behaves like a competitive inhibitor for H_2 oxidation, therefore may provide further information about H_2 binding at the active site.

Bagley and Albracht *et al.* found that exogenous CO can bind to *Av* MBH at its EPR-silent Ni(II) state and this CO-induced state is found to be light sensitive.[27] For the NiFe hydrogenases, it was suggested that Fe is the binding site for exogenous CO according to the DFT calculations.[118] However, later crystallographic evidence showed that distinct changes were observed in the electron density distribution of the Ni and the sulphur (one terminally bound cysteine ligand, Cys 546) atoms between the CO-bound and CO-free states.[119] Infrared spectroscopic evidence also showed that exogenous CO is probably bound to the Ni atom rather than Fe at the active site in the NiFe hydrogenases, as the wavenumber of exogenous CO is much higher (approximately 100 nm^{-1}) than that of the intrinsic CO ligand bound to Fe.[39,112,119] Table 1 also summarises the wavenumber of the vibrational band associated with exogenous CO-bound state Ni-SCO in some NiFe hydrogenases. The ‘S’ represents an EPR-silent state. Furthermore, it was also found by FTIR and EPR that there are two distinct CO-inhibited states, one is EPR-silent (Ni-SCO) and the other is a paramagnetic species (Ni-CO).[112,120] The EPR-detectable Ni-CO is formed by incubation of the Ni-L species with exogenous CO, rather than reaction of Ni-C with CO.[120] The reaction of the NiFe hydrogenase with CO is also summarised in Figure 1-13.

1.9.2 H_2S

A crystal structure of *Dv* MF NiFe hydrogenase in its oxidised state was obtained, but a bridging sulphur ligand was assigned at the active site, leading to controversy regarding the bridging ligand in the oxidised states of the NiFe hydrogenases.[36] In order to clarify the confusing bridging ligand at the active site, Vincent *et al.* examined the reaction of several NiFe hydrogenases from *D. vulgaris* MF, *D. gigas*, *D. fructosovorans* and *A. vinosum* with H_2S by protein film electrochemistry. It was found that sulphide can inactivate the NiFe hydrogenase at high potential and the corresponding sulphide-inhibited state, which is also summarised in Figure 1-13, can be reactivated at a higher potential than the O_2-inactivated state. Therefore, the findings by PFE are in line with the crystallographic results, but this sulphide-inhibited state is distinct from the O_2-inactivated state.[79] As *D. vulgaris* Miyazaki F is a sulphate-reducing bacterium, the exposure of its hydrogenase to H_2S during purification is not surprising and possibly generates a sulphur bridging ligand at the active site.

Table 1. Vibrational frequencies (cm^{-1}) of the CO and CN^{-} ligands coordinated on Fe at the active site of the NiFe hydrogenases in infrared spectra. The white part represents four ‘O$_2$-sensitive’ NiFe hydrogenases. The grey part represents two ‘O$_2$-tolerant’ NiFe hydrogenases: *Re* MBH and *Aa* MBH I.

redox	*D. gigas*[a]			*D. fructosovorans*[b]			*D. vulgaris* MF[c]			*A. vinosum*[d]			*Re* MBH [e]			*Aa* MBH I [f]		
state	ν(CO)	ν(CN)		ν(CO)	ν(CN)		ν(CO)	ν(CN)		ν(CO)	ν(CN)		ν(CO)	ν(CN)		ν(CO)	ν(CN)	
Ni-A	1947	2083	2093	1947	2084	2096	1956	2084	2094	1945	2082	2093	nd	nd		nd	nd	
Ni-B	1946	2079	2090	1946	2080	2091	1955	2081	2090	1943	2079	2090	1948	2081	2089	1939	2081	2092
Ni-C	1952	2073	2086	1951	2074	2086	1961	2074	2085	1951	2073	2085	1957	2075	2097	1949	2078	2088
Ni-SU	1950	2089	2099	1950	2091	2101	1946	2075	2086	1948	2088	2100	1943	2082	2104	nd	nd	
Ni-SI$_{I}$	1914	2055	2069	1913	2054	2069	1922	2056	2070	1910	2052	2067	1910	2055	2063	nd	nd	
Ni-SI$_{II}$	1934	2075	2086	1933	2074	2087	1943	2075	2086	1931	2073	2084	1936	2075	2093	1927	2077	2086
Ni-SCO	1932	2070	2083	1931	2069	2084	1941	2072	2086	1929	2069	2082	nd	nd		1925	2072	2082
	2056			2055			2061			2060						2066		
Ni-L	nd	nd		nd	nd		1911	2048	2061	1898	2044	2060	1899	2040	2065	1862[g]	2024	2045
																1900[h]	2049	2068
Ni-R$_{I}$	1940	2060	2073	1938	2060	2074	1948	2061	2074	1936	2059	2072	1948	2068	2087	nd	nd	
Ni-R$_{II}$	1923	2050	2060	1922	2051	2067	1933	nd		1921	2048	2064	1926	2049	2075	1910	2047	2066
Ni-R$_{III}$	nd	nd		nd	nd		1919	2050	2065	1913	2043	2058	1919	2046	2071	nd	nd	

[a] Data from ref[111]. [b] Data from ref[112]. [c] Data from ref[37,39]. [d] Data from refs[28,113]. [e] Data from ref[121]. [f] Data from refs[87,122,123]. [g] and [h] represent data obtained at 170 K and 100 K, respectively. nd represents not determined.

1.10 ‘O_2-tolerant’ NiFe hydrogenases?

The O_2-tolerant properties in NiFe hydrogenases are receiving more and more attention as their capability of functioning (catalysing H_2 oxidation or H^+ reduction) in the presence of O_2 is crucial for the H_2-based energy technologies, such as enzyme-based fuel cells or light-driven H_2 production.[124,125] In contrast to the so called ‘O_2-sensitive’ NiFe hydrogenases described as above, some NiFe hydrogenases such as *Re* MBH, *E. coli* Hyd-1 and *Aa* MBH I are found to be able to oxidise H_2 in the presence of O_2. Although later on, the so called O_2-sensitive NiFe hydrogenases are also capable of reducing H^+ in the presence of O_2 given the potential value is relatively low compared to the E_{switch}.[89,90] Some of the reasons for O_2 tolerance are gradually emerging. One clue is that the O_2-tolerant hydrogenases, such as *Re* MBH, *E. coli* Hyd-1 and *Aa* MBH I, only form Ni-B, i.e., lack Ni-A, as found by spectroscopy (FTIR and EPR) and PFE, when O_2 attacks.[85,87,121] As discussed above, Ni-B can be reactivated rapidly under mildly reducing conditions whereas Ni-A recovers slowly and requires more reducing conditions. In PFE, the slow phase recovery, as shown in Figure 1-10, is missing in *Re* MBH after O_2 attacks. Furthermore, due to a high value E_{switch}, the O_2-inactivated *Re* MBH recovers much faster at certain potentials than the ‘O_2-sensitive’ counterpart under analogous conditions.[10]

1.10.1 Observing and quantifying H_2 oxidation in the presence of O_2

Compared to the enzyme assays, protein film electrochemistry is a more direct and accurate way for measuring the H_2 oxidation activity of the hydrogenase in the presence of O_2. Although O_2 can be reduced below 0 V at a graphite electrode, the potential can be easily adjusted to avoid the O_2 reduction. The observed current at a constant potential (above 0 V) is directly proportional to the enzyme activity, therefore the H_2 oxidation activity of the enzyme (*Re* MBH) can be examined in the presence of O_2, as shown in Figure 1-14(B). As a control experiment, the enzyme activity for H_2 oxidation in *Av* MBH was completely inhibited by O_2 under analogous conditions, as shown in Figure 1-14(A). Furthermore, the affinity for the inhibitor O_2 ($K_{i(app)}^{O_2}$)

of *Re* MBH can also be obtained at a particular potential by injecting different amounts of O_2 and plotting the activity for H_2 oxidation as a function of O_2 concentration.[62,82] It can be used as a measurement of the O_2 tolerance for a hydrogenase and a high value $K_{i(app)}^{O_2}$ implies a high O_2 tolerance. In the enzyme assays, the H_2 uptake activity in the presence of O_2 will be affected by O_2 as the reduced MB or MV can be immediately re-oxidised by O_2, causing inaccuracy.

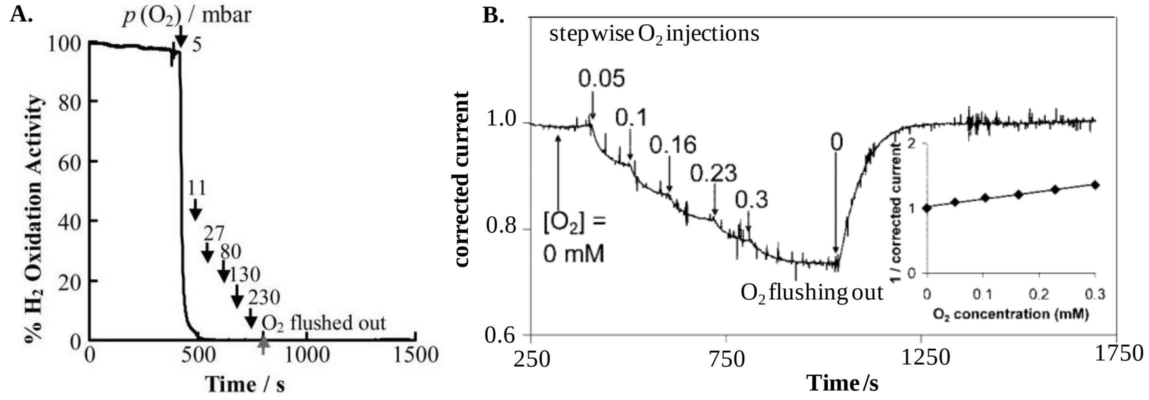

Figure 1-14. Panel A: Examining the reaction of *Av* MBH with O_2. Adapted with permission from reference 82. Copyright 2005 National Academy of Sciences, U.S.A. Panel B: Examining the H_2 oxidation activity of *Re* MBH in the presence of different O_2 partial pressure and obtaining the affinity for the inhibitor O_2. The inset shows a plot used to calculate the inhibition constant $K_{i(app)}^{O_2}$. Adapted with permission from reference 62. Copyright 2009 American Society for Biochemistry and Molecular Biology.

1.10.2 O_2 tolerance arising from limited gas access?

A hydrophobic gas channel in the NiFe hydrogenase from *D. gigas* and *D. fructosovorans* was first raised in 1997 by Fontecilla-Camps and co-workers. They exposed *Df* NiFe hydrogenase to 9 bar Xe and the corresponding X-ray diffraction data revealed 10 Xe molecules (Xe can be identified due to its high electron density) which was located within the putative gas channel formed by molecular dynamics calculations.[31] However, it should be pointed out that the Xe atoms are not close to the NiFe active site. The molecular dynamics calculations of the FeFe hydrogenases show that H_2 as a very small molecule can diffuse freely into the active site, not restricted by the putative gas channel. However, the inhibitors such as O_2 and CO have a larger size than H_2, and their diffusion may be restricted by the putative channel.[126,127]

In some NiFe hydrogenases (*D. gigas,*[26] *D. fructosovorans,*[128] *A. vinosum,*[97] and *Re* MBH[62]), the ends of the gas channel are gated by two conserved hydrophobic residues, valine (V) and leucine (L). However, in a subclass of H_2-sensing hydrogenases, such as *Re* RH and the HupUV proteins from *Rhodobacter capsulatus* and *Bradyrhizobium japonicum,* the conserved V and L are replaced by two more bulky residues isoleucine (I) and phenylalanine (F), respectively.[129,130] Volbeda *et al*. proposed that these two bulky residues I and F constructed a narrow bottleneck, therefore limiting the access of molecules larger than H_2 such as O_2 to the active site and contributing to the O_2 tolerance.[128] Furthermore, site-directed mutagenesis was performed on *Re* RH, converting the bulky residue I to V and F to L, in an attempt to widen the ends of the gas channel. All the variants (single mutation I62V or F110L and double mutation I62V/F110L) were affected by the presence of O_2, demonstrating that the removal of the bulky residue converted the O_2-tolerant *Re* RH to O_2-sensitive.[131] Therefore, this gas tunnel theory seemed to get support from the O_2 tolerance in *Re* RH.[131] However it should be noted that no crystal structure is available for wild type or variants of *Re* RH and these changes close to the active site could have other effects.

The same mutagenesis was performed in reverse in the wild-type *Re* MBH by converting the V77 and L125 to bulky residues I and F, respectively, expected to confer increased O_2 tolerance.[62] However, the variants are more O_2-sensitive than the wild-type protein, raising a doubt of the putative gas channel theory. Similarily, the same strategy was applied to the 'O_2-sensitive' *Df* NiFe hydrogenase to mimic the crowded environment near the Ni site in *Re* RH, however, the variant V74I/L122F is as O_2 sensitive as the wild type enzyme, although the CO diffusion rate is believed to be smaller than that in the wild type.[68,69,132] Even with regard to the gas access to the active site, the CO diffusion rate in the double variant V74M/L122M is found to be faster than that in the single variant V74M in *Df* NiFe hydrogenase, although the single variant is believed to have a wider gas channel near the end.[69] Interestingly, the variant V74M and V74C in *Df* NiFe hydrogenase showed improved O_2-tolerance although the amino acid, especially the cysteine (C) residue is not as bulky as I or F.[132,133] All the conversions between the 'O_2-sensitive' and 'O_2-tolerant' NiFe hydrogenase including the variants (involved in *Re* RH, *Re* MBH and *Df* NiFe hydrogenase) by site-directed mutagenesis discussed above are summarised in Table 2. In conclusion, the concept of O_2 tolerance arising from the limited gas access is doubtful.

Table 2. Inter-conversion between 'O_2-sensitive' and 'O_2-tolerant' behaviour of NiFe hydrogenases by site-directed mutagenesis near the Ni site in *Re* RH, *Re* MBH and *Df* hydrogenase.

	Re RH	*Re* MBH	*Df* hydrogenase
O_2-tolerant	**WT**[a]	**WT**[a]	V74M
			V74C
O_2-sensitive	I62V	V77I/L125F	**WT**[a]
	F110L		V74I/L122F
	I62V/F110L		

[a] wild type protein.

1.11 An 'O_2-tolerant' hydrogenase: *Re* MBH

1.11.1 The crystal structure

All the available crystal structures for NiFe hydrogenases prior to 2011 were obtained from the NiFe hydrogenases expressed by sulphate reducers, as described above. One exception is the *Av* MBH (at a 2.1 Å resolution) purified from a photosynthetic bacterium.[97] Recently the crystallographic structures of the membrane-bound NiFe hydrogenases from *Ralstonia eutropha*[134] and *Hydrogenovibrio marinus*[135] were revealed. In this Thesis, I mainly focus on reviewing *Re* MBH. It is a breakthrough to get the X-ray crystallographic structure of an O_2-tolerant NiFe hydrogenase at such a high resolution (1.5 Å) as the interpretations about the O_2 tolerance in the past are all based on extrapolation from the crystal structures of the NiFe hydrogenases from sulphate reducers.

In Figure 1-15(A), *Re* MBH shows a typical overall structure similar to *D. gigas* NiFe hydrogenase, i.e., it is also composed of two subunits: the large one houses the NiFe active site and the small subunit accommodates three FeS clusters. Furthermore, the active site of *Re* MBH is the same as that in other NiFe hydrogenases as described above, i.e. two cyanide (CN^-) and one carbonyl (CO) bound to the Fe site, two sulphur-cysteine ligands bridging the Ni and the Fe ions and two terminal sulphur-cysteine ligands coordinated on the Ni site. This finding also corresponds well with the previous infrared conclusion of a standard set of ligands at the active site.[82] This 'standard' active site implies that other factors rather than the coordination chemistry at the active site contribute to the O_2 tolerance.

The most different feature from the previously found NiFe counterparts is the proximal iron sulphur cluster, which is 4Fe3S rather than the conventional 4Fe4S. This unprecedented proximal 4Fe3S cluster was found near the Ni. Notably, three redox states were observed on this novel cluster by EPR. In the wild-type *Re* MBH, the proximal FeS cluster was found to have an additional high potential transition $4Fe3S^{5+/4+}$ apart from the low potential transition $4Fe3S^{4+/3+}$ by EPR measurements.[121,136,137] In EPR spectra taken at a high potential, a coupling was found both at the Ni(III) site and the oxidised medial $3Fe4S^+$ cluster (EPR active), implying a high-potential species exists between the active site and medial cluster, therefore the proximal 4Fe3S cluster is assigned to have an extra high potential redox transition. Normally FeS clusters in biology only cycle between two redox levels. A rare exception is the 4Fe4S cluster of the nitrogenase Fe protein which has been characterised in 3 redox levels (3+/2+, 2+/1+).[138] Furthermore, the two redox transitions in the 4Fe3S cluster of *Re* MBH undergo within an extraordinarily narrow potential window from -60 to +160 mV.[121] This physiological relevant potential window can be explained by the flexible 4Fe3S cluster conformation and the S-rich ligands bound to the Fe sites. Similarily, this extra high potential transition in the proximal FeS cluster is also found in other 'O_2-tolerant' hydrogenases, such as *E. coli* Hyd-1 and *Aa* MBH I.[86,139] Furthermore, the conformation of 4Fe3S proximal cluster was also found in the membrane-bound NiFe hydrogenase from *Hydrogenovibrio marinus*.[135] Therefore, this unique

4Fe3S cluster in *Re* MBH is closely related to the O_2 tolerance, as discussed below.

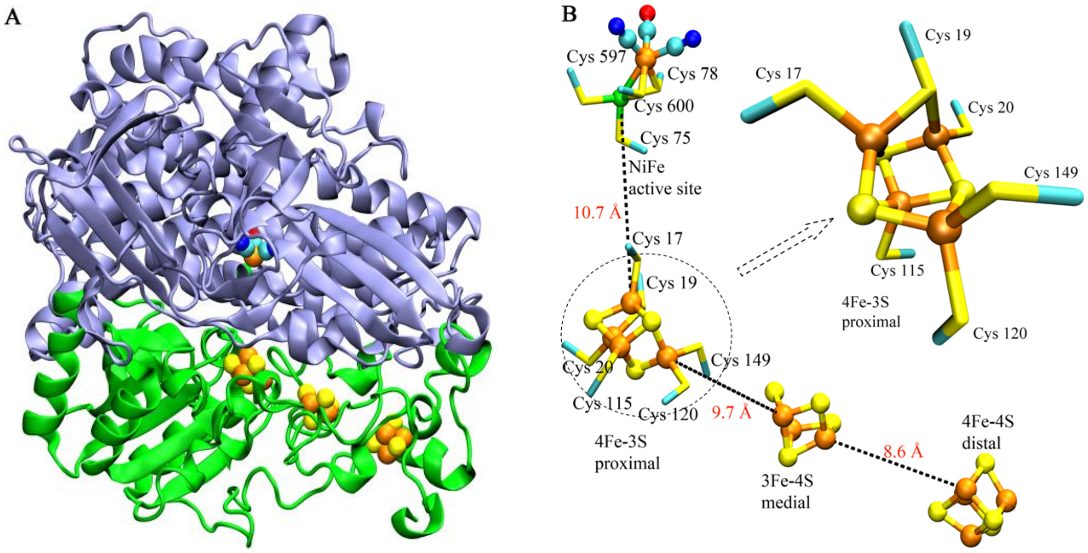

Figure 1-15. Panel A: The overall crystallographic structure of *Re* MBH (PDB: 3RGW; at a resolution of 1.5 Å).[134] Panel B: The enlargement of the active site and the iron-sulphur clusters.

1.11.2 The proximal FeS cluster and its relationship with O_2 tolerance

It was reported that O_2 can irreversibly damage the FeS clusters in FeFe hydrogenases.[7,140] However, very few studies on the reaction of O_2 with the FeS clusters in NiFe hydrogenases have been reported. So far, there was only one report about the oxidative damage of the proximal 4Fe4S cluster in NiFe hydrogenase from *D. desulfuricans* ATCC 27774.[32]

With the rising importance of the investigation of the 'O_2-tolerant' NiFe hydrogenases, more and more evidence has pointed to the relationship of the proximal iron sulphur cluster with the O_2 tolerance.[86,134,135,139,141] It was found that in *Re* MBH the proximal cluster 4Fe3S has six coordinated cysteines which are Cys20, Cys149, Cys115, Cys17, Cys19 and Cys120, in contrast to 4 cysteines (Cys20, Cys 148, Cys 112 and Cys 17) coordinated on the Fe site of the proximal 4Fe4S cluster in *D. gigas* NiFe hydrogenase, as shown in Figure 1-16. Therefore, there are two nonconserved cysteines (Cys19 and Cys120) in the *Re* MBH whereas the counterparts in *D. gigas* hydrogenase are Gly19 and Gly117.

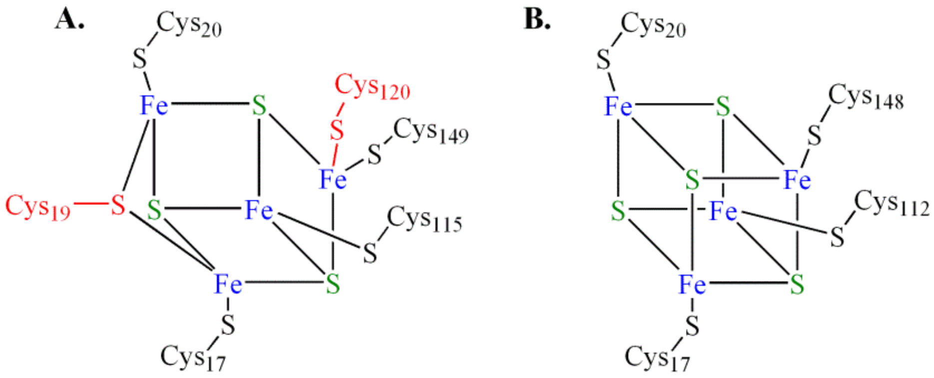

Figure 1-16. Schematic model of the proximal FeS cluster and the corresponding coordinating cysteine ligands. Panel A: The 4Fe3S cluster in *R. eutropha* MBH. Panel B: The 4Fe4S cluster in *D. gigas* NiFe hydrogenase.

A double variant (C19G/C120G) was constructed by Lenz and co-workers via replacing the nonconserved Cys with Gly residues to examine the function of the unusual coordination of the proximal FeS cluster.[141] Protein film electrochemistry experiments on the C19G/C120G variant and wild type MBH reveals that the variant behaves like wild type after exposure to O_2 for a short time but prolonged incubation with O_2 damages the variant, limits the accumulation of Ni-B species and forms a big portion of an irreversibly inactive state. The growth of the strain containing the mutation C19G/C120G is affected by the presence of O_2, whereas the wild-type strain growth is independent of O_2. Therefore, the variant C19G/C120G is indeed affected by O_2 especially after long-term exposure to O_2. The spectroscopic investigation by FTIR and EPR shows that the Unready Ni-A state is not observed in either wild-type or the variant. As described above, the fact that only the Ready Ni-B state is formed after exposure to O_2 in *Re* MBH is crucial for the enzyme to function in the presence of O_2 as Ni-B can be reactivated under mildly reducing conditions in a rapid manner. In order to avoid the formation of Ni-A in which a peroxide ligand is probably bridging between the Fe and the Ni site, sufficient and rapid electron flow is required to reduce O_2 which is a four electron process. As shown in Figure 1-11, the electron-rich condition favours the formation of Ni-B which requires three electrons. Although the Unready Ni-A state is not observed in the variant, the failure of accumulation of Ni-B and formation of a ‘dead’ state in the variant imply that the rapid and sufficient electron flow that exists in the wild type is damaged in the variant C19G/C120G as the coordination of the proximal FeS cluster is altered.

In the variant C19G/C120G, the complex coupling signal relating to the oxidised $4Fe3S^{5+}$ is missing, suggesting that this extra high potential transition may be crucial for the O_2 tolerance.[134] The reduction potentials of the FeS clusters in *Re* MBH are listed in Table 3, along with the counterparts in *D. gigas* NiFe hydrogenase. Compared to *D. gigas* hydrogenase which is connected with a *c*-type cytochrome as its *in vivo* redox partner, *Re* MBH is connected with a membrane-integral *b*-type cytochrome directly into the respiratory chain.[142] Clearly, the transition potentials for the FeS clusters in *Re* MBH are significantly more positive than those in *D. gigas* NiFe hydrogenase, an 'O_2-sensitive' NiFe hydrogenase. Therefore, *D. gigas* hydrogenase requires much lower potential electrons than *Re* MBH to reactivate the enzyme when O_2 attacks, i.e., electrons are more available to flow back to the active site in *Re* MBH. The structural flexible 4Fe3S proximal cluster may play dual roles: it receives electrons from the active site through the low potential transition $4Fe3S^{4+/3+}$ during enzyme turnover (H_2 oxidation) and delivers electrons to the active site through the high potential transition $4Fe3S^{5+/4+}$ when O_2 attacks.[134] This extra reducing force from the proximal iron-sulphur cluster through the high potential transition was also used to explain the O_2 tolerance of *Aa* MBH I.[139]

Table 3 Comparison of the midpoint potentials of the iron-sulphur clusters in the periplasmic NiFe hydrogenase from *D. gigas*[47] and *Re* MBH[137]

	E_m midpoint potential vs SHE *D. gigas* NiFe hydrogenase	E_m midpoint potential vs SHE *Re* MBH
in vivo redox partner	cyt *c* (-202 ~ -270 mV)[143]	cyt *b* (+10 ~ +160 mV)[142]
proximal FeS cluster	$4Fe4S^{2+/1+}$ (-340 mV)	$4Fe3S^{4+/3+}$ (-60 mV) $4Fe3S^{5+/4+}$(+160 mV)
medial FeS cluster	$3Fe4S^{1+/0}$(-70 mV)	$3Fe4S^{1+/0}$(+40 mV)
distal FeS cluster	$4Fe4S^{2+/1+}$(-290 mV)	$4Fe4S^{2+/1+}$(-180 mV)

A similar but more systematic investigation of the O_2-tolerant *E. coli* Hyd-1 was carried out by Lukey *et al*.[86] Although the crystal structure of the enzyme is not available yet, the authors constructed three variants with single mutations C120G, C19G and a double mutation C120G/C19G to mimic the coordination of the proximal FeS cluster in the 'O_2-sensitive' counterpart and clarify the individual contributions by C19 and C120. The C19G variant is O_2-sensitive whereas the C120G variant is O_2-tolerant, proving the C19 is a crucial amino acid residue for O_2 tolerance. The behaviour of the double variant C120G/C19G is similar to that of C19G. For the wild-type enzyme, no matter how long it is exposed to O_2, only Ni-B is formed. The O_2-tolerant variant C120G can still function in the presence of O_2 for 1 hour but forms some Ni-A in addition to Ni-B. In contrast, the C19G variant is very sensitive to O_2 and forms Ni-A and Ni-B. Additionally, a fraction of enzyme was found not to be recoverable even under very reducing potential for 10 hours. The double variant C120G/C19G is behaving similarly to the variant C120G/C19G in *Re* MBH in terms of the disappearance of the oxidised high potential transition of the proximal FeS cluster. However, the O_2-tolerant single variant C120G did not easily form the oxidised paramagnetic proximal FeS cluster even under very oxidising conditions. On the other hand, the O_2-sensitive single variant C19G presents the oxidised paramagnetic proximal cluster, in contrast to the double variant from this aspect. Therefore, this high potential transition of the proximal FeS cluster does not correlate with O_2 tolerance. Instead of delivering the extra electron by the proximal cluster, the authors raised the idea that O_2 tolerance correlates with the ease of formation of Ni-B which can be rapidly reactivated under mildly reducing conditions. The O_2-sensitive C19G variant exhibits a high switch potential E_{switch} like the wild-type and the C120G variant, implying that O_2 tolerance does not relate to E_{switch} but the latter is an important parameter for quantifying the ease of reducing Ni-B. The O_2 sensitivity in the C19G variant arises from the accumulation of an unrecoverable state and limited formation of Ni-B. By comparing the redox states in the C19G and C19G/C120G variants after prolonged exposure to O_2 under analogous conditions, more Ni-A is formed in the latter, implying that the C120 residue may play a role in long-term protection. A possible explanation was given by the authors that the C19 residue might improve the electron flow rate by lowering the reorganization energy of the proximal cluster or enhancing the electronic coupling with the active site when O_2 attacks.[86] A similar explanation for O_2 tolerance was made for the valine-to-cysteine mutation at position 74 in *Df* NiFe hydrogenase. This site-directed mutagenesis importantly converted the 'O_2-sensitive' *Df* NiFe hydrogenase into an O_2-tolerant enzyme. In the V74C variant, only Ni-B was formed after exposure to O_2 and the E_{switch} value is shifted more positive compared to the wild type, giving rise to a faster reactivation rate. Liebgott *et al.* ascribed the O_2 tolerance introduced by the cysteine residue to an improved electron flow towards the active site in response to O_2 attack.[133]

1.12 Three NiFe hydrogenases expressed by *Ralstonia eutropha* cells

Apart from *Re* MBH, the aerobic bacteria *Raltonia eutropha* produces two other NiFe hydrogenases: the soluble hydrogenase (SH) and the regulatory hydrogenase (RH).[11] Figure 1-17 shows the locations of the three NiFe hydrogenases in the cell, and their physiological roles. The MBH is anchored to the inner membrane and facing the periplasm. Furthermore, it is connected with the respiratory chain via a cytochrome *b*. The energy derived from H_2 oxidation catalysed by the MBH is stored as transmembrane H^+ gradient, and the electrons are transferred to a quinone pool where $O_{2,}$ as terminal electron acceptor, is reduced to H_2O.[144] The SH is located in the cytoplasm and consists of two catalytic moieties: a hydrogenase moiety and a diaphorase moiety. *In vivo*, the SH couples H_2 oxidation with NAD^+ reduction to produce the cell with reducing agent NADH which is involved in many biological processes.[145] The third RH is not involved in energy cycling, but is acting as a H_2 sensor to regulate the gene transcription in relation to the expression of the SH and MBH.[146]

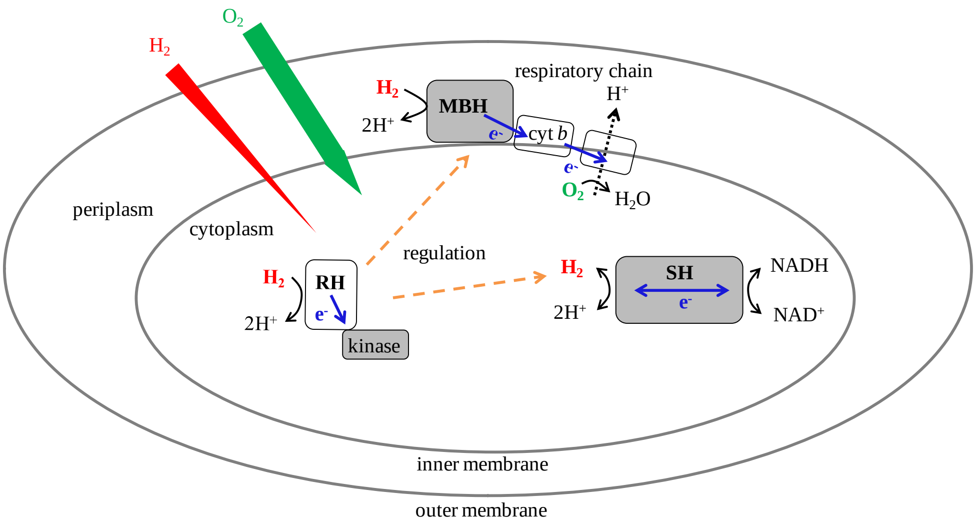

Figure 1-17. A schematic diagram showing three NiFe hydrogenases (RH: regulatory hydrogenase, SH: soluble hydrogenase, MBH: membrane-bound hydrogenase) in one *Ralstonia eutropha* cell. The microorganism lives on H_2 and O_2, and Nature designs an efficient way for the cell to cycle H_2 as an energy source and utilise O_2 as the final electron acceptor.

The aerobic organism such as *Ralstonia eutropha* lives in the upperland soil, as shown in Figure 1-1. This environment indicates very limited availability of H_2 and inevitable exposure of O_2, therefore forcing the bacteria to be capable of utilising low levels of H_2 and functioning in the presence of O_2. Along with the MBH, the SH and RH are also classified as 'O_2-tolerant' hydrogenases. In comparison with NiFe hydrogenases from sulphate reducers, the redox states experienced by the MBH, SH and RH are very different, especially when O_2 attacks. Table 4 summarises the redox states and the corresponding vibrational frequencies of the CO and CN^- ligands bound to Fe at the active site in the three enzymes. The MBH lacks Ni-A in contrast to the so called 'O_2-sensitive' hydrogenases when exposed to O_2. Furthermore, in addition to Ni-A, the Ready Ni-B state is also missing in the SH and RH when O_2 attacks, implying that these NiFe hydrogenases have their own ways to live in the aerobic environment.[62,147-149]

Table 4.Vibrational frequencies (cm^{-1}) of the CO and CN^{-} ligands coordinated on Fe at the active site of *Re* MBH, SH and RH.[62,147-149]

Redox States	MBH		SH		RH	
	υ(CO)	υ(CN^{-})	υ(CO)	υ(CN^{-})	υ(CO)	υ(CN^{-})
Ni-A	nd		nd		nd	
Ni-B	1948	2081/2089	nd		nd	
Ni-C	1957	2075/2097	1961	2080/2091	1962	2084/2072
'Ni-SU'	Ni$_u$-S		Ni-B like		nd	
	1943	2082/2104	1957	2079/2089		
'Ni-SI$_I$'	Ni$_r$-S		Ni-Ox1		Ni$_a$-S	
	1910	2055/2063	1956	2087/2096	1943	2081/2073
'Ni-SI$_{II}$'	Ni$_r$-S'		Ni-Ox2		nd	
	1936	2075/2093	1956	2052/2069		
Ni-L	1899	2040/2065	observed by EPR		nd	
Ni-CO	nd		observed by EPR		nd	
Ni-SR	1948	2068/2087	1946	2080/2090	nd	
Ni-SR'	1926	2049/2075	1922	2052/2068	nd	
Ni-SR''	1919	2046/2071	1913	2052/2068	nd	
Ni-SR2			1958	2068/2080	nd	

1.13 Applications of hydrogenases

Understanding H_2 cycling catalysed by hydrogenases and the capability of their functioning in the presence of O_2 is an important issue not only for basic scientific interest but also for possible applications of hydrogenases in the H_2-related energy field.[22,25,134,135,150-154] Furthermore, this may provide the fundamental knowledge for designing biomimetic artificial catalysts for large-scale hydrogen production.[155-160]

1.13.1 H_2 oxidation: enzyme-based fuel cell

In low temperature Proton Exchange Membrane Fuel Cells (PEMFCs) relying upon the oxidation of small organic molecules (HCOOH, CH_3OH and CH_3CH_2OH) or H_2, the catalyst used in the anode and cathode is typically based on the precious metal, platinum.[161-163] In biology, hydrogenases utilise the first-row transition metals (Ni and/or Fe) to catalyse H_2 cycling. The H_2 oxidation turnover rate catalysed by *Av* MBH adsorbed on a PGE electrode can reach 10, 000 s^{-1} per enzyme active site at 45 ^{o}C, which is comparable to that catalysed by Pt. Furthermore, the hydrogenase is less sensitive to CO poisoning than Pt.[74] With rising information on the O_2 and CO tolerant NiFe hydrogenases, the advantage of hydrogenases over Pt is more obvious apart from its high efficiency. If the enzyme can be operated in the presence of CO and O_2, it may replace the current precious metal Pt. Furthermore, this enzyme-based fuel cell can avoid the need for the expensive proton-transfer Nafion membrane which is used to separate the reactions in the anode and cathode, greatly reducing the cost. Several proof of concept hydrogenase-based fuel cells using different O_2-tolerant NiFe hydrogenases with low concentration of H_2 in the presence of O_2 or CO coupled with another O_2-reducing enzyme as the cathode catalyst have been set up by Armstrong and co-workers.[82,124,164,165]

1.13.2 H^+ reduction: photo-driven H_2 production

Dihydrogen H_2, as a high energy-density carrier, is a good option for the future energy strategy. Furthermore, the product of H_2 oxidation is water which is environment friendly. The NiFeSe hydrogenase from *Desulfomicrobium baculatum*, the NiFe hydrogenase from the *Ralstonia* species and even FeFe hydrogenases have been proved to be capable of reducing H^+ (H_2 production) in the presence of O_2,[80,83,89] which makes the production of H_2 in air possible. Reisner *et al.* developed a RuP/EDTA/TiO_2/H_2ase (RuP: $Ru(bpy)_2(H_4dpbyp)Br_2$, bpy: 2,2'-bipyridine, H_4dpbpy: 2,2'-bipyridine-4,4'-diylbis(phosphonic acid); EDTA: ethylenediaminetetraacetic acid) composite system to produce H_2 with the irradiation of the visible light.[125,166] Therefore, if the protein is stable over long times and can be produced in large scale, the biological production of H_2 with the help of sunlight is achievable and meaningful. This photochemical H_2 production set-up using O_2-tolerant H_2 producers moves closer to the photovoltaic generation of H_2 through the splitting of water.

1.13.3 Model compounds: Learning from the Nature

The active sites of the three unrelated classes of hydrogenses share the $Fe(CO)_x(SR)_y$ feature as discussed above. Driven by the possible application relating to the H_2 cycling in the energy field, extensive research has been carried out on the synthesis of model compounds incorporating the features of the CO, CN^- and thiolate coordination.[153,167-176] A very recent report shows that a synthetic Ni complex can catalyse the H_2 production with a turnover rate of over 100, 000 s^{-1} in the presence of water at a potential -0.49 V vs. SHE.[177] This turnover frequency exceeds that reported for H_2 production by the FeFe hydrogenase, 9, 000 s^{-1} at 30 ^oC.[178] However, this comparison is based on the fact that the overpotential of the enzyme is less than 100 mV, much lower than that in the synthesised complex. This still demonstrates a great promise of utilising the relative cheap and abundant first row transition metals to catalyse H_2 production for the future energy strategy.

1.13.4 Cofactor regeneration

In nature, hydrogenases are always connected with other redox partners. In *Re* SH, the electrons generated from H_2 oxidation by the hydrogenase moiety HoxHY can be passed to a diaphorase moiety HoxFU to reduce NAD^+, as described in **Section 1.7,** therefore the expensive cofactor NADH can be regenerated.[179] Similarly, hydrogenase I from *Pyrococcus furiosus* can regenerate an even more expensive cofactor NADPH at the expense of H_2 *in vivo* and *in vitro*.[180,181] A very recent study by Reeve *et al.* demonstrated that a NAD^+/NADH cycling enzyme adsorbed with a hydrogenase enzyme on pyrolytic graphite particles can carry out either the regeneration of NADH or NAD^+ using H_2 and H^+ as electron source or acceptor. The graphite particle is acting as an electric wire and the direction of cofactor regeneration can be tuned by appropriate choice of hydrogenase (H_2 oxidiser or H_2 producer) which is co-adsorbed on the particle.[182]

1.14 Aims and structure of this Thesis

1.14.1 Understanding H_2 cycling and O_2 tolerance of *Ralstonia eutropha* NiFe hydrogenases

In this Thesis, two NiFe hydrogenases (*Re* SH in Chapter 3 and *Re* RH in Chapter 4) are investigated by protein film electrochemistry. The MBH expressed by *R. eutropha* is so far the most extensively studied O_2-tolerant NiFe hydrogenase, as discussed above. The other two NiFe hydrogenases *Re* SH and *Re* RH are also classified as O_2-tolerant hydrogenases. In Chapter 3 and 4, the H_2 cycling and reaction with O_2 of the SH and RH will be explored by protein film electrochemistry. Furthermore, the O_2 tolerance mechanism of the SH and RH will be discussed and compared with other NiFe hydrogenases.

1.14.2 Developing a novel infrared spectroelectrochemical technique

Protein film electrochemistry has been proved to be a very sensitive and powerful tool to monitor enzyme activity as a function of potential and examine the reaction of enzymes with small molecules such as CO and O_2. In Chapter 4, CO and O_2 triggered states in the RH are for the first time identified by PFE. These states have not yet been identified using currently FTIR methods, possibly due to the slow electron transfer between the mediator and the hydrogenase in solution which compromises potential control. Therefore, a new technique is required by combining protein film electrochemistry and infrared spectroscopy to provide the structural evidence for the new observed states. The development of the new technique is not straightforward. In Chapter 5, carbon-supported noble metal nanoparticles (Pt, Pd and PtRu), mimicking the situation of the enzyme adsorbed on carbon particles, are applied to form a thin layer particle network acting as the working electrode and formic acid oxidation catalysed by the noble metal is tuned by direct electrochemical potential control. A flow capability is also developed in this technique to ensure sufficient substrate supply and to allow introduction of inhibitors. During the turnover, an important intermediate, CO, an infrared-active species, is formed, and its potential-dependent presence/absence is examined by infrared spectroscopy. In Chapter 6, some preliminary experiments using this infrared spectroelectrochemical technique developed in Chapter 5 were carried out to investigate the redox states of *Re* RH.

Chapter 2

Theory and Method

2.1 Theory

2.1.1 Protein film electrochemistry

In protein film electrochemistry, the current is proportional to the catalytic turnover rate of the enzyme. For hydrogenase protein film electrochemistry experiments, two main types of techniques are employed to measure the catalytic current as a function of the applied potential, concentration of the substrate and inhibitors. The first is cyclic voltammetry, in which the current is monitored while the potential is cycled between two limiting values. The second technique is chronoamperometry, in which the current is recorded as a function of time while the potential is stepped down or up or the composition of the substrate or inhibitor is changed.[92] Modern potentiostat softwares make it possible to combine sweeps and steps in a single experiment for more complex measurements.

Cyclic voltammetry experiment for studying hydrogenases

In electrochemistry, according to the IUPAC standard, a reduction current is always marked as negative and an oxidation current is positive. Figure 2-1 shows a sample representation of a cyclic voltammogram for a hydrogenase film (red trace). *Escherichia coli* Hyd-2 is chosen as a test system as it is good at both H_2 oxidation and H^+ reduction. Lukey *et al.* first characterised this enzyme using protein film electrochemistry.[85] An aliquot of *E. coli* Hyd-2 is spotted on the surface of a pyrolytic graphite 'edge' (PGE) electrode. The headspace gas is composed of 5% H_2 and 95% N_2 and high speed rotation is added to ensure substrate levels at the electrode at a similar concentration to that in the bulk and accelerate the exchange with the headspace gases. The enzyme modified electrode is poised at -550 mV for 300 seconds to reactivate the enzyme because it is purified in air.[85] A cyclic voltammogram of the bare electrode as a control experiment under analogous conditions is also shown as a black line in Figure 2-1. At the commencement of the scan indicated by a black arrow, the negative current corresponds to H^+ reduction. At low potentials, the electrode provides electrons to the enzyme to allow it to reduce

H^+. Thus the current is proportional to the activity of the enzyme, i.e., the bigger the current is, the more active the enzyme is as long as it is not limited by mass transport. As the potential is swept in the positive direction, the driving force for H^+ reduction is smaller and the corresponding current magnitude decreases. At the thermodynamic potential of the $2H^+/H_2$ indicated as a blue dashed line in Figure 2-1, *E. coli* Hyd-2 catalyses both H^+ reduction and H_2 oxidation at the same rate and the current trace cuts sharply the background scan. At potentials higher than E ($2H^+/H_2$), the positive current corresponds to H_2 oxidation. However, *E. coli* Hyd-2 switches off its activity for H_2 oxidation at very high potential. On its reverse scan, it will switch back on again at around -200 mV. This switching on/off behaviour is called reversible anaerobic oxidative inactivation. The cyclic voltammetry experiment provides a wide picture of H_2 oxidation and H^+ reduction catalysed by hydrogenases. Furthermore it can provide the information about the inactivation and reactivation experienced by the enzyme while the potential is swept.

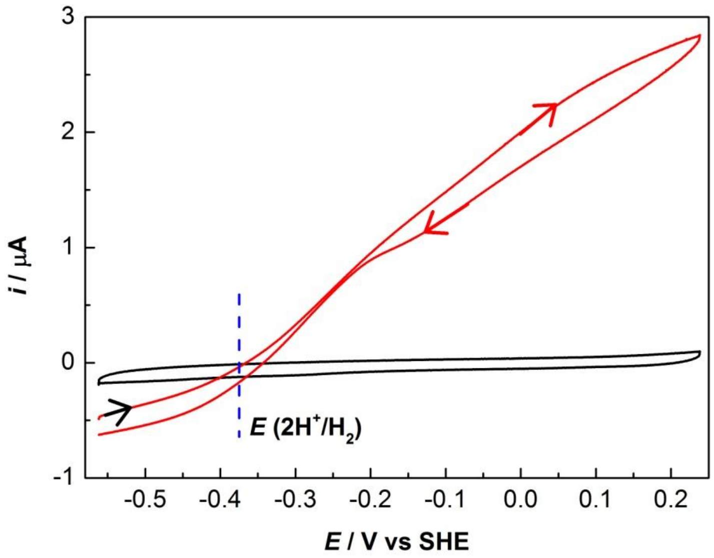

Figure 2-1. Cyclic voltammogram of *E. coli* Hyd-2 (red) on a PGE electrode in pH 7 KPB saturated with 5% H_2 : 95% N_2 at a scan rate of 10 mV/s. Other conditions: the rotation speed is 2500 rpm; the overall flow rate is 1000 mL/min; the direction of the scan is indicated by arrowheads; and the electrode is poised at -550 mV for 300 s to allow the enzyme to reactivate. A cyclic voltammogram at a bare electrode under analogous conditions is shown as the black line. The thermodynamic potential *E* ($2H^+/H_2$) corrected for the experimental condition, is shown as a blue dashed line.

Chronoamperometry experiment for studying hydrogenases

In chronoamperometry, the current-time trace can provide useful kinetic information following a perturbation. In Figure 2-2(A), the catalytic current, as a measure of the activity of the enzyme, changes immediately after injection of an inhibitor or stepping the potential to a value where the inactivation occurs. The kinetics of this inactivation is obtained through the changing current as a function of time. The reverse process after the removal of the inhibitor or stepping back to an activating potential, can also be observed and the corresponding kinetic information can therefore be obtained. In Chapter 3 and 4, the reaction of *Re* SH and RH with O_2 will be investigated using the chronoamperometry technique. Information such as the reaction order, the rate constant and half-life of the enzyme can be obtained through analysis of the inactivation kinetics. The detailed reaction kinetics will be described in **Section 2.1.5.**

The catalytic current is not only dependent on the activity of the enzyme, but also the concentration of the substrate or the inhibitor. Figure 2-2(B) depicts a stepwise change in current relating to the concentration of the substrate or the inhibitor. Through analysis of the relationship of the current with the concentration of the substrate or the inhibitor, the affinity for the substrate or inhibitor can be obtained. During this process, high speed rotation is required to ensure that the substrate/inhibitor level at the electrode is similar to that in the bulk and accelerate the gas exchange with the headspace above the electrolyte. In Chapter 4, the activity of *Re* RH for H_2 oxidation will be monitored following a stepwise change in the substrate (H_2) concentration, thus the affinity for H_2 can be obtained. The relationship of the enzyme activity with the substrate concentration will be described in more details in **Section 2.1.4.**

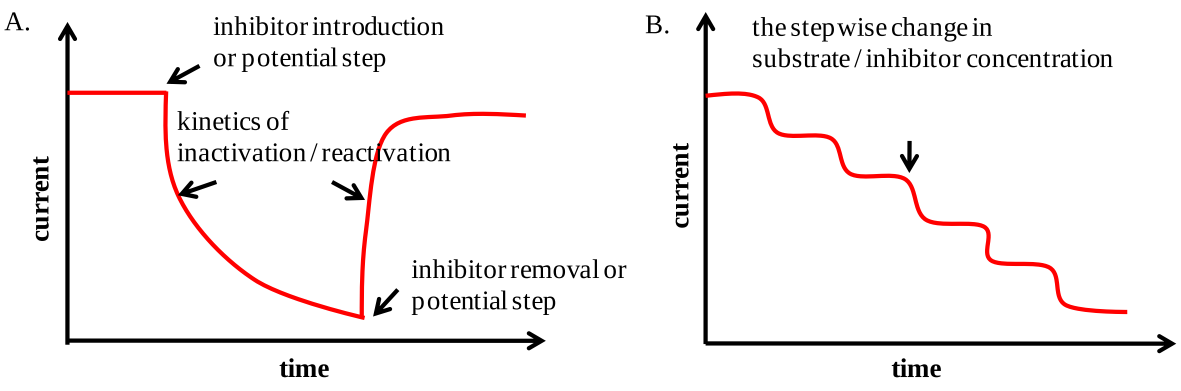

Figure 2-2. Schematic diagrams showing the current-time traces for different cases. Panel A: The current resulting from inactivation and reactivation of the enzyme in response to the applied potential or the presence/absence of an inhibitor; Panel B: The stepwise change in the current relating to a decrease in substrate concentration or an increase in inhibitor concentration.

2.1.2 Faradaic and non-Faradaic processes

Faradaic and non-Faradaic processes happen at the electrode-solution interface at the same time. Electrons transfer across the interface, which causes the reaction of oxidation or reduction to happen. The process obeys Faraday’s law (i.e., the amount of the chemical reaction which caused the flow of current is proportional to the amount of electrical current passed) and the current passed here is therefore called the Faradaic current.[70] However, under certain conditions, such as adsorption and desorption, current arises from a situation in which electrons do not transfer across the electrode-solution interface and this process is called a non-Faradaic process.[70] As the potential is changed, the electrode and the solution nearby behave like a capacitor (the current does not cross the interface), as shown in Figure 2-3. When a different potential is applied on the capacitor (the electrode-solution interface in this case), charge will leave or accumulate on the electrode, causing an external current to flow, and this external current is called charging current or capacitance current.

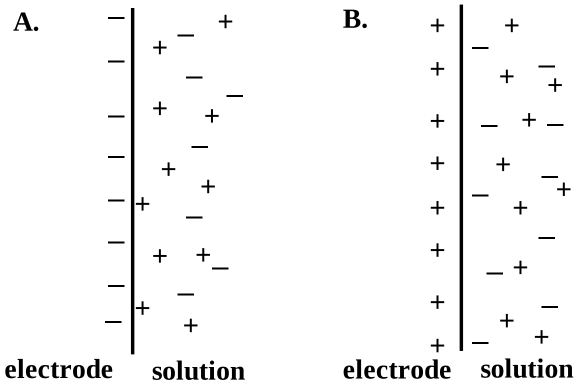

Figure 2-3. The electrode-solution interface as a capacitor with a charge on the electrode. Panel A: Negative charge on the electrode. Panel B: Positive charge on the electrode. Figure adapted from ref.[70].

In most cases, the Faradaic process is of our primary interest. However, when the currents arising from non-Faradaic and Faradaic processes are comparable, the effects of the non-Faradaic currents must be taken into account. In Chapter 3 and 4, *Re* SH and RH will be investigated by protein film electrochemistry. In contrast to some NiFe hydrogenases such as *E. coli* Hyd-1 and Hyd-2,[85] the enzyme activity for the SH and RH is two-fold lower in current magnitude, therefore, the capacitance contribution from the working electrode needs to be taken account of.

2.1.3 The Nernst Equation

In electrochemistry, the Nernst equation, as shown in eqn [2-1], is frequently used to look into the relation between the potential and the concentrations of the participants, determining the direction of the reaction or the interconversion of the oxidised (Ox) and reduced (Red) form of the reactant.

$$E = E^0 + \frac{RT}{nF}\ln\frac{[\mathrm{Ox}]}{[\mathrm{Red}]} \qquad [2\text{-}1]$$

where R is the gas constant, T is the absolute temperature, n is the number of the electrons involved in the reaction and F is Faraday constant (the charge of a mole of electrons).

Consider a reaction containing the oxidised and reduced forms of two different species, as shown in eqn [2-2]:

$$\mathrm{Ox_1} + \mathrm{Red_2} \leftrightarrow \mathrm{Red_1} + \mathrm{Ox_2} \qquad [2\text{-}2]$$

The overall reaction consists of two half-reactions, expressed as eqn [2-3] and [2-4]:

$$\mathrm{Ox_1} + ne^- \rightarrow \mathrm{Red_1} \qquad [2\text{-}3]$$

$$\mathrm{Red_2} \rightarrow \mathrm{Ox_2} + ne^- \qquad [2\text{-}4]$$

It is possible to measure the electron flow from $\mathrm{Red_2}$ to $\mathrm{Ox_1}$ by separating the two half-reactions in a two-compartment cell, i.e., the species 1 ($\mathrm{Ox_1}$ and $\mathrm{Red_1}$) in one and the species 2 ($\mathrm{Ox_2}$ and $\mathrm{Red_2}$) in the other compartment. Place two electrodes in each compartment and connect them. The electron flow is arising from the difference of E_1 and E_2 in each compartment, expressed as eqn [2-5] and [2-6]:

$$E_1 = E_1^0 + \frac{RT}{nF}\ln\frac{[\mathrm{Ox_1}]}{[\mathrm{Red_1}]} \qquad [2\text{-}5]$$

$$E_2 = E_2^0 + \frac{RT}{nF}\ln\frac{[\mathrm{Ox_2}]}{[\mathrm{Red_2}]} \qquad [2\text{-}6]$$

Another important relation between the potential and the Gibbs free energy is shown as follows [2-7]:

$$\Delta_r G^0 = -nFE_r^0 \qquad [2\text{-}7]$$

Therefore, the free energy of the reaction is given by eqn [2-8]:

$$\Delta_\mathrm{r} G = \Delta_\mathrm{r} G^0 + RT\ln\frac{[\mathrm{Red_1}][\mathrm{Ox_2}]}{[\mathrm{Ox_1}][\mathrm{Red_2}]} \qquad [2\text{-}8]$$

Initially, after a potential step, $\Delta_\mathrm{r} G$ is not zero (i.e., the system is not in equilibrium) and once the equilibrium is reached, $\Delta_\mathrm{r} G = 0$. An equilibrium constant K_{eq} is defined as follows eqn [2-9]:

$$K_{eq} = \frac{[\mathrm{Red_1}]_\mathrm{eq}[\mathrm{Ox_2}]_\mathrm{eq}}{[\mathrm{Red_2}]_\mathrm{eq}[\mathrm{Ox_2}]_\mathrm{eq}} \qquad [2\text{-}9]$$

Therefore, the concentrations of participants satisfy [2-10] obtained from eqn [2-7] and [2-8]:

$$K_{eq} = \frac{[\mathrm{Red_1}]_\mathrm{eq}[\mathrm{Ox_2}]_\mathrm{eq}}{[\mathrm{Red_2}]_\mathrm{eq}[\mathrm{Ox_2}]_\mathrm{eq}} = \exp[-\frac{nF}{RT}(E_2^0 - E_1^0)] \qquad [2\text{-}10]$$

The Nernst equation is widely applied in this Thesis. In protein film electrochemistry (Chapter 3 and Chapter 4 in this Thesis), when the potential is stepped or swept to a new value, the reaction will be driven to meet the new equilibrium predicted by eqns [2-5] and [2-6]. In Chapter 6, the ratio of the reduced and oxidised form of the reactant can be plotted as a function of applied potential and fitted to a curve obtained from Nernst equation. The reduction potential of the couple (Ox and Red) and the number of electrons involved in the inter-conversion can be thus deduced.

2.1.4 The Michaelis-Menten kinetics

Michaelis-Menten kinetics is one model of enzyme kinetics.[183] It describes the rates of irreversible enzymatic reactions by relating the reaction rate to the concentration of the substrate. The first step in the reaction is the binding of the substrate (S) to the enzyme (E) and an enzyme-substrate complex (ES) is formed. Michaelis and Menten proposed that this step is fast enough to be represented by an equilibrium constant for substrate dissociation related to the concentration of E and S, as shown in eqn [2-11]:

$$K_s = [E][S]/[ES] \qquad [2\text{-}11]$$

The second step is the irreversible formation of product (P) and the release of the free enzyme from the ES. The whole process could be given by eqn [2-12]:

$$E + S \overset{K_S}{\leftrightarrow} ES \overset{k_0}{\rightarrow} E + P \qquad [2\text{-}12]$$

The total enzyme concentration including two forms of E and ES is constant throughout the catalysis. Nearly all enzyme-catalysed reactions show a first-order dependence of rate on substrate in the region of low concentration, however, the rate levels off at high concentration of substrate as shown in Figure 2-4. This is known as the substrate saturation. Normally, the concentration of substrate is much higher than that of the enzyme and the substrate is supplied continuously, therefore it could be assumed that [S] is a constant. Since the first step is in equilibrium, the rate of the overall reaction is determined by the rate of the irreversible second step. The rate constant k_0 is indicated in eqn [2-12] and the rate is the first-order dependence on the concentration of ES. It should be pointed out that k_0 represents the capacity of forming the product from ES and it is also called the catalytic constant of the enzyme (symbolised as k_{cat}) or the turnover number. Briggs and Haldane later on pointed out that the first step is reversible, but not necessarily in equilibrium, as shown in eqn [2-13]:

$$E + S \xleftrightarrow{k_1/k_{-1}} ES \xrightarrow{k_2} E + P \qquad [2\text{-}13]$$

They assumed that the concentration of the intermediate *ES* changes much more slowly than those of the product and substrate: the steady-state assumption, i.e., the concentration change of *ES* is negligible. Therefore, the modified mathematical calculations to give the Michaelis Menten equation are shown as follows:

$$\frac{d[ES]}{dt} = k_1[E][S] - [ES](k_{-1} + k_2) = 0 \qquad [2\text{-}14]$$

$$v = \frac{d[P]}{dt} = k_2[ES] \qquad [2\text{-}15]$$

$$[E] + [ES] = [E]_0 \qquad [2\text{-}16]$$

Finally the Michaelis Menten equation is shown in eqn [2-17] :

$$v = \frac{k_2[E]_0[S]}{\frac{k_2 + k_{-1}}{k_1} + [S]} = \frac{v_{max}\,[S]}{K_\mathrm{m} + [S]} \qquad [2\text{-}17]$$

where v is the reaction rate catalysed by the enzyme and K_m is the affinity for the substrate. It can be deduced from eqn [2-17] that the concentration of the substrate is K_m when the rate of the enzyme catalysed reaction reaches half of its maximum rate v_max, as shown in Figure 2-4. The term, K_m, resembles the K_s as shown in eqn [2-11] and has a dimension of concentration. It is a dissociation constant, as shown in eqn [2-18]. Therefore, the higher the K_m is, the lower the affinity of the enzyme for the substrate is.

$$K_m = \frac{k_{-1} + k_2}{k_1} \qquad [2\text{-}18]$$

Therefore, the *Michaelis-Menten equation* shown in eqn (26) actually derives from the assumption of steady-state of the composite *ES* from Briggs and Haldane, rather than from the equilibrium assumption from Michaelis and Menten.

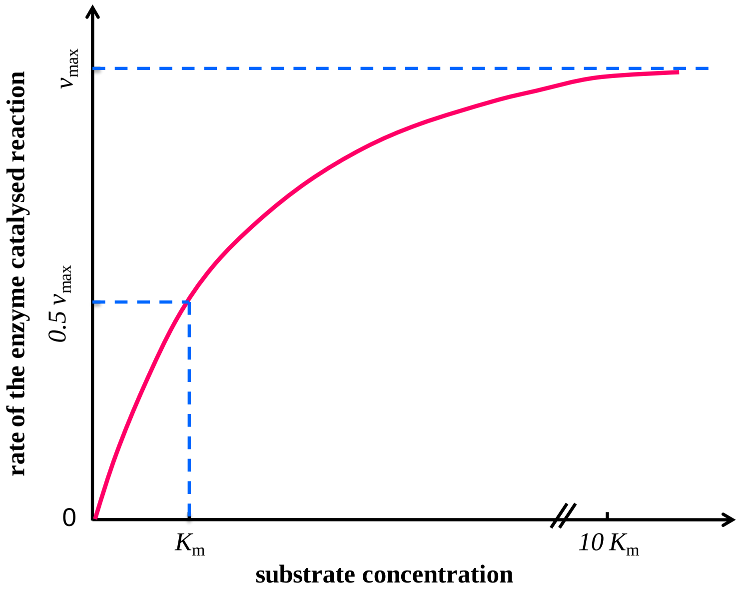

Figure 2-4. Schematic diagram showing the dependence of the enzyme-catalysed reaction rate on the substrate concentration. The labels v_{max} stands for the maximum rate of the reaction and K_m is the Michaelis constant for the substrate.

However, it should be noted that hydrogenases normally catalyse H_2 oxidation with a high turnover rate. Therefore, in the solution assays, the measured enzyme activity may not be accurate because the substrate is not supplied continuously and may run out during the assay. In Chapter 4, the affinity of *Re* RH for H_2 is examined by protein film electrochemistry, and the substrate H_2 can be supplied continuously by rotating the electrode.

2.1.5 First-order reaction kinetics

As described in **Section 2.1.1**, the information about the reaction kinetics (inactivation by introduction of an inhibitor or reactivation by applying an active potential) can be deduced from the slope of the current trace. A lot of enzyme-involved processes follow the first order reaction kinetics. The definition of the first order reaction is that the rate of the reaction is only proportional to the concentration of the reactant.[184] In mathematical form, it can be shown as eqn [2-19]:

$$-\frac{\mathrm{d}[A]}{\mathrm{d}t} = k[A] \qquad [2\text{-}19]$$

where t is the time, $[A]$ is the concentration of the reactant and k is the rate constant.

Equation [2-19] can also be written as below:

$$\frac{\mathrm{d}[A]}{[A]} = -k\mathrm{d}t \qquad [2\text{-}20]$$

Then, by integration as shown below:

$$\int_{[\mathrm{A}]_0}^{[\mathrm{A}]_\mathrm{t}} \frac{\mathrm{d}[A]}{[A]} = -k\int_0^\mathrm{t} \mathrm{dt} \qquad [2\text{-}21]$$

$$\ln[A]_\mathrm{t} - \ln[A]_0 = -kt \qquad [2\text{-}22]$$

At the first half-life of the reactant, $t_{1/2}$,

$$\ln 2 = kt_{1/2} \quad \text{i.e.} \quad t_{1/2} = \frac{\ln 2}{k} \qquad [2\text{-}23]$$

To check whether the reaction follows the first order reaction kinetics, a semi-log plot of the concentration of the reactant as a function of the time should be plotted. If the curve shows a linear behaviour, then the slope is the negative of the rate constant $-k$ and the intercept is $\ln[A]_0$. The half-life of the reaction can also be determined from eqn [2-23].

The reactions of the enzyme (*Re* SH in Chapter 3 and *Re* RH in Chapter 4) with inhibitor O_2 are investigated by chronoamperometry experiments. The concentration of the active enzyme is directly proportional to the catalytic current and a semi-log plot of the current after O_2 addition as a function of time is used to examine the reaction kinetics.

2.1.6 Infrared spectroscopy

The term infrared (IR) refers to light with wavelengths between 7.5×10^{-5} and 10^{-2} cm. In IR spectroscopy, wavenumber ($\tilde{\nu}$) rather than wavelength (λ) is reported and the relationship between them is shown as eqn [2-24]:

$$\tilde{\nu} = \frac{1}{\lambda} \qquad [2\text{-}24]$$

The infrared can be divided further into near- (~ 7.5 × 10^{-5} to 3 × 10^{-4} cm), mid- (~ 3 × 10^{-4} to 3 × 10^{-3} cm) and far-IR regions (~ 3 × 10^{-3} to 1 × 10^{-2} cm). The signals of interest to this Thesis fall within the mid-IR region in particular to the wavenumber range 4000 - 400 cm^{-1}. The higher the wavenumber is, the higher the energy E of the radiation, as expressed by eqn [2-25]:

$$E = \frac{hc}{\lambda} = hc\tilde{\upsilon} \qquad [2\text{-}25]$$

where h is Planck's constant and c is the speed of light.

If the energy of the infrared radiation matches the energy of the vibration of the molecule, then the infrared light is absorbed. The vibrations of a molecule include stretching and bending modes. As well as exciting individual vibrational modes, coupling can occur between different modes, resulting in combination bands. The number of vibrational modes depends on the number of atoms (N) in a molecule ($3N$ - 5 for linear molecules and $3N$ - 6 for nonlinear molecules), but the number of active modes depends upon the symmetry of the molecule. The wavenumber of a stretching band can be calculated using eqn [2-26],[40] assuming simple harmonic motion.

$$\tilde{\upsilon} = \frac{1}{2\pi c}\sqrt{\frac{k}{\mu}} \qquad [2\text{-}26]$$

The wavenumber $\tilde{\upsilon}$ is dependent on the force constant k (an indicator of the bond strength) and reduced mass μ (or effective mass of the mode). The molecular vibrations can be treated as though it corresponds to a spring which obeys Hooke's law which states 'the force required to extend the spring is proportional to the extention', and the proportionality constant is the force constant.

Equation [2-26] can also be used to calculate the isotope shift when carrying out an experiment using an isotopically labelled atom. In the case of ^{13}C-labelled diatomic CO molecule, the reduced mass can be calculated using eqn [2-27]:

$$\mu = \frac{\mathrm{m(C)m(O)}}{\mathrm{m(C) + m(O)}} \qquad [2\text{-}27]$$

If $\upsilon(^{12}CO)$ bound on noble metals is around 2000 cm^{-1}, the corresponding $\upsilon(^{13}CO)$ is calculated to be 1955 cm^{-1} according to eqn [2-26] and [2-27]. This isotope shift is useful to confirm assignments or to shift an absorption band out of a complicated region of the spectrum. In Chapter 5, a ^{13}C labelled formic acid ($H^{13}COOH$) experiment was performed to confirm the intermediate formed during the catalysis.

2.1.7 Attenuated total reflectance configuration

Attenuated total reflectance (ATR) spectroscopy is especially suitable for studying the interfacial properties that cannot be readily examined by the transmission method and can be applied to solids, liquids and gases. In this Thesis, the ATR configuration is employed, as shown in Figure 2-6. It has several advantages over the IRAS (Infrared Reflection-Absorption Spectroscopy, more detail in Chapter 5) geometry. Firstly, the ATR configuration allows efficient access of solutes in the electrolyte to the electrode, whereas in the IRAS configuration mass transport is poor because the solution layer trapped between the electrode and window must be very thin to minimise the background water absorbance. Secondly, multiple reflections can be employed in the ATR mode, thereby leading to better signal-to-noise for a given acquisition time.

Attenuated total reflectance occurs when the IR radiation enters from a more optically dense (with a higher refractive index) to a less optically dense medium (with a lower refractive index) above the critical angle θ_c. The reflectance increases with increasing incident angle. All the IR radiation is completely reflected when the incident angle is greater than the critical angle, as shown in Figure 2-5. The critical angle θ_c is defined as eqn [2-28], derived from Snell's law:

$$\theta_c = \arcsin\left(\frac{n_1}{n_2}\right) \qquad [2\text{-}28]$$

where n_1 is the refractive index of the sample and n_2 is that of the prism (n_2 is bigger than n_1).

The beam of the IR radiation penetrates a distance beyond the interface into the less-dense medium and this penetration is an evanescent wave with exponential decay, as shown in Figure 2-5. Typically, the penetration is a few micrometers and attenuated due to the absorption by the sample. The depth of the penetration can be calculated by eqn [2-29],

$$d_p = \frac{\lambda}{2\pi\sqrt{n_2^2\sin^2\theta - n_1^2}} \qquad [2\text{-}29]$$

Therefore, the penetration depth d_p is dependent on the wavelength λ, the incident angle θ and the refractive index of the sample and prism. The higher the wavenumber $\tilde{v}$ (which corresponds to a lower wavelength λ) is, the smaller the penetration depth is. The bigger the incident angle θ is, the smaller the penetration depth is. The bigger the refractive index of the prism n_2 is, the smaller $d_p$is. On the other hand, the bigger the refractive index of the sample n_1 is, the bigger d_p is.

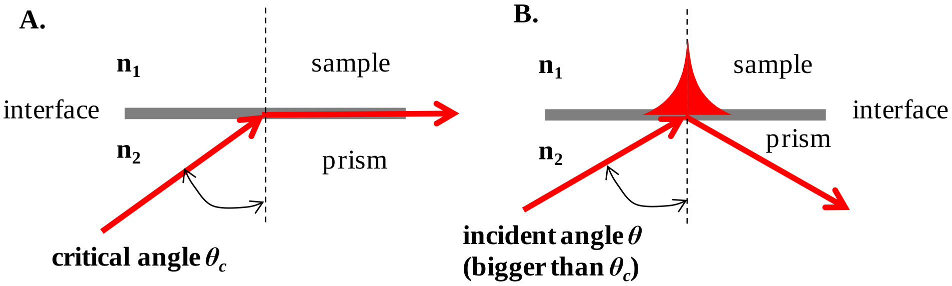

Figure 2-5. Panel A: Schematic representation of the critical angle θ_c. Panel B: Total internal reflection at the interface of the prism and the sample when the incidence angle is above θ_c.

In this Thesis, the sample I studied is a thin layer of 3-D carbon particle network loaded with catalyst (noble metal in Chapter 5 and *Re* RH in Chapter 6), as shown in Figure 2-6. The chemical process of interest happens at the interface of the modified carbon particle network and the solution nearby. This explains why the ATR-IR configuration is applied in this Thesis. Furthermore, a multi-bounce sampling is applied to enhance the signal-to-noise ratio and the number of bouncing can be adjusted by changing the incident angle θ, the length L and thickness d of the prism. The number of reflections N_r within the prism can be calculated by eqn [2-17].

$$N_r = \frac{L}{2d\tan\theta} \qquad [2\text{-}30]$$

Therefore, the bigger the incident angle θ is, the smaller N_r is; the thicker the prism is, the smaller N_r is; and the longer the prism is, the bigger N_r is. However, it should be noted that the more times the IR beam bounces, the less light the detector receives for a given time.

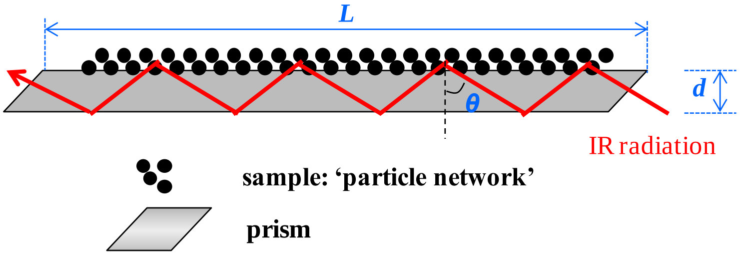

Figure 2-6. The geometry of multi-bounce ATR sampling used in this Thesis.

2.1.8 H_2O vibration modes

Water shows strong absorption in the infrared region and is the solvent for making the buffer in this Thesis, therefore it is required to clarify its background contribution in the spectra. The water absorption spectra vary according to the state of water, i.e., the gaseous, liquid and solid. There are mainly three modes of vibration in liquid water H_2O, i.e., the symmetrical, asymmetrical stretching and bending mode,[185] as shown in Figure 2-7. The infrared spectra in liquid water are very complex not only due to the vibration but also the combination with the libration. Compared to the gaseous form, the increasing hydrogen bonds in the liquid water contributes the broad feature of the stretching band and makes the stretching bands shift to lower wavenumbers as the increase in hydrogen bonding leads to a weakening in the covalent O-H bond strength. In the liquid water, rotations of the molecules are restricted by hydrogen bonds, and the frustrated rotation combines with the bending mode, producing a combination band at around 2127 cm^{-1}.[186]

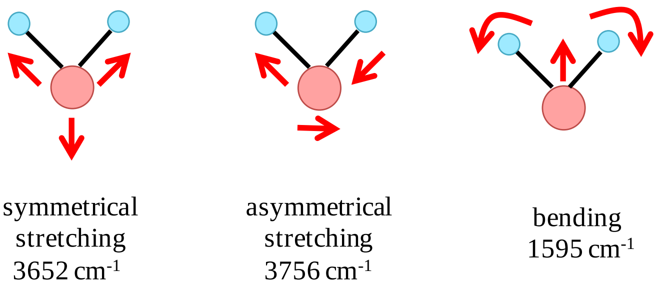

Figure 2-7.The vibration modes of liquid water. The small blue circle represents the H atom and the big red circle represents the O atom. The moving directions are indicated as the red arrowheads.

2.1.9 Infrared Studies of Hydrogenase Enzymes and CO-poisoned Noble Metals

Infrared spectroscopy can be used to study the redox states of hydrogenase enzymes through probing the stretching mode of carbonyl (CO) and cyanide (CN^-) ligands bound to Fe, further reflecting the electron environment of Ni in the case of NiFe hydrogenases.[23] Carbon monoxide (CO) is also the most studied intermediate adsorbed on the surface of the noble metals during the oxidation of small organic molecules.[187]

2.1.9.1 CO coordination in complexes

The wavenumber of the CO stretching mode for free CO, i.e., the gaseous state, is located at 2155 cm^{-1}. In most carbonyl complexes, the CO stretching mode, υ(CO), shifts to a lower wavenumber compared to free CO.[188] Figure 2-8(A) shows the molecular orbital diagram for CO and provides the information about the highest occupied molecular orbital (HOMO) and lowest unoccupied molecular orbital (LUMO) which are important in the metal complex formation when CO is acting as a ligand. Carbon monoxide is a common π-acceptor ligand in metal complexes. The LUMOs (two $2\pi^*$) orbitals can overlap the filled *d* orbitals of the metal and receive the electrons from the metal, as shown in Figure 2-8(B). The π-backbonding from the metal into the antibonding CO LUMO results in a decrease in υ(CO) because electron density is put into antibonding CO molecular orbitals, weakening the CO bond. Figure 2-8(C) shows that carbon monoxide can also serve as a (weak) σ-donor by contributing electrons from the HOMO to the empty *d* or *p* orbital of the metal. The HOMO is weakly antibonding with respect to the CO bond, and thus σ-donation strengthens the CO bond. Complexes of CO with high oxidation state metals where backbonding is insignificant result in a shift in υ(CO) to *higher* wavenumber indicating that σ-bonding is important in these cases. The σ-bonding and π-backbonding are synergic (the electrons contributed from the σ-bonding contribute to π-backbonding), and generally the net effect is that electrons from the metal are delocalised and shifted towards CO. Therefore, the wavenumber of CO in most metal complexes is lower than 2155 cm^{-1}.

In general, the υ(CO) is lowered as the negative charge on the complex increases,[189-191] as shown for the series of isoelectronic complexes of first row transition metals below:

$$\begin{array}{rccccccc} & [V(CO)_6]^- & & Cr(CO)_6 & & [Mn(CO)_6]^+ & & [Fe(CO)_6]^{2+} \\ \upsilon(CO)\ /\ cm^{-1}: & 2020 & < & 2119 & < & 2192 & < & 2241 \end{array}$$

This trend can be explained by the fact that as the negative charge builds up, the π-backbonding in the carbonyl complex increases, therefore weakening the CO bond and causing a decrease in υ(CO).

The formal oxidation state of the metal will also affect the υ(CO),[190,192,193] as shown below for a series of iron carbonyl complexes:

$$\begin{array}{rccccc} & [Fe(CO)_4]^{2-} & & Fe(CO)_5 & & [Fe(CO)_6]^{2+} \\ \upsilon(CO)\ /\ cm^{-1}: & 1788 & < & 2116 & < & 2241 \end{array}$$

The reason for this trend is essentially the same as above, i.e., the CO π-backbonding decreases as the oxidation state of the metal increases. For $[Fe(CO)_6]^{2+}$, υ(CO) is actually higher than for free CO, indicating that σ-donation from the ligand to the metal must be occurring, strengthening the CO bond by removing electron density from the weakly antibonding HOMO.

At the active site of a NiFe active site, three diatomic ligands, 2 CN^- and 1 CO are bound to the Fe site. In the case of NiFe and FeFe hydrogenases, the intrinsic carbon monoxide ligand is terminal, bound to one metal atom, Fe.[20] In the NiFe hydrogenases, υ(CO) ranges from *ca.* 1900 to 2100 cm^{-1}, depending on the redox level of the enzyme and the source of CO (intrinsic CO on Fe or exogenous CO on Ni).[23] Exogenous CO, bound to Ni, has a much higher wavenumber (2050 to 2070 cm^{-1}) than CO bound to Fe (II). However, the υ(CO) in the NiFe hydrogenase spectra is much lower than that in the synthesised homoleptic carbonyl Fe (II) complexes due to the combination of CO with other σ-donating ligands. The CN^{-} ligand (discussed below) is a better σ-donor than π-acceptor, thus will supply electrons to the metal, indirectly leading to an increase in the CO π-backbonding which corresponds to a lower υ(CO). As discussed in Chapter 1, the formal oxidation state of Fe in the NiFe hydrogenases is at +2 and does not change during the enzyme turnover. However it is found that the the υ(CO) shifts in response to the redox transition of the enzyme, implying that the CO bond is affected by other ligands bound to Fe and its important neighbour Ni which shuffles between +1, +2, and +3 during catalysis.

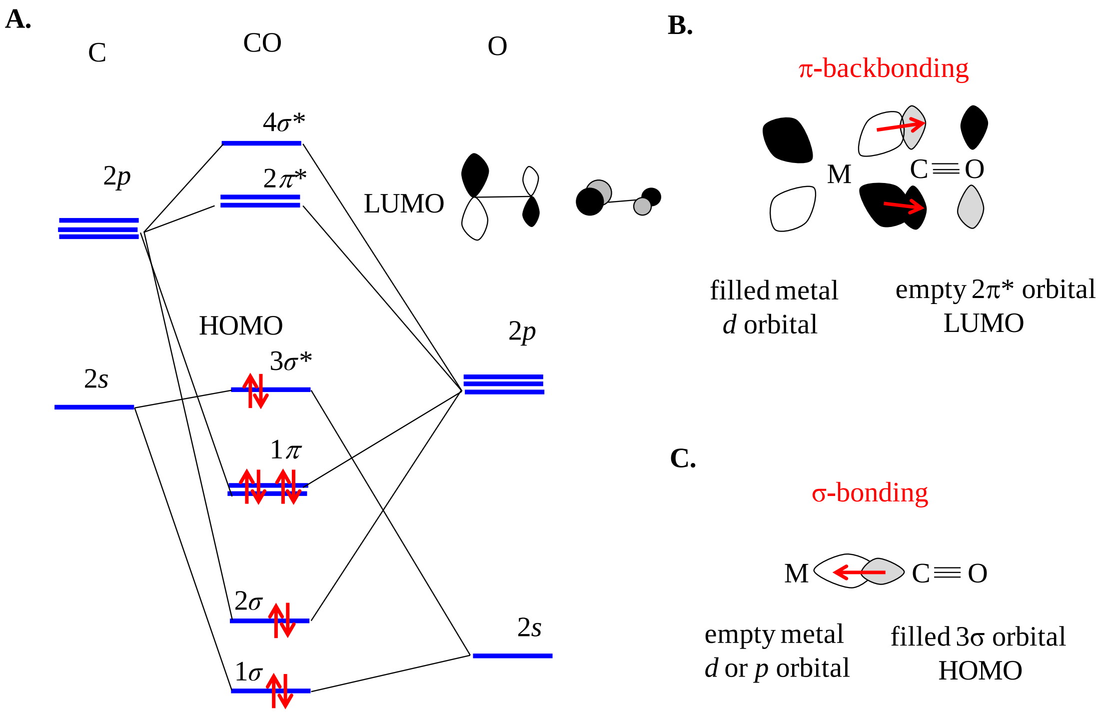

Figure 2-8. Panel A: The molecular orbital energy level diagram for CO. The high occupied molecular orbital (HOMO) is 3σ and the low unoccupied molecular orbital (LUMO) is 2π*. Panel B: The π-antibonding in the carbonyl complexes. Panel C: The σ-bonding in the carbonyl complexes. Figure adapted from ref.[194]

2.1.9.2 CO adsorbed on the surface

In other cases, like CO-poisoned noble metal surfaces (in Chapter 5), carbon monoxide can bridge two or three metal atoms.[195] The bonding is more complex in the bridge CO (M_2CO) and multi-bridge CO (M_3CO) than the linear CO (MCO). As the ligand CO bonds to more metal atoms, π-backbonding from the metals will increase, causing an increase in occupation of the $2\pi^*$ orbitals, the CO wavenumber thereby drops to a lower value, following the order MCO > M_2CO > M_3CO, as shown in Figure 2-9.

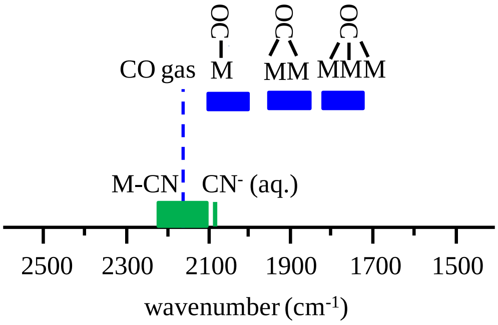

Figure 2-9. Approximate ranges for the CO (blue) and CN^- (green) stretching wavenumber in different forms.

2.1.9.3 CN^- coordination in complexes

Another important ligand in NiFe and FeFe hydrogenases is the cyanide anion (CN^-), as discussed above. The attachment of cyanide CN^- to the metal can be through the C or N atom. In the case of NiFe and FeFe hydrogenases, the attachment is through the C atom. Cyanide is iso-electronic with carbon monoxide, thus has similar molecular orbitals to CO, shown in Figure 2-8. The σ-donation of the electrons from CN^- to the metal causes an increase in $\upsilon(CN^-)$ as the 3σ orbital of CN^- is weakly antibonding. On the other hand, when cyanide is bound to low oxidation state metals, π-backbonding tends to decrease $\upsilon(CN^-)$ as it weakens the CN bond. However, in comparison to CO, CN^- is a better σ-donor than a π-acceptor.[2] Thus, the coordination of a cyanide ligand to a metal generally causes a wavenumber shift to a higher value than the free cyanide ion in aqueous solutions, which has a wavenumber of 2080 cm^{-1}.[188]

The infrared range of the cyanide complex and its comparison with the carbonyl complex are also shown in Figure 2-9.

The wavenumber of the cyanide ligand depends on the bonding metal. The electronegativity, oxidation state and coordination number of the metal will all affect the stretching of CN^-, as shown below.[196]

As the electronegativity increases in the order of Ni < Pd < Pt, the σ-donation by the CN^- correspondingly increases in the same order. Thus, the $\upsilon(CN^-)$ in $[Ni(CN)_4]^{2-}$ is expected to be the lowest.

$$\begin{array}{lccccc} & [Ni(CN)_4]^{2-} & & [Pd(CN)_4]^{2-} & & [Pt(CN)_4]^{2-} \\ \upsilon(CN^-) / cm^{-1}: & 2128 & < & 2143 & < & 2150 \end{array}$$

An increase in the number of CN^- ligands on a single metal centre leads to a decrease in the positive charge on the metal. Therefore, the σ-donation by CN^- will decrease, causing a decrease in $\upsilon(CN^-)$.

$$\begin{array}{lccccc} & [Ag(CN)_4]^{3-} & & [Ag(CN)_3]^{2-} & & [Ag(CN)_2]^{-} \\ \upsilon(CN^-) / cm^{-1}: & 2092 & < & 2105 & < & 2135 \end{array}$$

As the oxidation state of the metal increases, an increase in $\upsilon(CN^-)$ occurs due to an increase in σ donation by CN^-. In early transition metals like vanadium, π bonding is more important, and here the $\upsilon(CN^-)$ are lower than free cyanide indicating the presence of backbonding. As the oxidation state of V increases, the corresponding backbonding weakens, so that the $\upsilon(CN^-)$ approaches that of free cyanide.

$$\begin{array}{lccccc} & [V(CN)_6]^{5-} & & [V(CN)_6]^{4-} & & [V(CN)_6]^{3-} \\ \upsilon(CN^-) / cm^{-1}: & 1910 & < & 2065 & < & 2077 \end{array}$$

The wavenumber of CN^- in the iron cyano complexes exhibits a range of 2135 to 2044 cm^{-1}.[197] Similarly, in the NiFe hydrogenases the wavenumber of CN^- ligands which bond to Fe (II) at the active site falls into the region of 2100 to 2040 cm^{-1}, but υ(CN) shifts less than υ(CO) because of a balance between π acceptor and σ donor bonding.[23]

2.1.10 Henry's law

In this Thesis, dihydrogen, carbon monoxide, dinitrogen and dioxygen are frequently used as the substrate of the enzyme, an inhibitor or an inert background. Henry's law is therefore frequently used to determine the concentration of gases dissolved in the solution. It states that:

At a constant temperature, the amount of a given gas dissolved in a given type and volume of liquid is directly proportional to the partial pressure of that gas in equilibrium with that liquid.[40]

Normally, Henry's law can be expressed as eqn [2-31]:

$$c = k_H p \qquad [2\text{-}31]$$

where p is the partial pressure of the gas above the solution, c is the concentration of the gas in the solution, k_H is the Henry's law constant (i.e., the ratio between the concentrations of the given gas in solution-phase c and gas-phase p).

The constant k_H depends on the temperature and the relation between k_H and T can be given as eqn [2-32]:

$$k_H = k_H^o \times exp(\frac{-\Delta_{soln}H}{R}(\frac{1}{T} - \frac{1}{T^o})) \qquad [2\text{-}32]$$

where $\Delta_{soln}H$ is the enthalpy of solution, T^o is 298.15 K and k_H^o refers to k_H at 298.15 K.

Table 5 summarises the Henry's law constants for H_2, CO and O_2 and their temperature dependences.[198]

Table 5. The Henry's law constants for H_2, CO and O_2 and the temperature dependences

substance	k_H^o/ [M/atm]	$\frac{-d\ln k_H}{d\left(\frac{1}{T}\right)}$/[K]
H_2	7.8×10^{-4}	500
CO	9.5×10^{-4}	1300
O_2	1.3×10^{-3}	1700

In Chapter 3 and 4, inhibition experiments with precise O_2 concentration (2% O_2 in H_2, 1 bar) were performed on *Re* SH and RH at different temperatures (10 °C and 30 °C) aided by a water baths thermostat. According to eqn [2-32], the Henry's law constant k_H at 10 °C and 30 °C are calculated to be 0.96 mM/atm and 1.43 mM/atm, respectively, therefore, 2% O_2 corresponds to 19.2 μM and 28.6 μM, respectively.

2.2 Methods

2.2.1 Purification of the NiFe hydrogenases from *Ralstonia eutropha* and enzyme assays

The soluble hydrogenase from *Ralstonia eutropha*

The soluble hydrogenase from *Ralstonia eutropha* (Re SH or the SH) is a complex, six-subunit enzyme HoxHYFUI$_2$ and composed of two catalytic moieties: the hydrogenase moiety HoxHY (green) and the diaphorase moiety HoxFU (pink), as shown in Figure 2-10. Through a deletion of the genes encoding the diaphorase module HoxFU from the plasmid, the hydrogenase moiety HoxHY can be selectively grown and purified.[147,199] The tetrameric HoxHYFU can be purified through dissociation of HoxI (blue) from HoxHYFUI$_2$ at higher pH and ionic strengths.

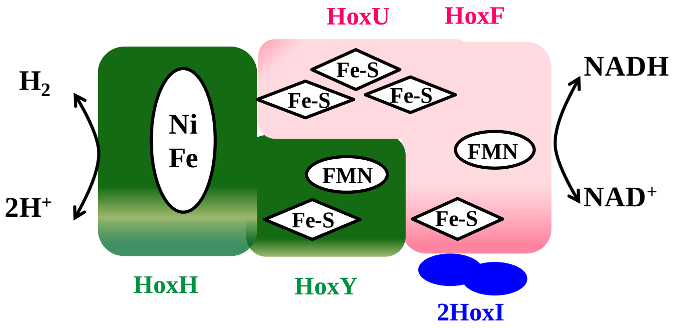

Figure 2-10. Schematic representation of the modules of the soluble hydrogenase from *Ralstonia eutropha*.

Purification of the hydrogenase moiety HoxHY

This *Re* SH purification including the hydrogenase moiety HoxHY and the whole enzyme $HoxHYFUI_2$ was carried out once under the guidance of Mr. Lars Lauterbach at Institut fuer Biologie/Mikrobiologie, Humboldt-Universitaet zu Berlin during this project.

The plasmid construction and the growth of the corresponding *Ralstonia eutropha* cells for the hydrogenase moiety HoxHY were performed following the procedures as described[147] and the genes for coding the diaphorase moiety HoxFU were deleted before the cultivation of the cells. The 5’ end of *hoxY* gene was equipped with a sequence that codes for the *Strep*-tag II peptide for later purification. The purification of HoxHY was carried out by *Strep*-Tactin affinity chromatography and it was performed in air. Figure 2-11(A) shows the two subunits HoxH and HoxY in the SDS-PAGE (sodium dodecyl sulphate polyacrylamide gel electrophoresis) analysis. The molecular weights of HoxH and HoxY are 55 and 23 kDa, respectively, determined by size-exclusion chromatography on a Sephadex G-200 column. First, the grown cells were re-suspended in two volumes of 50 mM Tris-HCl, 150 mM KCl, pH 8.0 buffer containing a protease inhibitor cocktail (EDTA-free Protease Inhibitor, Roche). Secondly, a French press was used to break the suspended cells at 6.2 MPa and the resulting suspension was centrifuged at 36,000 rpm for 45 min. The supernatant (soluble extract containing HoxHY) was applied to a 2 mL Strep-Tactin Superflow column (IBA), washed with 6 mL of resuspension buffer and eluted with the same buffer containing 5 mM desthiobiotin which specifically competes for the enzyme binding pocket. Protein fractions containing HoxHY were collected and concentrated in an Amicon Diaflo cell (YM 30 membrane; Amicon, Witten, Germany). It was demonstrated that HoxHY is purified in a homogeneous form by polyacrylamide gel electrophoresis.

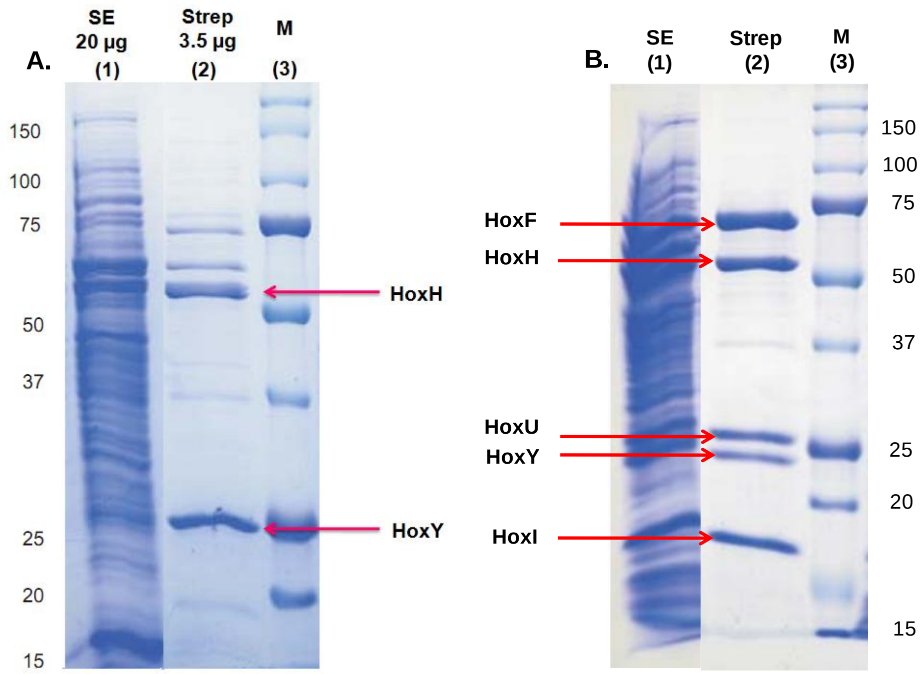

Figure 2-11. Purification of the soluble hydrogenase from *Ralstonia eutropha*. Panel A: The hydrogenase moiety HoxHY. Lane(1) corresponds to 20 µg of soluble extract; Lane(2) represents 3.5 µg of purified HoxHY. They were electrophoretically separated on a 12 % SDS-polyacrylamide gel and subsequently stained with Coomassie brilliant blue for 45 min. Panel B: The whole soluble hydrogenase HoxHYFUI$_2$: Lane(1) soluble extract and Lane(2) purified HoxHYFUI$_2$. Lane(3) in both panels shows marker proteins and their corresponding weight in kDa.

The enzyme assay for the hydrogenase moiety HoxHY

The specific activity for H^+ reduction was quantified at 30 °C using a modified Clark electrode and reduced methyl viologen (MV) as the electron donor. However, the H_2 oxidation activity for HoxHY only occurred after pre-incubation with a high concentration of dithionite, indicating that the as-isolated HoxHY is inactive for H_2 oxidation and reductive reactivation is required.

Table 6 shows the specific activity of H_2 oxidation and H^+ reduction by HoxHY coupled with the oxidised and reduced MV, respectively. One enzyme unit (1 U) is equal to 1 µmol/min, indicating the mole of substrate converted per unit time by total protein. The specific activity is a measure of the activity of an enzyme per milligram of total protein (expressed in U/mg). The protein concentrations were determined using the Bradford method.[200]

Table 6. Specific activity of H+ reduction and H2 oxidation for HoxHY coupled with reduced MV and oxidised MV, respectively.

Sample	H_2-dependent reduction of MV	H^+ reduction using red MV
HoxHY	1.02 U/mg	7.42 U/mg

Isolation of the whole *Re* SH

The cells containing the whole enzyme $HoxHYFUI_2$ were grown as described.[201] The 5’ end of *hoxF* gene was equipped with a sequence that codes for a *Strep*-tag II peptide for purification. The purification of the whole soluble hydrogenase was carried out in air by *Strep*-Tactin affinity chromatography. Figure 2-11(B) shows the subunits HoxH, HoxY, HoxF, HoxU and HoxY in the SDS-PAGE analysis. First, the cells were re-suspended in two volumes of Ar-flushed pH 7, 50 mM K_2HPO_4-KH_2PO_4 buffer containing a protease inhibitor cocktail (EDTA-free Protease Inhibitor, Roche). Here, pH 7 is a strict parameter for keeping the hexameric form of the soluble hydrogenase $HoxHYFUI_2$ intact as the two small HoxI subunits are easily dissociated from the main body of the enzyme even at pH 8.[201] After that, a French press was used to break open the suspended cells at 5.1 MPa and the resulting suspension was ultra centrifuged at 36,000 rpm at 4 ^{o}C for 45 min. The supernatant (soluble extract containing $HoxHYFUI_2$) was applied to a 1 mL Strep-Tag Superflow column washed with pH 7, 50 mM K_2HPO_4-KH_2PO_4 buffer and eluted with the same buffer containing 5 mM desthiobiotin. Protein fractions containing $HoxHYFUI_2$ were collected and concentrated in an Amicon Ultra 100 kDa cell. The complex hexameric form of the soluble hydrogenase was shown to be homogeneous by polyacrylamide gel electrophoresis.

The enzyme assay for the whole soluble hydrogenase $HoxHYFUI_2$

The specific activity for the reduction of NAD^+ coupled with H_2 oxidation by $HoxHYFUI_2$ was quantified by monitoring the UV/Vis absorbance (Varian Cary 300) of NADH at 340 nm, as shown in Table 7. The protein concentrations were determined using the Bradford method. The enzyme was incubated with different chemicals (FMN: Flavin mononucleotide; DT: Dithionite) before measuring the activity and more details will be described in Chapter 3.

Table 7. Specific activity of H_2-dependent NAD^+ reduction for $HoxHYFUI_2$ with different treatments.

Treatment	NA	FMN	DT	FMN/DT	Protein Conc. (mg/mL)
Spec. activity (U/mg)	44.8	101.7	102.8	128.3	0.56

NA means that $HoxHYFUI_2$ is in its as-isolated state without any treatment.

In Chapter 3, the dimeric (HoxHY), tetrameric (HoxHYFU) and hexameric ($HoxHYFUI_2$) form of the SH purified as above, will be investigated by protein film electrochemistry.

Purification of the regulatory hydrogenase from *Ralstonia eutropha* and the enzyme assay

The form of *Re* RH used throughout this Thesis is RHstop. *In vivo*, the wild type RH (RHwt) is composed of a dimer of HoxBC, namely, $(HoxBC)_2$. A monodimeric derivative HoxBC designated as RHstop was isolated and purified by a genetic deletion of the C-terminal 55 amino acids in HoxB. It was also purified in air as described previous.[202] The specific activity for H_2 oxidation in RHstop with methylene blue (MB) as electron acceptor was almost identical to that in RHwt, proving that RHstop maintains its catalytic function. The specific activity (H_2 : red. MB) determined is about 1 U/mg and similar to that for the soluble hydrogenase moiety HoxHY described above.

In Chapter 4 and 6, *Re* RH in the form of RHstop will be investigated by protein film electrochemistry and infrared spectroscopy, respectively.

2.2.2 Preparation of buffer for hydrogenase enzyme experiments

The solutions throughout the Thesis were all prepared using MilliQ water (Millipore) the resistivity of which was 18 MΩ cm. Three buffer systems were used in the protein-related work. The 50 mM Tris-HCl (Sigma) buffer system which is suitable between pH 7 and pH 8 was used for the soluble hydrogenase. For a wider pH window, a mixed buffer system composed of 25 mM CHES (*N*-Cyclohexyl-2-aminoethanesulfonic acid), TAPS (3-[[tris(hy-droxymethyl) methyl]amino] propanesulfonic acid), HEPES (*N*-(2-hydroxyethyl) piperazine-*N*’-2-ethanesulfonic acid), Tris (2-Amino-2-hydroxymethyl-propane-1,3-diol) and MES (4-morpholineethanesulfonic acid) was used for the experiment to measure the pH effect on the switch potential in the SH. The chemicals CHES, TAPS, HEPES and Tris were purchased from Sigma whereas MES was purchased from ACROS. The third buffer system was the potassium phosphate buffer (KPB, 50 mM K_2HPO_4/KH_2PO_4, ACROS), suitable for experiments between pH 6 and pH 8.

2.2.3 The set-up for the protein film electrochemistry

The pyrolytic graphite edge (PGE) electrode

The home-made working electrode is a small cylinder of pyrolytic graphite with the ‘edge’ plane exposed to the electrolyte. The graphite rod was mounted in a Kelf sheath and electrically connected to a stainless steel screw which is reversibly attached to the rotator (EG&G model 636). Prior to each experiment, the PGE electrode was polished with an aqueous slurry of 1 μm α-alumina powder (Buehler) against cotton wool and then sonicated in MilliQ water for around 5 seconds.[203]

The set-up of the electrochemical cell in protein film electrochemistry

The protein film electrochemistry experiments were carried out in the electrochemical cell as shown in Figure 2-12. It was designed for good control of the electrolyte temperature, gas composition and mass transfer near the working electrode. The water jacket outside the cell body is connected to a water circulator (Grant, GD120) which can provide flowing water of a precisely controlled temperature. The cell is sealed with an o-ring onto an electrode rotator, thus the rotation of the working electrode provides sufficient supply of the substrates and efficient product removal.[55] The rotating electrode also aids the quick gas exchange of the headspace gases with the electrolyte. The gas inlet fitting is connected to mass flow controllers which can provide a precise control over the gas composition. There is a specially designed sidearm for the injection of gas-saturated solutions which are stored in a thermostatted vial, via the needle through the rubber septum cap. The electrochemical cell was washed with aqua regia (concentrated hydrochloric and concentrated nitric acids: 1:3 in volume) after use to help remove traces of free flavin lost from the protein and then rinsed with MilliQ water before the next use. Normally, 2 mL of electrolyte was required for a measurement. Ideally, the reference electrode should be housed in a side arm separated by a Luggin capillary so that the reference electrode will not be affected by the cell temperature controlled by the thermostated water jacket. In this Thesis, almost all the experiments are performed at a single temperature, thus the measured potential should be accurate when corrected for the reference electrode temperature offset as shown in **Section 2.2.6**.

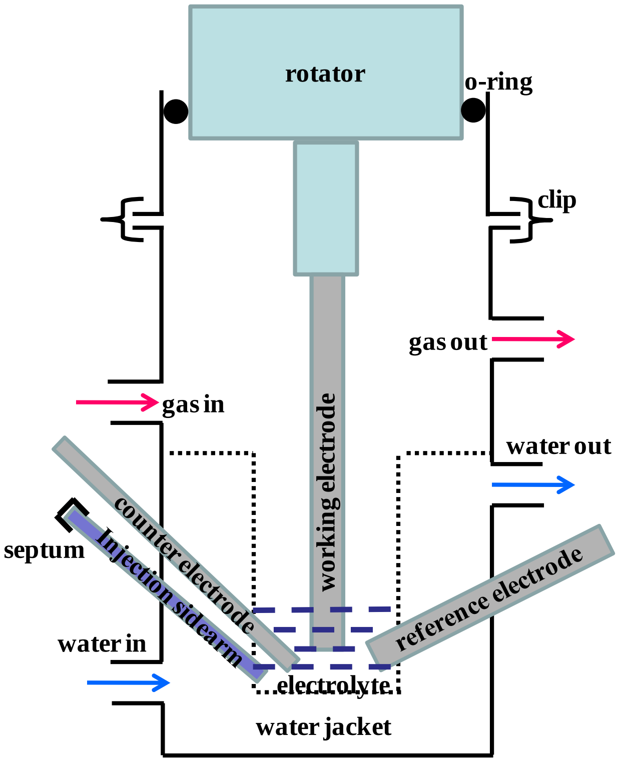

Figure 2-12. Schematic representation of the electrochemical cell used in protein film electrochemistry.

The preparation of a protein film on the PGE electrode

In protein film electrochemistry (PFE), a minuscule sample of protein (less than a picomole) is adsorbed directly on a PGE electrode to give a mono- or submonolayer film. A cartoon representation of the hydrogenase film on a PGE electrode is shown as Figure 2-13. The hydrogenase cartoon shown here is composed of two subunits: the large one houses the active site and the small one accommodates three FeS clusters to transfer electrons between the active site and the electrode. It does not necessarily represent the subunit composition or the FeS cluster arrangement in *Re* SH and RH studied in this Thesis.

Samples of the as-isolated HoxHY, HoxHYFU and $HoxHYFUI_2$ were kept on ice outside the glovebox in air to maintain the as-isolated state. Aliquots of protein (0.6 μL) were taken into the glovebox under a N_2 purge prior to making a film on the PGE electrode. The PGE electrode was polished with alumina powder (1 μm, Buehler) and then sonicated. The protein was then spotted onto the surface of the electrode and left to partially-dry for around 60 seconds. The enzyme-modified electrode was then put on the rotator and ready for measurement. Notably, it is important for the SH to be kept outside the glovebox before making an enzyme film. Inside the glovebox there is always trace H_2 which will reactivate the enzyme, thus the information of the as-isolated state will be lost.

In the case of the RH, the enzyme was stored inside the glovebox before the measurement. Aliquots of protein (0.5 μL) inside the glovebox were spotted onto a freshly polished PGE electrode. When the protein film looks partially-dry, the modified PGE electrode can then be connected with the potentiostat and is ready for experiments.

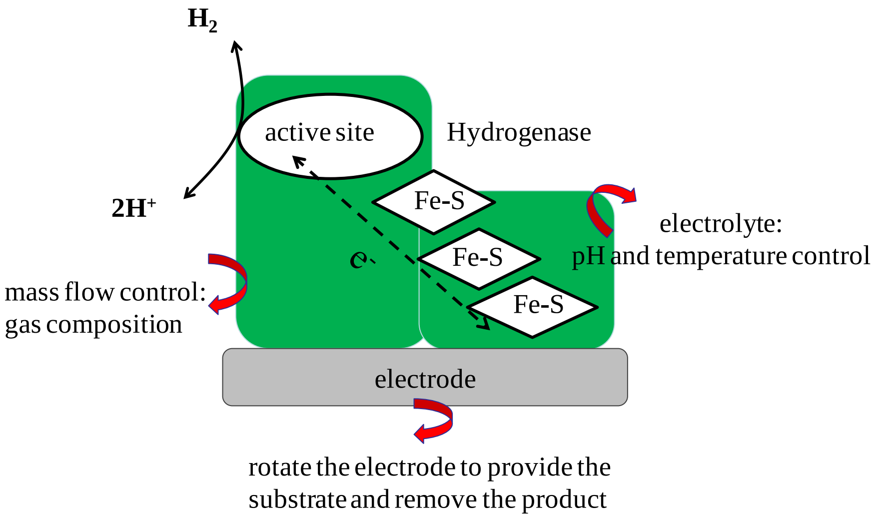

Figure 2-13. Cartoon showing a possible configuration of a hydrogenase molecule on a PGE electrode in protein film electrochemistry.

2.2.4 Glovebox and mass flow controllers

Glovebox

In the potential window for studying the hydrogenase adsorbed on the PGE electrode, the current coming from the O_2 reduction at graphite will cause a severe interference for the catalytic current of hydrogenases. Therefore, protein film electrochemistry experiments were all performed inside a N_2-filled wet glovebox (MBraun or Glovebox Technology, Cambridge).

Mass flow controllers and gases

Accurate gas mixtures were prepared using mass flow controllers (Brooks SLA series controlled by Digibox Lite) as shown in Figure 2-14 for experiments on hydrogenases. With the aid of mass flow controllers, it is easy to keep the concentration of substrate constant throughout an experiment and to introduce an inhibitor such as CO or O_2 in the middle of the experiment while avoiding a drop in current due to a decrease in substrate (H_2) concentration. The maximum gas flow limits of the devices varied from 0.1 to 1 L/min as shown in Figure 2-14, with a lower limit of 2% the maximum. Therefore, a mix such as 1% of O_2 in H_2 is achievable with this set up for very precise experiments. The gases used in this Thesis are pure analytical grade dihydrogen, dioxygen, nitrogen (oxygen free) and carbon monoxide. The H_2 and O_2 were obtained from Air Products, and the N_2 and CO were from BOC.

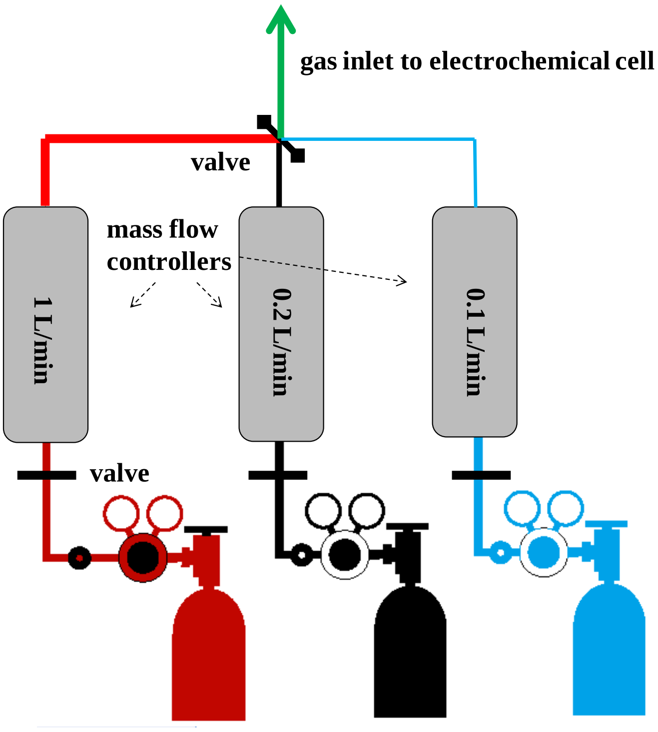

Figure 2-14. Schematic representation of mass flow controllers and cylinders.

2.2.5 Potentiostat

For all the protein film experiments, potentials were controlled using an Autolab 128N potentiostat (EcoChemie, the Netherlands). As the catalytic turnover rate of *Re* SH and RH was very low, the electrocatalytic currents are very small, within 100 nA. An ECD (Extreme Low Currents) module was required for measuring such low currents. A filter is built into the ECD module to make it possible to filter out noise. However, in order to avoid over-filtering and compromising the data, only a 0.001 s^{-1} filter was used when carrying out cyclic voltammetry experiments. In the chronoamperometry experiments which were usually used to obtain kinetic information on a reaction, no filter was applied. The corresponding software for the Autolab Potentiostat, GPES (General Purpose Electrochemical System), was used for collecting data.

2.2.6 Three-electrode system

The electrode of interest is called the working electrode and the reactions happening on its surface are of our interest. If the current (*i*) is low and the electrolyte is highly ionically conductive, a two electrode cell is sufficient for voltammetric measurement. However, if the current between the two electrodes is high or the electrolyte has high resistance *R*, the applied potential will not be identical to the desired potential at the working potential due to an Ohmic drop *iR*. Therefore, a three-electrode system is used to avoid the inaccurate control of potential at the working electrode. The three-electrode system is composed of a working electrode, a reference electrode and a counter electrode as shown in Figure 2-15. The reference electrode is approaching an ideal polarized electrode at which there is no charge transfer across the metal-solution interface regardless of the potential, and it has a known value of potential under specified conditions. The electrochemical properties of the counter electrode need to not affect the working electrode. The potential is measured between the working electrode and the reference electrode since the reference electrode has a fairly high impedance and the current is almost negligible. In order to keep the Ohmic drop as small as possible, the reference electrode needs to be placed as close as possible to the working electrode. The current is measured between the working electrode and the counter electrode.

The counter electrode used for the protein film electrochemistry experiments was a platinum wire with a diameter of 1 mm. An Ag/AgCl (3M NaCl) electrode or a saturated calomel electrode (SCE) was employed as the reference electrode. Potentials were converted to volts vs. the standard hydrogen electrode (SHE) using the conversions as shown in eqns [2-33], [2-34], [2-35] and [2-36].[70] A PGE electrode with a surface area of 0.03 cm^2 was used as the working electrode for protein film electrochemistry experiments.

$$E(\mathrm{SHE}) = E(\mathrm{Ag/AgCl, 3MNaCl}) + 0.201\ \mathrm{V\ at\ 30\ °C} \qquad [2\text{-}33]$$

$$E(\mathrm{SHE}) = E(\mathrm{Ag/AgCl, 3MNaCl}) + 0.216\ \mathrm{V\ at\ 10\ °C} \qquad [2\text{-}34]$$

$$E(\mathrm{SHE}) = E(\mathrm{SCE}) + 0.238\ \mathrm{V\ at\ 30\ °C} \qquad [2\text{-}35]$$

$$E(\mathrm{SHE}) = E(\mathrm{SCE}) + 0.250\ \mathrm{V\ at\ 10\ °C} \qquad [2\text{-}36]$$

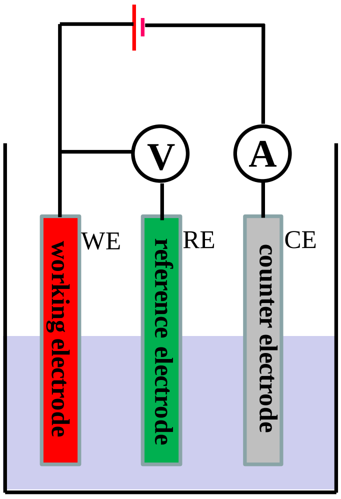

Figure 2-15. Schematic representation of a three-electrode setup: the potential (Volts) is measured between the working electrode and the reference electrode; the current (Amperes) is measured between the working electrode and the counter electrode.

2.2.7 Preparation of chemicals used in IR experiments

For the formic acid oxidation (Chapter 5), the supporting electrolyte was 0.5 M sulphuric acid (H_2SO_4, 98% Laboratory Reagent Grade, Fisher Scientific) in Milli-Q water and the substrate was either 0.5 M formic acid (HCOOH, 98% Fluka brand, Sigma) or 0.1 M ^{13}C-labelled formic acid ($H^{13}COOH$, 95 weight percent in H_2O, 99% of C is labelled ^{13}C, Sigma) in 0.5 M H_2SO_4. In the infrared spectroelectrochemistry experiments on RHstop (Chapter 6), the electrolyte was 50 mM potassium phosphate (ACROS) buffer (pH 6) in Milli-Q water. For the CO and O_2 inhibitor experiments, the purity is as described in **Section 2.2.4.**

2.2.8 The optical set-up of the ATR-IR SEC cell

In the work on formic acid oxidation catalysed by noble metals (Chapter 5) and the redox state investigation of *Re* RH (Chapter 6), an infrared spectroelectrochemical approach was developed to combine electrochemical control with infrared spectroscopy. The attenuated total reflectance (ATR) set-up used is shown in Figure 2-16. Different catalysts (noble metals in Chapter 5 and the RHstop in Chapter 6) either adsorbed on or mixed with carbon particles were investigated in a 3-D particle network form which could not be easily studied using a transmission geometry. Therefore, an ATR mode was chosen which is suitable for studying the solid/liquid interface, such as a particle 'film' in contact with electrolyte.

Figure 2-16(A) shows the optical set-up of the ATR-IR SEC cell (a dashed green oval) in the IR compartment including several mirrors. The beampath before entering and after leaving the cell is indicated as red lines and the direction is shown as the arrowhead. At the bottom left, a picture of a peristaltic pump (Watson-Marlow 101U/R) is also presented, which is used for the flow capability. Figure 2-16(B) shows the enlargement of the light pathway within the prism. Furthermore, a three-electrode configuration above the prism is also presented. More details will be discussed below.

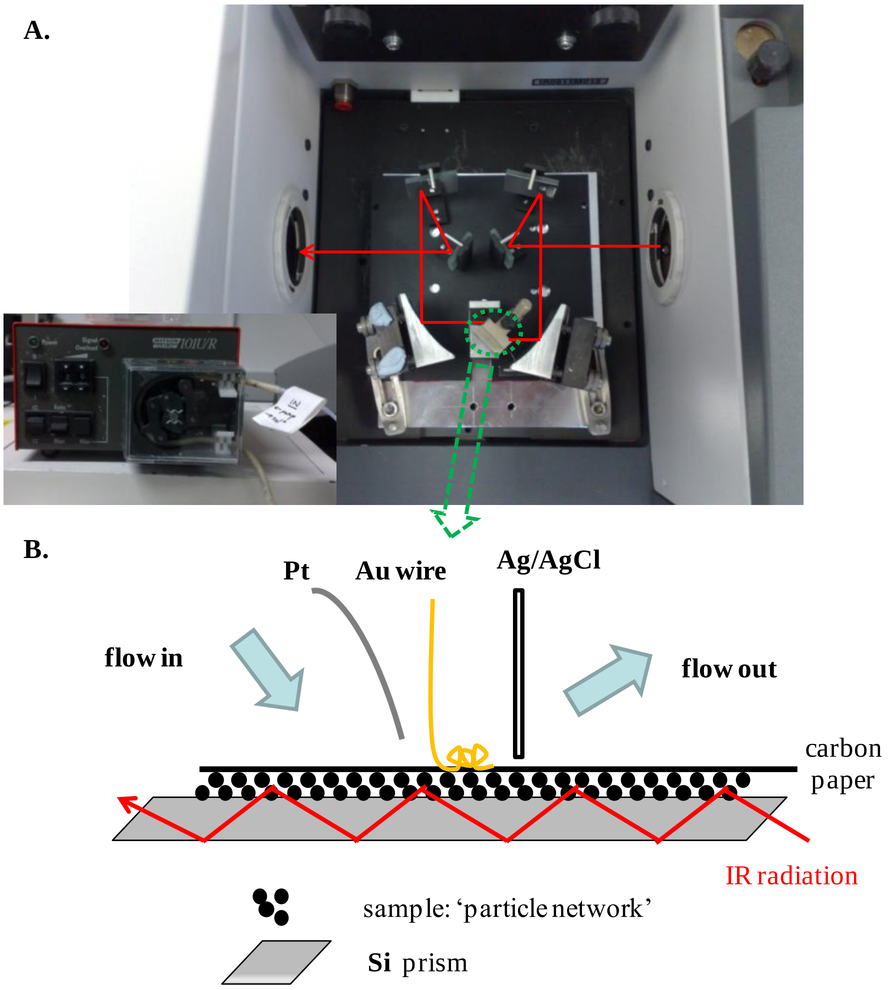

Figure 2-16. Diagram for the optical set-up of the ATR-IR SEC cell. Panel A: The light (red) pathway in the sampling compartment and the pump (left bottom) used for the flow. Panel B: The enlargement of light pathway within the prism and the three electrode configuration above the particle network sitting on the prism.

2.2.9 Preparation of the particle network – the working electrode composition

The working electrode in the ATR-IR SEC cell was composed of a carbon particle film (the carbon supported noble metal nanoparticle film used in Chapter 5 and the RHstop/carbon composite film used in Chapter 6), a backing-up carbon paper (AvCarb P50T Carbon Fiber Paper, 0.28 gm/cm^3, 175 μm thick) to enhance the lateral electrical conductivity and an Au wire (Aldrich, 0.127 mm diameter), as shown in Figure 2-17(B). Preparation of the particle film is described below.

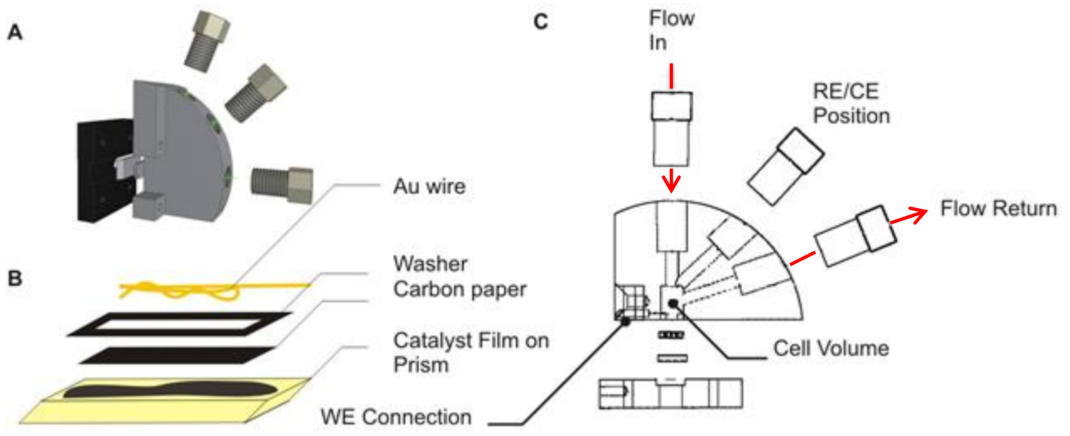

Figure 2-17. The design of the ATR-IR SEC cell. Panel A: An exploded perspective view of the cell in its vertical, operating position; Panel B: The components of the catalyst film, including the Au wire connecting the working electrode, a washer for seal, a carbon paper for lateral conductivity of the particle film and an actual particle film on prism; Panel C: The internal structure of Panel A, along with the locations of the three electrodes and the flow set-up.

The carbon-supported noble metal nanoparticle film

Three noble metal catalysts were used for the formic acid oxidation: Pt (20% on carbon black, Alfa Aesar), PtRu (Pt, 40%; Ru 20% on carbon black, Alfa Aesar) and Pd (20% on carbon black, Tsang Group, Department of Chemistry, Oxford). The diameter of the noble metal was less than 10 nm and it is therefore called nanoparticulate. Furthermore, the noble metal nanoparticle was not simply mixed with the carbon particle (85.6 μm in diameter), but directly immobilised onto the carbon particle. In this Thesis, this carbon-supported nobel metal nanoparticle is designated as noble metal@C, such as Pt@C. The Pt and PtRu particles had a diameter of 2.8 nm and 2.6 nm, respectively, according to the information provided by the company. The Pd particle in Pd@C was characterised to have a diameter of 5 nm.[204] Ethanol (pure analytical grade, Sigma Aldrich) was used to disperse the solid catalyst which is very hydrophobic, and Nafion®117 (5 wt% in lower aliphatic alcohols/H_2O mixture, Sigma Aldrich) was used to bind the particles together in films and act as electrolyte due to its high H^+ conductivity. Here only the Pt@C particle film preparation is described, as the other two catalyst films are prepared the same way. The Pt@C particles were dispersed in ethanol to get a 10 mg/mL mixture. Sonication for 10 min was performed to ensure full suspension of the catalyst particles in the alcoholic mixture. After that, Nafion was added to the 10 mg/mL Pt@C dispersion at a volume ratio of 1:9 and the mixture was thoroughly mixed using a vortex mixer. The catalyst ink was then ready for making the film. Another mixture was made without addition of Nafion for an important control experiment.

A parallelogram Si prism ($10 \times 5 \times 1$ mm^3, 45^o, Crystal GmbH) was first cleaned with ethanol. After evaporation of the ethanol, 2 µL of the catalyst ink prepared as described above was pipetted directly onto the prism to form a particle film (3-D network) and left to partially-dry for about 60 seconds. Then a piece of sulphuric acid wetted carbon paper (AvCarb P50, Ballard) was applied onto this partially-dry film. Then a rubber washer was put onto the carbon paper to make the cell sealed. The particle film configuration will be discussed in more detail in **Section 5.2**. Finally, the cell body was screwed on top and the cell was positioned in the sampling compartment of the spectrometer. The alignment in the compartment was applied to adjust the IR beam path as shown in Figure 2-16(A) and obtain an optimum signal.

The RHstop/carbon particle composite film

Firstly, 25 µL of 3 mg/mL RHstop was placed into the N_2-filled glovebox. The molecular weight of RHstop HoxBC is around 87,000 Da, therefore around 1 nmol of enzyme was utilised to make the film. Then, 1.5 µL of 10 mg/mL carbon black in pH 6 50 mM KPB was mixed with the enzyme to extend the conductive electrode into the film, and 2.5 µL of pH 6 Nafion in 50 mM KPB was also added to the enzyme mixture to provide the enzyme with a hydrated environment and minimise diffusion of enzyme out of the film into the liquid electrolyte in the back of the cell. A mixture of the enzyme, carbon black particles and Nafion was then spotted onto the Si prism. A piece of carbon paper decorated with carbon black particles and Nafion on one side was put onto the partially-dry enzyme film to provide good contact between the enzyme film and the carbon paper. Then the cell was assembled and aligned in the IR compartment as described above.

Multi-bounce reflection, penetration depth and film thickness calculation

The prism used in this Thesis is silicon which is chemically inert and is good for observing the absorbance occurred above 1100 cm^{-1} below which it becomes optically transparent. The length and thickness of the Si prism used in this Thesis is roughly 9.5 mm and 1 mm, respectively. Therefore, the number of reflections for the 45° prism is *ca.* 4, calculated from eqn [2-17], as shown in Figure 2-16(B). For the wavenumber 2000 cm^{-1}, according to eqn [2-29], the penetration depth is calculated to be 0.4 μm using 1.33 (water) as the refractive index of the sample. The refractive index of the carbon particle network which is the real sample, is not precisely known, but is believed to be higher than that of water, therefore, 0.4 μm gives a minimum estimation of the penetration depth according to eqn [2-29].

The thickness of the particle network is an important factor due to the penetration depth of the evanescent wave, and it can be controlled by changing the concentration of the dispersed particle in ethanol (Chapter 5) or the volume of enzyme-carbon mixture used (Chapter 6). Given a certain volume, the more concentrated the catalyst is, the thicker the film is. Calculation of the thickness of a particle film used in Chapter 5 is as shown below.

2 μL of particle mixture: $2 \times 10^{-6} \times 10^{3}\ cm^{3} = 2 \times 10^{-3}\ cm^{3}$

Film area on prism: $8\ mm \times 4\ mm = 32\ mm^{2} = 0.32\ cm^{2}$

The 'wet' film thickness: $2 \times 10^{-3}\ cm^{3}/0.32\ cm^{2} = 0.00625\ cm = 62.5\ \mu m$

However, because only 10% volume of the particle mixture is Nafion, after drying the actual film, the thickness will shrink to *ca.* 6 μm. Therefore, it gives a rough range of the film thickness when it is in operation: 6 ~ 60 μm.

2.2.10 Mini reference electrode and counter electrode in the ATR-IR SEC cell

The reference electrode was a mini leak-free Ag/AgCl electrode (Harvard Apparatus) and potentials were quoted versus SHE using eqn [2-33]. Compared to the Pt wire used in the protein film electrochemistry, the counter electrode Pt wire is thinner, only 0.127 mm in diameter (Alfa Aesar). The Pt wire was wrapped around the reference electrode to ensure sufficient surface area in solution and this assembly was inserted into the ATR-cell via a screw fitting. The cell body was equipped with three holes, like three side arms in the standard electrochemical cell in the Figure 2-12, for sitting the electrodes, introduction of an inhibitor and efficient substrate supply or product removal. The RE/CE assembly was situated in the middle for all the experiments.

2.2.11 Flow function

As shown in Figure 2-17(A) and (C), the lower and top holes were connected with the flow in and out tubing. A peristaltic pump as shown in Figure 2-16 was used to efficiently provide substrate and remove product. The maximum power for the pumping is around 2 mL/min solution exchange rate with the electrolyte inside the cell body. The volume of the cell is approximately 200 µL, thus at its maximum power the electrolyte in the cell is completely replaced every 6 seconds.

2.2.12 Infrared spectrometer and potentiostat

The infrared measurements were obtained using a DigiLab FTS 6000 spectrometer with a liquid nitrogen cooled mercury cadmium telluride (MCT, HgCdTe) detector. The sampling compartment and body of the spectrometer were purged with dry, CO_2-free air (Parker Balston purge gas generator) to maintain constant background levels of water vapour and CO_2. For the noble metal@C particle experiment, each spectrum in Chapter 5 was the average of 250 scans with a resolution of 4 cm^{-1}. For the RHstop/carbon particle experiment in Chapter 6, each spectrum was averaged over 500 scans with 2 cm^{-1} resolution. The electrochemical control was applied via a potentiostat (VersaSTAT 3, Princeton Applied Research) and the software Versa-studio was employed for collecting the electrochemistry data.

2.3 Relation of this Chapter with other Chapters

The experimental results sections of this Thesis mainly consist of two parts, the first half (Chapter 3 and 4) is focusing on the protein film electrochemical investigation of the soluble and regulatory hydrogenase from *Ralstonia eutropha* and the second half (Chapter 5 and 6) describes development of an ATR-IR SEC method to investigate the hydrogenase enzyme. Correspondingly, this Chapter is composed of two sections 'Theory' and 'Method', and each section is divided by disciplines of electrochemistry and infrared spectroscopy.

Chapter 3 Protein Film Electrochemical Investigation of *Ralstonia eutropha* Soluble Hydrogenase

3.1 The Soluble Hydrogenase of *Ralstonia eutropha*

3.1.1 Physiological role in the cell

The microorganism *Ralstonia eutropha* belongs to the Knallgas bacteria, which oxidise dihydrogen at ambient levels of O_2. *Ralstonia eutropha* is capable of growing under either anaerobic or aerobic environments. Therefore, it can switch easily between a heterotrophic lifestyle in which it uses organic compounds as an energy source and a lithoautotrophic lifestyle in which it uses dihydrogen as the sole energy source. As *Ralstonia eutropha* grows at the interface between the aerobic and anaerobic environments, it inevitably encounters a variable level of O_2 which can be used by this H_2-oxidising organism as the terminal electron acceptor.

The soluble hydrogenase from *Ralstonia eutropha* (*Re* SH or the SH) can couple the oxidation of H_2 with the reduction of NAD^+ and therefore provide the cell with reducing power in the form of NADH which then can be used to fix CO_2 in the Calvin cycle.[11] However, when the NAD^+/NADH pool becomes very reduced, the SH can work in the reverse direction, i.e., couple NADH oxidation to H^+ reduction.[205] Hydrogenases that can operate *in vitro* in the presence of O_2, like the as-isolated SH which can sustain $H_2 : NAD^+$ activity, are termed O_2-tolerant hydrogenases, although it is emerging that this is a complex and multi-faceted property as discussed in this Chapter and in Chapter 4 (*Re* RH).

The SH is structurally related to the bidirectional hydrogenases from the cyanobacterium *Synechocystis* sp. PCC 6803 (which obtains its energy through photosynthesis) and the actinomycete *Rhodococcus opacus* (which plays a crucial role in decomposing organic materials in soil, freshwater and the sea) sharing high similarity in amino acid sequence for both the hydrogenase moiety HoxHY and the diaphorase moiety HoxFU.[1,206] However, unlike *Ralstonia eutropha*, *Synechocystis* sp. PCC 6803 cannot grow under lithoautotrophic conditions and the physiological role of its bidirectional hydrogenase is still unknown. It is believed to act as a redox regulator to maintain a proper redox level in the cell.[207] Therefore, the results presented in this Chapter are discussed in the context of other relevant NiFe(Se) hydrogenases and the related bidirectional hydrogenase from *Synechocystis* sp. PCC 6803.

3.1.2 Catalytic moieties of *Re* SH

The SH is a complex, six-subunit enzyme $HoxHYFUI_2$ which catalyses H_2 oxidation coupled with NAD^+ reduction and its reverse reaction H^+ reduction coupled with NADH oxidation. The catalytic moiety which is responsible for the $2H^+/H_2$ cycling is called the hydrogenase dimer, HoxHY, and the other catalytic moiety which is responsible for the NAD^+/NADH cycling is called the diaphorase dimer, HoxFU, as shown in Figure 3-1. The SH harbours multiple redox cofactors: a NiFe active site which catalyses the $2H^+/H_2$ cycling, two non-covalently bound flavin mononucleotide (FMN-a and FMN-b) groups which may be involved in the hydride (H^-) transfer (FMN-b) and one-to-two electron converter (FMN-a),and a series of FeS clusters for intramolecular electron transfer, as shown in Figure 3-1.

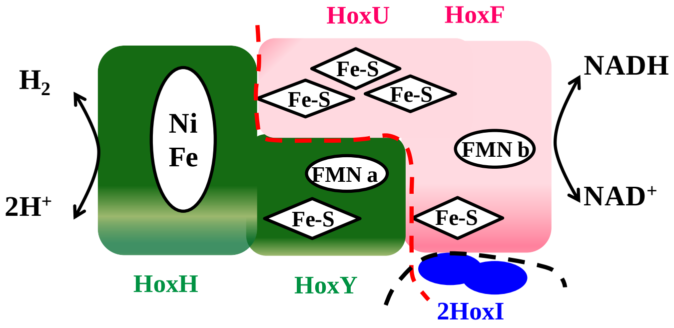

Figure 3-1. Schematic representation of the catalytic modules of the soluble NiFe hydrogenase from *Ralstonia eutropha* H16 ($HoxHYFUI_2$) consisting of the hydrogenase moiety (HoxHY), the diaphorase (HoxFU) moiety and two identical subunits HoxI. Other cofactors in the SH are the NiFe active site, two FMN groups and a series of FeS clusters. The dotted red line represents the fact that the SH can be selectively purified into a hydrogenase dimer (green) and a diaphorase dimer (pink) after a deletion of the corresponding gene in the framework. The black dotted line represents the dissociation of the small subunits HoxI under unfavourable conditions.

A clear evolutionary relationship exists between the SH and the mitochondrial NADH:ubiquinone oxidoreductase from *Thermus thermophilus* (Complex I) in terms of amino sequence similarity. The hydrogenase moiety HoxH and HoxY in the SH share similarities with the Nqo4 and Nqo6 subunits of Complex I, respectively. The main difference lies in the fact that the quinone-binding site in Nqo4 is replaced by the NiFe active site in HoxH. On the other hand, the diaphorase moiety HoxF and HoxU share high similarities to the subunits Nqo1, Nqo2 and Nqo3 which are responsible for the NAD^+/NADH cycling in Complex I. The HoxF subunit of the SH resembles a combination of Nqo1 and Nqo2 but lacks a 2Fe-2S cluster. The HoxU subunit of the SH corresponds to Nqo3 with a missing C-terminal peptide chain.[208,209] Therefore, an investigation of the SH may provide some insights into understanding the important NADH-ubiquinone oxidoreductases. A further biochemical study showed that the SH contains two additional identical small subunits HoxI which may provide a binding domain for NADPH: the location of HoxI is probably close to the HoxF subunit.[201] It was found that the hexameric SH ($HoxHYFUI_2$) showed NADPH-$K_3Fe(CN)_6$ activity in enzyme assays, indicating that the SH is capable of oxidising NADPH with $K_3Fe(CN)_6$ as electron acceptor, although at a low rate.[53,201] However, the stability of the hexameric SH depends highly on the ionic strength and the pH of the buffer because at higher ionic strength or alkaline pH the dissociation of HoxI from the main body HoxHYFU occurs.[201]

3.1.3 Results from biochemical assays

Stability and enzyme reactivation

The SH was purified in air between 0 and 4 °C. The as-isolated enzyme is inactive for H_2 oxidation, but can be activated by addition of reducing agents or catalytic amounts of NADH in the presence of H_2. It should be pointed out that incubation of the SH with only dihydrogen did not restore the activity in the enzyme assays.[53] One unique feature of the SH was that the oxidised inactive form was relatively stable and there was no loss of activity when stored aerobically at -20 °C for a couple of months. Only a 25% of decrease in enzyme activity was found for the aerobically purified SH at 4 °C. In contrast, the reduced active form was of poor stability. A complete loss of enzyme activity within 5 days at 4 °C was observed in the SH when stored with H_2 and 5 μM NADH.[53]

Reversibility of ***Re*** SH

The bidirectional functioning of the SH was investigated by the enzyme assays. It was found that under N_2 in the presence of NADH and dithionite the rate of H^+ reduction was 2.4 % of the reverse reaction: H_2 oxidation in the presence of NAD^+ and dithionite. This finding is in strong agreement with its physiological role in the cell: the enzyme is biased to production of NADH at the expense of H_2, therefore providing the cell with reducing power as NADH. However, when using reduced methyl viologen (MV) as an artificial electron donor, the rate for H_2 evolution was almost identical to that of H_2 oxidation, suggesting that different electron pathways may exist.[53]

The hydrogenase moiety HoxHY was selectively purified through a deletion of the HoxFU module in the framework.[147,199] The detailed purification procedure was as described in Chapter 2. The biochemical characterisation of HoxHY showed that the specific activity for H^+ reduction with MV as artificial electron donor was 10-12 Units/mg and the H_2-oxidation activity of 1 Units/mg in the presence of dithionite was obtained. Obviously, the catalytic bias for H_2 evolution in HoxHY determined by enzyme assays is dramatically different from that found for the whole native SH described above. However, incubation with exogenous FMN of HoxHY led to a 3-4 fold increase in the specific activity for H_2 oxidation. The substoichiometric amount of FMN in HoxY (0.05 equiv. of FMN per HoxHY) caused by the absence of the HoxFU module was possibly the reason for the anti-physiological bias in HoxHY. The role of FMN will be discussed **Section 3.1.6.** The diaphorase moiety HoxFU can also be selectively purified like the hydrogenase moiety by genetic deletion of the HoxHY module in the framework.[147,199,210] However, *in vitro* mixing the two modules can reconstitute the structure of the tetrameric SH and restore the specific activity of the native enzyme.[199]

Standard inhibitors of ***Re*** SH?

Carbon monoxide (CO) is a competitive and reversible inhibitor for most NiFe(Se) hydrogenases, such as *Av* MBH,[27,82] *Re* MBH,[82,83] *Df* NiFe hydrogenase,[67,112] *Dv* MF NiFe hydrogenase[119] and *Dm. b* NiFeSe hydrogenase.[89] The CO-inhibited states have been investigated and observed by a variety of methods, such as EPR,[98] FTIR,[27,112] PFE,[61] XAS[211] and crystal structure.[119] For the SH, according to the studies of solution assays, it was found that CO did not inhibit the enzyme activity ($H_2 : NAD^+$) no matter whether CO was introduced to the as-isolated or reductively activated state. Its CO tolerance corresponds well to the EPR results that no changes were observed after incubation of the enzyme with CO.[212] The FTIR studies also confirmed that no CO-induced states were found either in the as-isolated or reduced SH.[213,214] However, after prolonged incubation of the SH with NADH, the Ni-C state was formed, confirmed by EPR, and it can bind the exogenous CO to generate a Ni-CO signal in EPR spectra.[215]

All the hydrogenases obtained so far are reversibly or permanently inhibited by dioxygen (O_2).[75] In FeFe hydrogenases, the active site and iron-sulphur clusters are substantially damaged after O_2 attack.[5] Recently, some NiFe hydrogenases (*Re* MBH, *E. coli* Hyd-1, *Aa* MBH I) are found to be capable of oxidising H_2 in the presence of O_2 and termed O_2-tolerant hydrogenases.[82,85,87] The SH *in vivo* can couple H_2 oxidation with NAD^+ reduction in the presence of O_2. *In vitro*, the as-isolated inactive SH catalyses the reduction of NAD^+ at the expense of H_2 without preliminary reactivation.[53] However, a lag phase existed before the maximum reduction rate of NAD^+. The lag phase was eliminated by adding NAD(P)H or removing the remaining O_2 from solution.[53] Further O_2 effect experiments were performed to test the specific activity $H_2 : NAD^+$ of the SH and it was found that even 20% O_2 in H_2 did not cause any inhibition.[212]

3.1.4 EPR and IR investigation of redox states of *Re* SH

In contrast to 'O_2-sensitive' NiFe hydrogenases, the Unready Ni-A (Ni-A is preferably formed under electron-poor environment and is reactivated at a very slow rate) and the Ready Ni-B (Ni-B is preferably formed under electron-rich environment and is reactivated within a few seconds) states are missing in electron paramagnetic resonance (EPR) spectroscopy for the SH.

Only three EPR-active states so far have been observed: an active state Ni-C ($g_{x,y,z}$ = 2.20, 2.14, 2.01) after treatment with an excess of NADH or dithionite, a non-physiological, light-induced state Ni-L ($g_{x,y,z}$ = 2.28, 2.10, 2.05) and a CO-induced state Ni-CO ($g_{x,y,z}$ = 2.35, 2.08, 2.01) after exposure to CO of the NADH-reduced SH.[215] A more recent *in-situ* EPR investigation of the SH (the SH is present in the cytoplasm of the *Ralstonia eutropha* cells) was performed.[149] *Ralstonia eutropha* produces three NiFe hydrogenases (*Re* SH, *Re* MBH and *Re* RH) and the genes encoding for the other two hydrogenases (*Re* MBH and *Re* RH) were inactivated by a markerless inframe deletion. Therefore, the cell only generates the SH. It was found that in the living cells approximately 60% of the active sites stayed as the active Ni-C state ($g_{x,y,z}$ = 2.20, 2.14, 2.01) due to the reducing environment in the cytoplasm. Incubation with H_2 and NAD^+ anaerobically led to the disappearance of Ni-C, suggesting the redox changes at the Ni site. After illumination, the Ni-C state can be completely transformed to the Ni-L state ($g_{x,y,z}$ = 2.27, 2.10, 2.05) and this conversion is fully reversible. However, after incubation with the oxidant NAD^+, neither Ni-A nor Ni-B was found. The observation of Ni-C and Ni-L and the absence of Ni-A and Ni-B by *in-situ* EPR correspond well with earlier EPR studies.[149,215]

Earlier infrared spectra reported for the as-isolated SH showed four cyanide (CN^-) peaks and only one carbon monoxide (CO) peak.[29] Therefore, it was concluded that *Re* SH contained four cyanide ligands and one carbonyl ligand coordinated to the active site, shown as $(CN)_1NiFe(CO)_1(CN)_3$. Three of the four CN^- ligands were assigned to Fe and the last one was ascribed to Ni, and this unusual ligation was used to explain the tolerance to oxygen.[213] However, this coordination assignment breaks the classical 18-electron rule for the Ni atom (not for the Fe). A more recent *in-situ* FTIR study on the SH as a constituent in the cytoplasm showed that the SH actually owns a standard set of ligands, i.e., $NiFe(CN)_2(CO)_1$, rather than the previously proposed $(CN)_1NiFe(CO)_1(CN)_3$.[149,213] However, the O_2 tolerance mechanism needs to be re-investigated as the extra two cyanides which were suspected of blocking the reaction of the SH with O_2 do not actually exist. In the freshly harvested SH-containing cells, the infrared spectra showed the presence of the dominant Ni-C state (1961, 2080, 2091 cm^{-1})

and two other reduced states Ni-SR' (1922, 2052, 2068 cm^{-1}) and Ni-SR" (1913, 2052, 2068 cm^{-1}). The presence of dominant Ni-C observed by FTIR is in line with the corresponding *in-situ* EPR findings. The infrared investigation also confirmed the disappearance of Ni-C and a generation of Ni-SR (1946, 2080, 2090 cm^{-1}) and Ni-SR2 (1958, 2068, 2080 cm^{-1}) after incubation of the SH-containing cells with H_2. On the other hand, incubation of the freshly harvested *Re* SH either with NAD^+ anaerobically or with O_2 led to the disappearance of Ni-C, as seen by *in-situ* FTIR and this is also in agreement with the EPR findings. Furthermore, an unusual 'Ni-B like' state (1957, 2079, 2089 cm^{-1}) was generated after incubation with oxidants, however, it differs from Ni-B since it is an EPR-silent state.[149] The observation of Ni-C, Ni-SR, Ni-SR' and Ni-SR" in the SH by the *in-situ* FTIR corresponds well with earlier infrared spectroelectrochemical findings.[149,216] In this Thesis, the labels S and R represent EPR-silent and reduced states, respectively. The states Ni-B like, Ni-C and Ni-SR2 in *Re* SH are assigned by comparison with the bidirectional hydrogenase from *Synechocystis sp.* PCC 6803.[217] The three reduced states Ni-SR, Ni-SR' and Ni-SR" in the SH are termed by comparison with *Re* MBH.[121] A summary of different redox states of the whole SH by EPR and IR is presented in Figure 3-2.

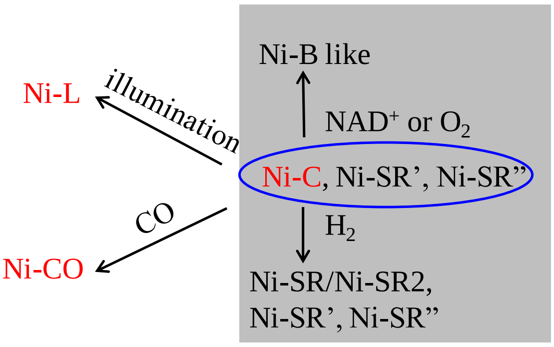

Figure 3-2. Scheme of different redox states experienced by *Re* SH as a whole enzyme.[149,215,216] The EPR-active states are labelled as red. The possible physiological states are marked inside a grey box. The redox states in the native SH within the living cells are indicated by a blue oval.

A very recent infrared spectroscopic investigation of the hydrogenase moiety HoxHY has been performed. In a typical purification of HoxHY, an oxidised inactive Ni-Ox state (1956, 2087, 2096 cm^{-1}) was predominant in the as-isolated HoxHY. Incubation of the as-isolated HoxHY with certain reducing agents generated a mixture of Ni-Ox2 (1938, 2065, 2079 cm^{-1}), Ni-SR' (1923, 2052, 2069 cm^{-1}) and Ni-SR states (1946 cm^{-1}), suggesting that Ni-Ox was a more oxidised state and Ni-Ox2 was an intermediate upon reduction of Ni-Ox. When O_2 was introduced to the reduced HoxHY, a mixture of Ni-Ox and Ni-Ox2 were re-formed. In this Chapter, the labels Ox and R represent the oxidised and reduced states. The Ni-SR, Ni-SR' and Ni-SR" states are termed based on the *in vivo* infrared spectroscopic investigation of the native SH within the living cells.[147,149] However, in an unusual purification of HoxHY, a second inactive Ni-Ox2 state was present in the purified enzyme. Reduction of Ni-Ox2 led to the formation of Ni-SR' and Ni-SR2 (1956, 2052, 2069 cm^{-1}). A slow flux of O_2 converted the reduced species completely to Ni-Ox2. An *in vivo* FTIR study on the HoxHY-containing cells showed that a mixture of Ni-Ox2 and Ni-SR2 were present, consistent with the reducing conditions in the cytoplasm. The redox states of HoxHY revealed by FTIR are summarised in Figure 3-3. The reduced states of HoxHY resemble those found in the whole SH. However, the difference between them mainly lies in the oxidised and active species. The lack of Ni-C and Ni-B-like species and the presence of two oxidised inactive Ni-Ox and Ni-Ox2 are likely related to the substoichiometric level of FMN-a and the deletion of the diaphorase moiety HoxFU, suggesting impaired electron transfer to the active site affects the redox states.

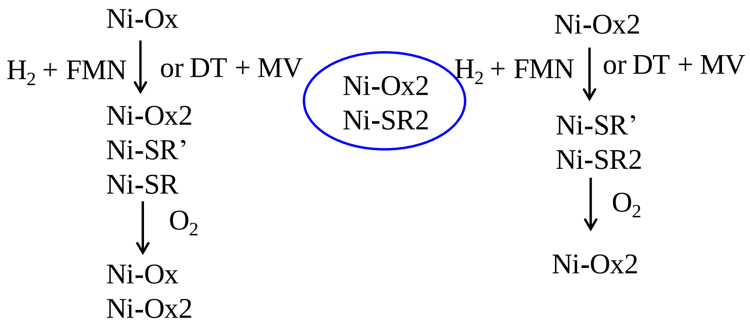

Figure 3-3. Scheme of different redox states experienced by *Re* HoxHY determined by FTIR.[147] The redox states in the HoxHY-containing living cells are indicated by a blue oval. The left panel represents the redox states of HoxHY obtained by a typical purification and the right panel reprsents the redox states of HoxHY obtained by an unusual purification.

3.1.5 Iron-sulphur clusters in *Re* SH

The standard NiFe hydrogenases harbour three iron-sulphur clusters: the proximal, medial and distal cluster which act as an electron relay to transfer electrons between the protein surface and the buried active site. However, the polypeptide HoxY in the SH, which is assigned as housing an electron transfer centre, is substantially smaller than its counterpart in standard NiFe hydrogenases and the limited structure predicts that only one 4Fe4S cluster is present close to the NiFe active site.[218]

Two forms of iron-sulphur clusters were found in *Re* SH by EPR, one is 4Fe4S cluster and the other is 2Fe2S cluster.[212] In the reduced SH, a signal with *g* values at 2.04 and 1.95 was ascribed to a single reduced $2Fe2S^{1+}$ cluster and at least one reduced $4Fe4S^{1+}$ centre, respectively.[215]

A very recent investigation of the FeS cluster in the hydrogenase moiety HoxHY by X-ray absorption spectroscopy (XAS) has been performed. This method can provide information about the oxidation state of the metal by X-ray absorption near edge structure (XANES) and the coordinated ligands in terms of the number of ligands, coordination atom, and the distance from the metal centre by extended X-ray absorption fine structure (EXAFS). When the crystal structure of the protein is absent, this method becomes more important to offer the oxidation state of the metal and the ligand information.[147,219-222] Analysis of the iron-to-iron distances and coordination situations at the Fe sites revealed by EXAFS along with the metal content determined by the total reflection X-ray fluorescence (TXRF), suggest the presence of one 4Fe4S cluster in HoxY.[147] A UV/visible absorption spectrum of the diaphorase moiety HoxFU showed shoulders at 322/380 nm and 421/480 nm which are ascribed to the 2Fe2S and 4Fe4S clusters, respectively.[210] Furthermore, based on the amino acid sequence similarities with the subunits Nqo6, Nqo3 and Nqo1 in *Thermus thermophilus* Complex I, one 2Fe2S and four 4Fe4S clusters are tentatively assigned as the constituents in *Re* SH.[209,210]

3.1.6 Existence and function of FMN in *Re* SH

One unique feature of the SH compared to other hydrogenases is that it contains the flavin cofactor, flavin mononucleotide (FMN). As apoflavodoxin (which is a bacterial protein containing FMN or flavin adenine dinucleotide (FAD)) specifically binds FMN tightly and rapidly, the quenching study of the fluorescence at 525 nm derived from FMN by titration with a standardised solution of apoflavodoxin can determine the content of FMN in the enzyme.[223] The content of FMN in different purifications was determined to vary from 1.1 to 1.4 molecules per molecule of SH. Furthermore, it was found that addition of exogenous FMN to the purified enzyme stimulated its catalytic activity. However, there was no promotion effect when adding FAD as a control experiment. Therefore, it is believed that a certain portion of FMN dissociates from the enzyme during the purification. Through analysis of the percentage of the activation by adding exogenous FMN, it was calculated that one molecule of the SH contains two molecules of FMN.[224] Albracht *et al.* later pointed out that the protein content was considerably overestimated by the colourimetric protein-determination methods. The FMN content was then compared with an internal standard, i.e., the spin concentration of the EPR signal from the $[2Fe2S]^{1+}$ cluster. The conclusion that the SH contains two FMN groups was made in a more precise way.[225]

Amino acid sequence study showed that two FMN cofactors in the SH are both non-covalently bound. One of the FMN groups (FMN-a) is selectively released upon long incubation of the as-isolated SH with NADH whereas the other FMN (FMN-b) is tightly bound. The activity for H_2 : NAD^+ is inhibited due to the release of FMN-a. However, the NADH-dehydrogenase and the benzyl viologen : H_2 activities are not affected. Furthermore, the activity for NAD^+ : H_2 can be restored by adding exogenous FMN to the reduced SH, indicating FMN-a plays a role in transferring electrons between the two catalytic moieties.[226] Standard NiFe hydrogenases do not contain any flavin cofactors probably due to the limited space in the small subunit which houses three iron-sulphur clusters. However, the C-terminal of the small subunit HoxY in the SH which should hold two extra FeS clusters (medial and distal) instead provides space for FMN.[209] As the FeS cluster functions as the centre for transferring one electron at a time, however, cycling between NAD^+ and NADH requires the transfer of two electrons and one proton, FMN-a is proposed to function as a one-to-two electron converter during the catalysis of H_2 : NADH.[226]

The high-resolution X-ray structure of Complex I from *T. thermophilus* showed that due to the stacking interaction between NADH and reduced FMN it is favourable for the hydride transfer directly from NADH to FMN in Nqo1.[227] As discussed above, the subunit HoxF of the SH shares high similarities in amino acid sequence to the fusion of Nqo1 and Nqo2 in Complex I, therefore FMN-b in HoxF is likely to function as a hydride carrier in the NAD^+/NADH cycling.[210] Figure 3-4 shows the process of hydride (H^-) transfer on the NAD^+ and the oxidised FMN, respectively.[228]

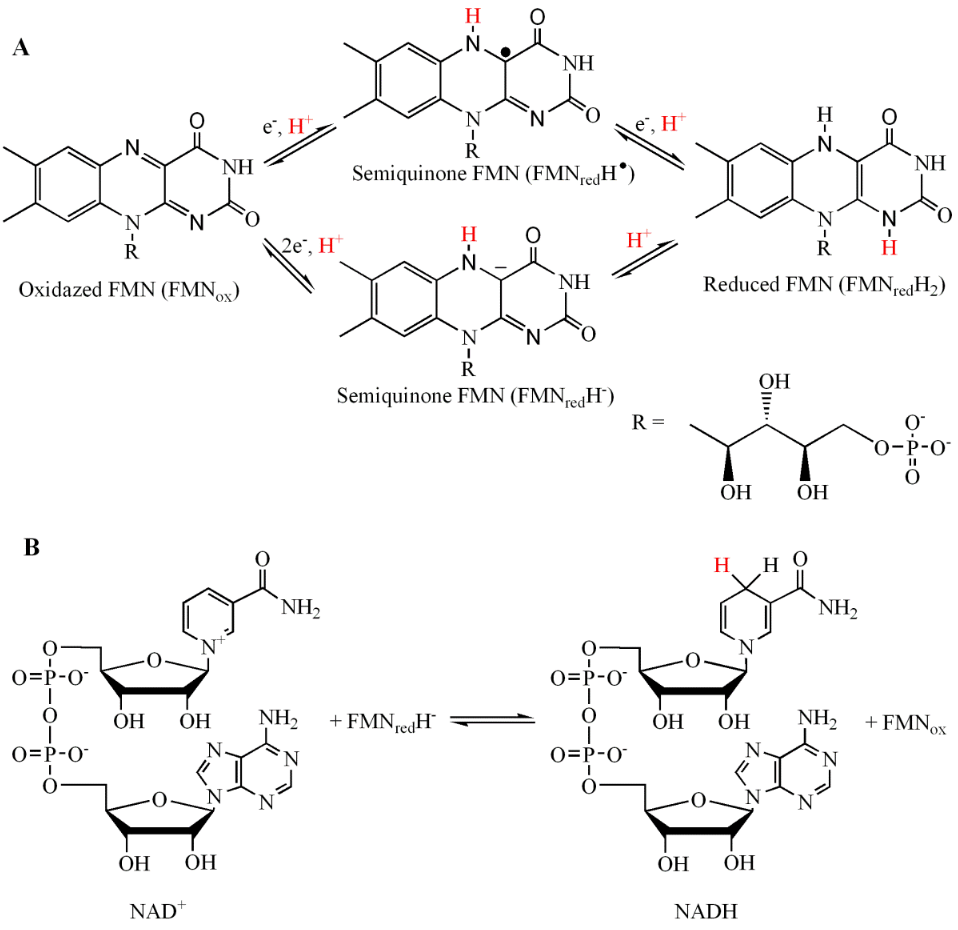

Figure 3-4. Panel A: The hydride (H^-) transfer at different forms of FMN; Panel B: Reduction of NAD^+ to NADH involved in hydride transfer.

3.2 Electrochemical investigation of *Re* SH

3.2.1 Relationship between dimeric, tetrameric and hexameric constructs of *Re* SH

In this Chapter, protein film electrochemical investigation of the SH was performed, including the H_2 cycling and its reaction with CO and O_2. As discussed above, the SH is a six-subunit enzyme consisting of two catalytic modules (the hydrogenase moiety HoxHY and the diaphorase moiety HoxFU) and two HoxI subunits which may provide the binding site for NADPH, as shown in Figure 3-1. Due to the multiple subunits and cofactors contained in the SH, it is desirable to break the whole enzyme into independent catalytic moieties to investigate the enzyme in both parts and as a whole. *In vitro*, a structurally related soluble hydrogenase from *Rhodococcus opacus* easily dissociates into the hydrogenase moiety HoxHY and the diaphorase moiety HoxFU.[206,229,230] In contrast, *Re* SH is very stable with respect to the dissociation.[53] However, the hydrogenase moiety HoxHY can be selectively purified by a deletion of the genes encoding for the diaphorase module HoxFU from the plasmid.[147,199] Through the same genetic strategy, the diaphorase moiety can also be solely purified.[210] The dashed red line in Figure 3-1 depicts the selective isolation of either HoxHY or HoxFU, and the black dashed line indicates the purification of the tetrameric SH through dissociation of HoxI from the hexameric SH which occurs at high pH and ionic strengths. Therefore, the purification of the hexameric SH (HoxHYFUI$_2$) needs to be carried out under strict conditions, i.e., in 50 mM pH 7 potassium phosphate buffer.[201]

So far, *Re* SH has never been studied by protein film electrochemistry though it has been investigated by IR and EPR. To start with, the hydrogenase moiety HoxHY is investigated without the interference of the diaphorase moiety, then the tetrameric and hexameric SH are examined.

3.2.2 The hydrogenase moiety HoxHY

3.2.2.1 As-isolated HoxHY on an electrode and definition of E_{switch}

Figure 3-5(A), a cyclic voltammogram (red) is shown for a film of as-isolated HoxHY adsorbed on the surface of a pyrolytic graphite 'edge' (PGE) electrode. A voltammogram for an unmodified electrode (grey) under analogous conditions was also recorded to clarify the capacitance of the electrode. No current was observed for H_2 oxidation or H^+ reduction by the bare electrode. The scan starts from 0 V vs. SHE (all the potentials in this Thesis are referenced to SHE) to examine the behaviour of as-isolated HoxHY before reductive activation, and at the very commencement the current is near zero, indicating that as-isolated HoxHY is inactive for H_2 oxidation. This electrochemical finding corresponds well with the result that the as-isolated HoxHY is inactive for H_2 oxidation observed by the solution assays.[53] On sweeping the potential in the reductive direction, there is a recovery peak just positive of the thermodynamic potential E ($2H^+/H_2$), which can be seen by a deviation to positive current from the background scan. As described before in Chapter 2, a positive current corresponds to an oxidation reaction whereas a negative current represents a reduction process. The enzyme activity is directly proportional to the catalytic current magnitude. Therefore, this peak is arising from H_2 oxidation, indicative of the reductive activation of as-isolated HoxHY. However, the current then drops as the driving force for H_2 oxidation is decreased. As the scan continues, the enzyme begins catalysing H^+ reduction immediately after the potential is swept below the E ($2H^+/H_2$). On the reverse scan, H^+ reduction continues until the E ($2H^+/H_2$) is reached, then H_2 is oxidised again. The current crosses the bare electrode scan very close to E ($2H^+/H_2$) indicating that HoxHY functions in either direction with minimal overpotential. In the process of reactivation of inactive hydrogenases, the potential of maximum slope in the current ascent has been defined as E_{switch} by Armstrong and co-workers,[64] as shown in Figure 3-5(B). The E_{switch} value (-345 mV at pH 7 and 1 bar H_2 with a scan rate of 1mV/s) is indicated in both panels as a vertical black bar.

It should be pointed out that the electrode was stationary throughout the experiment in order to diminish the film loss since the HoxHY film formed on the PGE electrode was unstable. However, the catalytic current is sufficiently small that it is likely that the H_2 oxidation rate is controlled by the enzyme activity rather than the substrate diffusion, as discussed in later section. Despite the low current, the potential dependence of catalytic features can be clearly observed. One thing that should be addressed here is that this reductive activation is irreversible for as-isolated HoxHY, i.e., the as-isolated state cannot be regenerated after activation even if O_2 is introduced under electron-rich/poor or H_2 /N_2-rich conditions (data not shown here).

Compared to other NiFe hydrogenases,[75,85,231] the catalytic activity of the hydrogenase moiety HoxHY is very low, i.e., the catalytic current for H_2 oxidation or H^+ reduction is lower than 100 nA compared to a few μA for other hydrogenases. For HoxHY, the enzyme activity observed on an electrode is proportional to its solution assay behaviour, suggesting that the activity is not being harmed by immobilisation of the electrode. The H_2 oxidation activity by HoxHY is only 1/50 to 1/100 of that by *Aa* MBH I as found by enzyme assays, and the corresponding catalytic current by HoxHY is also 1/50 to 1/100 of that by *Aa* MBH I in PFE.[87,147,232]

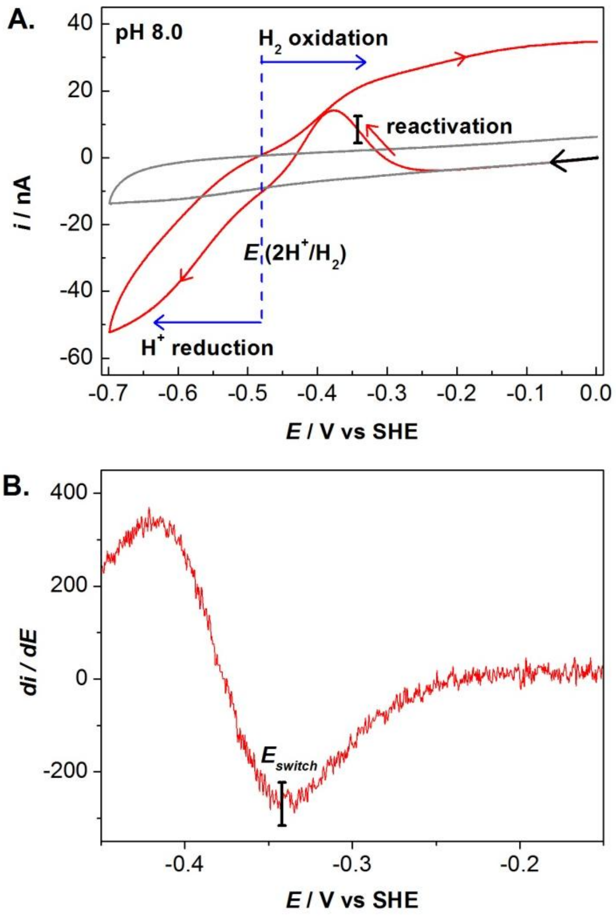

Figure 3-5. Panel A: Cyclic voltammogram of as-isolated HoxHY adsorbed (red) on a stationary pyrolytic graphite 'edge' (PGE) electrode in pH 8 (50 mM potassium phosphate) buffer (KPB). Conditions: the scan rate is 1 mV/s; 1 bar H_2; 30 ^{o}C; the scan direction is shown by the arrowheads; the blue vertical dashed line indicates the thermodynamic potential of the couple $2H^+/H_2$ corrected for the experimental conditions. A voltammogram of an unmodified electrode (grey) under analogous conditions was also recorded to clarify the capacitance of the electrode. Panel B: Derivative plot (d*i*/d*E* vs *E*) of the reductive portion of the voltammogram for adsorbed HoxHY in Panel A shows that E_{switch} is defined as the minimum in *di/dE*. The E_{switch} value is indicated in both panels as a vertical black bar.

The diaphorase moiety HoxFU on an electrode

A similar genetic strategy for the HoxHY isolation was also applied to purify the diaphorase moiety HoxFU which is responsible for catalysing NAD^+/NADH cycling in the SH. Figure 3-6 shows a voltammogram of a HoxFU-modified PGE electrode in the presence of 1 mM NAD^+ and 1 mM NADH at pH 8 and 30 ^{o}C. The electrode was rotated at 2500 rpm to provide substantial substrate to the electrode and remove the product away from the electrode. The thermodynamic potential *E* (NAD^+/NADH) corrected for the experimental conditions is indicated as the blue dashed line. A voltammogram recorded at an unmodified electrode in the presence of NADH and NAD^+ under analogous conditions is shown by the black line to clarify the capacitance contribution from the electrode, and no current was observed for NADH oxidation or NAD^+ reduction. The voltammogram in red clearly shows that NADH oxidation and NAD^+ reduction are catalysed by HoxFU above and below the *E* (NAD^+/NADH), respectively. The current crosses the background scan very close to the *E* (NAD^+/NADH), demonstrating that the diaphorase moiety HoxFU is capable of catalysing the NAD^+/NADH cycling with minimal overpotential. Furthermore, it shows that HoxFU on electrode is more biased towards the NAD^+ reduction at 1:1 ratio of NADH and NAD^+, which is in good agreement with its physiological role in the cell. The potential where the current trace crosses the background scan does not match the *E* (NAD^+/NADH) perfectly with around 20 mV gap. This is arising from the uncertainty in the ratio of [NAD^+]/[NADH] because the purchased NADH was slightly contaminated by NAD^+. The thermodynamic potential for the $2H^+/H_2$ couple with H_2 concentration between 100 nM and 10 µM is marked as the grey box in Figure 3-6, closely spaced with the *E* (NAD^+/NADH). As demonstrated above, both enzyme moieties (the hydrogenase and diaphorase) function at negligible overpotential, and this will be important in allowing the enzyme to catalyse NAD^+ reduction using electrons from H_2 oxidation since there is only a small electrochemical driving force available.

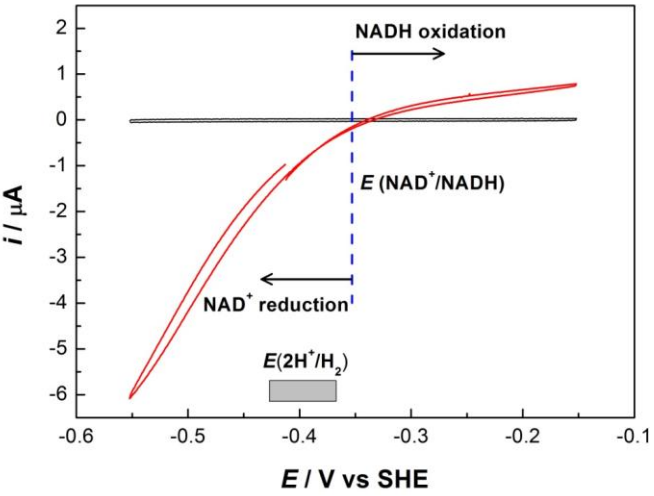

Figure 3-6. Cyclic voltammograms showing the NAD^+/NADH cycling (red) catalysed by the diaphorase moiety HoxFU adsorbed on a PGE electrode in the presence of 1 mM NAD^+ and 1 mM NADH. The black voltammogram was recorded for an unmodified electrode under analogous conditions. Other conditions: Tris-HCl buffer (50 mM, pH 8.0) at 30 °C, scan rate 10 mV/s, electrode rotation rate 2500 rpm. The grey box shows the range of the thermodynamic potentials of the couple $2H^+/H_2$ at pH 8.0 and 30 °C with the concentration of H_2 between 100 nM and 10 µM. The thermodynamic potential for *E* (NAD^+/NADH) corrected for the experimental conditions is indicated as the blue dashed line.[210]

The effect of pH on catalytic bias by HoxHY

Figure 3-7, together with Figure 3-5(A), presents the pH effects on the catalytic bias of $2H^+/H_2$ cycling catalysed by HoxHY. The *E* ($2H^+/H_2$) is corrected for the experimental conditions and marked as the dashed blue line. A voltammogram of an unmodified electrode under analogous condition was also recorded as the grey line in each panel. The contribution of capacitance is subtracted when measuring the catalytic bias. At pH 8.0 the activity for H^+ reduction at a potential 150 mV negative of *E* ($2H^+/H_2$) is 1.5 times that of H_2 oxidation at a potential 150 mV positive of *E* ($2H^+/H_2$); at pH 7.0 the H^+ reduction activity is 3 times that of H_2 oxidation; and at pH 6 it is 4 times. Generally, lower pH is more favourable for H^+ reduction and higher pH is for H_2 oxidation, as expected. The catalytic bias toward H^+ reduction by HoxHY adsorbed on electrode is not in line with its physiological role in the cell. The solution enzyme assay study on HoxHY also showed a biased catalysis towards H^+ reduction.[147] However, the catalytic bias observed *in vitro* does not necessarily match the cellular role of the enzyme as many factors can affect the bias. In the case of HoxHY, the substoichiometric FMN-a in the HoxY subunit may inhibit the electron transfer during H_2 oxidation as adding exogenous FMN to the reduced HoxHY greatly promotes the enzyme activity for H_2 oxidation.[147] More importantly, the redox environment provided *in vivo* by the living cells is different from those in electrochemistry and solution assays. In Nature, we often find enzymes 'just' working well enough. As long as HoxHY oxidises H_2, the rate for H^+ reduction does not matter. The electron pathway in the native SH is through H_2 to NAD^+ or its reverse reaction NADH to H^+. However, the electron transfer in the isolated HoxHY moiety has been altered compared to the whole enzyme. Therefore, it could also alter the catalytic bias.

In Figure 3-7(A), a short period of rotation of the electrode at 2000 rpm marked as a blue asterisk was added to confirm that the activity for H_2 oxidation is not limited by the substrate supply. There is no increase in current after adding rotation, indicating that H_2 oxidation is not limited by diffusion control under stationary conditions. A crossing occurred in Figure 3-7(A) between the voltammogram on the reverse scan before adding rotation and the reactivation peak on the forward scan. This is ascribed to the 'film loss'. The film loss can be arising from the dissociation of the enzyme film from the electrode, but can also be due to denaturation of the enzyme or loss of the cofactors within the enzyme.[76,210] Therefore, all experiments unless specified were carried out with the electrode stationary to avoid perturbing the film.

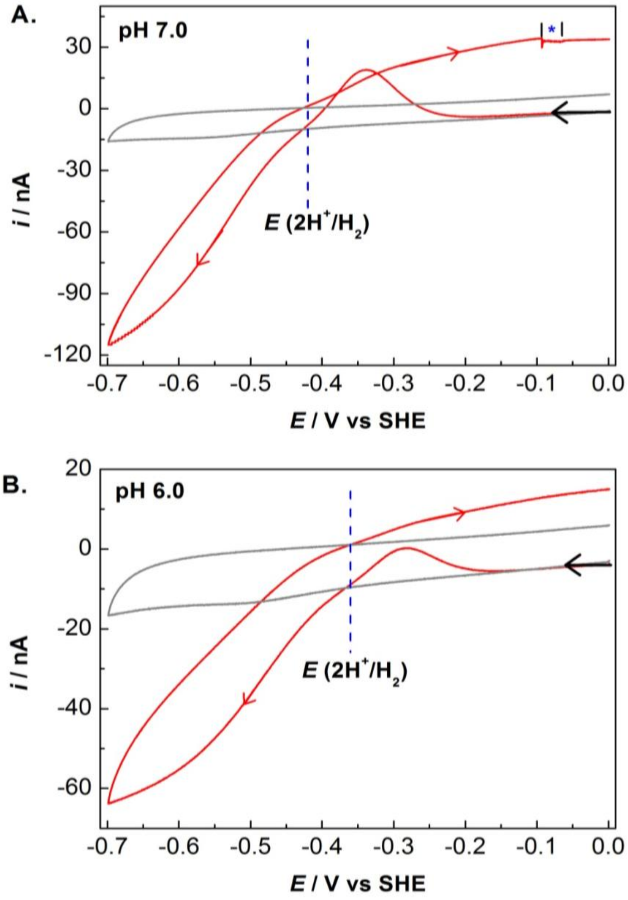

Figure 3-7. Panel A: Cyclic voltammgram of as-isolated HoxHY (red) under similar conditions as Figure 3-5 except at pH 7. A short rotation (2000 rpm) period is marked by a blue asterisk and confirms that the activity for H_2 oxidation is not limited by the substrate diffusion. Panel B: Cyclic voltammgram of as-isolated HoxHY (red) under similar conditions as Figure 3-5 except at pH 6.

Effects of scan rate and pH on E_{switch}

The value of E_{switch} at pH 8, 7 and 6 is clearly different under otherwise identical conditions (1 bar H_2, scan rate 1 mV/s) as shown above. This indicates the recovery process from the as-isolated HoxHY is dependent on pH. Another experiment (data not shown) at pH 8 with a scan rate of 10 mV/s was also performed but no reductive activation was observed, suggesting that the scan rate also affects the recovery. Therefore, a series of experiments under different pH and with different scan rates were carried out to investigate the pH and scan rate effect on E_{switch}. The value of E_{switch} is assumed to be a characteristic thermodynamic potential for the transition from an inactive state to an active state given that the scan rate is slow relative to the recovery rate.[55,75,79] Léger *et al.* recently reported that E_{switch} is a phenomenonological parameter for the rate of reactivation and is not related to the thermodynamics. They performed cyclic voltammetry experiments on *Aa* MBH I at different scan rates (ranging from 30 to 0.3 mV/s) to examine the scan rate dependence on the E_{switch} value, and found that E_{switch} is proportional to the log of the scan rate.[88] For as-isolated HoxHY, cyclic voltammgrams at three different scan rates (1, 0.3 and 0.1 mV/s) were carried out to examine the E_{switch} dependence on scan rates, as shown in Panel A of Figure 3-8. An as-isolated HoxHY adsorbed on a PGE electrode was freshly prepared under each scan rate. As described above, the reductive peak was not observed at high scan rate such as 10 mV/s. Therefore, 1 mV/s was chosen as the upper limit of the scan rate in order to observe the recovery in the cyclic voltammogram. On the other hand, due to the film loss, the voltammetry with a scan rate lower than 0.1 mV/s was not achievable. Therefore, as shown in Panel A, voltammograms at three scan rates indicated by different colours were recorded and clearly the E_{switch} value is dependent on the scan rate: the lower the scan rate is, the higher the E_{switch} obtained. The E_{switch} dependence on scan rates in HoxHY has the same trend as that in *Aa* MBH I, indicating the E_{switch} value is related to the competition between the scan rate of the voltammetry and the recovery rate. When the scan rate is bigger than that of recovery, a lag phase occurs and the E_{switch} value obtained is lower than the real value or even not observed. However, when the scan rate is slow relative to the recovery, the E_{switch} value is a meaningful potential required for the conversion from an inactive state to active. Therefore, E_{switch} is not a pure thermodynamic parameter but a combination of thermodynamic potential and kinetic reactivation rate of the enzyme.[147] It is still useful to compare the E_{switch} values of different hydrogenases provided that these are recorded at the same relatively slow scan rate and all the enzymes are in an inactive state.

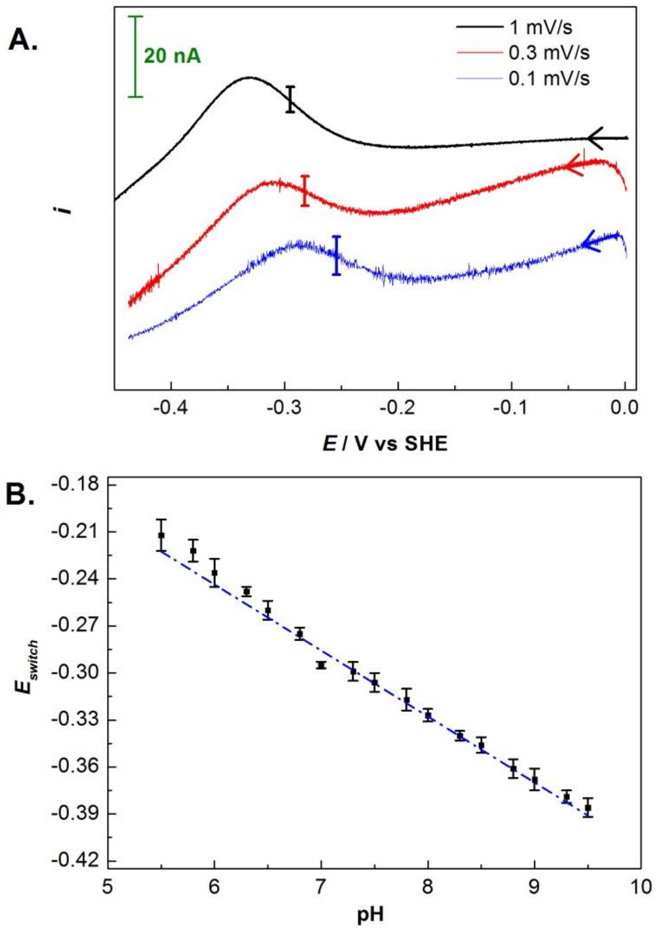

Figure 3-8. Panel A: The scan rate effect on the position of E_{switch}. The examination of the reactivation at three different scan rates was carried out at pH 7 and 30 ^{o}C under 1 bar H_2. The scan rates are marked by the legends and the E_{switch} value at each scan rate is indicated as a verticle bar. Panel B: A Pourbaix diagram was fit to examine the pH dependence of E_{switch} obtained with a scan rate of 1 mV/s for the as-isolated HoxHY. The error bar was determined by randomly picking 3 minimum *di/dE* as E_{switch} values at each pH and the uncertainty is half of the maximum range of the three values. Linear regression was applied to model the relationship of E_{switch} with pH (R^2 = 0.977). A linear dashed blue line was thus generated and has a gradient of 42 mV/pH unit.

A series of voltammgrams of as-isolated HoxHY at a scan rate of 1 mV/s and different pH indicate that E_{switch} depends linearly on pH as shown by the Pourbaix diagram in Figure 3-8(B), proving that this reductive reactivation for as-isolated HoxHY is a proton coupled process. An error-bar figure was plotted because there is inevitably an error when manually picking the E_{switch} at each pH. The error bar was determined by randomly picking 3 minimum *di/dE* as E_{switch} values at each pH and the uncertainty is half of the maximum range of the three values. Linear regression was applied to model the relationship of E_{switch} with pH (R^2 = 0.977). A linear line was thus generated and has a gradient of 42 mV/pH unit. An ideal $1H^+/1e^-$ coupled process should show a 59 mV/pH unit gradient based on the assumption that the rate of recovery does not change with pH.[64] However, this assumption is not necessarily true in this case and pH may actually affect on the rate of recovery. This may explain the deviation in slope to 42 mV/pH. Therefore, the recovery of as-isolated HoxHY could be a $1H^+/1e^-$ coupled process.

'Anaerobic inactivation ?'

Most NiFe hydrogenases undergo reversible anaerobic oxidative inactivation and reductive reactivation, i.e., the enzyme will switch off its activity for H_2 oxidation at high potential and as the potential is taken to more negative values it will switch back on again. This is readily observed in an electrochemistry experiment as well as in the enzyme assays. A cyclic voltammogram recorded for a pre-activated enzyme film is shown in Figure 3-9. On the forward scan, the current for H_2 oxidation does not decrease until 0.1 V. More importantly, on its return scan, the catalytic activity shows no evidence of a 'switch on'. The loss of activity on the forward scan could be attributed to film loss or the denaturing of the enzyme since the potential was at quite a high value, outside the physiological range. This is likely not to be reversible anaerobic oxidative inactivation. As the anaerobic inactivation for other NiFe hydrogenases has been shown to be dependent on the pH and the partial pressure of H_2, experiments (data not shown here) were also performed under different pH and H_2 concentration conditions. However, similar voltammetric shapes to that in Figure 3-9 were obtained by varying the pH and H_2 partial pressure. Thus, still no sign of reversible anaerobic inactivation was found for HoxHY. For other NiFe hydrogenases, it is now well established that this anaerobic oxidative inactivation is related to the formation of Ni-B state.[233] However, as discussed previously, *Re* SH does not show a standard Ni-B state in either IR or EPR spectra.[149] Therefore, it is not surprising that anaerobic inactivation in HoxHY is not seen electrochemically, as this is in agreement with the spectroscopic results.[147] This cyclic voltammetry experiment further confirms that the as-isolated state in HoxHY cannot be re-formed simply by applying a high potential.

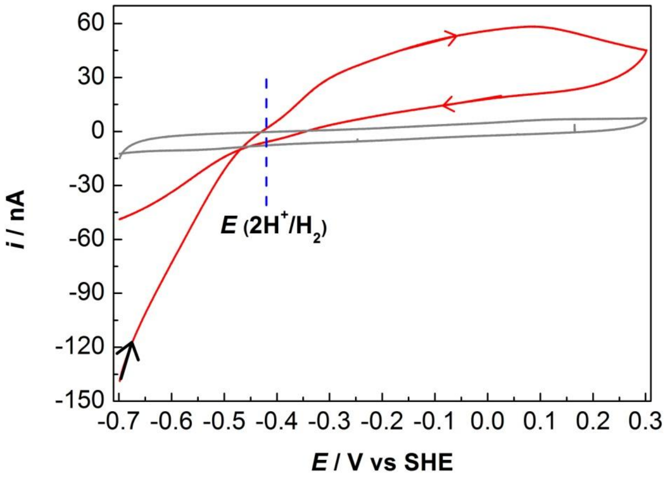

Figure 3-9. Cyclic voltammogram of pre-activated HoxHY (red) adsorbed on a stationary PGE electrode in pH 7 KPB recorded to investigate whether HoxHY undergoes the reversible "anaerobic inactivation". Other conditions: scan rate 1 mV/s; 1 bar H_2; 30 ^oC; the scan direction is shown by the arrowheads.

Product inhibition of H^+ reduction by HoxHY

In NiFe hydrogenases, the H^+ reduction is normally inhibited by its product H_2. However, HoxHY is capable of catalysing H^+ reduction even in the presence of 1 bar H_2, as shown in Figure 3-5, hence it would be interesting to investigate whether the product inhibition exists or not. Figure 3-10 shows an experiment performed on a film of as-isolated HoxHY adsorbed on PGE electrode. The electrode was first held at -584 mV to pre-activate the enzyme. Since gas exchange was required for the experiment, the electrode was rotated throughout in order to assist the gas equilibration with the headspace, but the experiment was performed at 10 ^oC to diminish the film loss. At t = 0 s, the current is negative, indicative of H^+ reduction at this potential under 1 bar of the insert gas N_2. The gradual decrease in the magnitude of the current is attributed to film loss. It has been shown previously that film loss fits well to a single exponential decay.[10,76] Thus, an exponential decay curve was calculated by interpolation of the line fitting initial and final data and is shown as a dotted black line in Figure 3-10 to indicate likely background film loss. A sharp decrease in the H^+ reduction current occurs immediately after N_2 is switched to H_2, indicating that H^+ reduction is inhibited by H_2. However, the H^+ reduction activity returns after changing back from H_2 to N_2. Therefore, H_2 is a rapid and reversible inhibitor for HoxHY in the region of H^+ reduction. In contrast to *Re* MBH which does not catalyse H^+ reduction under 1 bar H_2,[83] HoxHY is only slightly inhibited by H_2 for catalysing H^+ reduction as it still maintains *ca.* one third of its activity for H^+ reduction under H_2.

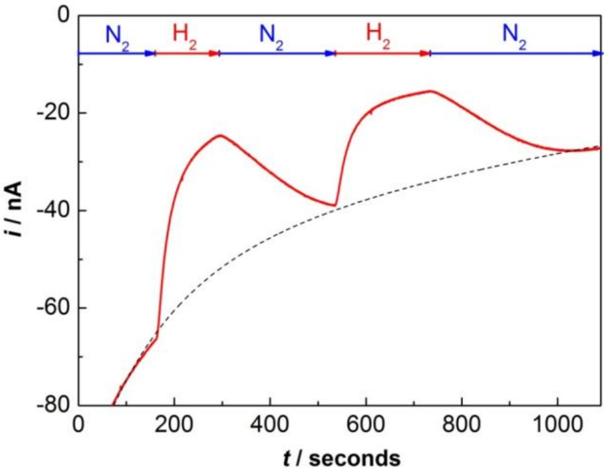

Figure 3-10. Current-time trace (red line) from an experiment designed to examine the effect of product inhibition on H^+ reduction. The gas was exchanged as shown in the arrows above. Conditions: the potential was held at -584 mV throughout the experiment; 10 °C; 2000 rpm; pH 7, 50 mM KPB; the overall flow rate of gas was 1000 mL/min. An exponential decay curve (dotted black line) was calculated by interpolation of the line fitting initial and final data to indicate likely background film loss.

Is H_2 required in the process of reactivation for as-isolated HoxHY?

The investigation of the as-isolated whole SH by solution assays showed that H_2 alone cannot restore the enzyme activity.[53] Several cyclic voltammetry experiments were carried out (data not shown here) on H_2-incubated HoxHY and the incubation time varied from seconds to hours with high or low H_2 concentrations. The scan starts at high potential and is swept towards low values at a slow scan rate in the presence of 1 bar H_2 to examine whether it is active for H_2 oxidtion or not. However, the voltammogram recorded for H_2-incubated HoxHY is the same shape as that of as-isolated HoxHY, i.e., the current at the commencement is near zero and there is a reductive activation peak on the forward scan, proving that the enzyme is not active for H_2 oxidation and requires a low potential activation before functioning. This finding seems to match the results from the enzyme assays. On the other hand, a cyclic voltammetry experiment under N_2 as shown in Figure 3-11 was performed to investigate whether low potential electrons provided by electrode alone can activate as-isolated HoxHY or not. A film of as-isolated HoxHY was formed on a PGE electrode and the potential is swept from high to low values then back. No H_2 oxidation current or recovery peak was observed as the experiment was carried out in the presence of N_2. Very clear H^+ reduction currents are observed in the low potential region, demonstrating that low potential electrons alone can activate the enzyme. However, it is possible that a few active molecules generate enough H_2 (product of H^+ reduction) to activate other molecules.

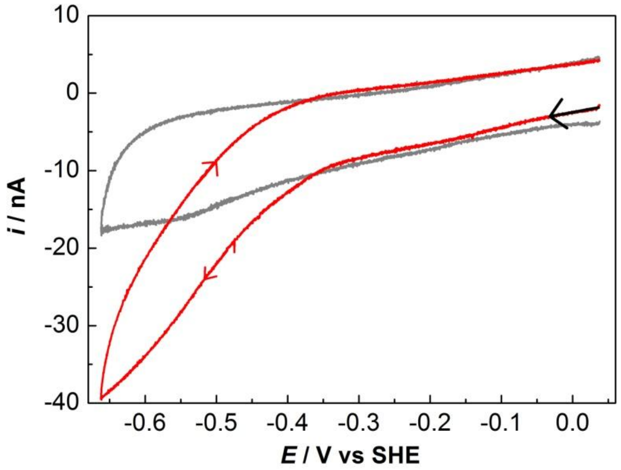

Figure 3-11. Cyclic voltammogram of as-isolated HoxHY (red) adsorbed on a PGE electrode. Conditions: 20 ^{o}C; 1 bar N_2; scan rate 1 mV/s; pH 7, 50 mM KPB. The scan direction is shown as the arrows.

CO as an inhibitor in the region of H^+ reduction for HoxHY

The SH has been classified as a CO-tolerant NiFe hydrogenase as CO does not inhibit the enzyme activity (H_2 : NAD^+).[212] With as-isolated HoxHY adsorbed on a PGE electrode, we have the opportunity to examine the potential dependence of inhibition more carefully. In Figure 3-12(A), the electrode is poised at -584 mV for activation of the enzyme and observation of H^+ reduction currents, and an inert gas N_2 is introduced at the commencement. The magnitude of the catalytic current for H^+ reduction decreases throughout the experiment due to the inevitable film loss. At around 70 s, CO is introduced into the electrochemical cell and the magnitude of H^+ reduction current drops sharply against the background of film loss. There is a lag in the change of catalytic current after introducing each new gas. The actual point of switching on the new gas is marked as a black square and there is about 40 s lag explained by the travel time of gas from the cylinder to the cell and from the headspace to the electrolyte. This makes it difficult to extract precise kinetics for the gas reactions. Then at 120 s, N_2 is switched back on. However, the recovery after CO inhibition is very slow relative to the recovery seen after H_2 inhibition. The activity for H^+ reduction is not fully recovered even after replacement of CO with N_2 for over 200 s. Therefore, in contrast to H_2 which is a rapid and reversible inhibitor for H^+ reduction, CO is only a reversible inhibitor. Further experiments were carried out to compare the CO and H_2 inhibition of H^+ reduction. In Figure 3-12(B), the experiment was started under a H_2 atmosphere. As H_2 is not a strong inhibitor for HoxHY, it is still capable of catalysing some H^+ reduction therefore a negative current is recorded. The current drops immediately after CO is introduced to replace H_2 at around 50 s, indicating that CO is inhibiting H^+ reduction more strongly than H_2.

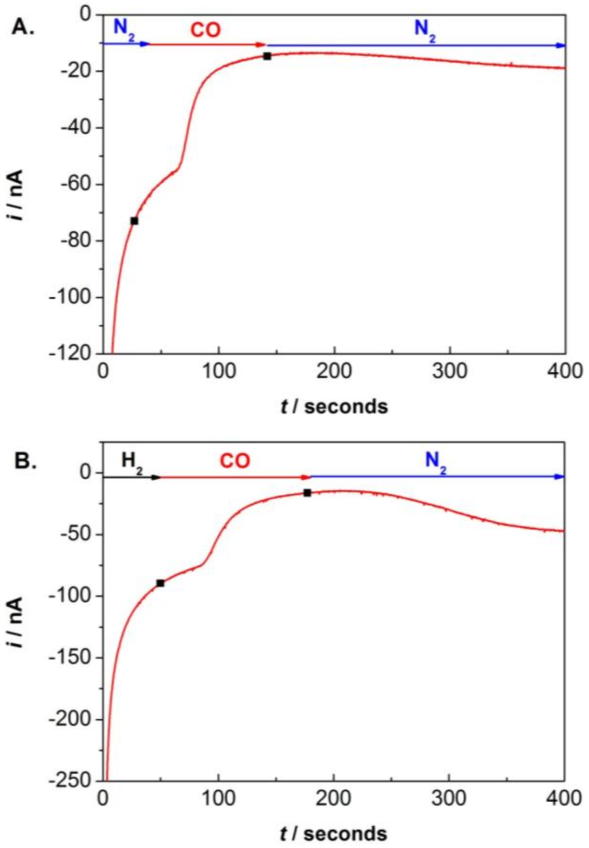

Figure 3-12. Panel A: Experiments designed to examine the inhibition of H^+ reduction by CO. Panel B: The comparison with H_2 on the extent of inhibition. The gas flushing through the headspace of the cell is indicated by the arrows. The electrode is poised at -584 mV. Other conditions: 10 ℃, pH 7.0, electrode rotation rate: 2100 rpm, the overall flow rate maintains 500 mL/min throughout the experiment.

Similar experiments were performed to investigate the CO effect on H_2 oxidation as shown in Figure 3-13. First, HoxHY was pre-activated by scanning the potential from high to low values and back to +216 mV which was held throughout the experiment for observing H_2 oxidation. The headspace was flushed with 10% N_2 : 90% H_2 at the beginning and then 10% CO was introduced to replace the N_2 component of the gas mix before returning to 10% N_2 : 90% H_2. The concentration of H_2 was kept constant throughout the experiment to exclude the decrease in the H_2 oxidation activity from the variable level of H_2. The introduction of CO at around 50 s does not affect H_2 oxidation as there is no sudden drop in the magnitude of the catalytic current apart from the decrease coming from the background film loss, suggesting that CO does not inhibit H_2 oxidation by HoxHY.

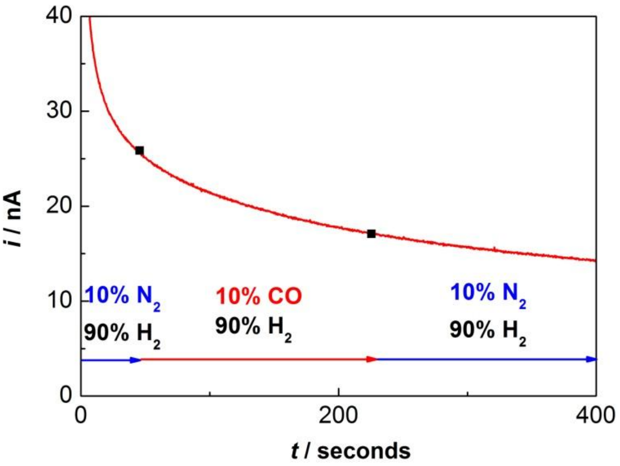

Figure 3-13. Experiment designed to examine whether CO inhibits H_2 oxidation by HoxHY or not. The enzyme adsorbed on a PGE electrode was pre-activated by scanning the potential from high to low values and back to +216 mV which was held throughout the experiment. The gas flushing through the headspace of the cell is indicated by the arrows. Other conditions: 10 ℃, pH 7.0, electrode rotation rate: 2100 rpm, the overall gas flow rate was maintained at 500 mL/min throughout the experiment.

3.2.2.2 O_2 reaction: inactivation and reductive reactivation under anaerobic conditions

The SH is classified as an O_2-tolerant NiFe hydrogenase based on the fact that it retains H_2: NAD^+ activity aerobically in biochemical solution assays.[11] However, the possibility to probe the isolated hydrogenase moiety HoxHY (without interference from the diaphorase moiety) by electrochemistry may be helpful for understanding the O_2 tolerance of the SH as an intact enzyme. The effect of O_2 on H_2 oxidation by HoxHY and its reductive recovery after removal of O_2 are first investigated.

The plan of this O_2 experiment is : (1) Pre-activated HoxHY adsorbed on a PGE electrode is first held at high potential in the H_2 oxidation region (+216 mV is chosen and high enough that O_2 reduction does not occur at the PGE electrode); (2) O_2 will be introduced to examine whether there is a drop in the H_2 oxidation current; (3) if inactivation caused by O_2 occurs, the potential will be stepped to a low potential (-384 mV) to reactivate the enzyme; (4) after the reductive poise, the potential will be stepped back to +216 mV to examine the extent of reductive recovery.

The red line in Figure 3-14(A) shows the current trace following a series of potential steps on a film of pre-activated HoxHY at 10 ^{o}C, pH 7 and 2000 rpm. From 0 to 90 s, the enzyme-modified electrode was held at +216 mV under 98% H_2 : 2% N_2. Dihydrogen was oxidised at this potential, but the current dropped fairly rapidly due to the film loss. At 90 s, an aliquot of O_2-saturated buffer was injected into the cell to quickly reach 2% O_2 in the electrolyte, and at the same time, the gas flowing through the headspace was switched to 98% H_2 : 2% O_2. The current dropped sharply after introducing O_2, thus taking account of the film loss, it is clear that O_2 inactivates the enzyme. At 250 s, the head gas was switched back to 98% H_2 : 2% N_2 and kept at this composition for the remainder of the experiment. The period in which 2% O_2 was present in the cell was thus from 90 to 250 s. The inactivation rate for this period can be calculated from the slope of the semi logarithmic plot of ln (current) vs. time shown in Figure 3-14(B). The red line shown in Panel B is the semi-logarithmic plot for the O_2 inactivation period indicated by a horizontal black bar in Panel A. The first 35 s after O_2 introduction was not considered as the concentration of O_2 was not stable during this period. A linear line with a gradient of 0.01 $s^{-1}$was fit to the data, shown as a black dashed line in Figure 3-14(B). Therefore the decay of the current after O_2 follows a single exponential function and the O_2 inactivation process is a first order reaction with a rate constant 0.01 s^{-1}.

At 580 s, after most the O_2 was removed, the potential was stepped to -384 mV to see whether O_2-inactivated HoxHY can be reductively reactivated in a series of short low-potential steps. First, the electrode was stepped to -384 mV for just 10 s. Then the potential was stepped back to +216 mV to examine whether the H_2 oxidation current had increased after the reductive step, i.e., undergone reductive reactivation. It is obvious that the current has increased compared to that before the short reductive potential step. At 890 s and 1250 s, the reductive potential steps were next lengthened for 60 s and 360 s, respectively, to examine the extent of recovery, but it is clear that there is no further recovery after the first 10 s reductive potential step. Thus reductive reactivation is possible and is relatively fast. A control experiment (green line, 10 ^{o}C) shown in in Figure 3-14(A) was performed under analogous conditions to confirm that the drop in current following injection of N_2-saturated buffer did not arise from decreasing the H_2 concentration and to clarify the capacitive contributions from the potential steps. In the data series shown by the green line, at 90 s an aliquot of N_2-saturated buffer (same volume as O_2-saturated buffer used above) was injected into the electrolyte. Apart from a slight perturbation the current was unaffected. Therefore, the decrease in the current in the red line is indeed coming from the O_2 inactivation rather than a temporary decrease in H_2 concentration. A dashed black line as shown in panel A is fitted as a single exponential curve to examine the effect of the film loss. The experiments were performed at two different temperatures (red line 10 ^{o}C, blue line 30 ^{o}C) as shown in Panel A to see the temperature effect on the rate of the reaction with O_2 for HoxHY. As the O_2 reaction data available for other hydrogenases were obtained at higher temperature than 10 ^{o}C, this 30 ^{o}C experiment would provide comparable data for HoxHY. The blue line in Panel A shows the current trace for the reaction with O_2 on a pre-activated HoxHY film at 30 ^{o}C. The film loss at this temperature is much more severe compared to that at 10 ^{o}C, therefore, the more complex experiments presented later were performed at 10 ^{o}C to help the film stability. The blue line shown in Figure 3-14(B) is the semi-logarithmic plot for the reaction of HoxHY with O_2 at 30 ^{o}C. Although a linear fit to the data is now poor due to the greater film loss, it is evident that the inactivation rate at 30 ^{o}C is approximately twice that at 10 ^{o}C.

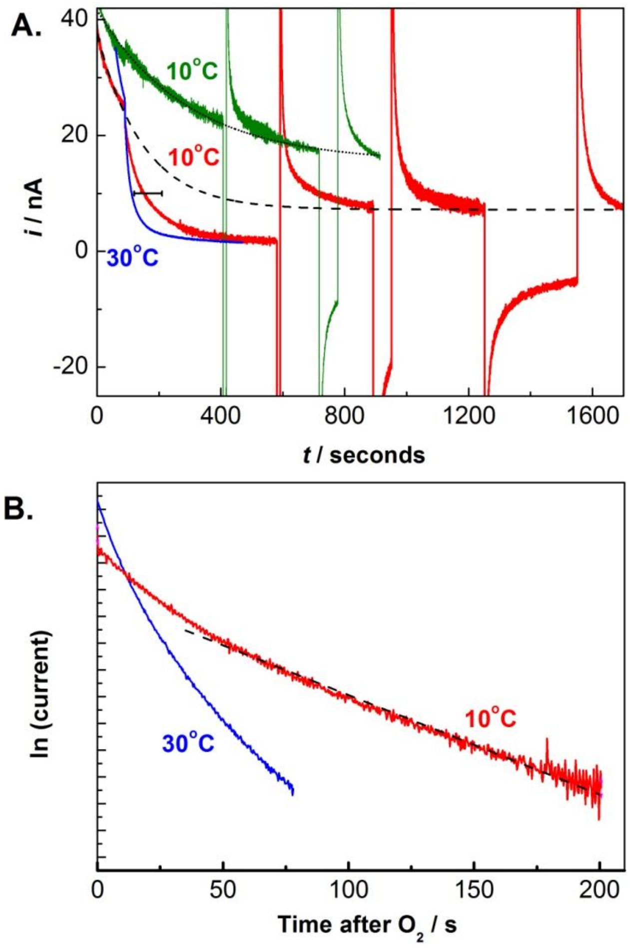

Figure 3-14. The reaction of HoxHY with O_2, and subsequent reductive reactivation under anaerobic conditions. Panel A: red line: pre-activated HoxHY was held at 10 °C and +216 mV under 98% H_2 : 2% N_2 and at 90 s, 80 µL of O_2-saturated buffer was injected into 4 mL electrolyte to quickly establish an O_2 concentration in the electrolyte equilibrated with 2% O_2 in the headspace. At the same time the gas flowing through the headspace was switched to 98% H_2 : 2% O_2. At 250 s, the headspace gas was switched back to 98% H_2 : 2% N_2 and kept under this anaerobic condition for the remainder of the experiment. The potential was stepped to -384 mV at 580 s for 10 s; at 890 s for 60 s and at 1250 s for 300 s and then back to +216 mV to monitor the extent of the reductive reactivation induced by holding at low potential for different time periods. Black dashed line: an exponential decay curve indicating the contribution from film loss was extrapolated based on the catalytic activity of HoxHY at +216 mV. Blue line: To examine the effect of temperature on the kinetics of the O_2 reaction, a similar O_2 reaction experiment was performed at 30 °C. Green line: A control experiment was carried out on pre-activated HoxHY at 10 °C with N_2 introduced in place of O_2. The headspace gas was kept at 98% H_2 : 2% N_2 throughout and at 90 s, 80 µL of N_2-saturated buffer was injected into the cell instead of O_2 and the potential is stepped down to -384 mV at 410 s for 10 s and at 720 s for 60 s. Black dotted line: an exponential decay curve indicating film loss is fitted based on the catalytic activity of HoxHY at +216 mV. Panel B: semi-logarithmic plots for the decay in current from HoxHY following introduction of O_2 both at 10 °C and 30 °C (over the period indicated by a bar in Panel A). A linear fit is indicated for 10 °C but not for 30 °C due to the greater film loss. Other experiment conditions: the electrode was rotated at 2000 rpm throughout and the flow rate of the head gas was kept at 1000 mL/min.

Can HoxHY oxidise H_2 in the presence of O_2 ?

By protein film electrochemistry, some O_2-tolerant NiFe hydrogenases have been proved to be capable of catalysing H_2 oxidation in the presence of O_2, such as *Re* MBH, *E. coli* Hyd-1 and *Aa* MBH I.[82,85,87] A natural and important question is raised for HoxHY: Can HoxHY oxidise H_2 in the presence of O_2? One common feature for *Re* MBH (+115 mV, pH 6, 1 mV/s),[75] *E. coli* Hyd-1 (+150 mV, pH 6, 1 mV/s)[85] and *Aa* MBH 1(+75 mV, pH 7, 0.3 mV/s)[88] is that they all have a high switch potential E_{switch} relative to the so called 'O_2-sensitive' NiFe hydrogenases (*Av* MBH -110 mV, *Dg* NiFe hydrogenase -115 mV at pH 6, 1 mV/s)[75] under analogous conditions including pH, H_2 pressure, temperature and scan rate. It is also known that O_2 is reduced at potentials below +200 mV on a PGE electrode therefore complicating investigation. For *Re* MBH, *E. coli* Hyd-1 and *Aa* MBH I, the H_2 oxidation activity can be detected in the presence of O_2 at high potentials as the O_2-induced inactive species can be reactivated at the applied potential due to the high E_{switch}. In some cases, as the enzyme is highly active, the H_2 oxidation activity is observed even though O_2 is reduced at the same time.[85] For HoxHY, the switch potential for the as-isolated state is -300 mV obtained at pH 7 and 1 mV/s, as shown in Figure 3-7. The potential window to examine whether HoxHY can oxidise H_2 in the presence of O_2 or not is approximately between -420 to -200 mV within which the O_2-inactivated species can be reactivated. However, the positive H_2 oxidation current will be greatly masked by the huge negative current arising from O_2 reduction. Apart from this, HoxHY is of low activity (within 100 nA) compared to those O_2-tolerant hydrogenases mentioned above (within 10 μA). Therefore, it is difficult to directly observe H_2 oxidation in the presence of O_2. Instead, a chronoamperometric experiment was designed to examine whether O_2-inactivated HoxHY can be reactivated in the presence of O_2, as shown in Figure 3-15. If the enzyme can be reactivated in the presence of O_2 within the potential window (-420 to -200 mV), then it can be used as indirect evidence to prove that the SH can work in O_2.

The red line in Figure 3-15 shows the current trace resulting from a series of potential steps in the presence of O_2 on a pre-activated HoxHY film. The electrode was first poised at +216 mV under 98% H_2 : 2% N_2 from 0 to 90 s. At 90 s, 2% O_2 was introduced (the H_2 concentration was kept constant at 98% throughout the experiment) and the current was observed to drop sharply due to the inactivation of the enzyme by O_2. At 580 s, the potential was stepped to -384 mV for 10 s with 2% O_2 still present. At 590 s, the potential was stepped back to +216 mV to examine the recovery. The current due to H_2 oxidation appeared to increase compared to that before the reductive potential step. However, the current decayed again since there was still 2% O_2 in the cell. A longer reductive potential step in the presence of O_2 at -384 mV was performed at around 900 s, however no further recovery was found compared to the previous recovery. At 1250 s, the fraction in the head gas 2% O_2 was switched to 2% N_2, and the potential was stepped to -384 mV for 360 s. By 1550 s, it was expected that O_2 had been removed almost completely. When the potential was stepped up to +216 mV, the current for H_2 oxidation came back and did not decay as sharply as previously since there was very low O_2 in the electrolyte. Since the catalytic current for HoxHY was very small, the capacitance decay should be taken account of. In order to examine the capacitance contribution from the enzyme-modified electrode more precisely, a 'dead' HoxHY film adsorbed on a PGE electrode was prepared by holding the potential at a very high potential for a couple of seconds to completely destroy the enzyme activity as the capacitance of the HoxHY adsorbed electrode should be slightly different from that of an unmodified electrode. The control experiment on the 'dead' HoxHY film is shown as a black line in Figure 3-15, carried out under analogous conditions. The blue line shows the black line subtracted from the red line, and supports the conclusion that HoxHY can re-activate at low potential even in the presence of O_2.The black dashed line shows a fit for the film loss as a single exponential curve from data points recorded under anaerobic conditions, assuming that the activity for H_2 oxidation after inactivation by O_2 is fully recovered in the final seconds of the experiment.

Although the H_2 oxidation activity for HoxHY in the presence of O_2 cannot be observed for the reasons described above, the O_2-induced inactive HoxHY is demonstrated to be reductively recovered even in the presence of O_2 at -384 mV, i.e., HoxHY is capable of functioning aerobically at this low potential. This also gives us a clue for further understanding O_2 tolerance of *Re* SH *in vivo*. The hydrogenase moiety HoxHY, the H_2 cycling engine of the whole *Re* SH, is coupled with HoxFU which catalyses the NAD^+/NADH cycling. Thus, the physiological potential of HoxHY is controlled by the NAD^+/NADH pool which probably stays within ±150 mV of the E ($2H^+/H_2$) (-393 mV, corrected for this experiment condition: pH 7, 10 ^oC). Therefore, the results are compatible with HoxHY retaining its activity within its physiological potential region in the presence of O_2. Furthermore, the inactivation by O_2 at high potential (+214 mV) is unlikely to happen in the bacterial cell as the NAD^+/NADH pool potential cannot provide the hydrogenase moiety such oxidising conditions.

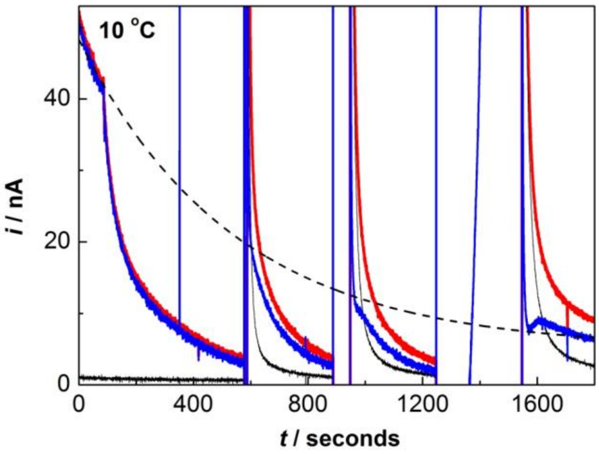

Figure 3-15. The reaction of HoxHY with O_2 and reductive reactivation under aerobic conditions. Red line: pre-activated HoxHY was held at 10 ^oC and +216 mV under 98% H_2 : 2% N_2, and at 90 s, 80 μL of O_2-saturated buffer is injected into 4 mL electrolyte to quickly establish an O_2 concentration in the electrolyte equilibrated with 2% O_2 in the headspace at the same time the gas flowing of the headspace was switched for 98% H_2 : 2% O_2 and kept at this composition for the remainder of the experiment. The potential is stepped to -384 mV at 580 s for 10 s; at 890 s for 60 s and at 1250 s for 300 s to monitor the extent of the reductive reactivation under aerobic conditions induced by holding at low potential for different time periods. Black dashed line: an exponential decay curve indicating the contribution from film loss is extrapolated based on the catalytic activity of HoxHY at +216 mV under anaerobic conditions. Black line: A control experiment was carried out on 'dead' HoxHY at 10 ^oC under exactly the same conditions as the red line to clarify the capacitive contribution. Blue line: red line subtracted by black line. Other experiment conditions: the electrode was rotated at 2000 rpm throughout and the flow rate of the heads gas was kept at 1000 mL/min.

Two reductive recovery potentials of HoxHY

Chronoamperometry was used above to investigate the reaction of pre-activated HoxHY with O_2 and the corresponding reductive reactivation because it is especially useful for studying reaction kinetics. On the other hand, cyclic voltammetry can also be used to study the reductive reactivation process after the reaction of pre-activated HoxHY with O_2, providing the information on the switch potential, in comparison to the reductive activation of as-isolated HoxHY. The red line in Figure 3-16 records the reactivation process of as-isolated HoxHY at pH 7. The O_2-inactivated HoxHY after pre-activation is shown as the blue line in Figure 3-16. In both cases, the scan starts from around 0 V where the current is almost zero, indicating that the enzyme is inactive for H_2 oxidation. As the potential is swept to more negative values as shown in the blue line, the enzyme begins to catalyse H_2 oxidation below *ca.* -100 mV and the E_{switch} for this process is around -170 mV. Notably, this reductive reactivation is distinct from that of as-isolated HoxHY. The difference in E_{switch} between the two reactivation processes is around 150 mV, i.e., the as-isolated state is clearly chemically different from the state generated when pre-activated HoxHY is exposed to O_2. It is very rare to see two distinct reductive activation potentials for NiFe hydrogenases: a notable exception is the NiFeSe hydrogenase from *Desulfomicrobium baculatum* (*Dm. b* NiFeSe hydrogenase).[89] In *Dm. b* NiFeSe hydrogenase, two reductive activation peaks are observed and introduction of O_2 under Ar-rich conditions favours the lower potential recovery peak. The lower reductive reactivation peak for the *Dm. b* NiFeSe hydrogenase is also very close to E ($2H^+/H_2$), similar to the as-isolated HoxHY.[89] Another example of a NiFe hydrogenase having more than one switch potentials is *D. vulgaris* MF NiFe hydrogenase. Apart from the switch potential for the anaerobically inactivated state, a higher switch potential is also observed for a sulphide-induced inactive state observed by cyclic voltammetry.[79] The implications of the two switch potentials for HoxHY, along with the similar observations in other NiFe hydrogenases and the infrared spectroscopic investigation of HoxHY, will be discussed in **Section 3.3.5**.

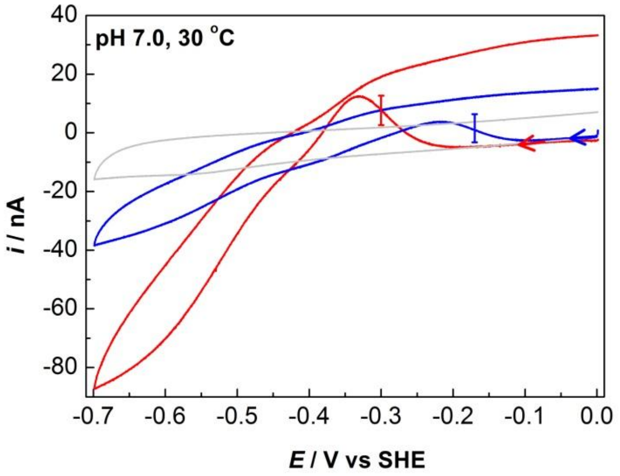

Figure 3-16. Cyclic voltammogram (blue) recorded at 1 mV/s, 30 ℃ and pH 7.0 at a stationary electrode after exposure of pre-activated HoxHY to O_2 (2% at 10 ℃) and subsequent removal of O_2 from the cell by gas exchange and electrode rotation. The red line reproduces the trace from Figure 3-7(A) for comparison. Switch potentials (recorded at 1 mV/s) determined from derivative plots are marked by vertical bars. A voltammogram (grey) at an unmodified electrode was recorded under analogous conditions.

3.2.3 Electrochemical investigation of the whole enzyme in the form of HoxHYFU

As-isolated HoxHYFU on an Electrode

The tetrameric form of *Re* SH, HoxHYFU, was purified in air as described in Chapter 2. During a day of experiments, samples of as-isolated HoxHYFU were left on ice outside the glove box under aerobic conditions to maintain the as-isolated state. Aliquots of protein (0.7 μL) were taken into the glove box under a N_2 purge immediately prior to formation of a film on the electrode. In Figure 3-17, the scan (red) starts from +0.15 V, and the potential is swept in the negative direction. No activity is observed for H_2 oxidation at the commencement, exactly the same as for the as-isolated HoxHY. For comparison, a voltammogram at an unmodified electrode was recorded under analogous conditions, shown as a grey line. However, it is difficult to obtain a suitable ‘zero current’ for HoxHY since the bare electrode is expected to show slightly different capacitive background. As the potential is decreased, HoxHYFU begins to oxidise H_2 beyond -0.25 V, indicating that the enzyme is able to activate at this potential. Furthermore, the position of the recovery potential is exactly the same as that of HoxHY under analogous conditions. However, a negative current was observed at potentials above the *E* ($2H^+/H_2$), shown as the green box in Figure 3-17. This, together with the small negative current at the commencement of the scan possibly arises from trace O_2 trapped in the enzyme. In order to maintain the as-isolated state of the enzyme and find a better way to get rid of O_2 inside the enzyme, a different way of preparing the enzyme film outside the N_2-filled glove box and immediately sending the electrode back into the glove box under a N_2 purge was tried, but it was found that the epoxy part of PGE electrode adsorbs O_2 and the electrochemistry experiment was severely affected by the retained O_2. Therefore, the film preparation method described at the beginning of this section was used. The HoxHYFU appears to reduce H^+ immediately after the potential goes below the *E* ($2H^+/H_2$). On its return, HoxHYFU switches its catalytic function from H^+ reduction to H_2 oxidation just above the thermodynamic potential *E* ($2H^+/H_2$), i.e., operating at minimum overpotential. The whole experiment was also performed on a stationary PGE electrode in order to diminish the film loss except for a short period marked by a blue asterisk. The H_2 oxidation current does not increase after adding the rotation, proving that the H_2 oxidation catalysed by HoxHYFU was not limited by diffusion control as the activity was low and the H_2 concentration around the electrode was enough. In conclusion, the catalytic redox behaviour in as-isolated HoxHYFU is almost the same as as-isolated HoxHY, indicating that the differences between HoxHY and HoxHYFU in terms of adsorption on the graphite electrode and orientation do not affect the electron transfer between the enzyme and the electrode, despite the fact that the tetrameric form HoxHYFU is more complex than the hydrogenase moiety HoxHY. However, it is possible that the electrode causes HoxHY and HoxFU to dissociate. Idris *et al.* in our group also performed cyclic voltammetry experiments on HoxHYFU adsorbed on a PGE electrode to examine whether the enzyme is capable of catalysing the NAD^+/NADH cycling. It turns out that adsorbed HoxHYFU on a PGE electrode can also reduce NAD^+ and oxidise NADH at minimum overpotential in the presence of NAD^+ and NADH.

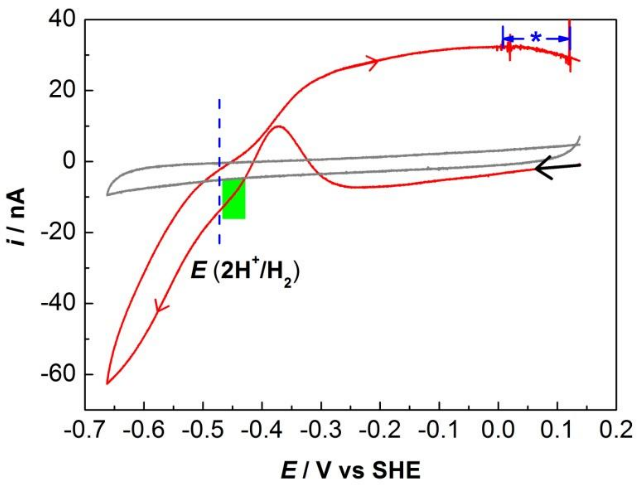

Figure 3-17. Cyclic voltammogram of as-isolated inactive HoxHYFU on a PGE electrode in pH 8 H_2-saturated 50 mM KPB at 25 ℃ with a scan rate of 1 mV/s. The scan (red) was initiated from +0.15 V after 10 s equilibration at this potential. The position of *E* ($2H^+/H_2$) corrected for experimental conditions is shown as a blue dashed vertical line and the voltammogram at a bare PGE electrode under analogous conditions is shown as a grey line. The electrode was rotated for a brief period, indicated by a blue asterisk to ensure that the H_2 oxidation was not limited by diffusion control and the remaining part of the experiment was carried out under stationary conditions. The direction of the scan is indicated by arrowheads.

Difference made by HoxFU moiety: Reaction of HoxHYFU with H_2

The as-isolated HoxHYFU was transfered into the glove box and stored at ice temperature under trace H_2 overnight. A cyclic voltammogram (data not shown) starting from high potential was perfomed to examine the effect of H_2 incubation on catalysis of H_2 oxidation. In the voltammogram, at the commencement of the scan at about +0.15 V there was an obvious positive current, indicating that the H_2-incubated enzyme is active for the oxidation of H_2 thus it is apparent that H_2 alone can activate the as-isolated HoxHYFU. This electrochemical finding is in contrast with the result from the solution assay. In the enzyme assays, incubation (30 minutes at 30 ^{o}C) or storage (several days at ice temperature) of the whole SH with H_2 in the absence of NAD(P)H or reducing agents did not activate the enzyme, suggesting that H_2 alone cannot restore the enzyme activity.[53] Furthermore, the characteristic reactivation peak for the as-isolated state as shown in Figure 3-17 disappeared which confirms that the enzyme is already activated by H_2. Further experiments show that incubation with trace H_2 for several hours is crucial for the activation of HoxHYFU. An experiment in which a film of as-isolated HoxHYFU adsorbed on a PGE electrode was immersed in H_2-saturated buffer for a couple of minutes was performed to see whether incubation with a higher level of H_2 for a short time has the same activation effect or not. However, a voltammogram (data not shown) on this film starting from about +0.15 V looked exactly the same as that of as-isolated HoxHYFU in Figure 3-17, indicating that long term incubation with H_2 is essential for the activation process.

In contrast to HoxHY as described in **Section 3.2.2**, incubation of HoxHYFU with H_2 can restore the enzyme activity for H_2 oxidation, as demonstrated by protein film electrochemistry, suggesting that the presence of the diaphorase moiety HoxFU allows HoxHYFU to be activated by H_2. On the other hand, the different behaviour of the H_2-incubated HoxHYFU from HoxHY demonstrate the tetrameric form of the SH should be intact on the PGE electrode, rather than dissociated into two independent moieties.

Is H_2 required for the reactivation of as-isolated HoxHYFU

As discussed above, *Re* SH in the form of HoxHY and HoxHYFU is inactive in the as-isolated state. In solution asssays, reducing agents, such as NADH and H_2, are required to restore the enzyme activity. In protein film electrochemistry, it is found that H_2 alone can activate HoxHYFU (not HoxHY) after a long incubation. The electrode functions as an artificial redox partner of the enzyme. Therefore, a question is raised whether the reductive poise by the electrode alone can activate the enzyme. In order to avoid the effect of H_2 as a reducing agent, 1 bar N_2 was used to saturate the electrolyte throughout the experiment. In Figure 3-18, the scan (red) starts from about +0.15 V as indicated by the black arrow. At the commencement, a ‘zero current’ was observed compared to the scan on an unmodified electrode (grey), indicating that no reaction happens. As H_2 was not present in the electrolyte, the typical reactivation peak did not occur as the potential was swept to low values. However, after the potential was swept beyond -0.3 V, a negative current was recorded, indicating that HoxHYFU is active for H^+ reduction. This demonstrates that the low potential electrons alone provided by the electrode can also activate the as-isolated HoxHYFU, consistent with the findings for HoxHY. However, there is a possibility that a few active HoxHYFU can supply H_2 generated by H^+ reduction to activate the remaining enzyme samples.

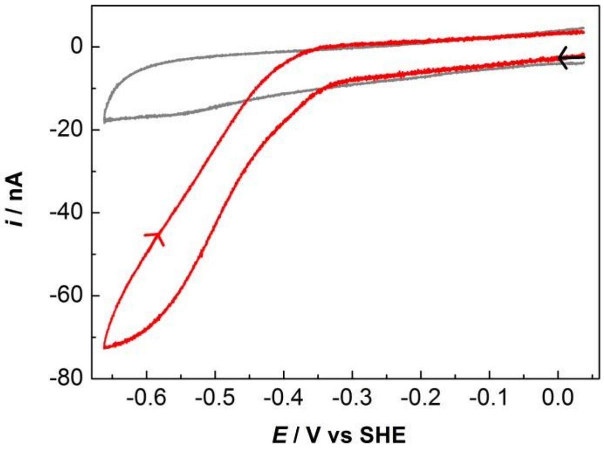

Figure 3-18. Cyclic voltammogram of as-isolated HoxHYFU (red) adsorbed on a PGE electrode. Conditions: 30 ^{o}C; 1 bar N_2; 1 mV/s; pH 7 KPB. The scan direction is shown by the arrowheads. A voltammogram at a bare electrode (grey) is also shown, recorded under the analogous condition.

Anaerobic oxidative inactivation for HoxHYFU?

Although the hydrogenase dimer HoxHY does not show the reversible anaerobic oxidative inactivation, an experiment was still performed on HoxHYFU to examine whether this was also the case for the tetrameric form of the enzyme. The voltammogram in Figure 3-19 shows that the enzyme does not begin to switch off its catalytic activity for H_2 oxidation until above +0.1 V and on the reverse scan the activity does not switch back on. The loss of activity for H_2 oxidation at high potentials could be simply due to dissociation of the enzyme from the electrode or damage of the film by the non-physiologically relevant high potential. Therefore, the reversible anaerobic oxidative inactivation is not observed for HoxHYFU, similar to HoxHY.

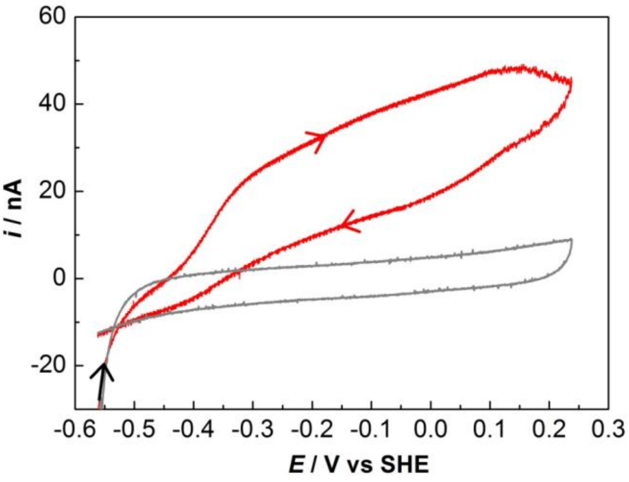

Figure 3-19. Cyclic voltammogram of HoxHYFU on a PGE electrode in pH 8 H_2-saturated KPB at 30 ℃ with a scan rate of 1 mV/s. The scan (red) started from -0.55 V after 10 s equilibration at this potential. The voltammogram at a bare PGE electrode under analogous conditions is shown as a grey line.

Reaction of H_2-incubated HoxHYFU with O_2

The previous experiments show that after long incubation with H_2 inside the glovebox, HoxHYFU is active for H_2 oxidation. This raises the question as to whether the as-isolated state can be regenerated. Therefore, an experiment was performed in which the H_2-incubated HoxHYFU was exposed to O_2 again. The activated HoxHYFU adsorbed on a PGE electrode was immersed into an O_2-saturated buffer before measurement. Then, a cyclic voltammogram was performed to examine the redox state of the enzyme. As shown in Figure 3-20, at the commencement of the scan the enzyme is inactive for H_2 oxidation as the current is almost zero, indicating that O_2 inactivates the H_2-incubated HoxHYFU. However, as the potential is swept more negative, two distinct reactivation peaks (at +50 mV and -200 mV) appear. By comparison, neither of them is identical to the reactivation peak of the as-isolated HoxHYFU, proving that the as-isolated state cannot be reformed. It is possible that a mixture of two different inactive states are generated after exposure to O_2 as there are two distinctive reactivation peaks. Furthermore, the reactivation peak at lower potential may correspond to the reactivation of the O_2-inactivated HoxHY in Figure 3-16. The reason for the three switch potentials in HoxHYFU is still unclear. It seems that the as-isolated HoxHYFU is the most oxidised state and the other two inactive states after exposure to O_2 are partially oxidised states. The implication of the switch potentials owned by HoxHYFU, along with the two E_{switch} in HoxHY will be discussed in more detail in **Section 3.3.5**. As the potential is swept beyond the E ($2H^+/H_2$) in the negative direction, the enzyme starts to catalyse H^+ reduction. However, a negative current occurs even before the E ($2H^+/H_2$) shown by the green box in Figure 3-20, and this also occurs when examining the as-isolated state of HoxHYFU in Figure 3-17. The unusual negative current above the E ($2H^+/H_2$) is possibly arising from the reduction of O_2 trapped inside HoxHYFU. On the reverse scan, the current trace due to H_2 oxidation crosses over the reactivation peak at lower potential, suggesting that the enzyme activity for H_2 oxidation decreases quickly.

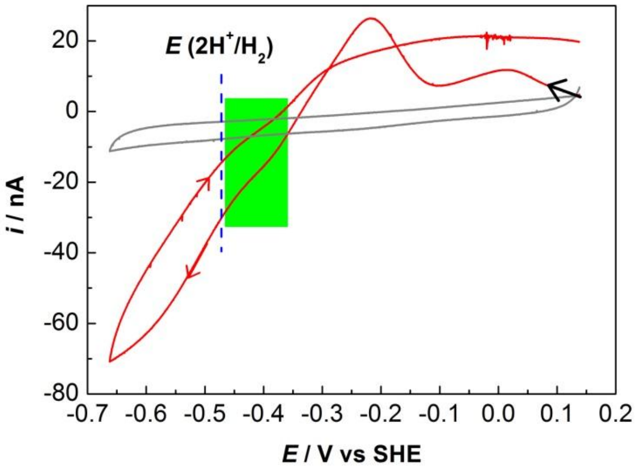

Figure 3-20. Cyclic voltammogram of O_2-reoxidised inactive HoxHYFU on a PGE electrode in pH 8 H_2-saturated KPB at 30 ℃ with a scan rate of 1 mV/s. The scan (red) started from +0.15 V after 10 s equilibration at this potential. The voltammogram at a bare PGE electrode under analogous conditions is shown as a grey line.

Instability of HoxHYFU caused by loss of FMN?

The tetrameric SH, HoxHYFU, houses two non-covalently bound flavin monoucleotide (FMN-a and FMN-b) cofactors. Among them, FMN-a in HoxHY is known to be selectively released upon long incubation with NADH whereas the other FMN (FMN-b) is relatively tightly bound.[210,226] In the purified hydrogenase moiety HoxHY, substoichiometric amounts of FMN-a were identified: 0.05 equiv. FMN per HoxHY unit.[147] The loss of FMN-a is also used to explain the low enzyme activity and it is found that adding exogenous FMN can enhance the activity

(H_2 : NAD^+).[147,226] The amount of FMN-a in HoxHYFU was found to be slightly higher than that in HoxHY.[234] The NAD^+/NADH cycling catalysed by the diaphorase moiety HoxFU is an interconversion involved with two electrons (e^-) and one proton (H^+). The FMN-b in HoxFU is believed to be the hydride (H^-) carrier. However, in the hydrogenase moiety, the binding and cleavage of H_2 is a process of one-electron at a time through the iron-sulphur cluster. Therefore, FMN-a in the hydrogenase moiety is proposed to act as a one-to-two electron converter in the whole SH.[226] As discussed earlier, the SH is of very low activity, and very unstable not only on electrode but also in solution. A voltammogram in Figure 3-21 shows that for some HoxHYFU films a pair of peaks marked by blue asterisks appear, characteristic of adsorbed FMN signals, indicating that FMN easily falls out of the enzyme. This is one factor contributing to instability of the soluble hydrogenase. Furthermore, a voltammogram in Figure 3-22 shows that incubation of HoxHYFU with FMN did not restore the activity for H_2 oxidation. Only a catalytic amount of FMN (about 10 pmol) was used to incubate with the enzyme as such a low concentration of FMN is assumed not to be capable of providing the enzyme with reducing or oxidising power and can only function as a constituent of the enzyme. A control experiment in Figure 3-23 shows that FMN stuck to the electrode very tightly and the signal from FMN was much stronger than the catalytic current,[210] therefore it is very difficult to study the SH pre-treated with FMN in protein film electrochemistry.

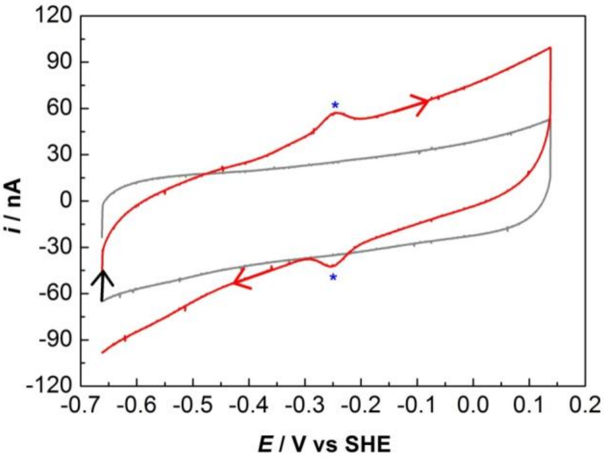

Figure 3-21. Cyclic voltammogram of HoxHYFU adsorbed on a PGE electrode in pH 7 H_2-saturated KPB at 30 ℃ with a scan rate of 10 mV/s. The scan (red) started from -0.65 V after 20 s equilibration at this potential. The voltammogram at a bare PGE electrode under analogous conditions is shown as a grey line. The direction of each scan is indicated by arrowheads.

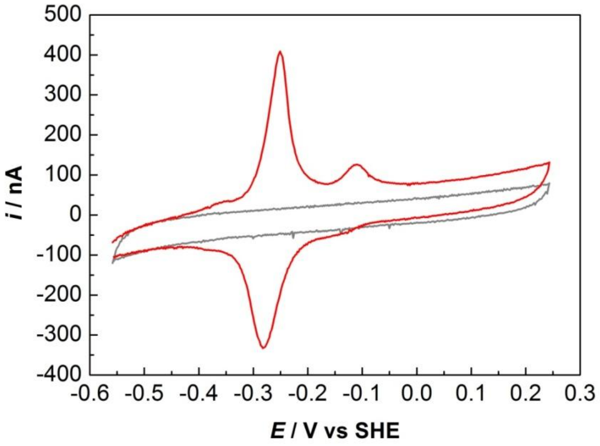

Figure 3-22. Cyclic voltammogram of HoxHYFU (red) adsorbed on a PGE electrode after incubation with catalytic amounts of FMN (about 10 pmol) in pH 7 H_2-saturated KPB (50 mM) at 30 ℃ with a scan rate of 10 mV/s. The voltammogram at a bare electrode recorded in the absence of FMN is shown as a grey line.

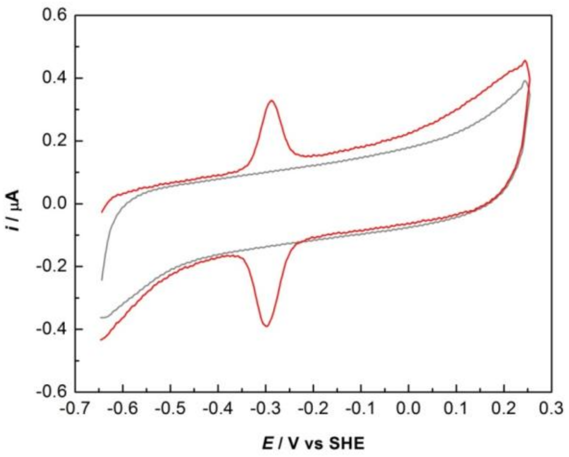

Figure 3-23. Cyclic voltammogram (in red) of an aliquot of FMN on a PGE electrode in pH 8 Tris buffer (50 mM) at 6 ℃ with a scan rate of 100 mV/s. The voltammogram of a bare electrode in the absence of FMN is shown as a gray line.[210]

3.2.4 Electrochemical investigation of the whole enzyme in the form of HoxHYFUI$_2$

As-isolated HoxHYFUI$_2$ on electrode

The as-isolated state of the hexameric SH HoxHYFUI$_2$ was examined by cyclic voltammetry, similar to HoxHY and HoxHYFU. In Figure 3-24, a voltammogram was recorded of HoxHYFUI$_2$ adsorbed on a PGE electrode in the presence of 1 bar H_2 at 1 mV/s. In the first cycle of HoxHYFUI$_2$ (red), the scan starts from +0.245 V. Considering the slight difference in capacitance between an unmodified and enzyme adsorbed electrode, the current at the commencement can be treated as ‘zero’, indicating the enzyme is inactive for H_2 oxidation. As the potential is swept to lower values, a reductive recovery peak appears, indicating that the switch potential of HoxHYFUI$_2$ is identical to that of HoxHY and HoxHYFU for the same process under analogous conditions. As the potential is swept beyond the E ($2H^+/H_2$), the enzyme begins to catalyse H^+ reduction, demonstrating that the hexameric SH works with minimum overpotential, similar to HoxHY and HoxHYFU. On the reverse scan, the enzyme switches to catalyse H_2 oxidation immediately as the potential is swept beyond the E ($2H^+/H_2$). The magnitude of the H_2 oxidation current starts to decrease after 0 V, possibly attributed to film loss or denaturing of the enzyme. However, on the consecutive scan (green), no recovery is observed and the enzyme is dead as there is not either H_2 oxidation or H^+ reduction. The behaviour of $HoxHYFUI_2$ for the $2H^+/H_2$ cycling is almost the same as that of HoxHY and HoxHYFU, although there is a possibility that the hydrogenase moiety HoxHY is separated from the whole enzyme on the electrode. By comparison, the catalytic activity of $HoxHYFUI_2$ is the lowest among the three forms of SH (HoxHY, HoxHYFU and $HoxHYFUI_2$) and the experiment can only be performed in pH 7 KPB to avoid dissociation of HoxI.

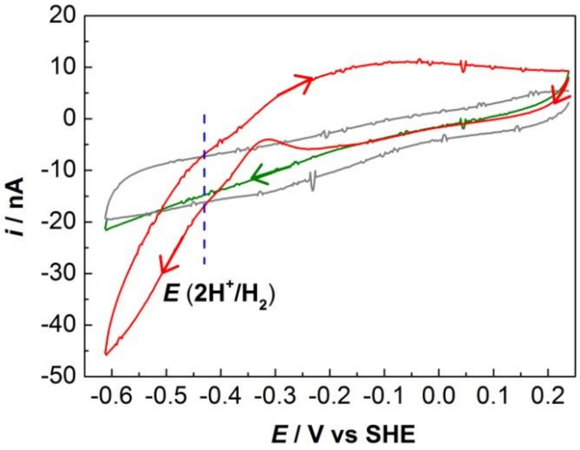

Figure 3-24. Cyclic voltammograms of as-isolated inactive $HoxHYFUI_2$ adsorbed on a PGE electrode in pH 7 KPB (50 mM) at 30 ℃ with a scan rate of 1 mV/s. The first scan (red) was started at +0.24 V after 10 s equilibration at this potential. The second cycle is also shown (green). The position of E ($2H^+/H_2$) corrected for experimental conditions is shown as a blue dashed vertical line. A voltammogram at a bare electrode recorded under analogous conditions is shown as a grey line. The direction of the scans is indicated by arrowheads.

Reaction of $HoxHYFUI_2$ with O_2

Considering the activity and stability of $HoxHYFUI_2$, only its reaction with O_2 is shown in Figure 3-25. Rotation was required to let O_2 quickly reach and leave the electrode and low temperature (10 ^oC) was applied in order to diminish the film loss. Before introduction of O_2, the enzyme film was cycled from +216 mV to -584 mV and back to +216 mV to activate the enzyme, and the electrochemical cell was left on after the activation procedure. Then the electrode was held at +216 mV and the current recorded as shown in Figure 3-25(A). The electrolyte was saturated with 98% H_2 : 2% N_2. Dihydrogen is oxidised at this potential and at

50 s the gas flowing above the electrolyte was switched to 98% H_2 : 2% O_2. At the same time an aliquot of O_2-saturated buffer was injected into the electrochemical cell to quickly reach 2% O_2 in the electrolyte. The concentration of H_2 was kept constant throughout the experiment. The current immediately dropped after O_2 addition, indicating that the enzyme is inactivated by O_2. Further information on the kinetics of its reaction with O_2 is shown in Figure 3-25(B). A semi-log plot of the catalytic current as a function of the time after O_2 injection is plotted, and the curve fits well to a straight line, consistent with a first-order reaction, i.e., the reaction rate is only proportional to the concentration of the active enzyme. The slope gives a negative rate constant $-k$ (k: 0.008 s^{-1}), so the half-life of the reaction is around 84 s. At 200 s, the flowing head gas was switched to 98 % H_2 : 2% N_2 and kept at this for the remainder of the experiment. After removal of O_2, the potential was then jumped to -384 mV to apply a reductive poise for 1 s and jumped back to +216 mV. The H_2 oxidation current showed a significant increase after the reductive poise, indicating the reactivation occurs even within 1 s. Another two reductive poises at the same potential -384 mV for different periods (10 s and 60 s) were applied later, however, no further reactivation happened, indicating that the reactivation after O_2 inhibition is complete within 1 second.

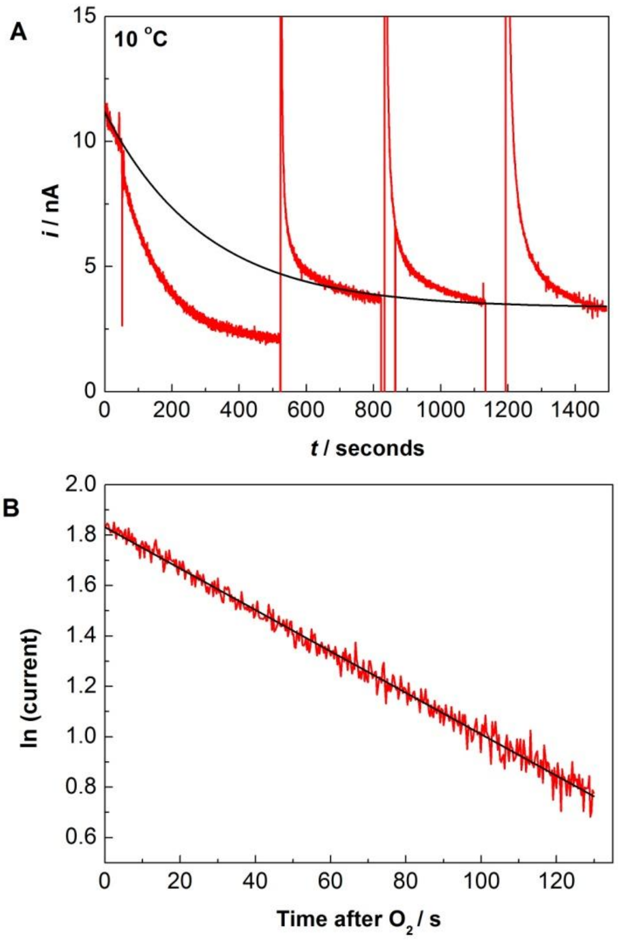

Figure 3-25. Panel A: The reaction of pre-activated HoxHYFUI$_2$ with O$_2$ and reductive reactivation under anaerobic conditions. Red line: pre-activated HoxHY was held at 10 °C and +216 mV under 98% H$_2$: 2% N$_2$ and at 50 s, 80 µL of O$_2$-saturated buffer was injected into 4 mL electrolyte to quickly set up the 2% O$_2$ concentration in the electrolyte, and at the same time the gas flow through the headspace was switched to 98% H$_2$: 2% O$_2$ and kept at this mix until around 200 s. After that, the headspace was flushed with 98% H$_2$: 2% N$_2$ for the remainder of the experiment. The potential was stepped to -384 mV at 520 s for 1 s; at 820 s for 10 s and at 830 s for 60 s to monitor the extent of the reductive reactivation under anaerobic conditions induced by holding at a low potential for different time periods. Black line: an exponential decay curve is fitted based on the catalytic activity of HoxHYFUI$_2$ at +216 mV under anaerobic conditions attributed to film loss. Panel B. The semi-logarithmic plot for the decay following introduction of O$_2$. A linear fit is fitted to obtain the first order rate constant for O$_2$ reaction. Other experimental conditions: the electrode was rotated at 2000 rpm throughout and the flow rate of gas through the headspace was kept at 1000 mL/min.

3.3 Discussion

This Chapter has presented the first electrochemistry of H$_2$ cycling by catalytic moiety of *Re* SH. It has been proved that the SH is capable of catalysing H$_2$ oxidation and H$^+$ reduction (H$_2$

production) under certain conditions. The ability to work close to the thermodynamic potential of the couple $2H^+/H_2$ is important for coupling with the diaphorase moiety.

3.3.1 Implications for the O_2 tolerance of *Re* SH

The SH has been classified as an O_2-tolerant NiFe hydrogenase based on the fact that in solution assays it retains the enzyme activity for H_2 : NAD^+ in the presence of O_2.[53] *In vivo* the SH couples NAD^+ reduction to H_2 oxidation in the presence of O_2. Protein film electrochemical results presented in this Chapter have shown that a low switch potential (E_{switch}, close to the onset of H^+ reduction) is required to restore activity to the hydrogenase moiety HoxHY in the as-isolated state. The same E_{switch} is also required for as-isolated tetrameric (HoxHYFU) or hexameric SH ($HoxHYFUI_2$) to restore the enzyme activity under analogous conditions including pH and scan rate. For as-isolated HoxHY, E_{switch} values obtained with a scan rate of 1 mV/s at pH 6, 7 and 8 in the presence of 1 bar H_2 are -340, -300 and -245 mV, respectively. A second switch potential (-170 mV at pH 7 and 1mV/s) is obtained during reductive recovery after pre-activated SH reacts with O_2. In contrast, the E_{switch} is much more positive for reactivation of the inactive oxidised state of other O_2-tolerant NiFe hydrogenases, such as *Re* MBH (+115 mV at pH 6 and 1 mV/s),[75] *E. coli* Hyd-1 (+150 mV at pH 6 and 1 mV/s),[85] *Aa* MBH I (+75 mV at 0.3 mV/s corresponding to – 280 mV at 0.3 mV/s in HoxHY at pH 7)[88] and *Salmonella enterica* serovar Typhimurium Hyd-5 (+130 mV at 2 mV/s and pH 6)[84]. That is, other O_2-tolerant hydrogenases are able to reactivate at a much higher potential, approximately 300 to 400 mV more positive than that required by HoxHY. In practical terms, this limits the potential window in which the SH could recover from O_2, and therefore oxidise H_2 in the presence of O_2. Is this compatible with the physiological role of the SH?

For the hydrogenase moiety HoxHY, the observation of the low potential reactivation is compatible with the fact that *in vivo* the low potential electrons can be provided by the $NAD^+/NADH$ pool potential, which is experienced by the hydrogenase moiety via connection to its physiological partner HoxFU. On the other hand, the O_2-tolerant membrane-associated hydrogenases mentioned above are all connected to a higher potential of the periplasmic membrane quinone pool through a *b*-type cytochrome cyt *b* (+10 to *ca.* +160 mV).[142] Thus the value of the switch potential seems to correspond well to the physiological redox partner of the hydrogenase in the cell. Although injection of O_2 inactivates these membrane-bound enzymes, the existence of a high switch potential ensures a fast recovery after O_2 attack, even at a higher potential provided by their redox partner. Therefore, they can still catalyse H_2 oxidation in the presence of O_2 in a relatively wide potential window.[10,82] However, for HoxHY, the very low E_{switch} implies a narrow potential window for H_2 oxidation in which there could be fast recovery after O_2 attack.

It was not possible to directly confirm O_2-tolerant H_2 oxidation by the SH within this narrow window due to low currents for H_2 oxidation and huge interference coming from direct O_2 reduction at the electrode. Similar to the SH, a very low switch potential was also observed for *Dm. b* (*Desulfomicrobium baculatum*) NiFeSe hydrogenase and *Synechocystis* sp. PCC 6803 NiFe hydrogenase.[89,90] Although both of these enzymes are very active and stable on an electrode, the H_2 oxidation activity is inhibited by adding O_2 at potentials which are far above their switch potential. However, the authors of these studies found that in the presence of 1% O_2 either H_2 or CO can inhibit H^+ reduction activity by the enzyme, indirectly proving that the enzyme is capable of catalysing H^+ reduction in the presence of O_2. This demonstrates the importance of fast recovery for the enzyme being able to work in the presence of O_2. A similar experiment was performed on HoxHY to test whether it can reduce H^+ in the presence of O_2. However, as discussed earlier, the enzyme activity for HoxHY on an electrode is only 1/50 to 1/100 that of the hydrogenases mentioned above and films are not very stable, and the current arising from H^+ reduction is therefore minimal relative to the huge O_2 reduction current, therefore, a new experimental protocol was designed to show how HoxHY can function in the presence of O_2. As shown in Figure 3-15, a short period of reductive poise (1 second at -384 mV) was applied on O_2-inactivated HoxHY in the presence of O_2 and the potential was then stepped up to +216 mV to examine the H_2 oxidation activity. It was found that the H_2 oxidation activity after the reductive poise increased compared to that before the reductive poise. Furthermore, longer periods of reductive poise were also applied, but no further recovery was found, indicating that the reductive reactivation in the presence of O_2 *is* rapid: even 1 second is long enough for complete recovery. This experiment also indirectly shows that the SH can work in the presence of O_2 at low potentials, despite its low reactivation potential. Furthermore, the inactivation caused by O_2 at high potentials presumably does not matter for the SH as the enzyme is unlikely to experience such a high redox potential *in vivo*.

The SH can be treated as an example for an O_2-tolerant NiFe hydrogenase for having a low reactivation potential. On the other hand, Lukey *et al.* recently purified an *E. coli* Hyd-1 variant C19G which is highly O_2-sensitive whereas the wild-type enzyme is O_2-tolerant. Similar to the wild-type, the C19G variant also has a high switch potential, suggesting that there is no direct correlation of O_2 tolerance with the E_{switch} value.[86] However, the switch potential E_{switch} obtained under analogous conditions and at a relatively slow scan rate, can be used to compare the recovery rate of different hydrogenases after O_2 attack at a certain potential. The value of E_{switch} can be used as an indicator, providing information on the potential above which the recovery from O_2 is not able to happen or occurs at a meaninglessly slow rate.

3.3.2 O_2 inactivation rate in *Re* SH

The reaction rate of the whole SH HoxHYFUI$_2$ with O_2 is almost the same as that of the hydrogenase moiety HoxHY under analogous conditions, i.e., pH, temperature, O_2 and H_2 levels, as shown in Figure 3-14 and Figure 3-25. In both cases given that the O_2 concentration is constant (28.6 μM in solution), the reaction with O_2 was first-order dependent, i.e., the inactivation rate is dependent on the concentration of the active enzyme. The half-life for both HoxHY and HoxHYFUI$_2$ is around 70 s. Furthermore, the reactivation of HoxHY and HoxHYFUI$_2$ after O_2 removal is rapid and complete within seconds.

The reaction rate of HoxHY with 28.6 μM O_2 (2% O_2 in solution) at 30 ^{o}C, +216 mV and pH 7 is approximately 0.02 s^{-1}, slow relative to the O_2-sensitive NiFe hydrogenase from *Desulfovibrio fructosovorans* (*ca.* 1.09 s^{-1} at pH 7, +200 mV and 40 ^{o}C).[69,147] In *Re* MBH, the reaction rate with O_2 (25 % O_2 in solution) at pH 5.5, +213 mV and 30 ^{o}C is approximately 0.31 s^{-1} and the reaction is also first-order dependent, relying on the active enzyme concentration. A lower temperature experiment on *Re* MBH at 10 ^{o}C was also performed and the reaction rate is around 0.11 s^{-1} at pH 5.5 and +192 mV(corresponding to 0.01 s^{-1} for HoxHY at pH 7, 10 ^{o}C and +216 mV).[10] However, due to the high switch potential, the MBH can be rapidly recovered at the same potential as applied on the O_2-sensitive counterpart. In summary, the reaction of the SH with O_2 is much slower than many other NiFe hydrogenases, but the reason for it is still unclear.

3.3.3 Is there an overpotential requirement for O_2 tolerant hydrogenases?

Periplasmic soluble NiFe hydrogenases are exchanging electrons with a tetraheme cytochrome *c* which has mid-point potentials between -202 and -277 mV, in contrast to the periplasmic membrane-associated NiFe hydrogenases which are connected to a two heme cytochrome *b* group.[142,143,235-237] The cytochrome *b* with two redox potentials of +10 and +160 mV is integrated into the respiratory chain and the electrons from H_2 splitting are eventually delivered to the ubiquinone pool (around +90 mV) which is in redox equilibrium with cytochrome *b*.[142]

The periplasmic soluble NiFe hydrogenases such as *D. gigas* NiFe hydrogenase, is classified as a so called 'O_2-sensitive' hydrogenase and it was found that only minimal overpotential is required for driving H_2 oxidation.[75] However, for the O_2-tolerant membrane-associated hydrogenases, such as the enzymes from *R. eutropha, E. coli, A. aeolicus* and *Salmonella,* an overpotential of *ca.* 100 mV is required for H_2 oxidation at 1 bar H_2 and this requirement seems to be a common feature in the O_2-tolerant hydrogenases.[75,84,85,87]

Protein film electrochemistry experiments shown above on HoxHY, HoxHYFU and $HoxHYFUI_2$, however, indicate that both H_2 oxidation and H^+ reduction occur close to the thermodynamic potential E ($2H^+/H_2$) corrected for the experimental conditions. On the other hand, the diaphorase moiety HoxFU also catalyses NAD^+ reduction and NADH oxidation with minimum overpotential relative to the E (NAD^+/NADH) corrected for the experimental conditions. The minimal overpotential requirement for both H^+/H_2 and NAD^+/NADH cyclings will be important in allowing the native enzyme to catalyse NAD^+ reduction by the small electrochemical driving force available from H_2 oxidation. Although the physiological levels of H_2, NAD^+ and NADH in the *Ralstonia eutropha* cell are not known, redox potential windows for the $2H^+/H_2$ couple when the partial pressure of H_2 is between 1 to 10^4 ppm and the NAD^+/NADH couple when the concentration ratio is between 100 to 0.01 are plotted as shown in Figure 3-26. It can be found that E ($2H^+/H_2$) is very closely spaced in potential to E (NAD^+/NADH), allowing minimal driving force for $H_2 : NAD^+$ activity. It is thought that the SH may also work in the reverse direction, i.e., catalyse NADH oxidation coupled with H^+ reduction, when the NAD^+/NADH pool has become too reduced. When the active site of HoxHY is inhibited by O_2, it can be rapidly recovered by the available low potential electrons provided by the NAD^+/NADH pool. For the same reasons, the minimal overpotential for driving H_2 oxidation in 'O_2-sensitive' NiFe hydrogenases such as *D. gigas* NiFe hydrogenase is provided by the closely spaced redox partner cytochrome *c* in potential, as shown in Figure 3-26. On the other hand, a bigger gap exists between the $2H^+/H_2$ pool and the redox potential of cytochrome *b* in the membrane-associated hydrogenases from *R. eutropha*, *E. coli*, *A. aeolicus* and *Salmonella*.[75,84,85,87] This may explain why the overpotential requirement for driving H_2 oxidation in these hydrogenases is not a big problem. Furthermore, the O_2-sensitive C19G variant in *E. coli* Hyd-1 (described above) requires a similar overpotential to the wild type for driving H_2 oxidation.[86] Therefore there is no direct correlation of O_2 tolerance with an overpotential requirement in hydrogenases. On the other hand, the redox potential of its physiological partner may determine how much of an overpotential is tolerated for driving the $2H^+/H_2$ cycling by a hydrogenase.

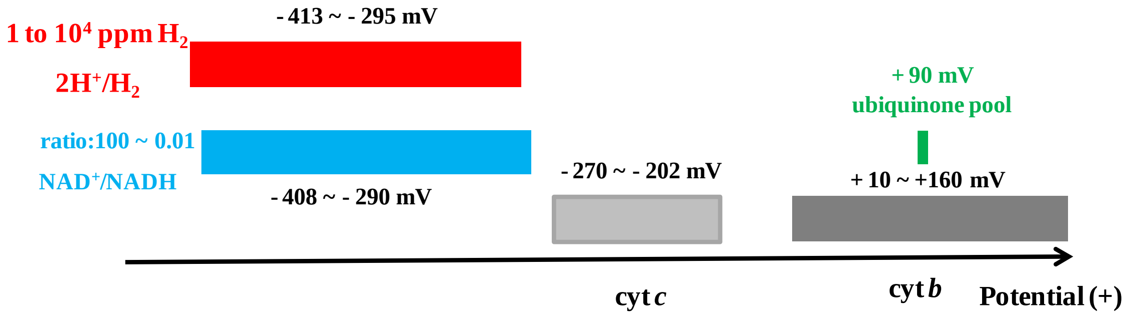

Figure 3-26. Redox potential windows for the couple $2H^+/H_2$ (red), $NAD^+/NADH$ (blue) in *R. eutropha* SH and some physiological redox partners in periplasmic (cyt *c*)[143] and membrane-associated NiFe hydrogeanses (cyt *b*)[142]. The *E* ($2H^+/H_2$) and *E* ($NAD^+/NADH$) are corrected at pH 8 and 25 °C, and the H_2 partial pressure and the ratio of $NAD^+/NADH$ is also indicated. The midpoint potential of ubiquinone pool is around +90 mV.[2,238,239]

3.3.4 Bidirectional catalysis by *Re* SH

Protein film electrochemistry results described in this Chapter for HoxHY, HoxHYFU and $HoxHYFUI_2$ show that the SH is equipped with the ability to catalyse both H_2 oxidation and H^+ reduction in the presence of 1 bar H_2. Normally, the NiFe hydrogenase is a better H_2-oxidising performer than H_2-producer. However, it was shown that almost all the NiFe hydrogenases can reduce H^+ in the absence of H_2, but this activity is greatly inhibited by the presence of H_2 (product inhibition). For *Re* MBH, its catalytic activity for H^+ reduction is inhibited by the product H_2 so strongly that it cannot operate H^+ reduction in the presence of H_2.[83] In contrast, the product inhibition is weaker for the SH: the SH still retains approximately 30% of its maximum activity for reducing H^+ even under 1 bar H_2. The SH is termed a bidirectional NiFe hydrogenase based on the fact *in vivo* it can catalyse H_2 : NAD^+ and NADH : H^+ conversions in both directions under certain conditions. Its capability of reducing H^+ in the presence of H_2 observed by protein film electrochemistry is possibly related to its physiological role in the cell. A recent report shows that a structurally related bidirectional hydrogenase from *Synechocystis* sp. PCC 6803 is also capable of catalysing H^+ reduction in the presence of 1 bar H_2. Furthermore, *Synechocystis* sp. PCC 6803 NiFe hydrogenase is even capable of producing H_2 in the presence of O_2 as discussed above.[90] Similar to the hydrogenase from *Synechocystis* sp. PCC 6803, *Dm. b* NiFeSe hydrogenase can also operate in reducing H^+ in the presence of H_2 or O_2.[89] The soluble hydrogenase from *Ralstonia eutropha*, together with *Synechocystis* sp. PCC 6803 and *Dm. b* NiFe(Se) hydrogenases may provide some insights into the possibility of producing H_2 in the presence of O_2 and H_2 for future energy technology.[125,166]

3.3.5 Redox states exhibited by *Re* SH and comparison with other related hydrogenases

Redox states of *Re* SH

A redox state scheme for HoxHY and the whole SH based on the findings from EPR, FTIR and protein film electrochemistry is shown in Figure 3-27. The summary of redox states detected for HoxHY is shown in the left box whereas states detected for the whole enzyme are listed in the right box. All the EPR-active states are marked by blue characters or boxes. The IR-detectable species are indicated by black characters without boxes. The observations by protein film electrochemistry are shown by the red boxes. The *y* axis in green indicates the electron environment experienced by the enzyme.

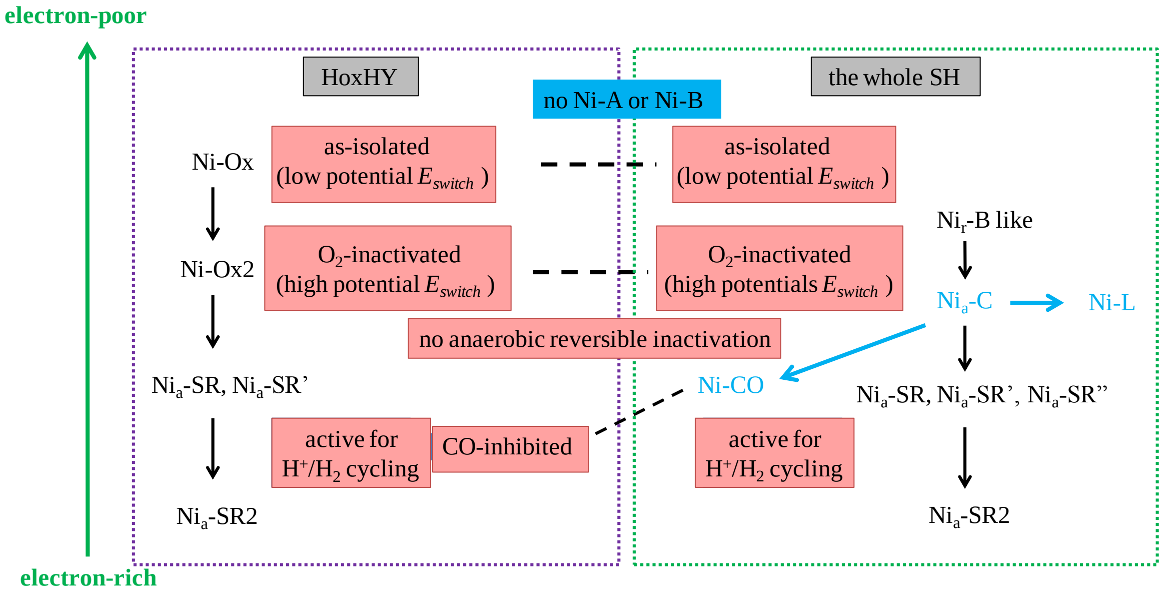

Figure 3-27. Redox state scheme for HoxHY (left box) and the whole SH (right box). The EPR-active states are marked by blue characters or background. IR-detectable states are labelled by black characters. The findings from protein film electrochemistry are indicated by the red boxes.

In either HoxHY or the whole SH, the Unready Ni-A and Ready Ni-B species have never been observed by EPR, suggesting that the low potential activation process of the as-isolated enzymes (HoxHY, HoxHYFU and HoxHYFUI$_2$) does not relate to either of them. The lack of Ni-B in the SH is also confirmed by the electrochemical results, i.e., no evidence is found for reversible anaerobic oxidative inactivation. A Ni-C species in the whole SH is detected by EPR after prolonged incubation with NADH of the enzyme and is also observed in the freshly harvested cells by a recently-developed *in-situ* FTIR method.[149,215] However, this Ni-C state is missing in the hydrogenase moiety HoxHY determined by this *in-situ* FTIR method, and the lack of Ni-C might be related to the deletion of the diaphorase moiety HoxFU.[147] Based on the observation of Ni-C, it was further found that adding exogenous CO or illumination generates other EPR-active states, i.e., Ni-CO and Ni-L, respectively.[215] In protein film electrochemistry, it was also found that CO can reversibly inhibit H^+ reduction in HoxHY, indicating that HoxHY or the whole SH can react with CO under certain conditions. Although the oxidised inactive Ni-A and Ni-B states are missing in the SH, two oxidative states termed Ni-Ox and Ni-Ox2 are observed in HoxHY by IR and the Ni-Ox2 state is possibly an intermediate during the conversion of Ni-Ox to the reduced states (Ni_a-SR, Ni_a-SR' and Ni_a-SR2).[147] In protein film electrochemistry, two unusual switch potentials were found in HoxHY: one is corresponding to a very low activation potential for the as-isolated enzyme (-300 mV at pH 7, 30 °C and 1 mV/s) and this process is found to be irreversible, the other higher potential E_{switch} (-170 mV at pH 7, 30 °C and 1 mV/s) occurs in the reductive reactivation process after the active HoxHY is attacked by O_2. Although the experimental conditions for the electrochemistry and IR are not identical, it seems that two different oxidative states are independently observed by these two methods. The protein film electrochemical investigation of the whole enzyme also presents similar results, i.e., the reaction of the active HoxHYFU with O_2 generates a mixture of oxidative inactive states, corresponding to two other switch potentials apart from the very low one. Each switch potential should represent a redox state reflecting the active site and the electron transfer chain in the hydrogenases. In the native whole SH, a new Ni-B-like state was designated as its IR spectrum resembles that of a state found in *Synechocystis* sp. PCC 6803 hydrogenase which was earlier termed Ni-B-like.[149,217] However, this state is EPR-silent, therefore it is only like and essentially not Ni-B.

In summary, the Ni-A and Ni-B states are absent in *Re* SH including the hydrogenase moiety HoxHY and the whole enzyme. In the whole enzyme, Ni-C is found by EPR and IR. However, Ni-C is missing in HoxHY, suggesting that the absence of diaphorase moiety HoxFU or the substoichiometric amount of FMN alters the redox state of the enzyme. Upon oxidising Ni-C, a Ni-B-like EPR-silent state was designated by IR in the whole enzyme. Under oxidising or electron-poor conditions, two oxidised states Ni-Ox1 and Ni-Ox2 are formed in HoxHY either of which is not identical to the Ni-B-like state. In protein film electrochemistry, more than one oxidised states are found, confirmed by at least two switch potentials. Under reducing or electron-rich environments, both HoxHY and the whole enzyme exhibit several reduced states. Carbon monoxide can react with the enzyme under certain conditions found by EPR and PFE.

Comparison with other related hydrogenases

The absence of Ni-A and Ni-B is also the case in the bidirectional NiFe hydrogenase from *Synechocystis* sp. PCC 6803.[90] However, the reversible anaerobic inactivation which usually corresponds to formation of Ni-B is observed by chronoamperometry within a narrow potential window in *Synechocystis* sp. PCC 6803 NiFe hydrogenase.[90] With respect to more than one oxidised states observed in *Re* SH, it was also found in *Dm. b* NiFeSe hydrogenase and the bidirectional NiFe hydrogenase from *Synechocystis* sp. PCC 6803 that two switch potentials exist during the reductive recovery after O_2 attack.[89,90]

It is worth mentioning that the redox states of *Re* SH resemble very much those of the *Desulfovibrio vulgaris* Hildenborough (*D. vulgaris* Hildenborough) NiFeSe hydrogenase, i.e., the Ni-A and Ni-B are also missing in the latter and only Ni-C is observed by EPR.[20] The crystal structure in its oxidised as-isolated state for the first time revealed that a bridging ligand (hydroxide or peroxide) is absent at the active site.[240] Furthermore, IR studies show that oxidation of the reduced *D. vulgaris* Hildenborough NiFeSe hydrogeanse leads to an inactive species that is different from the as-isolated enzyme,[114] consistent with the findings in *Re* SH. Based on the structural information, the oxidative as-isolated form is shown in Figure 3-28. Three conformers are present with a ratio of 70:15:15 in the purified enzyme.

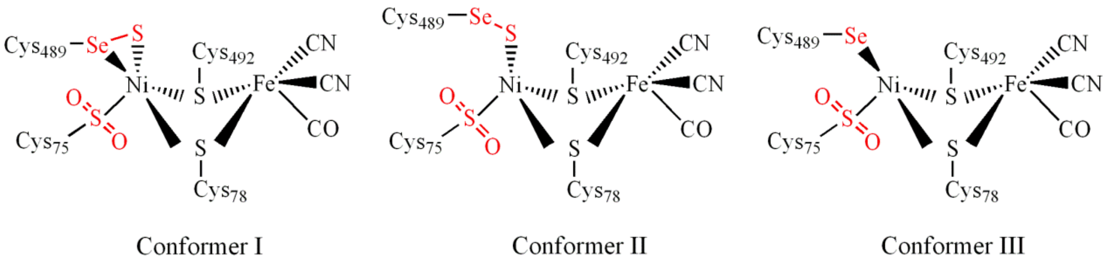

Figure 3-28. The active site of the *D. vulgaris* Hildenborough NiFeSe hydrogenase and three conformers. Figure adapted from ref [240].

The extra sulphur coordination in Conformer I and II is not too surprising as *D. vulgaris* Hildenborough as a sulphate-reducing bacterium should produce large amounts of sulphide in the cell. In comparison, a cyclic voltammetry study on several NiFe hydrogenases shows that adding extra sulphide to the hydrogenase enzyme within a certain potential window generates a reversible inactive species that is distinct from Ni-A or Ni-B and a sulphide ligand is possibly bridging between the Ni and the Fe.[79] Furthermore, it was found that the *D. vulgaris* Hildenborough NiFeSe hydrogenase retains its enzyme activity (capable of producing H_2) in the presence of O_2.[237] The missing bridging ligand leads to a shorter distance between Ni and Fe. The extra S coordination and the relative large size of the Se atom compared to S may block or limit the access of the inhibitor O_2.[240] One common feature in the NiFeSe hydrogenases from *D. vulgaris* Hildenborough and *Dm. baculatum* is that both enzymes have a very low recovery potential for the inactive species.[89,114] It was observed that one terminal cysteine coordinated to Ni is oxidised to a cysteine-S-dioxide and 40% of the proximal 4Fe-4S cluster is oxidised to $Fe_4S_3O_3$ after O_2 attack. The presence of the cysteine-S-dioxide and $Fe_4S_3O_3$ possibly contributes to the low reductive activation potential.[240] In comparison with *D. vulgaris* Hildenborough NiFeSe hydrogenase, the EXAFS analysis of *Re* SH also revealed a low amount of Fe-O bonds of 2.14 Å, possibly arising from the oxidised Fe-O-Fe motif in the modified proximal 4Fe-4S cluster.[147] Therefore, a lot of features are shared between the *D. vulgaris* Hildenborough NiFeSe hydrogenase and the SH including the absence of Ni-A and Ni-B, the oxidatively modified proximal 4Fe-4S cluster, two distinct inactive oxidative states (corresponding to two different recovery potentials in HoxHY and one is very close to *E* ($2H^+/H_2$)) and O_2 tolerance within a certain potential window. Although the crystal structure of *Re* SH is still not available yet, the structure of the *D. vulgaris* Hildenborough NiFeSe hydrogenase and its redox states may provide some insights into the O_2 tolerance of the SH.

3.3.6 What contributes to O_2 tolerance in *Re* SH?

As discussed above, the presence of oxidatively modified proximal 4Fe-4S cluster in *Re* SH may imply the proximal FeS cluster is capable of reacting with O_2, and therefore indirectly protects the active site of the SH. Recently, a review by Darensbourg *et al.* proposed that S-oxygenation at or near the active site of the enzyme may represent the repair mechanism for reversible O_2-inhibition processes in NiFe hydrogenases.[241] Furthermore, the absence of Ni-A and Ni-B implys that a hydroxide or peroxide ligand is missing between the Ni and the Fe, thus the distance in-between is shorter than the standard NiFe hydrogenases, and this crowded environment may lead to a slower reaction with O_2, which is consistent with the electrochemical findings in this Chapter.

Another important feature about *Re* SH is the presence of two FMN cofactors, as shown in Figure 3-1. Unlike other standard NiFe hydrogenases in which three FeS clusters are functioning to transfer electrons to and from the active site, FMN in *Re* SH is also playing a special role in electron transfer within the enzyme. One evidence from the biochemical assays is that the release of FMN-a in the HoxY upon reducing the whole SH leads to an impaired enzyme activity $H_2 : NAD^+$, implying FMN-a *is* an electron transfer centre as well. Furthermore, as discussed in **Section 3.1.6**, FMN-a is proposed to function as a one-to-two electron converter during the catalysis as the FeS cluster functions as the centre for transferring one electron at a time and cycling between NAD^+ and NADH requires the transfer of two electrons and one proton.[147] Therefore, this unique electron transfer chain in terms of the presence of FMN in *Re* SH may be crucial for the enzyme to survive when O_2 attacks because it may provide rapid electron back to the active centre and effectively reduce or remove O_2.

3.3.7 Future work

As discussed in **Section 3.2**, the stability of the enzyme is a big problem for further understanding the O_2 tolerance, not only in HoxHY but also in more complex HoxHYFU and $HoxHYFUI_2$. It was found that only 0.05 equiv. of FMN per HoxHY is present in HoxHY,[147] which might explain the poor stability of the enzyme as an important constituent is missing. Although exogenous FMN was added to *Re* SH under different conditions, no signs of enhanced activity or stability were observed in electrochemistry, implying the enzyme might be damaged at the first place due to the substoichiometric amount of FMN. In the future, beyond the scope of this study, stable enzyme purification is counted on. Furthermore, so far the findings of *Re*

SH by PFE and IR are not obtained under analogous conditions, as shown above. Therefore, it will be good to perform the infrared spectroelectrochemical investigation to study the SH and compare the IR results with the protein film electrochemical findings to get further understanding of O_2 tolerance in *Re* SH.

Chapter 4

Protein Film Electrochemical Investigation of *Ralstonia eutropha* Regulatory Hydrogenase

4.1 The regulatory hydrogenase of *Ralstonia eutropha*

4.1.1 Biochemical investigations

Dihydrogen is an energy source for many microorganisms. Dihydrogen produced by anaerobic fermentative bacteria is mostly consumed by other anaerobic H_2 uptake microbes, before it enters an aerobic environment. Thus, aerobic H_2-oxidizing organisms like *Ralstonia* (*R.*) *eutropha* receive H_2 in a limited manner,[242] and the expression of the hydrogenases involved in energy conservation in *R. eutropha* has to be efficiently regulated in response to H_2.[1] The sensing of H_2 in *R. eutropha* is co-regulated by a regulatory hydrogenase and a histidine protein kinase.

The RH of *R. eutropha* (*Re* RH or the RH) is composed of a small subunit HoxB and a large subunit HoxC, resembling the dimeric standard NiFe hydrogenases.[243] HoxB and HoxC represent polypeptides of 34.5 and 52.5 kDa, respectively. Analysis of the amino acid sequence shows that the four cysteine residues coordinating the active site are also conserved in the RH (Cys 60, Cys 63, Cys 479 and Cys 482) like standard NiFe hydrogenases, and two of them are bridging ligands between the Ni and the Fe and the other two are terminal ligands coordinated to Ni.[244] Unlike other NiFe hydrogenases which are usually coupled with their redox partners, the RH is connected with a histidine protein kinase HoxJ. Hydrogenase gene transcription was completely abolished by a deletion of HoxB, indicating that the H_2 sensor exerts a positive effect on *hox* gene transcription.[202] However, a deletion of HoxJ leads to a high level of hydrogenase gene transcription even in the absence of H_2, indicating that HoxJ exerts a negative effect on the *hox* gene expression.[146,202] Like many NiFe hydrogenases, the small subunit HoxB houses a series of FeS clusters. A variant in which the C-terminal 55 amino acid residues in HoxB were deleted, lost the ability of signal transduction, but retained H_2 oxidation activity in the solution assays. The truncated HoxBC may cause the iron-sulphur cluster to be damaged and therefore impair the electron transfer between the active site and the kinase. The blocked signal transduction suggests that the process of H_2 sensing is dependent on the electron transfer between RH and HoxJ.[202,245] Apart from HoxBC and HoxJ described above, another important protein HoxA is required for the signal transduction. HoxA is a member of the NtrC family of response regulators.[245] In the absence of H_2, as no H_2-sensing signal is passed to HoxJ from HoxBC, HoxJ inactivates HoxA by phosphorylation and leads to a limited hydrogenase gene expression. However, in the presence of H_2 this phosphorylation process is blocked and the active HoxA leads to a H_2-dependent hydrogenase gene expression as HoxBC passes the signal to HoxJ after receiving H_2.[245] The whole regulation process starting from H_2 sensing to signal transforming is summarised as shown in Figure 4-1.

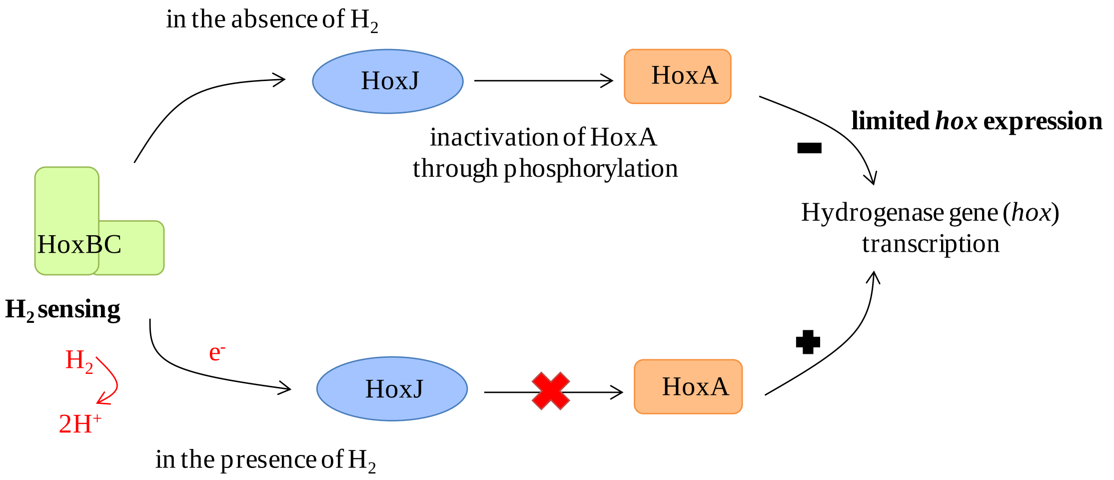

Figure 4-1. The H_2 sensing signal transduction by the RH to control the hydrogenase gene expression in *Ralstonia eutropha* microbe. Figure adapted from ref[146].

As discussed above, the electron transfer from HoxBC to HoxJ, after receiving H_2, plays an important role in the signal transduction and the iron-sulphur clusters housed in the small subunit HoxB are crucial for the intramolecular electron transfer. In contrast to standard NiFe hydrogenases, the FeS clusters in the RH show very different redox behaviours. Firstly, no signal for $3Fe4S^{1+}$ was observed in the oxidised RH even after treatment with excess oxidant DCPIP (dichloroindophenol) by EPR. Secondly, the standard spin-to-spin coupling between the reduced proximal $4Fe4S^{1+}$ and the Ni (III) species at a low temperature was not observed in the

RH when the enzyme was incubated with 100% H_2 and dithionite.[43,246] All these observations indicate that the iron-sulphur clusters within the RH are different from those in standard NiFe hydrogenases, i.e., the proximal 4Fe4S, medial 3Fe4S and distal 4Fe4S clusters. An EXAFS investigation also confirmed the different arrangement of FeS clusters in the RH compared to standard NiFe hydrogenases and led to a proposal that two 2Fe2S clusters and one 4Fe species which may be a 4Fe-3S-3O cluster are the most likely options located in HoxB.[247]

There are several forms of *Re* RH that need to be addressed here. *In vivo*, the HoxBC subunits form a dimer $(HoxBC)_2$ designated as RHwt. The purified HoxJ was found to be a homotetramer form by the mass determination.[202] It is proposed that the H_2-sensing complex of *R. eutropha* consists of one dimeric heterodimer $(HoxBC)_2$ and a tetramer of the kinase HoxJ $(HoxJ)_4$. Artificially, a monodimeric derivative HoxBC, designated RHstop, was isolated and purified through a genetic deletion of a C-terminal peptide of 55 amino acids in HoxB.[247] The RHstop fails to form a complex with HoxJ and therefore the signal transcription is abolished. However, the solution assay analysis showed that the variant still retained the enzyme activity for H_2 oxidation.[202] Analysis of the Fe contents by AAS (Atomic Absorption Spectroscopy) and TRXF (Total Reflection X-ray Fluorescence) independently showed that each HoxBC unit of RHwt contained 8-9 Fe atoms whereas the iron content of RHstop is 4-6, lower than the wildtype counterpart. Therefore, one 4Fe sulphur species might be lost in the RHstop, although the chemical analysis of metal contents is variable.[247]

The RH samples used throughout the Thesis (this Chapter and Chapter 6) is RHstop as it has several advantages for *in vitro* studies: (i) the replacement of the C-terminal 55 amino acids by a Strep-tag II sequence allows facile isolation; (ii) this RH derivative forms a monodimer HoxBC rather than $(HoxBC)_2$ and is not complexed with the kinase HoxJ; and (iii) it resembles the standard heterodimeric NiFe hydrogenases which have been widely studied by protein film electrochemistry.[131]

4.1.2 O_2 tolerance arising from the limited gas channel in *Re* RH?

In enzyme assays, it was found that the rate of H_2 oxidation in the presence of O_2 catalysed by the RH with methylene blue (MB) or benzyl viologen (BV) as the electron acceptor is the same as that obtained in anaerobic solution.[148,246] It has thus been classified as an O_2-tolerant NiFe hydrogenase as it is capable of oxidising H_2 in the presence of O_2.[148] It was suggested that the presence of two bulky amino acid residues (isoleucine 62 and phenylalanine 110) close to the nickel of the active site, rather than the highly conserved relatively small residues (valine and leucine) in the other NiFe hydrogenases (*D. gigas*,[26] *D. fructosovorans,*[128] *A. vinosum*,[97] and *Re* MBH[62]), leads to limited access for molecules larger than H_2, such as O_2 and CO, to the active site.[128,131] Therefore, the site-directed mutagenesis from isoleucine (I) to valine (V) and/or from phenylalanine (F) to leucine (L) near the Ni atom in the putative gas channel was designed (I62V, F110L, and I62V/F110L) to generate a situation similar to that found in the O_2 sensitive NiFe hydrogenase. The enzyme assay analysis showed that the enzyme activity for H_2 oxidation with MB in both the single variant and the double variants was affected greatly after exposure to O_2.[131] As a conclusion, the variants of the RH are indeed transformed to be O_2-sensitive. Apart from the shape modification in the putative gas channel, however, other changes may also be introduced by the amino acid replacement near the Ni atom, such as alteration of the coordination chemistry near the active site and variation of the electron or proton pathway involved in the enzyme turnover.

Based on the idea of restricting gas access, the reverse site-directed mutagenesis was conducted on *D. fructosovorans* NiFe hydrogenase by Rousset and co-workers in order to mimic the bulky residues close to the Ni atom in the RH. However, it was found that the variant did not show O_2-tolerance after placing the two bulky isoleucine and phenylalanine residues at the end of the putative gas channel near the active site. The gas diffusion slowed down for the variant but the inactivation rate by O_2 was the same as the wild type.[68] Surprisingly, the mutagenesis by introducing a normal sized residue, methionine, does introduce some O_2 tolerance to the *D. fructosovorans* NiFe hydrogenase.[132] Therefore, the restricted gas channel used to explain the O_2

tolerance in the RH is not convincing and its mechanism is re-investigated in the present study, using protein film electrochemistry as discussed in this Chapter.

4.1.3 Spectroscopic investigation of the redox states in *Re* RH

Studies by FTIR show that the RH carries a standard set of diatomic ligands on Fe, i.e., two CN^- and one CO bound to Fe. However, in contrast to other standard NiFe hydrogenases, only two redox states are observed for the RH, i.e. the as-isolated Ni_a-S (υ(CO): 1943 cm^{-1}; $\upsilon(CN^-)$: 2081/2073 cm^{-1}) and the H_2-incubated Ni_a-C state (υ(CO): 1962 cm^{-1}; $\upsilon(CN^-)$: 2084/2072 cm^{-1}). The RH is always active for H_2 oxidation even in its as-isolated state although it is purified in air. It does not appear to react with O_2 and lacks the corresponding inactive Ni-A or Ni-B states found in standard NiFe hydrogenases. Introduction of CO has not been found to generate any new states either.[148,246]

The EPR investigation of the RH shows that incubation with H_2 leads to the EPR-detectable Ni-C state of the protein whereas the as-isolated state Ni_a-S designated by IR is found to be EPR-silent.[43,247] The observation of the Ni-C state in the RH by EPR corresponds well with the results from FTIR. Advanced HYSCORE and ENDOR spectroscopy further demonstrate that the exchangeable proton residing in a bridging position between the Ni and the Fe, is formally assigned as a hydride ion.[43] The Ni-C state in the RH after reduction with H_2 is very similar to the reduced Ni-C state of standard NiFe hydrogenases. After illumination at low temperature (T = 10 K), the Ni-L state is formed artificially. For the Ni-L state, the strong hyperfine coupling observed for the exchangeable hydrogen in Ni-C is lost, indicating a cleavage of the metal-hydride bond(s).[43] The EXAFS spectra also indicate a change in the Ni coordination in the RH after incubation with H_2.[222] However, although only Ni_a-S and Ni-C are observed so far, it cannot exclude the possibility of other states formed transiently during the enzyme turnover.

4.2 Electrochemical Results on *Re* RH

As mentioned above, the RH sample used in this Chapter and Chapter 6 is the RHstop. Some of the electrochemical experiments in this Chapter including the measurement of the H_2 affinity and the reaction with carbon monoxide were carried out by a summer student Thomas Simler working under my supervision.

4.2.1 H_2 cycling by the RHstop

The RHstop on an electrode

An aliquot of RHstop was spotted onto a pyrolytic graphite 'edge' (PGE) electrode inside the N_2-filled glovebox. In Figure 4-2, the scan starts from -0.65 V and the potential is swept towards +0.2 V, as indicated by the red arrows. At the commencement of the scan, the negative current indicates that the enzyme is active for H^+ reduction. It is interesting to observe the H^+ reduction catalysed by the RHstop adsorbed on a PGE electrode in the presence of 1 bar H_2, as *in vivo* the physiological role of the enzyme is sensing H_2. This electrochemical finding is in line with the benzyl viologen-dependent H_2 evolution by the RH in the enzyme assay.[246] Almost all the NiFe hydrogenases studied so far are capable of catalysing H^+ reduction *in vivo* even though their physiological role in the cell is more related to H_2 oxidation. In order to clarify the contribution from the electrode capacitance, a cyclic voltammogram at an unmodified electrode was recorded under analogous conditions, as shown by the grey line. The dashed blue line is the thermodynamic potential for $2H^+/H_2$ corrected for the experimental conditions. The enzyme activity turns into H_2 oxidation immediately after the potential is swept beyond the thermodynamic potential, demonstrating that the RHstop is capable of catalysing both H_2 oxidation and H^+ reduction with minimal overpotential, similar to the SH discussed in Chapter 3. On the reverse scan, the voltammetry gives a similar shape for essentially the same reasons. In subsequent scans indicated by the small black arrow, the activity for H_2 oxidation is almost unaltered, indicating that the RHstop is fairly stable on a PGE electrode. The RHstop modified electrode is stationary in the voltammograms shown in Figure 4-2. In another experiment performed under identical conditions, except with electrode rotation at 2000 rpm (data not shown), no increase in H_2 oxidation was found, indicating that H_2 oxidation by the RHstop was not limited by the substrate supply. This is consistent with the low activity of the RHstop. Subsequent experiments were performed without rotation except where specified.

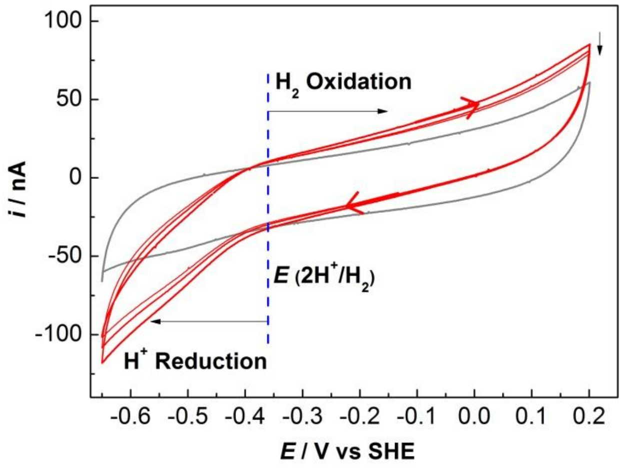

Figure 4-2. Cyclic voltammograms for a bare (grey) and RHstop modified (red) PGE electrode at pH 6 and 30 ^{o}C. Other conditions: 10 mV/s, 1 bar H_2, electrode not rotating; the direction of the scans is shown by red arrowheads and the change over three successive scans is indicated by the vertical black arrow.

The RHstop on a PGE electrode shows very low activity for both H_2 oxidation and H^+ reduction relative to other NiFe hydrogenases. This is not surprising as the physiological role of the RH is sensing H_2 rather than the generation of energy from H_2, as is the case for the MBH or SH. The catalytic activity of the adsorbed RHstop on the electrode is also in agreement with the results from the solution assays, in which the RH shows an enzyme activity two orders of magnitude lower for H_2 oxidation than the standard hydrogenases.[246] Although RHstop is not very active on the electrode, it is sufficiently stable that I can study the RHstop by protein film electrochemistry as it is a very sensitive technique.

Investigation of the as-isolated state for the RHstop

The RHstop is purified in air, as are many other NiFe hydrogenases,[85,87] including the SH[1] and MBH[82] from the same microorganism *R. eutropha*. Generally, a mixture of Ni-A and Ni-B states are generated when O_2-sensitive NiFe hydrogenases are purified in air[23] and reducing agents are required to restore the H_2 oxidation activity of hydrogenases. However, data from solution assays showed that the RHstop was active for H_2 oxidation with MB as electron acceptor even in its isolated-state.[148] The as-isolated state of RHstop was examined by voltammetry as shown in Figure 4-3. A film was formed on a PGE electrode immediately after an aliquot of as-isolated RHstop was placed into the N_2-filled glovebox and the electrolyte was saturated with H_2 before measurement. At the commencement of the scan, around +0.25 V, a positive current is observed, indicating that the enzyme in its as-isolated state is active for H_2 oxidation, whereas in contrast the as-isolated SH is inactive for H_2 oxidation and requires a reductive reactivation. As the potential is swept to lower values, there is not a clear reductive recovery as is found for the as-isolated SH. As the enzyme activity is very low, the contribution from the electrode needs to be considered and a voltammogram (grey) of an unmodified electrode was recorded under analogous conditions. At around -0.1 V, there is a small increase in current for the RHstop but a similar peak is also found in the background voltammogram of a bare electrode, apparently related to an adsorption reaction related to buffer on the first cycle with a freshly polished electrode. Therefore, this small increase can be attributed to the electrode and no reductive activation is obvious for the as-isolated RHstop. Its capability to catalyse H_2 oxidation with no requirement for low potential activation confirms that the as-isolated RHstop is active, even though it is purified in air. As the potential is swept below the thermodynamic potential E ($2H^+/H_2$), the RHstop starts to catalyse H^+ reduction, indicated by a negative current. The minimal overpotential requirement of the RHstop to catalyse $2H^+/H_2$ cycling, in addition to that observed for the SH discussed in Chapter 3, further demonstrates that it is not essential for O_2-tolerant hydrogenases to have a sizable overpotential for H_2 oxidation.

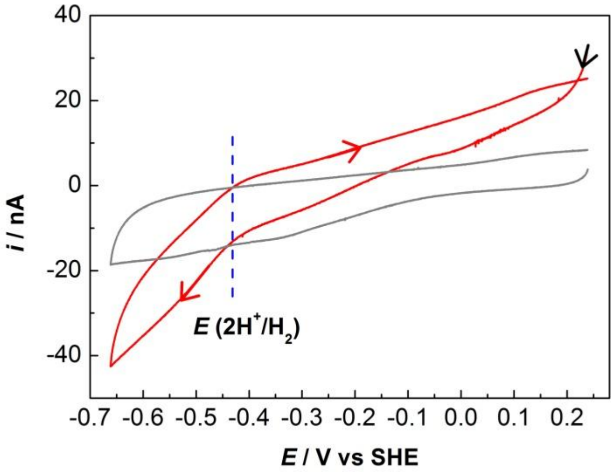

Figure 4-3. Cyclic voltammogram (red) of the as-isolated RHstop adsorbed on a stationary PGE electrode in pH 7.2, 50 mM potassium phosphate buffer (KPB). Conditions: 1 mV/s; 1 bar H_2; 28 ^oC; a vertical blue dashed line indicates the thermodynamic $2H^+/H_2$ potential corrected for the experimental conditions. A voltammogram (grey) of an unmodified electrode under analogous conditions is also shown as the catalytic activity of RHstop is small and the small contribution from the electrode needs to be considered.

Effect of pH on catalysis

Cyclic voltammograms shown in Figure 4-4 were used to study the pH effect (pH 6, 7 and 8) on the catalysis by the RHstop. At pH 6 and 7 under H_2 in Panel A and C, there is not much difference in the catalytic activity for both H_2 oxidation and H^+ reduction by the RHstop. Although these results were not obtained on the same film, several experiments under the same conditions were carried out to confirm that at pH 6 and 7 the activity of the RHstop was almost identical. The enzyme activity was also tested under 1 bar N_2 at pH 6 and 7 in Panel B and D, and only H^+ reduction was observed. As there was no substrate present, it made sense that H_2 oxidation was not observed. By comparing Panel A and Panel B at pH 6 or Panel C and Panel D at pH 7, it is found that H^+ reduction seems more pronounced under N_2, suggesting that H_2 probably inhibits H^+ reduction due to product inhibition. However, it is not possible to make an accurate comparison from these experiments as there is film-to-film difference. A more precise experiment in the next section will examine whether there is product inhibition in the region of H^+ reduction for the RHstop. Furthermore, the capability of H^+ reduction under 1 bar H_2 by the RHstop is similar to that by *Re* SH,[147] whereas the H^+ reduction under H_2 by *Re* MBH is negligible.[83] At pH 8 under 1 bar H_2 in Panel E or N_2 in Panel F, the catalytic activity for H^+ reduction or H_2 oxidation is fairly low, almost identical to the capacitance of the bare electrode shown in grey line in each panel under analogous conditions, indicating that pH 8 is not good for the enzyme function. As pH 6 and 7 are optimum for the RHstop to function, the experiments throughout this Chapter were all performed between pH 6 and 7.

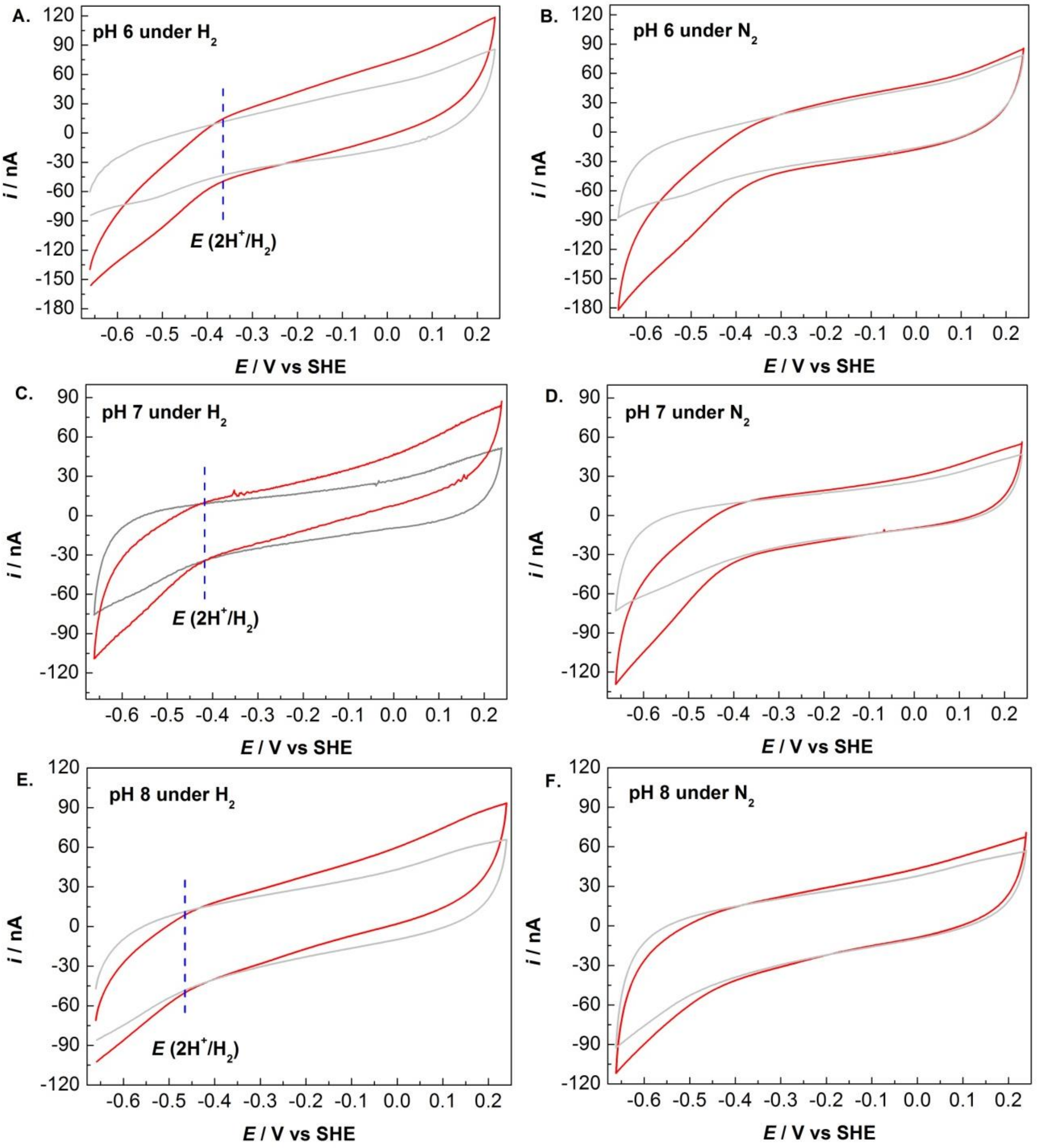

Figure 4-4. Cyclic votammograms of the RHstop (red) on a PGE electrode at different pH and gas atmosphere. Panel A and B: pH 6 under 1 bar H_2 and N_2, respectively; Panel C and D: pH 7 under 1 bar H_2 and N_2, respectively; Panel E and F: pH 8 under 1 bar H_2 and N_2, respectively. As the catalytic currents for H_2 oxidation or H^+ reduction by RHstop are small, the response of the bare electrode under analogous conditions needs to be considered and is shown as the grey line in each panel. The thermodynamic potential for *E* ($2H^+/H_2$) corrected for the experimental condition in Panel A, C and E is indicated as a dashed blue line. Other conditions: 10 mV/s, 30 °C and electrode not rotating.

Product inhibition of H^+ reduction

In order to examine whether there is product inhibition for H^+ reduction by the RHstop, a chronoamperometry experiment as shown in Figure 4-5 was performed. The electrode was poised at -500 mV. An inert gas, N_2 in this case, was first flushed through the headspace and the negative current in the red line indicated that H^+ was reduced at this potential. The rapid decay in current during the first 50 seconds was due to the decay in capacitance of the electrode when a potential was applied. At around 190 s when the catalytic current reached a relatively stable value, H_2 (which is also the product of H^+ reduction) was introduced to replace N_2 and the magnitude of the catalytic current immediately dropped, indicating that H_2 indeed inhibits H^+ reduction. At around 370 s, N_2 was switched back on and the current recovered quickly, further demonstrating that H_2 is a rapid and reversible inhibitor. A control experiment on a bare PGE electrode under analogous conditions was also performed, shown as the grey line in Figure 4-5 to clarify the contribution from the capacitance of the electrode. The reversible product inhibition in the RHstop is similar to that in other NiFe hydrogenases. However, the extent of inhibition is fairly light in the RHstop compared to other NiFe hydrogenases as it still maintains over two thirds of its maximum activity in the presence of 1 bar H_2.

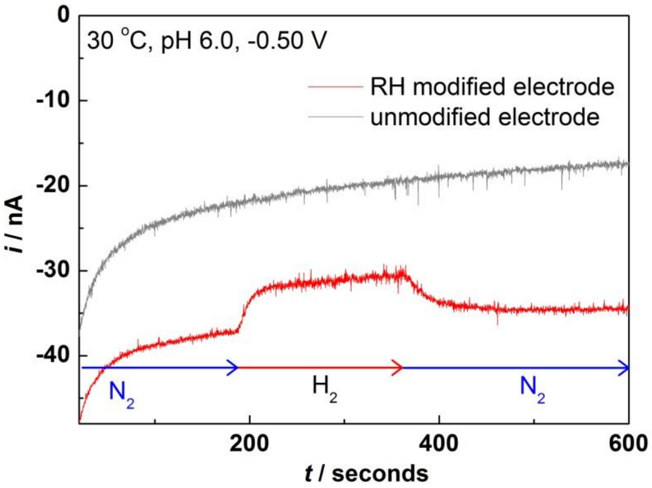

Figure 4-5. Experiments designed to examine inhibition of H^+ reduction by H_2 in the RHstop (red). The gas flushing through the headspace of the cell was exchanged at the times indicated while maintaining an overall flow rate of 1 L min^{-1}. Other conditions: 30 ℃, pH 6.0, electrode rotation rate: 4000 rpm, electrode potential: -0.5 V vs. SHE.

Anaerobic inactivation in RHstop?

Most NiFe hydrogenases undergo reversible anaerobic inactivation at high potentials. A cyclic voltammogram with a wide potential window as shown in Figure 4-6 was performed to examine whether or not the RHstop undergoes this reversible anaerobic inactivation. The scan starts from -0.65 V indicated by a black arrow and the potential is swept up to +0.42 V. However, there is not an obvious "switching off" for H_2 oxidation. A broad bump around +0.25 V occurs on the forward scan and looks a little confusing given that the anaerobic inactivation normally happens near there. However, a control experiment on a bare PGE electrode, shown by the grey line in Figure 4-6, was carried out and shows that the bump actually comes from the background. On the reverse scan there is no evidence of reactivation related to the anaerobic oxidative inactivation. The absence of the reversible anaerobic inactivation in the RHstop investigated by protein film electrochemistry is in agreement with the studies by EPR and FTIR that only two states (Ni_a-S and Ni-C) are observed so far in the RH and the standard inactive Ni-B state which is generated under oxidative conditions is not formed in the RH under these conditions.[148]

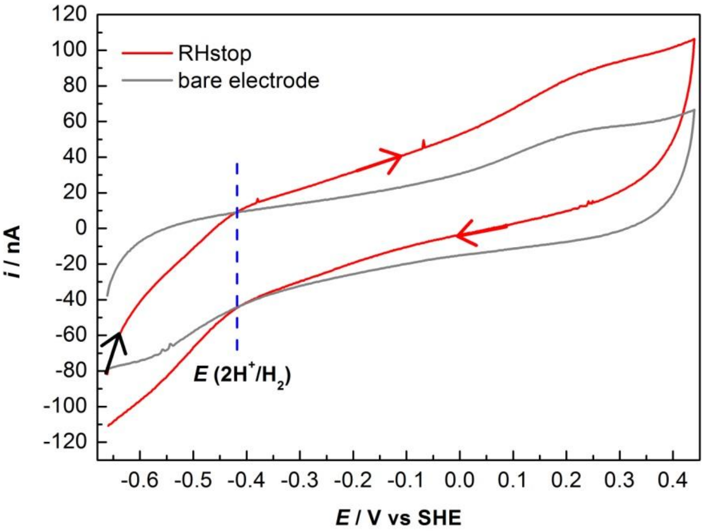

Figure 4-6. Cyclic voltammogram of RHstop (red) adsorbed on a stationary PGE electrode in pH 7 potassium phosphate buffer. Other conditions: 10 mV/s; 1 bar H_2 and 30 ^oC. The response of a bare electrode under analogous conditions is also shown by the grey line.

Affinity of the RHstop for H_2

The physiological role of the RH is sensing H_2 in the cell to regulate the gene expression of the SH and MBH.[146] Therefore, it is important and informative to investigate the affinity of the RHstop for H_2 and compare it with the other two hydrogenases under analogous conditions. Protein film electrochemistry is a useful and sensitive method to monitor the catalytic activity (current) as a function of potential and substrate or inhibitor concentration.[92] A chronoamperometry experiment was performed to investigate how H_2 oxidation activity (current) changes as a function of the concentration of H_2. The electrode was poised at +0.15 V throughout the experiment and the oxidation of H_2 was catalysed by the RHstop under this condition. In comparison to other NiFe hydrogenases, it is easier to measure the affinity for H_2 of the RHstop at H_2-oxidising potentials as there is no complexity caused by the oxidative anaerobic inactivation. In Figure 4-7, the initial concentration of H_2 is 100% with a flow rate of 1 L/min regulated by mass flow controllers (MFCs). According to Henry's law, this corresponds to 0.76 mM H_2 in solution corrected for this experimental condition. Then mixtures of N_2 and H_2 were introduced into the sealed electrochemical cell, in which H_2 partial pressure is regulated by MFCs as indicated in Figure 4-7. A high rotation rate, 3300 rpm, was set to accelerate the gas exchange between the headspace and the electrolyte throughout the experiment. At around 2800 s, the H_2 concentration goes to zero and the corresponding current for H_2 oxidation is also close to zero. In the end, 100% H_2 was switched back into the cell and the current for H_2 oxidation recovers, indicating that the enzyme film is still active after one hour's experiment. Compared to other hydrogenases, the catalytic activity for RHstop is extremely low, therefore it is important to be very careful when calculating the K_m for H_2. Two important factors need to be considered carefully in this case. One is the inevitable film loss and the other one is the background contribution from the electrode. Figure 4-8(A) shows the data after subtraction of the contribution from the electrode as in theory the current should be exactly zero when the concentration of H_2 is 0 µM. A black line shows a possible fit for film loss with an exponential decay function, extrapolated from data recorded at 100% H_2.[10] Figure 4-8(B) shows data further corrected for film loss. Therefore the current for H_2 oxidation at 1 bar at the beginning and at the end is the same.

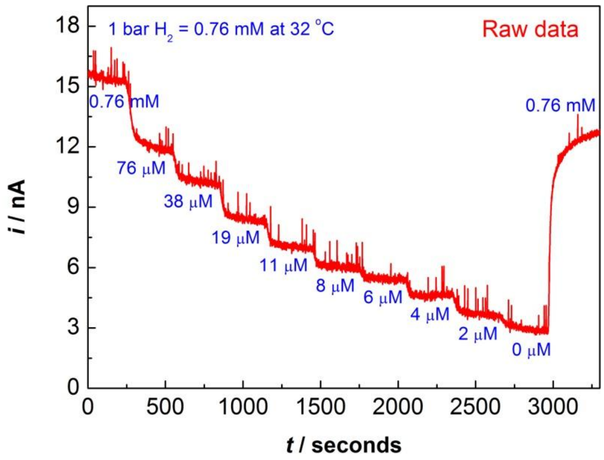

Figure 4-7. Chronoamperometry experiment to determine the K_m by monitoring how H_2 oxidation activity (current) changes as a function of the concentration of H_2. The electrode is held at +0.15 V. Other conditions: pH 6, 32 °C and 3300 rpm. The gas flushing through the headspace of the cell maintained an overall flow rate of 1L/min.

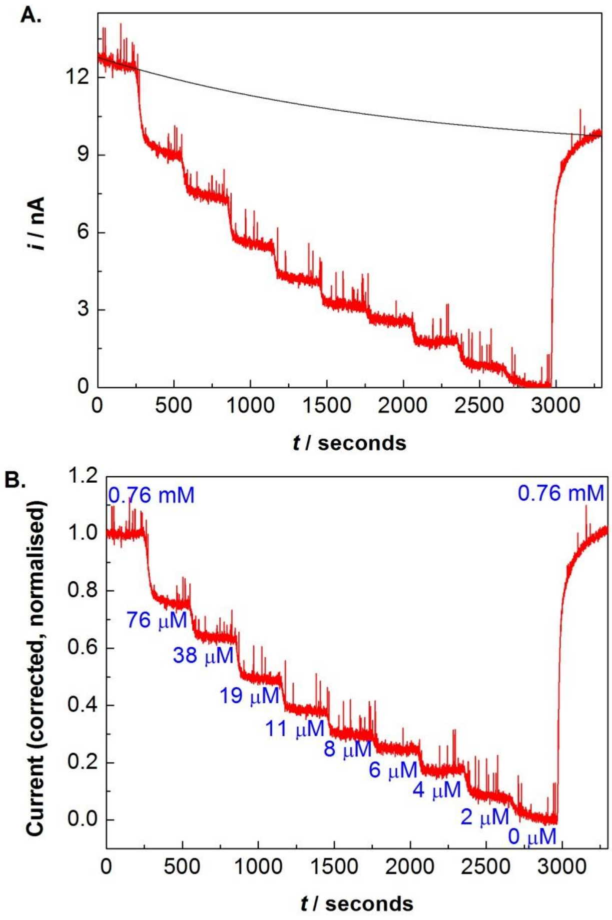

Figure 4-8. Panel A: Current (red) from Figure 4-7 corrected by removing the contribution from the electrode and an exponential decay (black) to fit the film loss. Panel B: Current corrected by removing the film loss and normalised to the initial current at 1 bar H_2.

Then, the Michaelis-Menten model is used to fit the corrected data and calculate the affinity of the RHstop for its substrate H_2. More details about this theory are described in Chapter 2. The Michaelis Menten equation is shown as eqn [4-1], where [S] is the concentration of the substrate, v and v_{max} represent the reaction rate and its maximum rate catalysed by the enzyme, respectively, and K_m is the concentration of the substrate when the rate of the enzyme catalysed reaction reaches half of its maximum rate. The reaction rate v or the turnover frequency of the enzyme relates directly to the catalytic current i, or in this case the corrected, normalised catalytic current i_{cn}. The corrected and normalised current is plotted as a function of the H_2 concentration, indicated by the black filled squares in Figure 4-9(A). Then a hyperbolic model function with the form $y = P_1 * x / (P_2 + x)$ is used to fit the data, as shown by the red line, where

P_1 and P_2 are constants equivalent to v_{max} and K_m, respectively. The corresponding R^2 value is 0.994 and P_2 is fitted to be 19.7 μM, indicating a value of 19.7 μM for K_m.

$$v = \frac{v_{max}\,[S]}{K_\mathrm{m} + [S]} \qquad [4\text{-}1]$$

The eqn [4-1] can be rewritten as below:

$$\frac{1}{v} = \frac{K_\mathrm{m} + [\mathrm{S}]}{v_{max}[\mathrm{S}]} = \frac{1}{v_{max}} + \frac{K_\mathrm{m}}{v_{max}}\frac{1}{[\mathrm{S}]} \qquad [4\text{-}2]$$

The data are also plotted in the form of a Lineweaver-Burk plot in Figure 4-9(B). It can be seen from the rearranged eqn [4-2] that a plot of $\frac{1}{v}$ vs. $\frac{1}{[\mathrm{S}]}$ should be linear with the horizontal axis intercept at $\frac{1}{[\mathrm{S}]} = -\frac{1}{K_\mathrm{m}}$. It fits well to a straight line (R^2=0.9986) with an intercept on the *x* axis, giving a value of 17.5 μM for K_m (H_2).

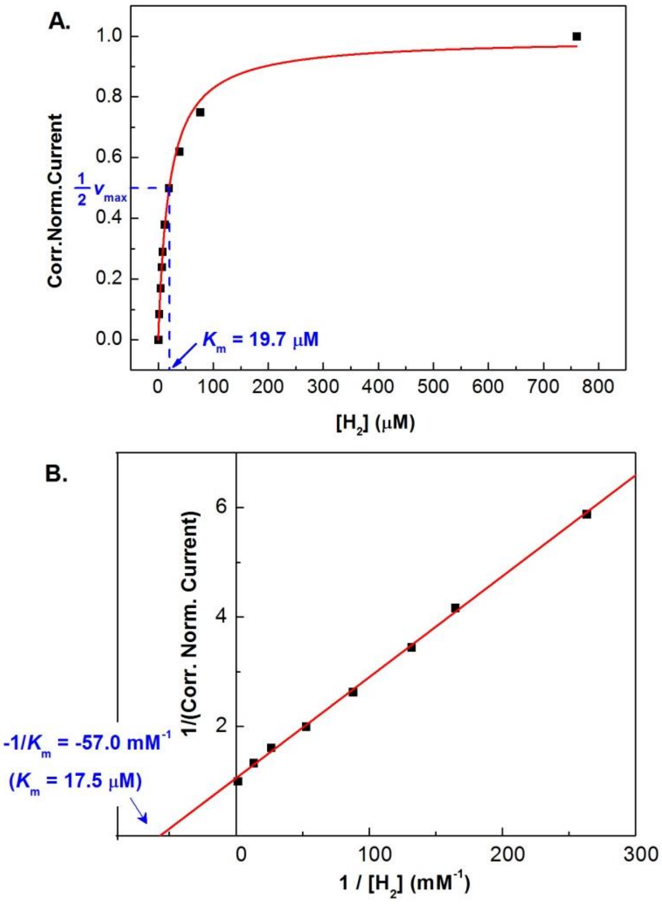

Figure 4-9. Application of *Michaelis Menten* equation in different forms to calculate the K_m of the RHstop for H_2. Panel A: i_{cn} vs. $[H_2]$. Panel B: Lineweaver–Burk plot 1 / i_{cn} vs. 1 / $[H_2]$.

Figure 4-7 shows data from just one experiment and this experiment was performed 10 times under exactly the same conditions, giving an average value of K_m for H_2 15.3 ± 3.4 μM (the second deviation) using Lineweaver-Burk plot. The error may be introduced by the film-to-film difference in stability of the enzyme on the PGE electrode and inaccuracy in the H_2 equilibrium at each step. A K_m value of 5 μM was obtained for the RHwt by Pierik *et al.* through measuring the hydrogen uptake (H_2 oxidation) activity with benzyl viologen (the midpoint potential is -0.374 V[248]) as electron acceptor in air-saturated solution.[148] The difference in K_m value (15.3 ± 3.4 μM and 5 μM) determined by these two different methods may be related to the driving force for H_2 oxidation provided by different redox partners (it is not possible to conduct electrochemical experiments at this potential -0.374 V because activity is too low) and specific type of the RH (RHstop in my work and RHwt in the enzyme assays).

Electrochemical K_m determination experiments were also performed at other potentials (-0.05 and +0.05 V) and no significant difference in the K_m value (15.5 μM at -0.05 V and 18.9 μM at +0.05 V) were observed, as shown in Figure 4-10. Therefore, the affinity for H_2 of the RHstop is not as sensitive to the potential as *R. eutropha* MBH.[249] In the MBH, the E_{switch} is around +0.115 V measured at 1 mV/s and pH 6. When its K_m (H_2) is measured at potentials below E_{switch}, it does not vary very much (8 μM at -0.158 V, 6 μM at -0.058 V and 14 μM at 0.042 V). However, in the region above E_{switch}, the K_m (H_2) increases significantly, i.e., 100 μM at +0.142 V and 130 μM at +0.242 V. Therefore, the potential independence in K_m (H_2) in the RHstop is probably related to the lack of oxidative anaerobic inactivation as demonstrated above.

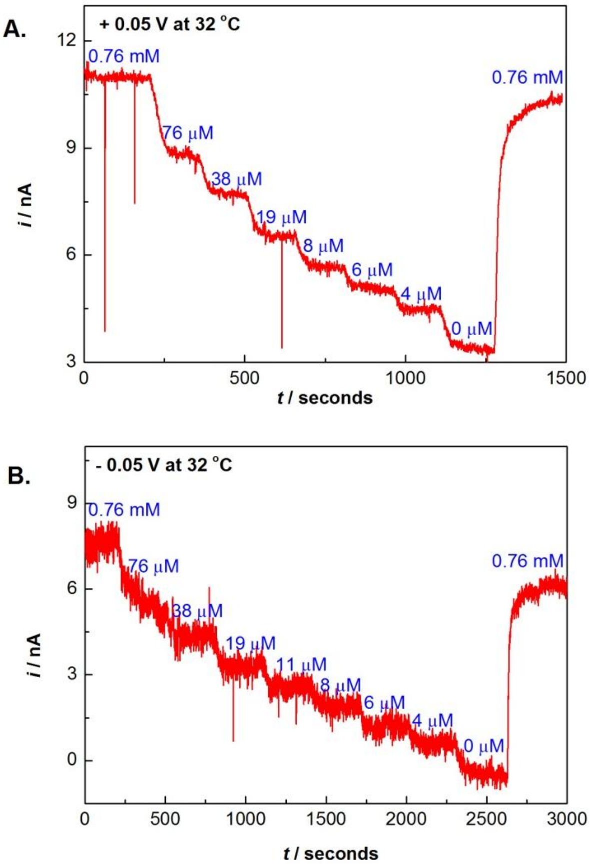

Figure 4-10. Electrochemical measurements of K_m for H_2 oxidation at different potentials. Panel A: The potential is held at +0.05 V. Panel B: The potential is held at -0.05 V. All the data shown here are raw data without correction for film loss and non-Faradaic current offset. Other conditions: pH 6, 32 °C and 3300 rpm. The H_2 concentration is indicated in each panel.

4.2.2 Reaction of the RHstop with CO?

CO inhibition in the region of H^+ reduction?

The RH has been classified as a CO-tolerant hydrogenase. The infrared results showed that adding 100% CO to either as-isolated RH or reduced RH did not generate a detectable CO-induced state.[148] As the CO molecule has a hard-sphere volume of 26.9 Å^3 similar to O_2 23.5 Å^3 (both are calculated from gas viscosities[250]), the idea of a restricted gas channel was also used to explain the CO tolerance in the RH.[31] However, as discussed in **Section 4.1.2**, it is not convincing that the O_2 or CO tolerance arises solely from the restricted gas access to the active site. The reaction with CO of the RHstop is therefore investigated to evaluate the gas channel argument.

A chronoamperometry experiment was designed to examine whether CO inhibits H^+ reduction and if so whether it has a greater effect than H_2 on H^+ reduction. The electrode was poised at -0.5 V and N_2 as an inert gas was initially introduced into the cell. The negative current in the Figure 4-11 (red) indicates H^+ reduction at this applied potential catalysed by the RHstop. At 200 s, H_2 was introduced to replace N_2 and the magnitude of the H^+ reduction current decreased due to product inhibition as discussed in the previous section. At 370 s, CO was introduced to replace H_2 and the magnitude of the current further dropped, demonstrating that CO is also inhibiting H^+ reduction and is a stronger inhibitor than H_2. At 500 s, H_2 was switched back to replace CO and the current immediately increased, indicating that CO is a reversible inhibitor. Another two gas exchanges at 650 s and 800 s, respectively, were performed to confirm the conclusions above. A control experiment on a bare electrode was performed to clarify the contribution from the electrode under analogous conditions, i.e., experienced the same gas exchanges, shown as a black line in Figure 4-11, indicating that gas exchange has no effect in the absence of the enzyme.

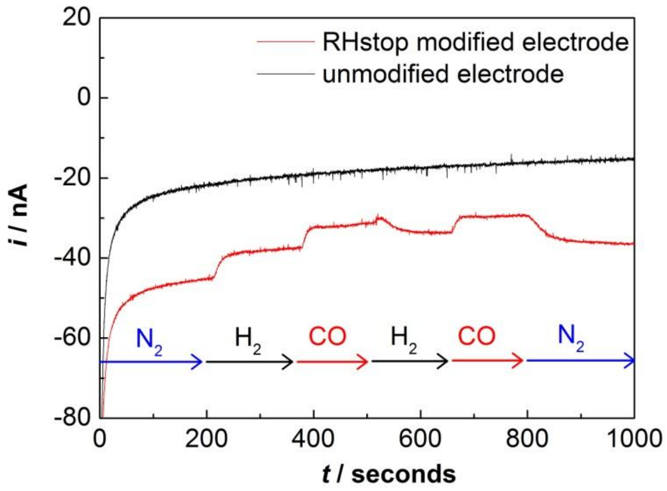

Figure 4-11. Experiments designed to examine inhibition of H^+ reduction by CO and H_2 in the RHstop (red). The gas flushing through the headspace of the cell was exchanged at the times indicated, maintaining an overall flow rate of 1L/min. Other conditions: 30 ℃, pH 6.0, electrode rotation rate: 4000 rpm, electrode potential: -0.5 V.

CO inhibition in the region of H_2 oxidation

Similarly, a chronoamperometry experiment was performed to examine whether CO inhibits the oxidation of H_2. As no oxidative anaerobic inactivation is found in the RHstop, there is no special requirement for the choice of the potential. To allow for a large driving force for H_2 oxidation, the electrode was poised at +0.15 V throughout the experiment. As shown in Figure 4-12, the gas flowed through the headspace firstly was composed of 10% H_2 and 90% N_2 and the rotation of the electrode was added to accelerate the equilibrium with the gas in the headspace. The positive current demonstrates that H_2 is oxidised by the RHstop even though the concentration of H_2 is low. At around 200 s, CO was introduced to replace N_2 while the concentration of H_2 was kept constant to rule out any drop of current arising from a variation of the H_2 level. The overall flow rate of gases was kept constant throughout the experiment. The current for H_2 oxidation immediately drops after replacing N_2 with CO, indicating that CO also inhibits the oxidation of H_2 in the RHstop. At 450 s, N_2 was switched back on to replace CO and the current increases immediately, demonstrating that CO is a reversible and rapid inhibitor for H_2 oxidation. In order to examine the contribution the electrode and the extent of CO inhibition, at 700 s 100% N_2 was introduced to remove all of the substrate H_2. The current drops sharply to a background current of 2 nA. This further demonstrates that even high concentration of CO only partially inhibits H_2 oxidation.

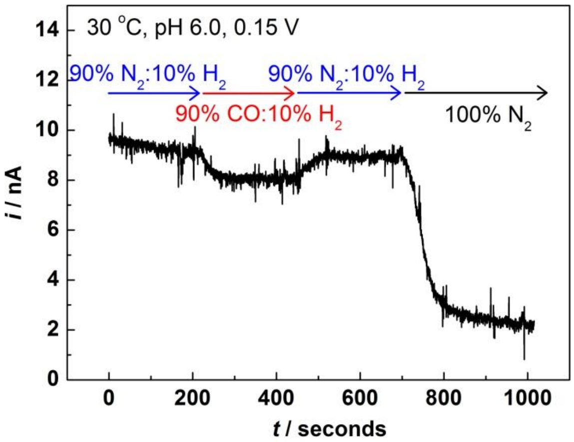

Figure 4-12. Experiments designed to examine inhibition of H_2 oxidation by CO. The headspace gas is exchanged as indicated. Other conditions: 30 ℃, pH 6.0, electrode rotation rate: 3000 rpm, electrode potential: 0.15 V.

As discussed above, previous studies by enzyme assays and spectroscopy did not show any evidence that CO inhibits the functioning of the RH.[148] However, CO inhibition for both H_2 oxidation and H^+ reduction are clearly demonstrated by protein film electrochemistry, suggesting that PFE is a more sensitive technique to study the reaction of hydrogenases with small inhibitor molecules. A more interesting question is raised as whether the RH also reacts with O_2 because CO is slightly bigger than O_2 and inhibits the enzyme activity for both H_2 oxidation and H^+ reduction.

4.2.3 Reaction of the RHstop with O_2?

A chronoamperometry experiment was designed to study the reaction of the RHstop with O_2. As shown in Figure 4-13, the electrode was firstly poised at +200 mV. It is very important to hold the electrode at such a high potential (+200 mV) to drive H_2 oxidation and ensure that oxygen cannot be reduced, as the enzyme activity is very low. Another experiment was performed (data not shown) by holding the potential at +100 mV and introducing O_2, but it was difficult to tell whether the drop in the current was arising from the inactivation of the enzyme or the reduction of O_2 at graphite because a control experiment on a bare electrode showed that at +100 mV a drop in the current on a similar scale was observed when O_2 was introduced. The gas flowing through the headspace was 98% H_2 : 2% N_2 and a positive current was observed due to H_2 oxidation. At around 370 s, the current for H_2 oxidation dropped sharply immediately after 2% O_2 was introduced to replace N_2, indicating that O_2 indeed inactivates the RH at high potential. At around 940 s, 2% N_2 was switched back on to replace O_2, as shown by a vertical dashed black line in Figure 4-13. The H_2 concentration was kept constant throughout the experiment to rule out the possibility that the drop in current was arising from a variation of the H_2 level. Then at 1080 s, a very short reductive poise at -400 mV for 1 s was applied to examine whether the enzyme can be reactivated. After the poise, the potential was stepped back to +200 mV and the current clearly increased, indicating that the reactivation of the RHstop occurs. A black dashed line in Figure 4-13 shows an exponential decay curve fitted for the film loss using the data before O_2 introduction and the current trace in the end when most the O_2 was removed. Two further longer reductive poises at 1210 s and 1510 s for 120 s and 300 s were applied to examine whether there is further reactivation. It is clear that there is further reactivation upon holding the potential at -400 mV for longer because the current at +200 mV is higher in each case after the reductive step. Two possible reasons could explain this. One is that there is still some trace O_2 inside the electrolyte after the first short reductive poise as 140 s (from 940 to 1080s) is not long enough under rotation to remove most of the O_2. The other explanation is that the reactivation rate is slow and needs time to fully recover from O_2 attack. One more experiment for giving more time to flush most of the O_2 should be performed to examining this further recovery is coming from the remaining O_2 in the cell or the slow reductive activation of the enzyme. Unfortunately, all the enzyme samples from that purification were used up.

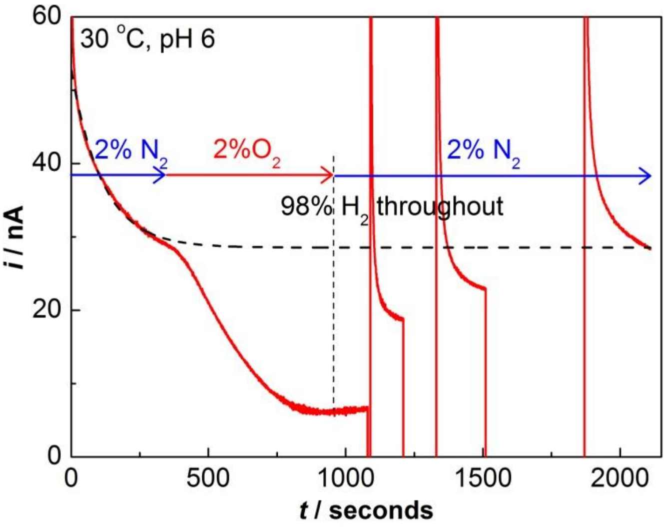

Figure 4-13. The reaction of the RHstop with O_2 and reductive reactivation under anaerobic conditions. Red line: the RHstop was held at 30 °C and +200 mV under 98% H_2 : 2% N_2 and at 370 s, the gas flow of the headspace was switched to 98% H_2 : 2% O_2. At 940 s the gas was exchanged to 98% H_2 : 2% N_2 and was kept at this composition for the remainder of the experiment. The potential was stepped to -400 mV at 1080 s for 1 s; at 1210 s for 120 s and at 1510 s for 300 s. Black dashed line: an exponential decay curve indicating the contribution from film loss was extrapolated based on the catalytic activity of the RHstop at +200 mV under anaerobic conditions. Other experimental conditions: the electrode was rotated at 2000 rpm throughout and the flow rate of the headgas was kept at 0.5 L/min.

Rate of inactivation with O_2

The O_2 introduction with the aid of mass flow controllers, as shown in Figure 4-13, occurs in the space of approximately 200 seconds due to the equilibrium time between the headspace and the solution, so it is not clear how quickly the RH reacts with O_2. Another experiment using a different method to introduce O_2 is performed to explore the reaction rate of the RH with O_2. As shown in Figure 4-14(A), at 340 s, 2% N_2 was replaced by 2% O_2 meanwhile an aliquot of O_2-saturated buffer (40 μL) was injected into the sealed cell (2 mL electrolyte in a typical experiment) to quickly set up the concentration of O_2 in the electrolyte. Notably, the activity for H_2 oxidation was inactivated in a slow manner after O_2 introduction. An exponential decay curve (blue) indicating the possible film loss is extrapolated based on the catalytic activity of the RHstop at +200 mV before O_2 introduction, as shown in Figure 4-14(A). Based on the fitted film loss, it can be seen that the activity for H_2 oxidation is relatively stable when O_2 is introduced. A semi-log plot of the current after O_2 injection as a function of time is shown in Figure 4-14(B). The first 30-second period is ignored as the level of O_2 is not accurately known due to the solution mixing phase. After this initial period, the semi-log plot is linear, consistent with a first-order dependence on the concentration of the enzyme given the constant O_2 concentration (2% O_2 at 1 bar corresponds to 28.6 μM in solution under this condition). A first order rate constant k obtained from the slope is 0.002 s^{-1}, indicating that the half-life of the reaction is around 5 minutes. The reaction rate is very low, only 1/10 of that for the SH under analogous conditions (Chapter 3).[147]

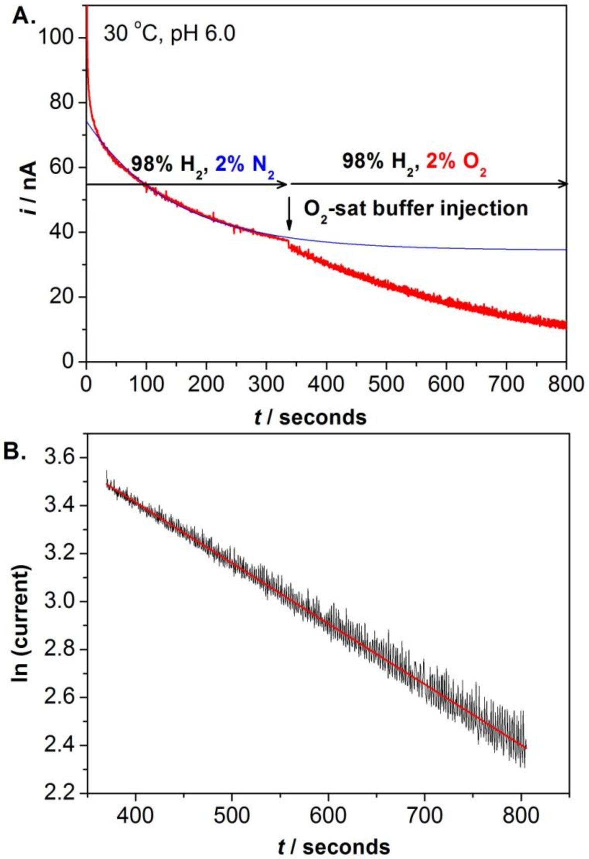

Figure 4-14. Experiments designed to explore the reaction rate of the RHstop with O_2. Panel A: Current-time trace of the reaction with O_2. The electrode is held at +200 mV and 98% H_2 was kept constant throughout the experiment. The gas flowing through the headspace is indicated as the arrows. At 340 s, 2% N_2 was replaced by 2% O_2 meanwhile 40 μL of O_2-saturated buffer was injected into 2 mL of the electrolyte. Panel B: The semi-log plot of the current as a function of time after O_2 introduction. The first 30 s after O_2 addition is ignored to allow thorough mixing. Other experiment conditions: the electrode was rotated at 2000 rpm throughout and the flow rate of the headspace gas was kept at 0.5 L/min.

4.3 Discussion

4.3.1 H_2 cycling in the *Re* cell

The microorganism *R. eutropha* can live on H_2 and O_2 as the sole energy source and the final electron acceptor respectively. This raises a question as to how the *R. eutropha* bacterium efficiently regulates the H_2 cycling which involves at least three distinct NiFe hydrogenases the membrane-bound hydrogenase (MBH), the soluble hydrogenase (SH) and the regulatory hydrogenase (RH), as this aerobic organism receives very limited H_2 compared to the sulphate-reducing anaerobic bacteria as shown in Figure 1-1.[55] As discussed in **Section 4.1.1**, the physiological role of the RH is sensing the level of H_2 in the cell and transmitting the signal to regulate the *hox* genes which code for expression of the SH and MBH. Therefore, the affinity for H_2 (K_m) of the RH is an important parameter for its functioning. Electrochemical experiments described in this Chapter were performed to measure the $K_m(H_2)$ at different potentials and a value of 15.3 ± 3.4 μM is obtained when the potential is held between -0.05 and +0.15 V. Cracknell *et al.* measured the $K_m(H_2)$ of the MBH under analogous conditions using protein film electrochemistry method and a value of 6.1 μM was obtained.[62] For the SH (Chapter 3), as it is not very stable on the electrode even at low temperature, experiments similar to those shown in Figure 4-7 and Figure 4-10 are not achievable. Keefe *et al.* used solution assays to measure the H_2 uptake activity by the SH with NAD^+ as the electron acceptor at different concentrations of H_2.[251] A trend of a high substrate affinity at low H_2 concentrations and a decrease in substrate affinity with increasing H_2 concentrations was observed for the SH, indicating that the substrate H_2 inhibits H_2 oxidation at high concentrations.[53,251] However, it is unlikely for the SH to experience high levels of H_2 in the cell. A value of 11 ± 0.9 μM was measured for the $K_m(H_2)$ of the SH.[251] Thus the $K_m(H_2)$ of the RH is the highest measured for the three hydrogenases from *R. eutropha*, meaning a lowest affinity for H_2. What does it imply? A hypothesis is made as below about a physiological role for the high $K_m(H_2)$ in the RH.

As shown in Figure 1-1, *Ralstonia eutropha*, an aerobic H_2-oxidiser, lives in the upperland of the sediments and receives H_2 in a limited manner. Therefore, the threshold value for H_2 uptake is as low as 0.35 nM in the aerobic H_2-oxidiser.[12] This distribution of H_2 raises the challenges for *R. eutropha* to efficiently utilise H_2. When the H_2 level in the biological cell is low, the number of the SH and MBH molecules is sufficient for oxidation of the available H_2. The RH under this condition will not sense H_2 due to a high $K_m(H_2)$, therefore the kinase exerts a negative effect on the hydrogenase gene regulation to limit the expression of new SH and MBH. On the other hand, when the H_2 level is high in the cell, more SH and MBH are needed to take advantage of the available H_2 as an energy source for further cell growth. Under this condition, the RH senses the H_2 and electrons are passed to HoxJ, thus the negative control is blocked. The down-regulation of *hox* gene expression will be released and more SH and MBH will be produced. Therefore, a low $K_m(H_2)$ for the RH (high affinity for H_2) would mean down-regulation in *R. eutropha* of the SH and MBH expression could be released too easily in response to availability of just a trace of H_2. This would mean a wasteful of resources in the cell. This may explain why the RH has a relatively high $K_m(H_2)$ compared to the SH and MBH.

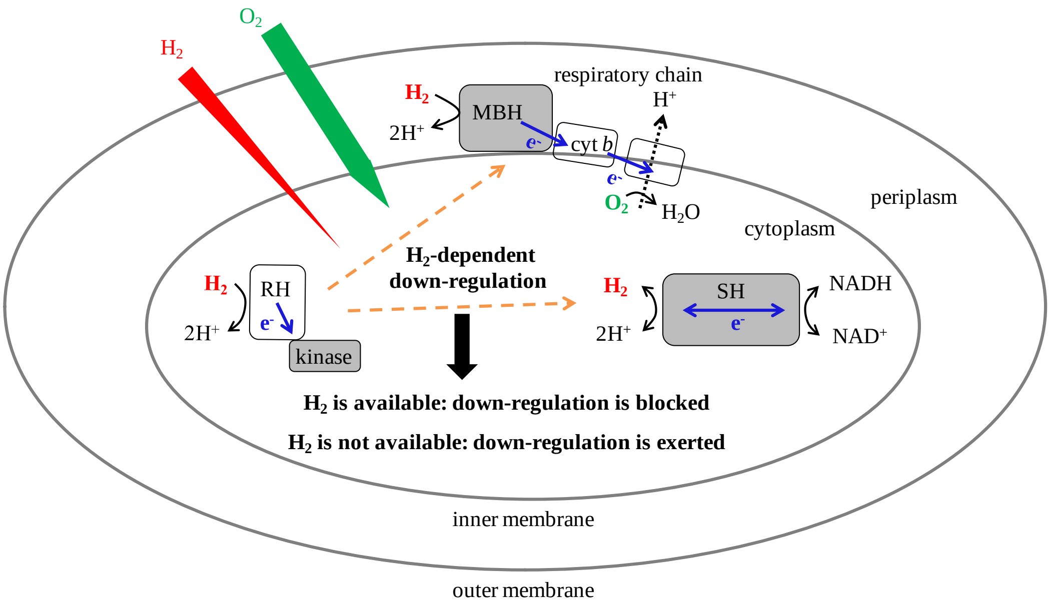

Figure 4-15. A schematic diagram showing the role of three NiFe hydrogenases (RH: regulatory hydrogenase, SH: soluble hydrogenase, MBH: membrane-bound hydrogenase) in one *Ralstonia eutropha* cell. The microorganism lives on H_2 and O_2, and Nature designs an efficient way for the cell to cycle H_2 as an energy source and utilise O_2 as the final electron acceptor.

The H_2 cycling by the MBH, SH and RH is schematically presented in Figure 4-15. The MBH is anchored to the periplasmic side of the inner membrane and composed of a small subunit HoxK and a large subunit HoxG. The physiological role of the MBH is to store energy as a transmembrane H^+ gradient through catalysing the periplasmic oxidation of H_2 coupled to cytoplasmic O_2 reduction involved in the respiratory chain.[62,82] The SH is located inside the cytoplasm and is composed of six subunits $HoxHYFUI_2$. It couples the oxidation of H_2 with the reduction of NAD^+ *in vivo*, providing the cell with energy in the form of NADH which is involved in many biological processes. When the NAD^+/NADH pool becomes very reduced, the SH can also catalyse H^+ reduction coupled with NADH oxidation, therefore it is termed as a bidirectional NiFe hydrogenase.[147,210] The RH as discussed above, is sensing the H_2 level in the cell, rather than being involved in H_2-related energy cycling.

4.3.2 The O_2 tolerance of *Re* RH

The RH has been classified as an O_2-tolerant NiFe hydrogenase based on the fact that it retains the H_2 oxidation activity in the presence of O_2. No oxygen-induced inactive species have been observed by FTIR or EPR, i.e., the standard Ni-A and Ni-B states have never been observed in the RH. Although it is purified in air, it seems to be always active for H_2 oxidation. However, protein film electrochemistry experiments in this Chapter demonstrate that O_2 can actually inactivate the enzyme at high potentials but at a very slow rate, and another inhibitor CO can also reversibly inhibit the enzyme in the region of either H_2 oxidation or H^+ reduction. Previously, it was suggested that the unusual bulky amino acid residues located at the end of the putative gas channel (I62 and F110) greatly limit the gas access to the active site and therefore make the RH tolerant to O_2 and CO.[141] The site-directed variants (I62V, F110L and I62V/F110L) were designed to widen the gas channel by replacing the bulky residue isoleucine (I) and phenylalanine (F) with relatively small valine (V) and leucine (L), respectively, and it was found that the activity of either the single variant or the double variant was sensitive to O_2. However, according to this strategy, reverse variants were performed in the O_2-tolerant MBH in which the conserved amino acid residues (V77 and L125) are located near the end of the putative gas channel, in an attempt to make the enzyme more O_2-tolerant. The double variant (V77I/L125F) exhibits a 100-fold increase in $K_m(H_2)$. However, the apparent O_2-inhibition constant decreased from 1000 to 260 μM, indicating the variant is more O_2-sensitive instead of being more tolerant to O_2.[62] The same strategy was also applied to the O_2-sensitive NiFe hydrogenase from *D. fructosovorans*. It was found that $K_m(H_2)$ increased and the inhibition rate by CO decreased in the double variant (V74I/L122F), consistent with a limited gas access to the active site.[68] However, the variant does not show any improvement in O_2 tolerance.[132] Even worse, the overall O_2 reaction rate in the variant V74I/L122F is higher than that in the wild type, implying the 'limited' gas access is not the limiting step.[132] Interestingly, variants with methionine (M) to replace V74 and L122 were constructed in the *D. fructosovorans* NiFe hydrogenase and the variants (V74M and V74M/L122M) were found to be transformed to be O_2-tolerant, i.e. active in the presence of O_2. The double variant (V74M/L122M) after exposure to O_2 can even be simultaneously reactivated under very oxidising conditions (+190 mV). The observation of Ni-A and Ni-B in the variant by EPR demonstrated that the replacement of methionine amino acid at the end of the gas channel did not change the catalytic cycle. However, the methionine may interact with the active site due to its location and help the O_2-inactive enzyme to recover at a rapid speed.[132] Dementin *et al.* suggested that the presence of methionine may form weak S-O bonds due to the affinity of the sulphur atom for oxygen and this S-O network may provide the enzyme with extra force to remove the bridging oxygen species (hydroxide in Ni-B and peroxide in Ni-A) from the active site.[132] A recent report shows a variant (V74C) at the same position in *D. fructosovorans* NiFe hydrogenase which was constructed and proved to be an O_2-tolerant NiFe hydrogenase.[133] Notably, the size of the cysteine (C) is similar to that of the valine (V). The common feature in cysteine and methionine is that both amino acid residues have a sulphur (S) atom in the side chain. Further kinetic experiments using protein film electrochemistry demonstrated that the diffusion process in V74M and V74M/L122M is blocked to different extents. The double variant V74M/L122M should have a narrower bottleneck of the putative gas channel but the diffusion rate of CO is not affected more than in the single variant V74M. The latter (V74M) decreases the diffusion rate so much that the overall O_2 reaction rate is limited by the O_2 accessibility rather than the inactivation rate at the active site. Therefore, along with the findings in the variants of the MBH and *D. fructosovorans* NiFe hydrogenase, the role of gas channels in the O_2 tolerance of NiFe hydrogenases is in doubt. In this study of RH, it has been demonstrated that CO rapidly and reversibly inhibits the enzyme during catalysis in either direction. As CO has a similar Van der Waals volume to O_2 and thus can be used as a probe to measure the diffusion of O_2 from the protein surface to the buried active site, the O_2 tolerance in the RH cannot be explained by limited gas access. Due to the rapid binding of CO presumably with the active site, it can be concluded that the overall reaction of the RH with O_2 is not limited by the gas diffusion.

It was found by protein film electrochemistry that the O_2 inactivation rate (0.002 s^{-1} at 30 ^oC, +200 mV and pH 6 with 28.6 μM O_2) is extremely small compared to other NiFe hydrogenases under analogous conditions. The reaction rate of the SH with O_2 under analogous conditions (pH 7, 30 ^oC, +216 mV and 28.6 μM O_2) is 0.02 s^{-1} which is ten times that in the RH. For the MBH, the rate of O_2 reaction (25% O_2, at 30 ^oC, +197 mV and pH 5.5) is 0.31 s^{-1}.[10] Therefore, in comparison with the SH and MBH, the rate of O_2 reaction in the RH is the slowest and 0.002 s^{-1} means the half-life of the enzyme in the presence of O_2 is around 300 s. Further comparisons are also made with the O_2-sensitive *D. fructosovorans* NiFe hydrogenase. The wild-type is measured to have an inactivation rate of 0.915 s^{-1} at 40 ^oC with 28.6 μM O_2. For the O_2-tolerant variants V74M/L122 M and V74M, the reaction rate is 0.858 s^{-1} and 0.186 s^{-1}, respectively. For the most impaired gas access variant V74Q, the reaction rate is around 0.114 s^{-1}.[69] Therefore, compared to other O_2-tolerant or O_2-sensitive or limited gas accessed NiFe hydrogenases, the reaction of the RH with O_2 is the slowest. The preliminary electrochemistry experiment further demonstrate that the recovery of the O_2-inactivated RH is complete within tens of seconds, much quicker than the inactivation by O_2. The extremly low inactivation rate and relatively high reactivation rate may actually be the reason for the RH to remain active in air, rather than the limited gas access.

4.3.3 Work towards developing an infrared spectroelectrochemistry technique to investigate the O_2-induced inactive state of *Re* RH

As discussed in **Section 4.1.3**, only two physiologically relevant states Ni_a-S and Ni-C in the RH are observed by FTIR whereas only Ni-C is detected by EPR. The oxygen-induced Ni-A and Ni-B are not observed in the RH. However, we cannot exclude the possibility that such oxidised species are formed at certain potentials but are too short-lived to be detected. Protein film electrochemistry has been proved to be a sensitive tool for studying the reaction of the enzyme with small molecules, such as H_2, CO, O_2, H_2S and formaldehyde.[55,78,79,82] In this study, the O_2-inactivated states of the RH in the presence of H_2 at high potentials (+200 mV) and CO-inhibited states of the RH have been observed by protein film electrochemistry. As discussed above, the O_2-inactivated state may be a transiently-lived species as it is formed at an extremely slow rate and can be reactivated within tens of seconds. This may be the reason why it is not observed by solution FTIR experiments in which a transmission cell is used and a mediator cocktail is added to regulate the redox level, since the electrochemical control is indirect and the electron transfer to and from the enzyme is not efficient.[148] On the other hand, in protein film electrochemistry, the enzyme is adsorbed on the surface of the graphite electrode and the direct potential control is efficient, thus the O_2/CO-induced species are observed. Furthermore, electrochemical results in this Chapter suggest that special conditions are required to generate this O_2-inactivated state, i.e., at high potential in the presence of H_2, as the as-isolated RH seems to be fully catalytically active. Therefore, the next chapters (Chapter 5 and 6) describe developments towards a new infrared spectroelectrochemistry technique combining protein film electrochemistry and infrared spectroscopy to aid characterisation of these O_2/CO-induced inactive species in the RH. The development of this technique and some preliminary infrared investigations on the RH will be discussed in Chapter 5 and Chapter 6, respectively.[252]

Chapter 5

In-situ Infrared Spectroelectrochemical Investigation of Formic Acid Oxidation Catalysed by Carbon Supported Pt/Pd/PtRu Nanoparticles

The ultimate goal for developing this *in-situ* infrared spectroelectrochemical method is to investigate redox proteins adsorbed on carbon particles. In this Chapter, formic acid (HCOOH) oxidation catalysed by carbon-supported Pt, Pd and PtRu nanoparticles is investigated to develop the cell and method. Formic acid oxidation has two main advantages as an initial test of this spectroelectrochemical method. Firstly, the electrochemistry of this system is well documented and the composite particle including the catalyst and carbon support can be purchased and thus is readily available. Secondly, the catalyst nanoparticles are adsorbed on the surface of the carbon particle, resembling enzyme adsorbed on the surface of the carbon particle, so this is a real test of the ability of the cell to allow spectroscopic observation of surface species.

5.1 Formic acid oxidation and relevant infrared spectroelectrochemistry techniques

5.1.1 Electrocatalysis in proton exchange membrane fuel cells

In low temperature proton exchange membrane fuel cells (PEMFCs), the anode and cathode catalyst typically use platinum-based materials as catalysts.[253,254] The fuel - small molecules such as dihydrogen (H_2),[255] methanol (CH_3OH)[162] and formic acid (HCOOH)[256] - is introduced into the anode where it is oxidised,[257] generating protons (H^+) and electrons (e^-). The protons travel to the cathode through a proton-conducting polymer (Nafion) membrane, whereas the electrons go through a wire to reach the cathode. At the cathode, O_2 is reduced.[258] Therefore, the chemical energy from the fuel is directly converted into electricity.[259] The electrocatalysis processes in PEMFCs using different fuels are summarised in Table 8.

Table 8. Reactions at anode and cathode in PEMFCs using different fuels.

	Chemicals	Reactions
Anode	H_2	$H_2 \rightarrow 2H^+ + 2e^-$
Anode	HCOOH	$HCOOH \rightarrow CO_2 + 2H^+ + 2e^-$
Anode	CH_3OH	$CH_3OH + H_2O \rightarrow CO_2 + 6H^+ + 6e^-$
Cathode	O_2	$O_2 + 4H^+ + 4e^- \rightarrow 2H_2O$

Since Pt is a precious metal, and there are only limited amounts on the Earth, different ways are found to use the noble metal efficiently, such as bottom-up preparations of nanoparticle,[260] and highly dispersed nanoparticles supported by carbon with high surface area[261]. In real fuel cells, the Pt-based catalysts are used in the form of nanoparticles (typically less than 100 nm diameter) adsorbed on a carbon support.[262-267] The catalyst in its nano-form means a much larger surface area to volume ratio than in the macroscopic form.[268,269] Furthermore, the surface structure of nanoparticles is very different from a flat metal surface as the population of the defect sites in nanoparticles, such as terraces and steps, is much different. The species adsorbed on the surface of nanoparticles should be the same, but their relative numbers will be different from the flat surface.[270]

A major problem with the use of Pt is the presence of carbon monoxide as a poisoning adsorbate. When dihydrogen is produced by steam reforming of methanol or hydrocarbons, CO is always formed as a by-product. Carbon monoxide is also formed as a poisoning intermediate during CH_3OH or HCOOH oxidation. In order to make more CO-tolerant catalysts, a second metal is usually added, and the most studied bimetal model catalyst is PtRu as the presence of Ru is found to enable formation of a surface oxygen species at a significantly lower potential than on pure Pt which favours the oxidising-off of CO.[262,271-273]

5.1.2 Chemistry of HCOOH oxidation and mechanism

Formic acid oxidation catalysed by Pt or Pd is considered as a model system in electrocatalysis.[256,274,275] In contrast to methanol oxidation which is a complex six-electron process (Table 8) and involves the breaking of three C-H bonds,[162] formic acid oxidation only involves two electrons and one C-H cleavage.[274]

The cyclic voltammogram of formic acid oxidation shows five current peaks, and has been studied extensively.[276,277] Figure 5-1 shows a voltammogram performed on a Pt@C/Nafion (Pt nanoparticles adsorbed at carbon black particles and mixed with Nafion, more details in Chapter 2) modified rotating glassy carbon electrode in the standard electrochemistry cell. On the sweep towards more positive potentials, there are three peaks: Peak I at *ca.* 0.5 V, Peak II at *ca.* 0.9 V and Peak III at over 1.6 V. On the reverse scan, two peaks occur, at *ca.* 0.65 V (Peak IV) and *ca.* 0.4 V (Peak V), present as a small shoulder.

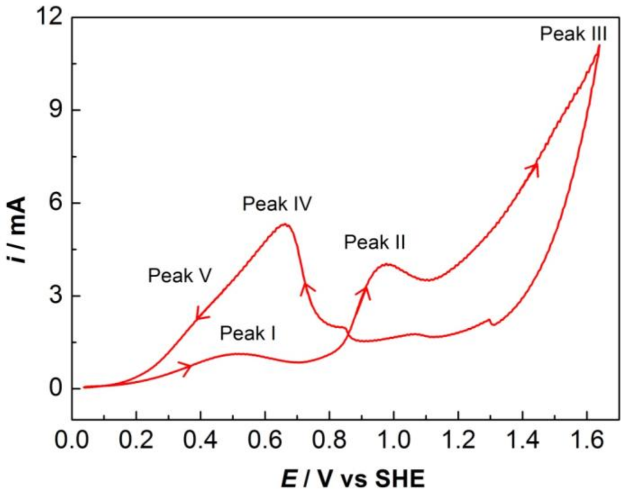

Figure 5-1. Cyclic voltammetry of HCOOH oxidation on Pt@C /Nafion modified rotating glassy carbon electrode. Rotation of 2000 rpm was added to provide sufficient substrate. The scan rate is 10 mV/s.

The origin of these five peaks was discussed by Okamoto *et al.*[277] Peak I is related to the direct pathway for the formic acid oxidation, shown as eqns [5-1] and [5-2]:

$$\mathrm{HCOOH} + \mathrm{Pt} \rightarrow \mathrm{HCOO{\sim}Pt} + \mathrm{H^+} + \mathrm{e^-} \qquad [5\text{-}1]$$

$$\mathrm{HCOO{\sim}Pt} \rightarrow \mathrm{CO_2} + \mathrm{H^+} + \mathrm{e^-} + \mathrm{Pt} \qquad [5\text{-}2]$$

As the poisoning intermediate, adsorbed CO,[252] gradually builds up and occupies the active sites of Pt, the catalytic current for the oxidation of formic acid is suppressed, shown as eqn [5-3]:

$$\mathrm{HCOOH} + \mathrm{Pt} \rightarrow \mathrm{CO{\sim}Pt} + \mathrm{H_2O} \qquad [5\text{-}3]$$

Peak II is related to oxidation of the poisoning CO, as described in eqn [5-4] and it is known as the indirect pathway.

$$\mathrm{CO{\sim}Pt} + \mathrm{H_2O{\sim}Pt} \rightarrow \mathrm{CO_2} + 2\mathrm{H^+} + 2\mathrm{e^-} + 2\mathrm{Pt} \qquad [5\text{-}4]$$

As the active sites of Pt are released, the oxidation of formic acid through the direct pathway as shown in eqns [5-1] and [5-2] begins to function again. However, as the potential is swept to higher values, the formation of Pt oxides or hydroxides as shown in eqns [5-5] and [5-6] causes further inactivation of the surface.

$$\mathrm{H_2O} + \mathrm{Pt} \rightarrow \mathrm{OH{\sim}Pt} + \mathrm{H^+} + \mathrm{e^-} \qquad [5\text{-}5]$$

$$\mathrm{H_2O} + \mathrm{Pt} \rightarrow \mathrm{O{\sim}Pt} + 2\mathrm{H^+} + 2\mathrm{e^-} \qquad [5\text{-}6]$$

At very high positive potentials, the energy provided is sufficiently high to allow for oxidation of formic acid on the oxidised surface. This is used to explain Peak III. It should be noted that oxidation of water also happens near this high potential.

On the reverse scan, the oxidised Pt surface is reductively reactivated and more formic acid should be oxidised on the surface of active Pt, giving rise to the sharp Peak IV. As the oxidative driving force drops, the poisoning CO occupies the active site again. The origin of Peak V is still unclear. Possible explanations include the reorganisation of the surface, or disruption of an unknown poisoning intermediate.[278]

A widely accepted dual-path mechanism for HCOOH oxidation was suggested by Capon and Parsons,[276,279-281], as shown in Figure 5-2. The direct pathway, which is also called the dehydrogenation pathway is believed to proceed via an active intermediate or intermediates at a lower potential and Osawa *et al.* later proposed that the active intermediate is the formate anion,[187] although this is still under debate.[282] It is widely accepted that adsorbed CO is identified as a poisoning intermediate during HCOOH oxidation, determined by infrared spectroscopy.[280] An indirect pathway involves formation of this intermediate CO and further oxidation of CO at a higher potential than that in the direct pathway, as described above.[252,283-286] The adsorbed CO may have different binding modes: terminal, bridging and multi-bonded form, as shown in Figure 5-2.[287]

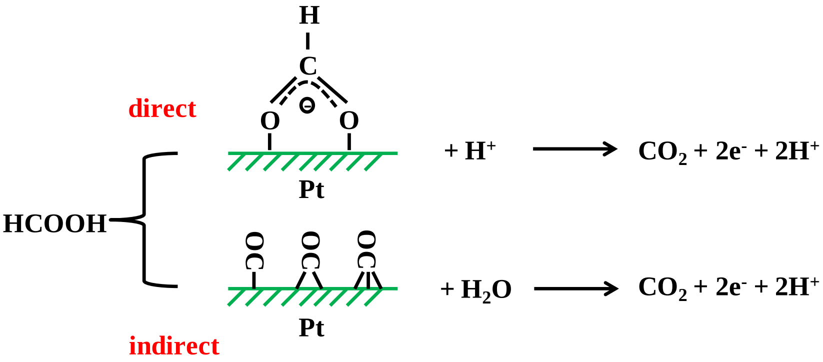

Figure 5-2. The dual-path mechanism for formic acid oxidation, as suggested by Capon and Parsons.[276,279-281]

5.1.3 Relevant infrared spectroelectrochemical techniques for studying HCOOH oxidation

Electrochemical methods provide kinetic and thermodynamic information about heterogeneous redox processes, as discussed in Chapter 1 and 2. Electrochemistry alone, however, does not provide detailed information about or allow identification of species adsorbed on the surface of the catalyst. *In-situ* spectroscopy has therefore been used in combination with electrochemistry to gain chemical insight into the reaction of interest.[187,252,288] Infrared spectroscopy is a valuable technique which provides specific information about functional groups within a molecule and thus can be used to identify changes involved in the catalytic cycle. The two most widely used *in-situ* infrared spectroelectrochemical techniques, infrared reflection-absorption spectroscopy and surface enhanced infrared absorption spectroscopy, are discussed below. Table 9 summarises the vibrational modes of species that might be involved in formic acid oxidation, including the electrolyte.

Table 9. Vibrational modes of species involved in HCOOH oxidation.

Molecules	Vibrational mode	Wavenumber (cm^{-1})	Refs
CO	Linear	2100 ~ 2000	287
	Bridge	1900 ~ 1850	
	Multi	1840 ~ 1710	
$HCOO^-$	COO symmetric	1351 ~ 1325	187,188
	COO asymmetric	1585	
HCOOH	C=O stretch	1730 ~ 1700	289,290
	C-H wagging	1385	
	C-O stretch	1320 ~ 1210	
H_2SO_4	SO_4 symmetric stretch	983	188
	O-S-O bend	450	
	SO_4 asymmetric stretch	1105	
	O-S-O bend	611	
$HClO_4$	ClO_4 symmetric stretch	928	188
	O-Cl-O bend	459	
	ClO_4 asymmetric stretch	1119	
	O-Cl-O bend	625	
CO_2	OCO asymmetric stretch	2350	188
H_2O	OH stretch	3500 ~ 3000	287
	HOH scissors	1650	
	Combination	2250 ~ 1950	
Nafion	CF asymmetric stretch	1211	291
	CF symmetric stretch	1153	
	SO asymmetric stretch	1350 ~ 1250	
	SO symmetric stretch	1060	

Infrared reflection-absorption spectroscopy

Infrared reflection-absorption spectroscopy (IRAS, also referred to as IRRAS, RAIRS) at an electrode surface offers structural information about species adsorbed at the electrode and also solution species close to the electrode.[252,288] Compared to the solid/gas interface, the electrode/electrolyte interface is relatively complex consisting of solvent molecules, ions and dipolar species whose orientation near the electrode surface is dependent on the applied potential. The optical configuration of an IRAS experiment is shown in Figure 5-3(A). Since the IR beam passes twice through the electrolyte to reach and leave the electrode surface, the path-length through 'bulk' solution is greater than that from the interface. This is particularly problematic when the solvent is water which exhibits strong absorption bands in the mid-IR region (See Table 9). Spectroscopically therefore, a very thin layer (typically between 1 to 10 μm) is needed and is formed by pressing the working electrode against a window (usually CaF_2) to make the path length of the IR beam through the electrolyte as short as possible. However, this causes serious electrochemical problems: substrate supply and product removal are not efficient and the thin layer itself will cause a high electrolyte resistance and hence the cell will have a relatively slow time response. Therefore, the electrochemical potential drifts due to slow diffusion and the applied potential is not accurate due to the large resistance of the electrolyte.

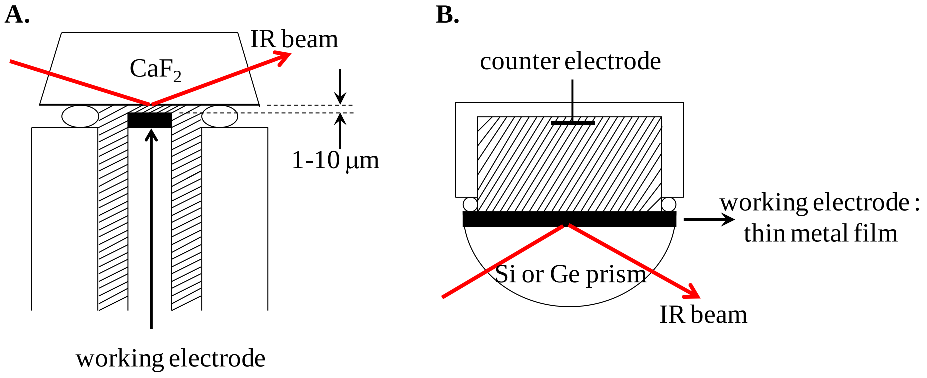

Figure 5-3. *In-situ* monitoring of an electrochemical interface by (A) IRAS and (B) ATR-SEIRAS. Figure adapted from ref[292].

Surface-enhanced infrared absorption spectroscopy

The electrochemical problems associated with IRAS can be solved by the use of an attenuated-total-reflectance (ATR) configuration, as shown in Figure 5-3 (B). The ATR sampling geometry overcomes the lack of substrate supply and enables more precise electrochemical control as there is no requirement for a thin layer cell. The requirement for the prism is that it needs to be infrared transparent and have a high refractive index, such as Si and Ge. The IR beam is totally internally reflected at the prism/electrolyte interface, and an evanescent wave penetrates the sample with an exponential decay. The penetration depth is of the order of the wavelength, i.e., a few micrometers in the IR. In contrast to the external reflection mode in Figure 5-3 (A) which severely suffers from the interference from the bulk solution, this ATR mode has a better sensitivity to interfacial species due to the shorter effective path length through the bulk electrolyte. A thin metal film (around 100 nm) which is rough on the nanoscale is coated on the top surface of the prism and used as the working electrode. In addition to the advantages of effective beam path length and precise electrochemistry control, a surface-enhancement effect is found on such surfaces, providing more intense signals of the species adsorbed on the metal. The detailed mechanism of the surface enhancement is still controversial, and at least two mechanisms, the electromagnetic and chemical mechanisms are generally accepted.[293-296] There is a very strict requirement for making the thin metal film due to the limited penetration depth within the sample. Vacuum evaporation, electroless plating and electrochemical deposition are mainly used.[187,293,297] These requirements make it difficult to study either a bimetallic metal system or nanoparticle catalysts with controlled compositions and sizes by this ATR-SEIRAS (surface-enhanced infrared absorption spectroscopy) technique.

In summary, the ATR-SEIRAS method is not suitable for studying the nanoparticle and multi-metal system. The IRAS on the other hand can be applied to study the nanoparticles with different compositions, morphologies and sizes. However, the problems due to the huge absorption by the solution and lack of solute access are hurdles for further understanding the mechanism and the kinetics of the reaction catalysed by the metal nanoparticles.[298-303] Therefore, the current *in-situ* infrared spectroelectrochemistry techniques are not suitable for studying the nanoparticles. A new *in-situ* infrared spectroelectrochemical cell is required to investigate the carbon-supported metal nanoparticles.

5.1.4 The goal of this Chapter

A new *in-situ* infrared spectroelectrochemical cell combining good electrochemical properties attainable using an ATR geometry with the capability to study carbon-supported species under direct potential control has been developed. Formic acid oxidation catalysed by carbon-supported Pt/Pd/PtRu is used as a proof of concept to analyse the performance of this attenuated total reflectance infrared spectroelectrochemical (ATR-IR SEC) cell. This test system will demonstrate the infrared detection of the species formed during HCOOH oxidation under direct electrochemical control. This will provide proof of concept spectra for a method suitable for extension to investigation of the metalloenzyme (the size of the protein is also in nanometer scale) adsorbed on carbon particles in the later work.

5.2 Cell Development

5.2.1 Acid tolerant cell body

Initial designs for the ATR cell were adapted from an ATR-IR liquid cell designed by Dr. Robert Jacobs (Oxford). The cell body was originally made of Delrin (a polyoxymethylene plastic structure), as shown in Figure 5-4(A). However, it is quickly degraded through acid hydrolysis of the polymer chains and therefore is not suitable for use under acidic conditions.[304] In the formic acid oxidation experiments, low concentrations of H_2SO_4 were used as supporting electrolyte and HCOOH itself is corrosive. Therefore, an acid-tolerant cell was needed. To solve this problem, PEEK (Polyether Ether Ketone) was used instead of Delrin because it is very robust in terms of excellent mechanical and chemical resistance properties, and is found to be formic-acid tolerant as shown in Figure 5-4(B).

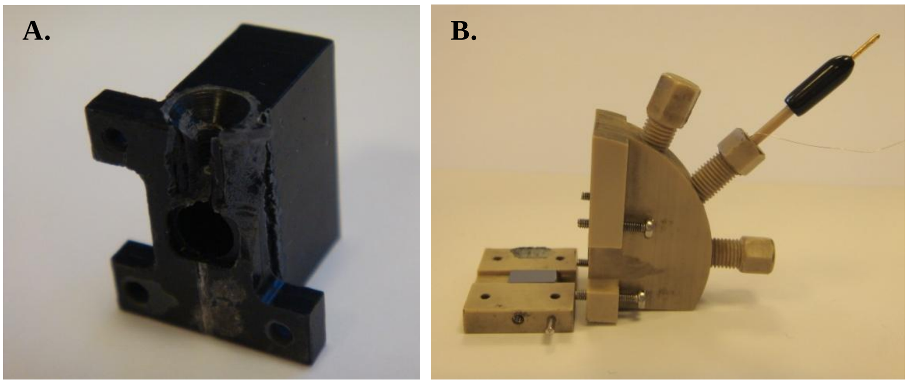

Figure 5-4. Panel A: an ATR-SEC cell made of Delrin showing damage by exposure to formic acid; Panel B: an ATR-SEC cell made of PEEK, complete with screw fittings for the electrodes.

5.2.2 Introduction of mini reference electrode and counter electrode

Standard-sized reference electrodes cannot be used due to the small volume of our ATR-SEC cell, and therefore a mini reference electrode was required in order to set up a three-electrode system. Initially, a simple silver wire as shown in Figure 5-5(A) was used to act as a pseudo-reference electrode as it could easily be fitted into the small cell. However, the disadvantage of the silver wire is that it cannot provide precise potential control over the working electrode and the measured potential varied between experiments, preventing easy comparison of results. Therefore the silver wire is a poor reference electrode. Later on, two designs of mini Ag/AgCl reference electrodes were used as shown in Figure 5-5(B) and (C). They are essentially the same except that the brown one in Figure 5-5(C) is believed to have smaller pores in the frit and it is therefore ‘leak-free’ and can be stored without any electrolyte. All the work in this Chapter were carried out using the brown ‘leak-free’ reference electrode which is also made from PEEK and therefore resistant to formic acid. After adaptation of the mini Ag/AgCl reference electrode, precise electrochemical control is successfully achieved. A thin Pt wire was used as the counter electrode and wrapped around the mini reference electrode to be put into the cell, as described in Chapter 2.

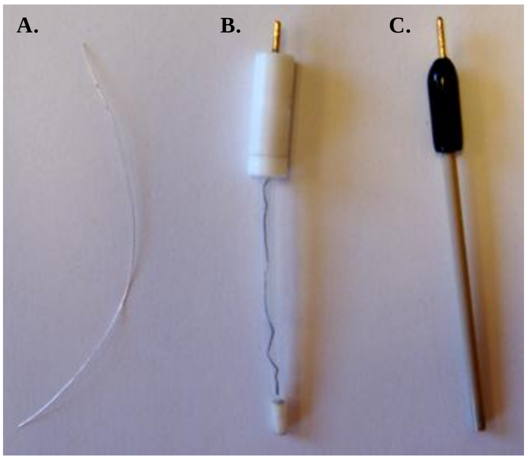

Figure 5-5. The reference electrodes used in the ATR-SEC cell. Panel A: A silver wire was used as the reference electrode during initial experiments; Panel B: The white Ag/AgCl reference electrode to get more precise electrochemical control is used under benign conditions; Panel C: A mini 'leak-free' Ag/AgCl PEEK reference electrode can be used under harsher experimental condition.

5.2.3 The set up of the ATR-IR SEC cell

The orientation of the prism along with the ATR-SEC cell is vertical rather than horizontal when in operation as shown in Figure 5-6(A). Three threaded holes were drilled to allow flow of substrate/electrolyte and positioning of the electrodes. In order to get a continuous flow and ensure efficient electrolyte exchange, the bottom hole was used to flow in the electrolyte and the top hole was used for the flow out as shown in Figure 5-6(C). The middle hole was for fitting the mini reference electrode wrapped with the Pt wire counter electrode. Each hole was fitted with an *o*-ring seal to ensure leak-free flow of the electrolyte.

Figure 5-6(B) shows an enlargement of the working electrode (WE) in the ATR-IR SEC cell and its position with respect to the prism. The working electrode is built up from multiple components. A film of carbon-supported metal nanoparticle catalyst is drop-cast onto a Si prism. However, the lateral conductivity of this particle network electrode is poor and so a piece of carbon paper is introduced to improve the conductivity. A gold wire is contacted to the carbon paper to provide connection between the working electrode and the potentiostat. The cell is sealed using a rubber washer placed in-between the Au wire and the carbon paper.

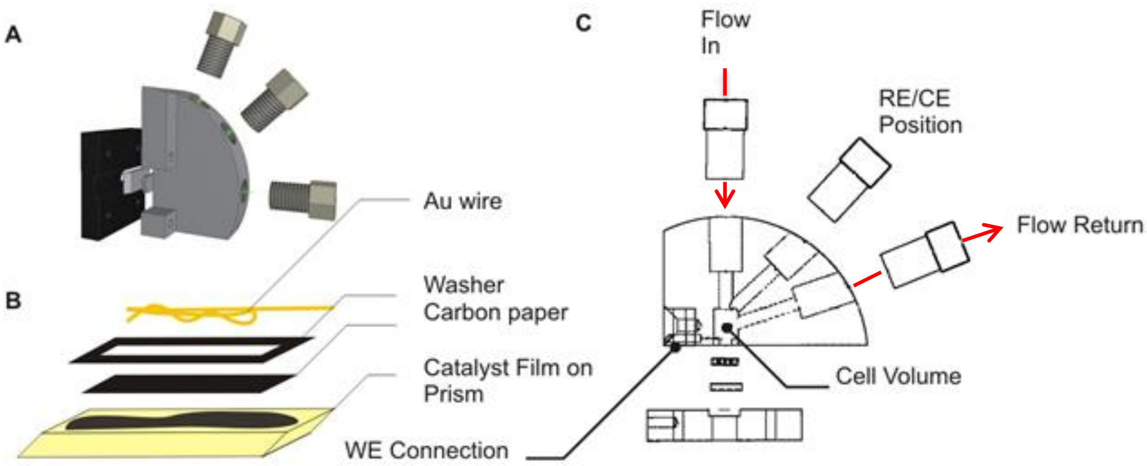

Figure 5-6. The design of the ATR-IR SEC cell. Panel A: An exploded perspective view of the cell in its vertical, operating position; Panel B: The components of the catalyst film, including the Au wire connecting the working electrode, a washer for seal, a piece of carbon paper for lateral conductivity of the particle film and a particle network on the prism; Panel C: The internal structure of the cell, along with the locations of the three electrodes and the flow set-up. RE: reference electrode; CE: counter electrode; and WE: working electrode.

5.2.4 Study chemical processes in the ATR-IR SEC cell

The catalyst is attached to the surface of carbon which is dispersed in the Nafion, as shown in Figure 5-7. Therefore, the chemistry of formic acid oxidation is triggered by direct electron transfer between the working electrode and the catalyst as shown by the blue bidirectional arrow in Figure 5-7. As the cell is equipped with flow capability, electrochemistry should not be limited by diffusion of formic acid or other substrates to the catalyst. In the process of formic acid oxidation triggered by direct electrochemistry, some adsorbed species are monitored by infrared spectroscopy. It is also possible to observe the signals from the electrolyte close to the prism sitting between the carbon particles by this cell because the space between the particles is mainly filled with the electrolyte. As discussed in **Section 5.1.1**, carbon monoxide (CO) is a poisoning intermediate during the oxidation of formic acid through the indirect pathway and greatly reduces the efficiency of the catalyst. The strength of the CO bond is sensitive to electron density on the metal and this makes CO a useful probe as it absorbs strongly in the IR, shown as the green dashed box in Figure 5-7.

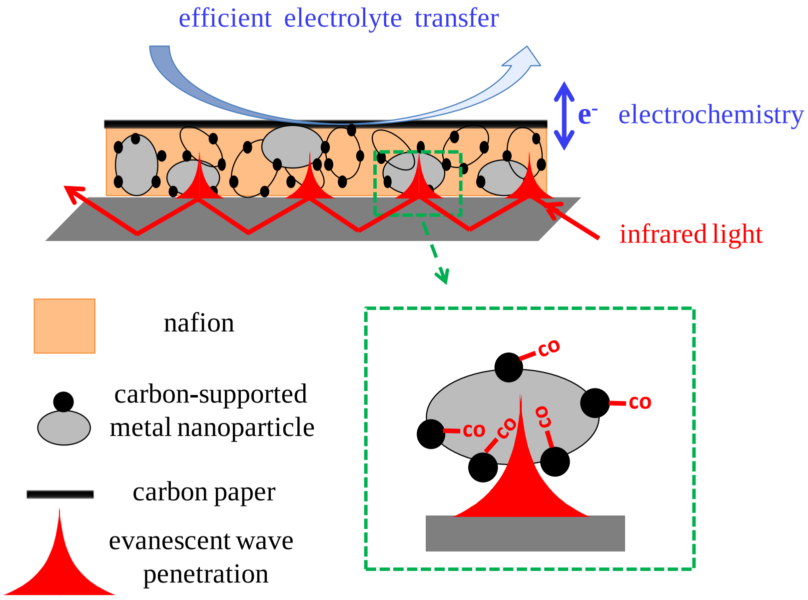

Figure 5-7. Chemistry on the surface of a particle-modified prism in the ATR-IR SEC cell.

Furthermore, multiple reflections (4 reflections in this case, and the calculation of reflection number is described in Chapter 2) in the ATR mode are applied for this cell to get a better signal-to-noise for a given acquisition time, shown as the red line with arrows in Figure 5-7. The number of reflections can be controlled by the thickness and length of the prism and the incidence angle, as described in Chapter 2. A thin layer of carbon-supported metal nanoparticle film is coated onto the top surface of an ATR prism (45-degree of Si was used through this Chapter), and penetration of an evanescent wave into the region above the prism permits sampling of adsorbed catalysts. One advantage of the particle film is that it is composed of three-dimensional particles which will increase the loading of the catalysts. However, the 3-D presents other experimental challenges. The penetration depth of the evanescent wave is several μm, therefore good control of the film thickness is required. A small portion of particles may lose precise potential control if the 3-D film is not very uniform, for example the far left particle shown in Figure 5-7.

5.2.5 Proof of Flow

Monitoring HCOOH flowing in and out of the cell by IR and Electrochemistry

In order to examine whether formic acid can reach the surface of the catalyst particles or not, infrared spectra were recorded to monitor the switching process of replacing the supporting electrolyte (0.5 M H_2SO_4) with 0.5 M H_2SO_4 + 0.5 M HCOOH. The background spectrum was taken as the same film with 0.5 M H_2SO_4 at open circuit potential (OCP). The potential was left at OCP throughout the experiment to avoid any changes coming from the formic acid oxidation reaction.

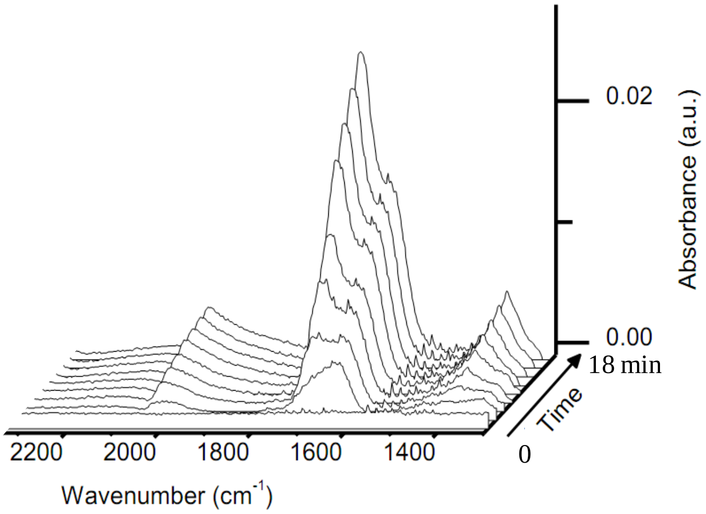

Figure 5-8. Monitoring the flowing in of 0.5 M HCOOH in 0.5 M H_2SO_4 to a Pd@C film in the ATR-IR SEC cell at OCP. The background spectrum is recorded for the same film with 0.5 M H_2SO_4 at OCP. The spectra were taken every two minutes. 250 scans are co-added for each spectrum at 4 cm^{-1} resolution.

As formic acid was introduced into the cell, as shown in Figure 5-8, the first spectrum is almost unchanged compared to the background. It may be explained by the fact that it needs time for formic acid to penetrate the carbon paper and the catalyst film. No changes have occurred until 2 minutes after the first spectrum (the second spectrum). In the second spectrum, one obvious change is a broad peak at around 1650 cm^{-1} with a small shoulder at 1700 cm^{-1} and there is also a small peak centred at around 2000 cm^{-1}. The 1650 cm^{-1} peak should arise from the combination band of H_2O (see Table 9). The potential was left at OCP, and no exchange current arising from formic acid oxidation should occur. However, self-decomposition of the formic acid still happens at the surface of Pd.[305,306] Therefore, the 2000 cm^{-1} peak can be ascribed to the linear CO.[307] In the third spectrum and spectra afterwards, another spectral feature can be seen at around 1700 cm^{-1}. It looks like a main peak at around 1700 cm^{-1} with a shoulder at 1650 cm^{-1}. The 1700 cm^{-1} peak can be ascribed to the C=O stretching band of HCOOH (See Table 9). With increasing time, the linear CO peak (2000 cm^{-1}) and the solution HCOOH peak (1700 cm^{-1}) become more and more intense. Apart from the linear CO adsorbed on Pd and the solution HCOOH, a third new peak at around 1400 cm^{-1} appears after 4 minutes (the 3rd spectrum). This peak can be explained by the wagging mode of C-H in HCOOH. Furthermore, the intensities of the peaks at 1700 cm^{-1} and 1400 cm^{-1} increased at the same rate, suggesting that they are correlated and both related to the solution formic acid. This experiment indicates that it takes around 2-3 minutes for HCOOH to reach the surface of the catalyst after being introduced to the cell. Importantly, not only peaks of the solution species but also the surface species can be observed by this ATR-IR SEC technique, implying that the changes both at the surface and in the solution can be monitored simultaneously.

Figure 5-9 shows the exchange of electrolyte monitored by electrochemistry in the ATR-IR SEC cell. Under analogous conditions as Figure 5-8, the electrolyte was originally 0.5 M H_2SO_4 in the absence of HCOOH, which can be easily seen by the typical reduction peak of platinum oxide at around 0.6 V and the hydrogen adsorption and desorption peaks near 0.1 V, as shown by the black line. At the end of the black cycle, the electrolyte was switched to 0.5 M HCOOH in 0.5 M H_2SO_4. In order to allow time for HCOOH to go through the film, a scan taken immediately after this was slowed down to 1 mV/s. In contrast to the black line, the red line resembles a classical cyclic voltammogram of the formic acid oxidation compared to that in Figure 5-1. Furthermore, the disappearance of hydrogen absorption and desorption demonstrates that the active sites of Pt are occupied by the newly introduced HCOOH or other species involved in the catalysis. The large catalytic currents on the forward and backward scan indicate

HCOOH managed to get through the carbon paper and reach the surface of the catalyst. The spikes in the red line in Figure 5-9 are caused by the pump, correlating with the frequency of pump pulses arising from the peristaltic mechanism. In all, both infrared spectroscopy and electrochemistry prove that the switch of the electrolyte from the background supporting electrolyte to the fuel (HCOOH in this case) is successfully achieved by this ATR-IR SEC flow set-up.

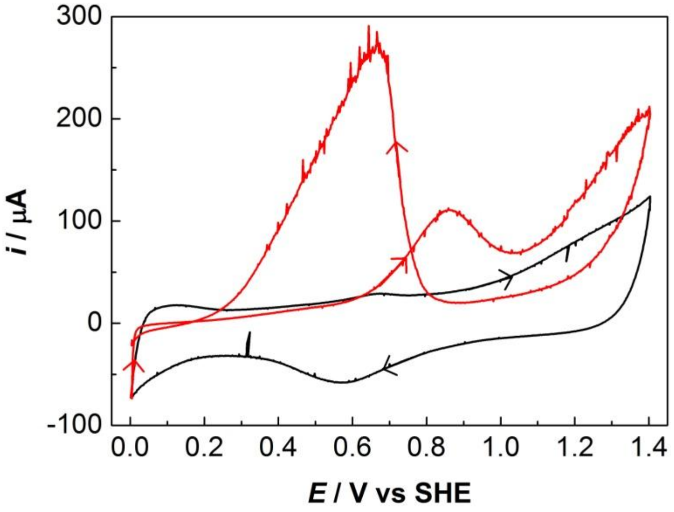

Figure 5-9. Cyclic voltammetry to monitor the introduction of HCOOH to the ATR-IR SEC cell. The black line shows the typical electrochemical behaviour of Pt in H_2SO_4 at 10 mV/s. Then the electrolyte was switched to HCOOH in H_2SO_4 and the scan rate was slowed down to 1 mV/s to give enough time for HCOOH to go through the carbon paper and the catalyst film. The red line shows the electrochemical behaviour of HCOOH oxidation catalysed by Pt as the fuel starts to be flowed into the cell. Other conditions: the flow rate was at 50% of its maximum rate, and the direction of the scans is shown by arrowheads.

Another experiment was performed to examine the other direction, removal of HCOOH. The flowing rate was set at 95% of the maximum in order to pump out all the fuel as quickly as possible. A Pd@C/Nafion film was made, which has similar behaviour in terms of the shape of the cyclic voltammogram in H_2SO_4 and for HCOOH oxidation. The red line in Figure 5-10 shows the cyclic voltammogram in the presence of HCOOH, which looks similar to the corresponding voltammogram in Figure 5-9, demonstrating there is formic acid inside the ATR-IR SEC cell. Around 15 minutes after beginning the electrolyte switch, shown as the black line, the shape of the cyclic voltammogram is identical to that of a Pd film in pure H_2SO_4, indicating that HCOOH was flushed out of the cell. Comparing these two cyclic voltammograms, two characteristic features are evident. Firstly, in the initial cycle the hydrogen adsorption peak near 0.1 V is missing and re-appears after HCOOH was flushed out, shown by the black line. Secondly, there are still some catalytic currents for HCOOH oxidation in the red line whereas the black line only shows the reduction current of Pt oxide and the double-layer capacitance. This experiment proves that the complete removal of HCOOH is achieved within around 15 minutes.

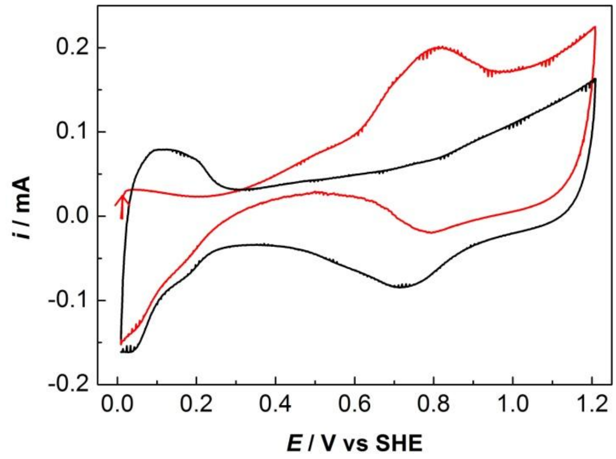

Figure 5-10. Cyclic voltammetry to monitor the switch of the electrolyte from HCOOH in H_2SO_4 to pure H_2SO_4 for a Pd@C (9:1 ratio to Nafion) film inside the ATR-IR SEC cell. The red scan stands for the first scan immediately taken after the electrolyte was switched from 0.5 M HCOOH in 0.5 M H_2SO_4 to 0.5 M H_2SO_4 and the black scan is the subsequent fifth cycle (*ca.* 15 minutes after switch). The scan rate is 10 mV/s and the flowing rate was at 95% of maximum flow.

Film stability and catalyst loading

The idea of a flow cell is to provide enough fresh substrate to the surface of the catalyst-modified electrode and remove the product from the electrode. However, the flow should not disturb the catalyst particle film. One experiment, shown in Figure 5-11, examined the stability of the film by estimating the catalyst surface area before and after a long period of catalysis. The cyclic voltammogram in red was taken in the presence of H_2SO_4, before introducing HCOOH to the cell. The surface of Pt was first activated by repeated electrochemical adsorption and desorption of hydrogen. Once a stable surface was achieved, the actual catalyst surface area can be calculated from the charge associated with hydrogen adsorption as each Pt atom adsorbed or desorbed one hydrogen atom, shown by the red hashed area in Figure 5-11. A monolayer of hydrogen adsorbed on polycrystalline platinum with a factor 210 μC/cm^2 is widely used.[308] Therefore, the active surface area of Pt@C particle film in the ATR cell is calculated to be 1.67 cm^2 by measuring the charge passed in the hashed region. The geometrical area of the catalyst film is around 32 mm^2 (4 mm × 8 mm). Comparing the total Pt active area and the geometrical area, it can be concluded that this three-dimensional carbon-supported Pt nanoparticle film has high catalyst loading.

Formic acid was then pumped in and other experiments were carried out to investigate HCOOH oxidation. After around 3 hours, pure H_2SO_4 was flowed in again to replace HCOOH + H_2SO_4. A second cyclic voltammogram shown in the black line in Figure 5-11 was taken under analogous conditions to those of the initial voltammogram. The surface area of Pt after 3 hours' catalysis did not change significantly, demonstrating that the particle film inside the cell is not destroyed by flow.

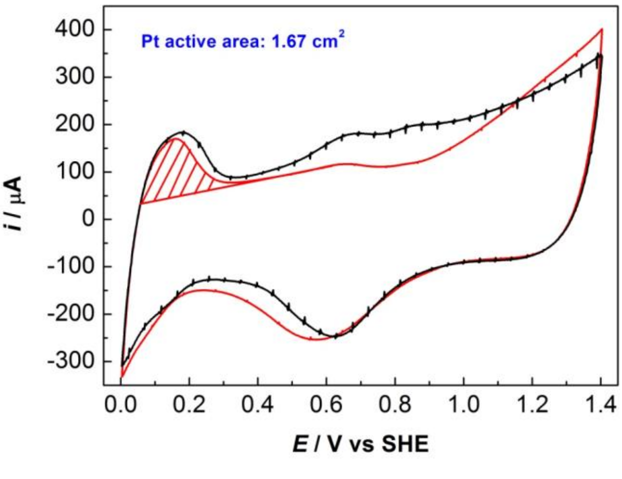

Figure 5-11. Cyclic voltammetry of a Pt@C/Nafion film in the ATR-IR SEC cell before flowing in HCOOH (red) and after flowing out of HCOOH (black) to examine the stability of the film. The two cyclic voltammograms were taken three hours apart. The scan rate was 50 mV/s and the flow rate was at its 50% maximum.

Efficient substrate supply by flow

To ensure the turnover of the catalyst was not limited by the substrate supply or the product removal, an experiment was carried out to examine the efficiency of substrate supply by observing the difference in catalytic currents with and without flow. As shown in Figure 5-12, the blue line is the first cycle with flowing of HCOOH at 50% of the maximum rate. The periodic spikes arise from the pump as mentioned above. The flow was then stopped after the first cycle. Consecutive cycles were taken (data not shown here) after stopping flow, showing a decrease in catalytic current due to formic acid depletion over time. The red line represents a cyclic voltammogram taken around 20 minutes after stopping the flow of HCOOH. The catalytic current at Peak IV, indicated by the red arrow, is used to compare the behaviours with or without flow. Clearly, the current in the red line drops to only half of that in the blue line, proving that the substrate depletion occurs within 20 minutes and a flow capability is crucial for our experiments (almost all experiments shown in this Chapter take longer than 20 min, on a time scale of hours). Then, flow was restarted at the initial rate, the catalytic current increased immediately, and it took *ca.* 4 minutes to reach the same level as before, shown by the black line. A four minute timescale agrees well with the amount of time it takes for material to reach the film, as shown by Figure 5-8.

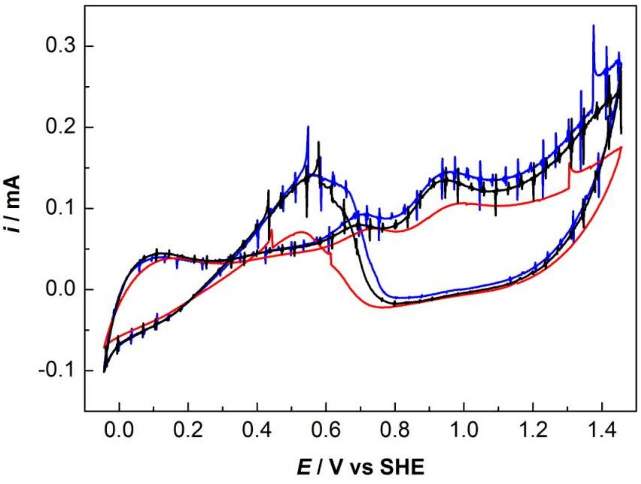

Figure 5-12. Demonstration of a functional flow ATR-IR SEC cell by cyclic voltammetry. A Pt@C/Nafion particle film (1 µL 25 mg/mL 20% Pt@C with 9:1 ratio to Nafion) was made and 0.5 M HCOOH in 0.5 M H_2SO_4 was used as the fuel. The blue cycle is the first cycle with flow at 50% of its maximum rate; the red cycle is taken 20 min after stopping flow and the blue cycle represents a cyclic voltammogram 4 min after adding back flow at the original rate. The scan rate was 20 mV/s.

As a conclusion, the ATR-IR SEC cell greatly diminishes the substrate depletion, providing better and more precise electrochemical control.

5.2.6 Electrochemical control vs. IR sampling

The best electrochemical control and the best spectroscopic sampling occur at opposite ‘sides’ of the film, as shown in Figure 5-7, earlier. The film thickness measurement and control are described in more detail in Chapter 2. If the film is too thick, the electrochemical control is not very accurate as electrons from the carbon paper need to go through several layers of particles to reach the particles close to the prism. It is also more difficult for the substrate to reach all the particles and the film is therefore more prone to substrate depletion, especially at a high turnover rate. On the other hand, if the film is too thin, not many particles are close to the prism and the IR absorption signals arising from the species on the surface of the catalyst will be of low intensity. Four different loadings of Pt@C particles in ethanol, 2 µL of 5 mg/mL, 10 mg/mL, 25 mg/mL and 50 mg/mL (data not shown here), were examined to find the optimum loading. There are two criteria applied to find a good film loading, by infrared spectroscopy. Firstly, linearly bound CO should be observed on the Pt at low potentials, and secondly, HCOOH should be present in solution near the prism at high potentials. It was found that 2 μL of 10 mg/mL catalyst particles gave the best loading while still maintaining good substrate supply and easily detection of adsorbed species. All the results in this Chapter are based on a 2 μL of 10 mg/mL catalyst loading.

5.2.7 Co-existing bands in addition to species adsorbed on catalyst

5.2.7.1 Water at the interface

As discussed above, the ATR sampling is also sensitive to the solution surrounding the particles, therefore, the measured spectra will contain large features due to water. As shown in Figure 5-13, there are three broad and intense water bands over the full mid-infrared region. The most intense band, located at around 3300 cm^{-1}, is the O-H stretching region, a broad feature due to the hydrogen bonding between the water molecules and the arrangement of water molecules around solutes and surfaces. The sharper peak around 1630 cm^{-1} is due to the H-O-H scissors-bending. A third, less intense, broad feature around 2100 cm^{-1} is assigned to a combination band, resulting from the coupling of the scissors-bending with a libration band in the near-infrared.[287] In the case of formic acid oxidation, the bands due to CO adsorbed on noble metals are located in the combination region and the solution formic acid band is very close to the scissors-bending band of water (see Figure 5-8, earlier), therefore special care should be taken when analysing the data.

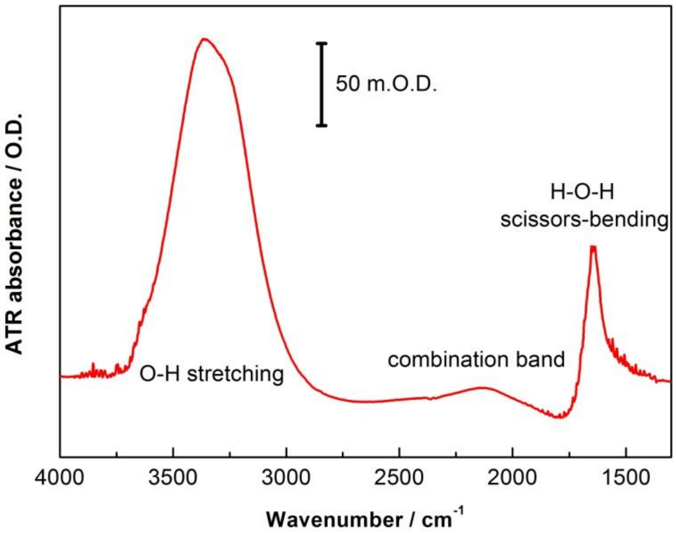

Figure 5-13. ATR-IR spectrum of water in a Pt@C/Nafion film coated onto the top surface of Si prism. The spectrum resolution is 4 cm^{-1}.

Potential-dependent reorientation of water at an electrode/electrolyte interface

Figure 5-14 shows a series of infrared spectra of the Pt/H_2SO_4 interface acquired continuously during a negative-going potential sweep from 1490 to -50 mV at a scan rate of 1 mV/s. Each spectrum corresponds to an average over a potential window of 60 mV. The reference spectrum is acquired at open circuit potential. At high potentials above 790 mV (shown as the bold black line), the water bands, including the O-H stretching and the H-O-H bending were observed as negative-going bands. At low potentials below 790 mV, the water bands become positive, as demonstrated by the spectrum at -50 mV (bold red line). In the potential regions around 790 mV, the water bands show very weak signals. The O-H stretching mode of the water at the interface shows that not only its negative or positive trend depends on the applied potential but also the peak position of the band also shifts as a function of potential, shown as the dashed black line in Figure 5-14. The broadness and shift of the O-H stretching band are related to the hydrogen bonding between water molecules, and potential dependent interactions between water molecules and the Pt surface.

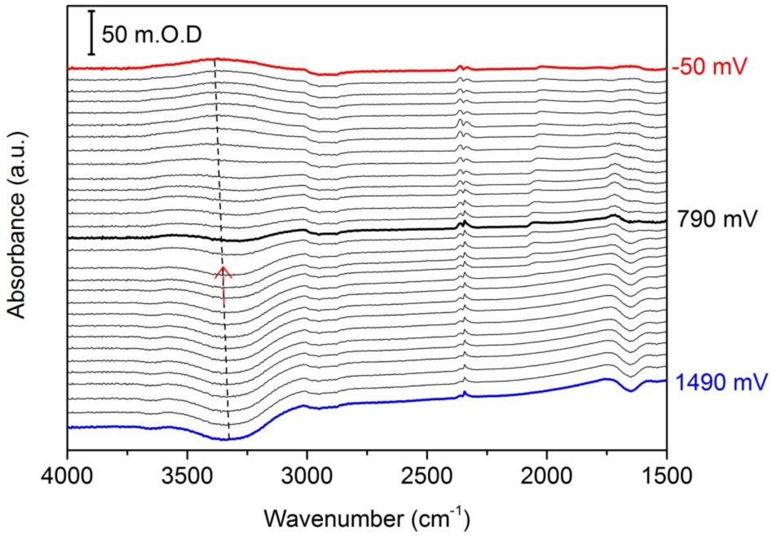

Figure 5-14. A series of infrared spectra at the Pt/C@Nafion electrode in 0.5 M H_2SO_4 as a function of applied potential. The spectra were acquired during a potential sweep from 1.49 to -0.05 V at a rate of 1 mV/s and each spectrum represents an average over a potential window of 60 mV. The reference spectrum was taken at OCP. Other conditions: the resolution is 4 cm^{-1} and 250 scans were collected for each spectrum.

The spectral changes shown in Figure 5-14 are similar to those seen by Osawa *et al.* as a function of applied potential at a flat electrode, which were explained by the surface selection rule and changes in orientation of interfacial water with surface charge.[309,310] The surface selection indicates that any species with its dipole oriented parallel to the surface will not be observed, and Figure 5-15 depicts this situation. The potential at which species close to the electrode will lead to their dipole oriented parallel to the surface is defined as the potential of zero charge (pzc). At potentials above pzc, it is more likely for the O atom in the water to be close to the surface. At potentials below pzc, the situation is the opposite, i.e., the two H atoms are closer to the surface.

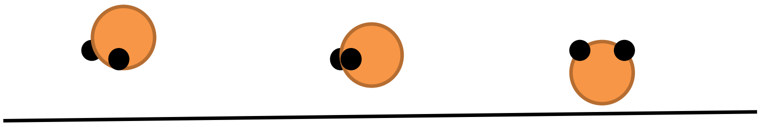

a. $E <$ pzc b. $E \approx$ pzc c. $E >$ pzc

Figure 5-15. Possible orientations of water at the Pt/H_2SO_4 interface when the applied potential is below, around or above the pzc. The orange ball represents the O atom in H_2O and the black ball is the H atom.

Background from Nafion and H_2SO_4

Two important control experiments were performed to examine the pure supporting electrolyte H_2SO_4 and the dry Nafion film, as shown in Figure 5-16. A relatively strong peak appears in both pure H_2SO_4 and dry Nafion at around 1300 cm^{-1} arising from asymmetric sulphate stretching, and it is not related to formation of other intermediates during HCOOH oxidation, as it is independent of the applied potential. In the H_2SO_4 spectrum as shown by red, an intense peak at around 1100 cm^{-1} was observed, corresponding to the $\{SO_4\}$ asymmetric stretch. In the Nafion spectrum as shown in black, three strong absorption peaks appear around 1050, 1150 and 1200 cm^{-1} which are arising from the SO symmetric, CF symmetric and CF asymmetric stretch, respectively, as summarised in Table 9.

In order to avoid interference from the Nafion or the strongly absorbing H_2SO_4, particle films were made up without Nafion (blue) and the electrolyte was replaced by less strongly IR absorbing $HClO_4$ (red), as shown in Figure 5-17. Carbon monoxide was observed in both spectra at *ca.* 2050 cm^{-1}, indicating that the lack of Nafion or the replacing of the electrolyte does not affect the absorption of the intermediate formed during the oxidation of formic acid catalysed by Pt@C or PtRu@C. However, the intensity of adsorbed CO on PtRu was smaller than that on Pt under analogous conditions, as shown by the grey box in Figure 5-17. This can be explained by the fact that the presence of the second metal Ru facilitates the CO stripping during catalysis as discussed above. More importantly, this PtRu experiment demonstrates that our ATR-IR SEC cell is suitable for studying the bimetallic and even multi-metallic nanoparticles.

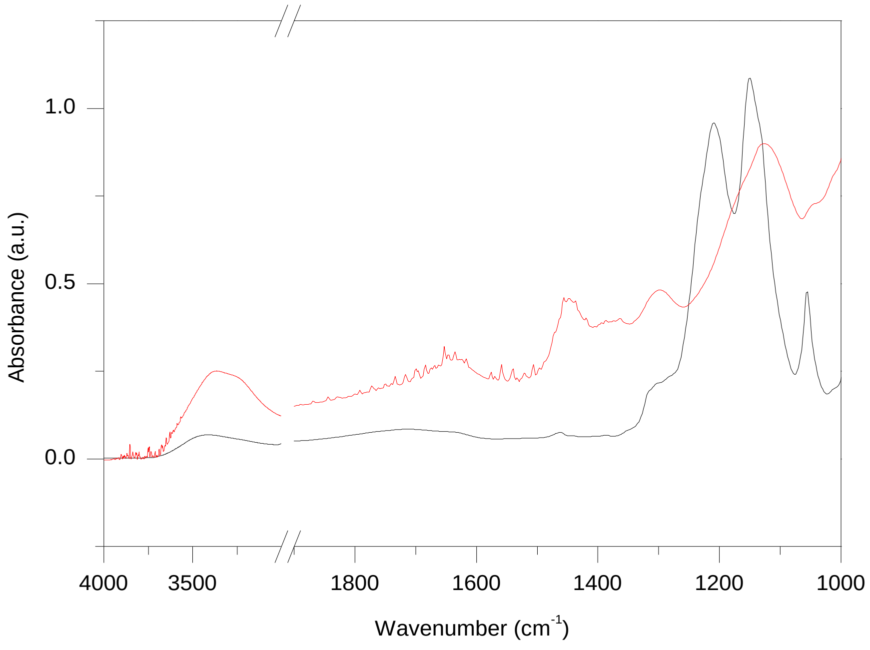

Figure 5-16. Infrared spectra of a film in pure supporting electrolyte H_2SO_4 (red) and of dry Nafion (black) for comparison. The Nafion spectrum is obtained on a diamond ATR prism.

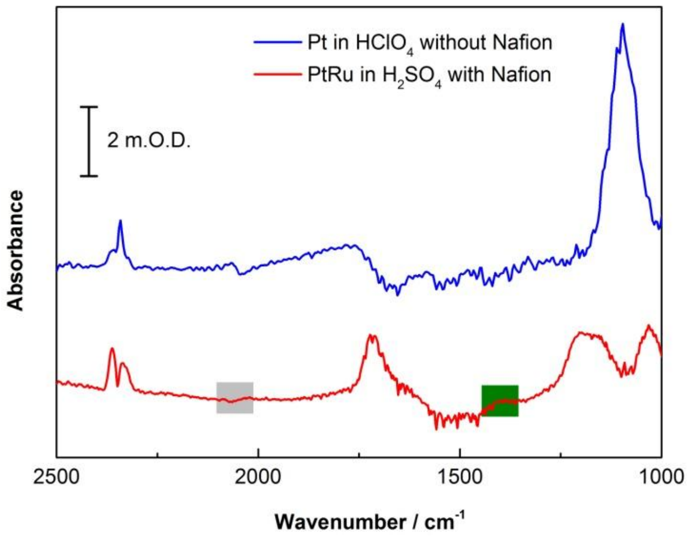

Figure 5-17. Infrared spectra of a Pt@C film without Nafion in 0.1 M HCOOH/0.1 M $HClO_4$ (blue) and of a PtRu@C/Nafion film in 0.5 M HCOOH/0.5 M H_2SO_4 (red).

5.3 Infrared changes with direct electrochemical control

5.3.1 *In-situ* CO poisoning and stripping off with potential control

Pd@C with Nafion

One experiment, shown in Figure 5-18, was designed to monitor the *in-situ* building-up of CO on the surface of the Pd@C catalyst by flowing CO-containing electrolyte through the cell. The electrolyte, 0.5 M H_2SO_4, was gassed with CO for 10 minutes. The flow was at 50 % of its maximum rate throughout the experiment. The cell was initially filled with CO-free H_2SO_4 and a background spectrum was recorded. In order to minimise changes in background water absorption, the potential was held at 0 mV throughout the experiment as shown in Figure 5-18(B). This potential favours adsorption of CO onto the metal surface.[311] CO-containing H_2SO_4 was then introduced and 30 spectra were taken continuously to monitor CO poisoning of the surface. The CO stretching region of spectra taken at 1, 6, 11, 16 and 21 minutes is shown in the inset of Figure 5-18(A). The spectra clearly indicate the presence of surface-bound linear CO at around 2050 cm^{-1}， in good agreement with the literature.[312] Notably, the shape of the adsorbed CO peak is bipolar, rather than showing a sharp feature. Chen *et al.* proposed that this bipolar shape of CO peak i.e., the antiabsorption peak arises from the strong interaction between nanoparticles and the collective interaction between CO adsorbate and nanoparticles.[303] According to the literature, it should be easier for the multi-bonded CO to be formed on the surface of Pd rather than the linear CO.[313] However, no evidence was found for other types of CO formed except for linear CO. The reason for the presence of only linear CO in this ATR-IR SEC cell will be discussed later in **Section 5.4.4**.

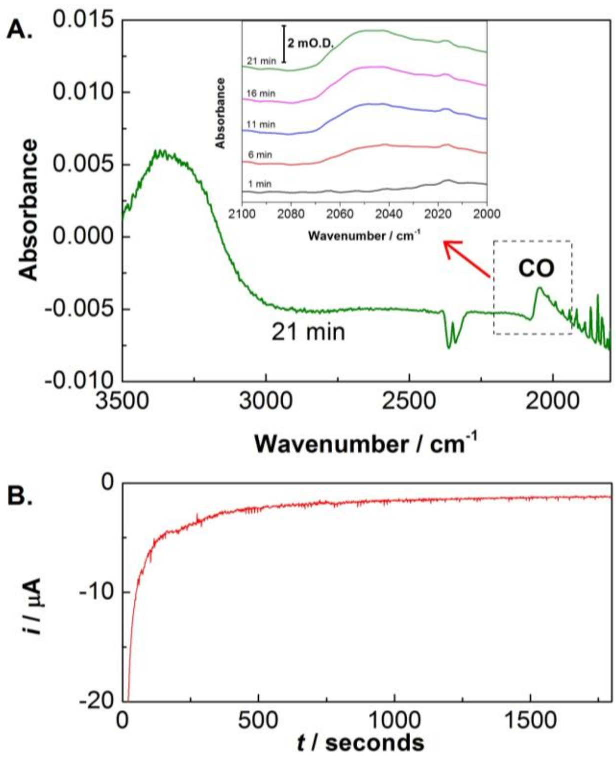

Figure 5-18. Experiment designed to monitor the *in-situ* building-up of CO on the surface of Pd by infrared spectroscopy at a potential of 0 mV. Panel A: The infrared spectrum taken 21 minutes after CO-containing electrolyte (0.5 M H_2SO_4) was introduced to the cell. The inset is an enlargement of the linear CO adsorbed on Pd at different times after starting the flow. The background spectrum was taken before flowing the CO-containing electrolyte. Panel B: The current-time trace for the CO adsorption while holding the potential at 0 mV. The flow lasted 30 minutes and the rate was 50 % of its maximum rate.

After the surface of Pd was poisoned *in-situ* by CO, the CO was removed electrochemically by scanning the potential to high values. A simultaneous cyclic voltammogram and infrared spectra were recorded in Figure 5-19. As shown in Figure 5-19(B), at the beginning of the first scan (red), no H desorption peak occurs, indicating that the surface of Pd is occupied by CO. This is confirmed by infrared spectroscopy as shown in Figure 5-19(A), where the initial spectra show obvious linear CO adsorbed on the surface of Pd. At around 600 mV on the positive sweep, the current increases and an obvious peak appears, indicating CO being oxidised from the surface. Again this is confirmed by the infrared spectroscopy, the CO peak quickly diminishes after 600 mV, proving that the current peak is due to CO being stripped from the surface. On the reverse scan in Figure 5-19(B), the H adsorption appears at around 200 mV, indicating that the surface is no longer occupied by CO. On the second scan in black in Panel B, the H desorption appears in contrast to the first cycle. An integration of the CO peak area, plotted as a function of the applied potential, is also shown in Figure 5-19(B) (blue line and symbols). The integrated area for CO is calculated using the blue hashed region shown in the first spectrum in Figure 5-19(A). The CO intensity stays constant as the potential is swept to roughly 600 mV and suddenly drops after 600 mV in the forward scan. The CO stripping peak in the voltammetry corresponds well with the drop in the integrated CO intensity obtained from the infrared spectra. This demonstrates that both good infrared information from the catalyst surface and simultaneous electrochemical control over the catalyst surface is achieved.

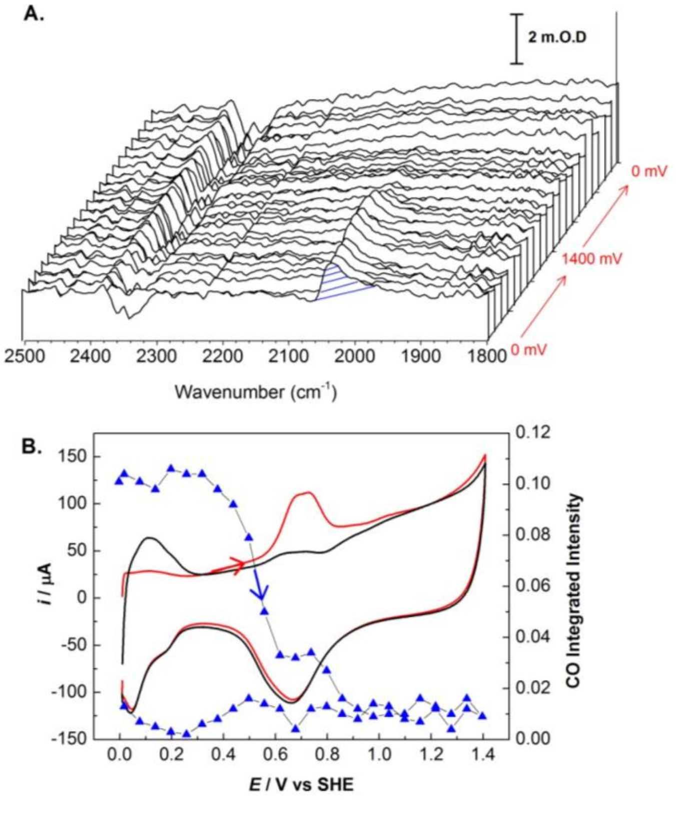

Figure 5-19. The oxidative dissociation of adsorbed CO on Pd examined by infrared spectroelectrochemistry. Panel A: 3-D plot for infrared spectroscopy of CO stripping with potential control. The spectra in Panel A correspond to the cyclic voltammogram in red in Panel B. Each spectrum was taken every 6 s and represents a potential window of 60 mV. The background spectrum was taken for a clean (CO-free) surface. Panel B: The red and black lines show two consecutive cyclic voltammograms on CO-poisoned Pd taken at 10 mV/s. The blue line and symbol represents the integration of linear CO, indicated by the hashed area in Panel A, as a function of potential. The CO-free H_2SO_4 was flowed throughout the experiment at 50% of its maximum rate.

Pt@C with Nafion

A similar set of experiments were performed on a Pt@C/Nafion film to examine the difference in the binding modes of CO, and the stripping behaviour. In comparison with Figure 5-18, Figure 5-20 shows the same information, i.e., it takes around 5 minutes for CO to be adsorbed on the surface of Pt at 0 mV. The form of CO adsorbed is the same, linear CO. The success of CO building-up on Pt demonstrates that the access of gas to the surface of the catalyst is successful.

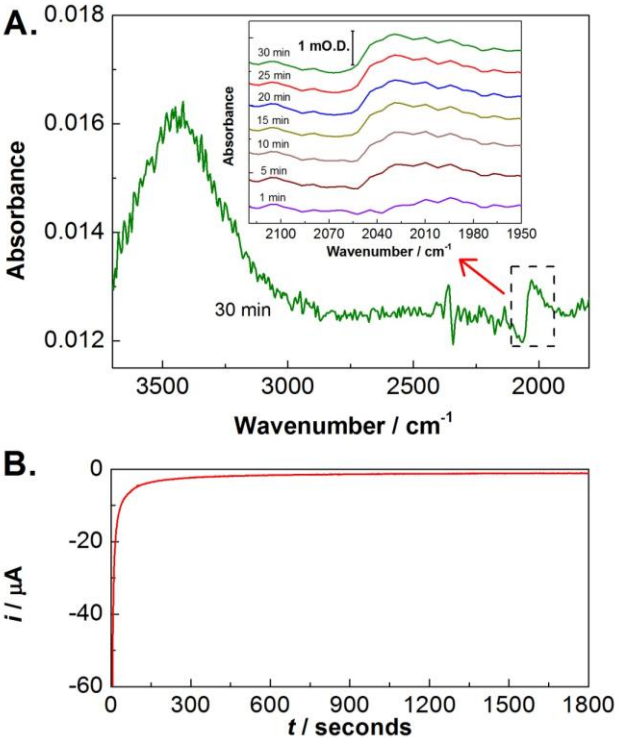

Figure 5-20. Experiment designed to monitor the *in-situ* building-up of CO on the surface of Pt by infrared spectroscopy with the potential held at 0 V. Panel A: The infrared spectrum taken at 30 minutes after CO-containing electrolyte (0.5 M H_2SO_4) began flowing into the ATR cell. The inset is the enlargement of the linear CO adsorbed on Pt at different times. The background spectrum was taken before flowing the CO-containing electrolyte. Panel B: The current-time trace for the CO adsorption while holding the potential at 0 V. The flow lasted 30 minutes at 50% of its maximum rate.

After poisoning the surface of Pt with CO, a cyclic voltammetry experiment (Figure 5-21) was then performed to examine the oxidising-off of CO. As shown in Figure 5-21(B), the red line represents the poisoned Pt, confirmed by the absence of H desorption. The onset potential for

CO stripping is around 700 mV which is in agreement with the literature.[311] The difference in the onset potential for CO stripping between Pt and Pd further demonstrates that precise surface electrochemistry control is obtained. The corresponding infrared changes as shown in Figure 5-21(A) also depict the process of CO stripping. The intensity of CO integrated as the area of the peak is plotted as a function of the applied potential and is shown by the blue line and symbol in Figure 5-21(B). The excellent agreement between the infrared and electrochemical changes as a function of applied potential demonstrates that direct electrochemical control is achieved over the adsorbed CO on the catalyst surface.

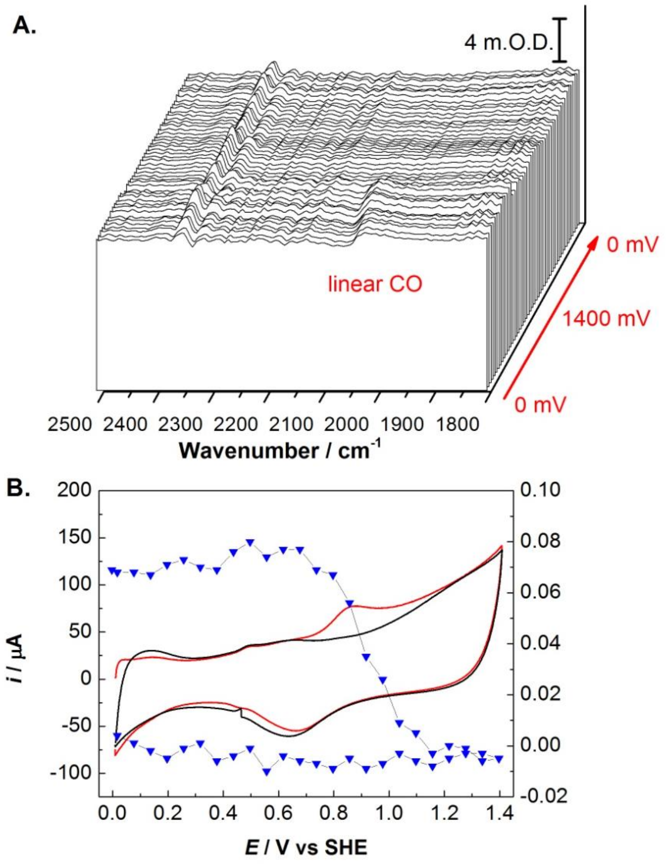

Figure 5-21. The electrochemical oxidation of CO adsorbed on Pt examined by infrared spectroelectrochemistry. Panel A: 3-D plot for infrared spectroscopy of CO stripping with potential control. The spectra in Panel A correspond to the cyclic voltammogram in red in Panel B. Spectra were collected every 6 s, therefore each spectrum represents a potential window of 60 mV. The background spectrum was taken from a surface free of CO. Panel B: The red and black lines represent two consecutive cyclic voltammograms on CO-adsorbed Pd with a scan rate of 10 mV/s. The blue line and symbol represents the integration of linear CO as a function of potential. The CO-free H_2SO_4 was flowed throughout the experiment at 50% of its maximum rate.

5.3.2 Infrared spectroelectrochemical investigation of formic acid oxidation

This section explores potential dependent surface and solution species formed during formic acid oxidation on metal surfaces, and uses exchange between natural abundance (HCOOH) and ^{13}C enriched (H^{13}COOH) formic acid to confirm assignments. Formic acid oxidation catalysed by Pt was examined using infrared spectroelectrochemistry. The ATR-IR SEC cell with a Pt@C/Nafion film was set up, and 0.5 M HCOOH in 0.5 M H_2SO_4 was flowed through the cell at 10 % of the maximum rate. A cyclic voltammogram was then recorded with a scan rate of 1 mV/s, as shown in the red line of Figure 5-22, and a simultaneous series of spectra were collected as shown in Figure 5-23.

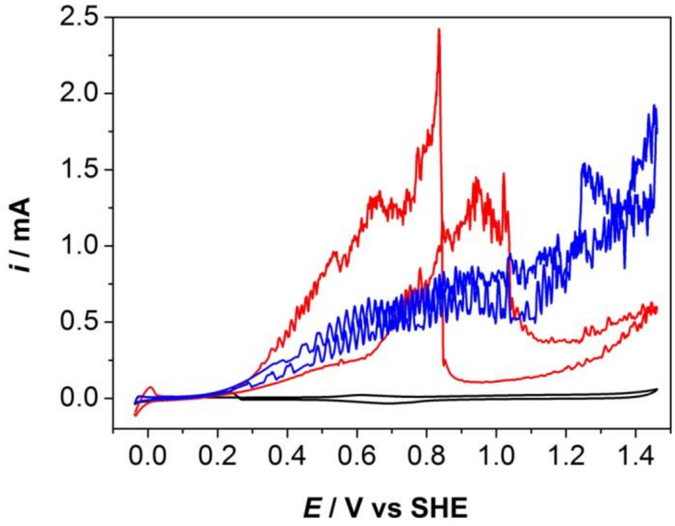

Figure 5-22. Isotope exchange experiments: cyclic voltammgrams of a Pt@C/Nafion film as flowing different electrolytes into the ATR-IR SEC cell. The electrolytes can be distinguished by the colours: the red line represents 0.5 M H^{12}COOH in 0.5 M H_2SO_4, then 0.5 M H_2SO_4 was introduced later to wash away the remaining H^{12}COOH, as shown in black, and around 0.1 M H^{13}COOH in 0.5 M H_2SO_4 was flowed in, shown by the blue line. Other conditions: the scan rate was 1 mV/s and the flow rate was 10% of its maximum.

Each spectrum took around 60 seconds and therefore covered around an average over a potential window of 60 mV. The linear CO centred at around 2050 cm^{-1} is very obvious at the beginning of the scan. It has not completely gone until the 12th spectrum which corresponds to the potential window around 720 mV in the cyclic voltammetry. The potential for oxidising CO adsorbed on Pt during formic acid oxidation corresponds to that observed previously (Figure 5-21). The peak around 2350 cm^{-1} arises from carbon dioxide in solution, which is the final product of formic acid oxidation. However, small changes in the purge of the spectrometer may also contribute to the variation in this region. Therefore, it is difficult to quantify the relation between the CO and the CO_2. The shape of the voltammogram is as expected. In the forward scan, there are two peaks, a little bump at around 500 mV and a broad peak centred at 900 mV which correspond well with standard electrochemistry as shown in Figure 5-1. On the reverse scan, a sharp peak occurs at 700 mV. In the infrared spectra, CO, as an important indicator for the oxidation of formic acid, occurs from 700 mV on the reverse scan. In summary, CO disappears between 700 to 1450 mV and exists between -50 to 700 mV. This result is in agreement with previously reported findings by SEIRA.[187]

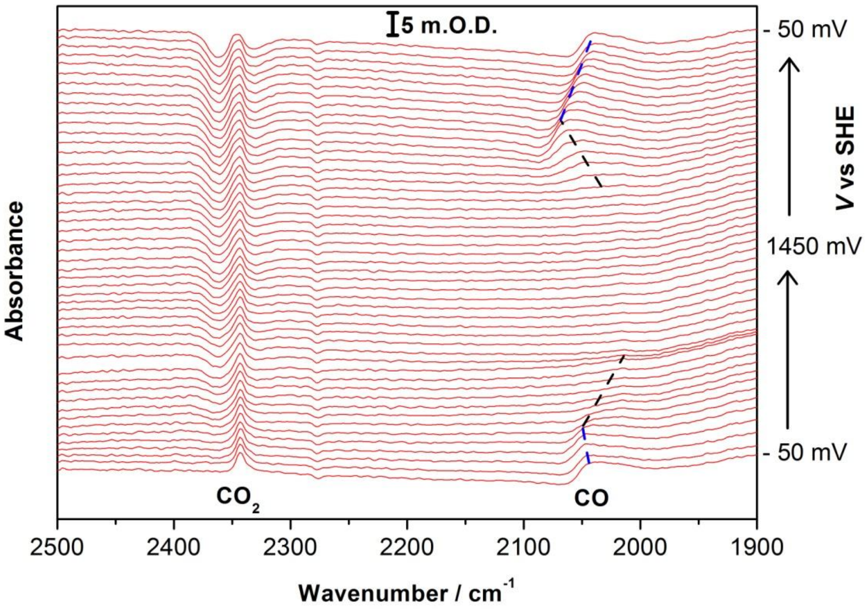

Figure 5-23. Infrared spectra of formic acid oxidation catalysed by Pt@C/Nafion in the ATR-IR SEC cell. A series of spectra in 0.5 M H^{12}COOH + 0.5 M H_2SO_4: at the same time a cyclic voltammogram was taken, shown by the red line of Figure 5-22. Each spectrum represents an average over a potential window of 60 mV. The spectra were taken against the spectrum taken at OCP in pure H_2SO_4. Other conditions: the resolution is 4 cm^{-1} and 250 scans were collected for each spectrum.

In order to further confirm that the 2050 cm^{-1} peak is adsorbed linear CO, an isotope exchange experiment with 13-C labelled $H^{13}COOH$ was also performed on the same film. Before introducing $H^{13}COOH$, H_2SO_4 was flowed in to wash away the remaining HCOOH and to collect a new reference spectrum. Then 0.1 M $H^{13}COOH$ was flowed into the cell. Figure 5-22 shows that cyclic voltammograms in the presence of HCOOH (red) and $H^{13}COOH$ (blue) are distinct from that in pure H_2SO_4 (black), confirming successful exchange of electrolyte. As the $H^{13}COOH$ is expensive, a lower concentration of $H^{13}COOH$ (around 0.1 M) was used here. Again, 10% of the maximum flow rate was applied. A series of spectra were also taken when $H^{13}COOH$ was flowed in at a constant rate and a voltammogram with a slow scan rate was performed. The experimental condition was exactly the same as that of HCOOH except for the lower concentration of HCOOH. One spectrum electrochemically located at around 250 mV for both HCOOH and $H^{13}COOH$ was chosen, shown in Figure 5-24. Two important features are shown here, the first is the peak shift of both linear CO and the product CO_2. With the labelled formic acid, the peaks of CO and CO_2 all shift to lower wavenumber (redshift) as the carbon is heavier and the reduced mass μ (where $\frac{1}{\mu} = \frac{1}{m_1} + \frac{1}{m_2}$) becomes larger. The shift of ^{13}CO compared to ^{12}CO by around 40 cm^{-1} can then be explained by eqn [5-7], as the peak position is proportional to $1/\sqrt{\mu}$.

$$\tilde{v} = \frac{1}{2\pi c}\sqrt{\frac{k}{\mu}} \qquad [5\text{-}7]$$

where $\bar{v}$ is the wavenumber and *k* is the force constant of the bond.

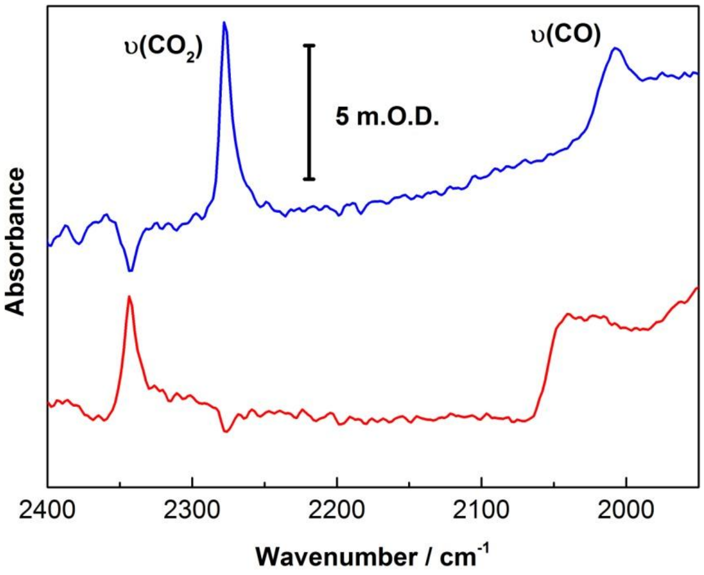

Figure 5-24. Infrared spectra of formic acid oxidation catalysed by Pt@C/Nafion in the ATR-IR SEC cell. A comparison of spectra taken under analogous conditions at the same potential, on the same Pt@C/Nafion film, when 13-C labelled H^{13}COOH replaced HCOOH. The blue spectrum is selected when the potential was swept around 250 mV and 0.1 M H^{13}COOH/0.5 M H_2SO_4 was introduced. The red spectrum is chosen from Figure 5-23 when the potential region is also around 250 mV. Other conditions: the resolution is 4 cm^{-1} and 250 scans were collected for each spectrum.

5.4 Discussion

5.4.1 Peak I and II in the cyclic voltammogram and the corresponding infrared spectrum

Peak I in the voltammogram as shown in Figure 5-1 is corresponding to the oxidation of the formic acid through the direct pathway.[277] However, as electrochemistry alone cannot provide structural information, the infrared spectra must be used to determine whether Peak I is related to the formation of CO_2 through the direct pathway. The infrared signal of the gaseous CO_2 is around 2350 cm^{-1}, shown as the double peaks in Figure 5-26. In practice, it is difficult to analyse the direct pathway for formic acid oxidation as gaseous CO_2 introduced by the small changes in the purge of the spectrometer appears in the same spectral region. However, this can be solved by using ^{13}C-labelled HCOOH. Figure 5-26 shows the infrared spectra of adsorbed ^{13}CO and solution $^{13}CO_2$, formed during the oxidation of H^{13}COOH with the direct electrochemical control. Each spectrum represents an average over a potential window of 60 mV. Three consecutive spectra in Figure 5-26(A) with the potential region, indicated on the right, include the potential regions before and after the onset of the Peak I (*ca.* 200 mV). The spectrum, taken between 130 and 190 mV (black), only shows the linear ^{13}CO peak at around 2010 cm^{-1}. The spectrum between 190 and 250 mV corresponds to the onset of Peak I in the voltammogram. The intensity of the ^{13}CO peak increases compared to the spectrum at lower potential, and a peak around 2280 cm^{-1} can be seen, which is ascribed to $^{13}CO_2$. When the potential is increased further, both the $^{13}CO_2$ and linear ^{13}CO peaks became more intense, as shown in the spectrum recorded between 250 and 310 mV. Therefore, it can be concluded that Peak I in the voltammogram correlates with the onset of CO_2 formation through the direct pathway of formic acid oxidation. As well as acting as poison to the direct pathway, the adsorbed CO is an intermediate in the indirect pathway. The direct pathway as shown in eqns [5-8] and [5-9] is gradually inhibited as the active sites of Pt are poisoned by CO, as shown by eqn [5-10].

$$\mathrm{HCOOH} + \mathrm{Pt} \rightarrow \mathrm{HCOO{\sim}Pt} + \mathrm{H}^{+} + \mathrm{e}^{-} \qquad [5\text{-}8]$$

$$\mathrm{HCOO{\sim}Pt} \rightarrow \mathrm{CO_2} + \mathrm{H}^{+} + \mathrm{e}^{-} + \mathrm{Pt} \qquad [5\text{-}9]$$

$$\mathrm{HCOOH} + \mathrm{Pt} \rightarrow \mathrm{CO{\sim}Pt} + \mathrm{H_2O} \qquad [5\text{-}10]$$

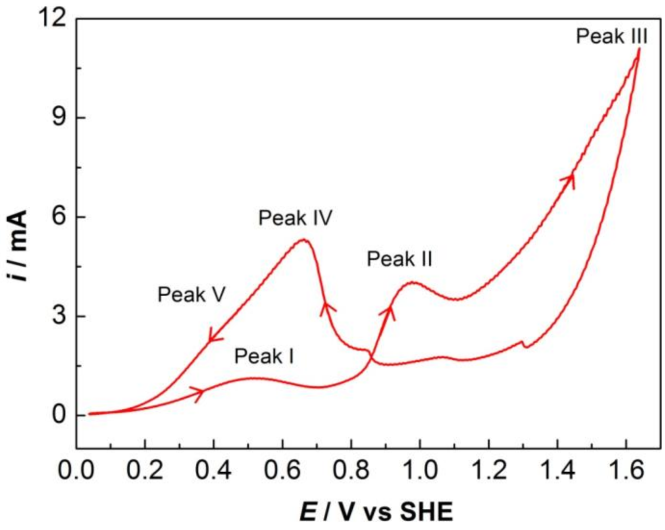

Figure 5-25. Reproduced from Figure 5-1.

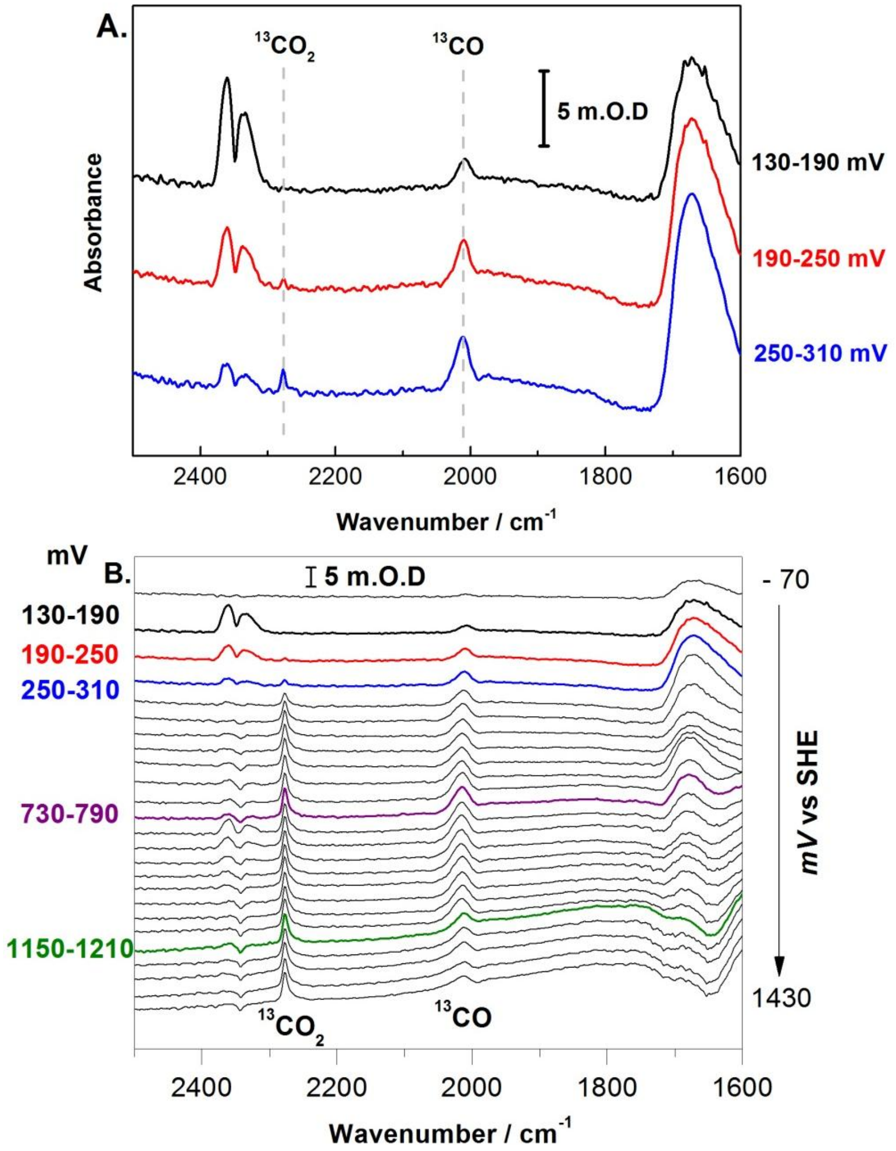

Figure 5-26. Infrared spectra of ^{13}C-labelled formic acid oxidation catalysed by Pt@C/Nafion in the ATR-IR SEC cell. Panel A: Three consecutive spectra are selected from the set of spectra shown in Panel B which were recorded while taking a voltammogram and the potential window for each is indicated on the right. Each spectrum represents an average over a potential window of 60 mV. The spectra were taken against the spectrum at OCP in pure H_2SO_4. Panel B: A series of spectra were taken while the cyclic voltammogram in the positive sweep was underway at 1 mV/s in 0.1 M $H^{13}COOH$ +0.5 M H_2SO_4. Other conditions: the resolution is 4 cm^{-1} and 250 scans were collected for each spectrum.

Peak II in Figure 5-25 has been assigned as the further oxidation of CO adsorbed on the surface of Pt, but spectroscopic support for this argument is lacking.[277] In Figure 5-26(B), the intensity of the ^{13}CO peak increases until the potential around 800 mV is reached, shown by the purple line. Above 800 mV, the CO peak intensity begins to drop, as shown by the green line, which corresponds to a potential region around 1200 mV. However, when the potential is swept to even higher values, the CO peak intensity remains the same, indicating that part of the Pt@C/Nafion film could be out of electrochemical control. The potential region between the purple and the green spectra corresponds to Peak II in the cycle voltammogram, proving that Peak II represents the further oxidation of the intermediate CO. Figure 5-23 shows a set of experiments under analogous conditions in which natural abundance HCOOH was used. These data correspond well to those shown in Figure 5-26, and appear to have more complete electrochemical control, confirming that the potential region for oxidising off CO correlates well with Peak II in the voltammogram.

5.4.2 Potential dependence of the CO position during HCOOH oxidation

Apart from the potential dependence of the CO building-up and stripping-off during formic acid oxidation, the peak position of the linear CO is found to shift as a function of applied potential, described as the Stark effect.[303] There are two trends in the shift. When the potential is swept up to 800 mV in the anodic direction, a positive shift is found, shown by the blue dashed lines in Figure 5-23. When the potential is swept from 800 mV to 1450 mV, a negative shift of the CO position is found, shown by the black dashed lines. The higher wavenumber the peak position is, the more energy is required for the vibrational transition to occur. There are two independent effects which determine the position of the absorption band for the linearly adsorbed CO.[252] The first is the effect of increasing the potential at the metal which results in a decrease in the occupancy of the CO π^* antibonding orbital and an increase in the σ bonding, i.e., a strengthening of the CO bond, therefore shifting υ(CO) to a higher wavenumber. The second is the effect of decreasing CO coverage as CO is oxidised off the surface at high potential. Decreased coverage increases π backbonding to adsorbed CO, therefore shifting υ(CO) to a lower wavenumber. This leads to a positive shift in υ(CO) from 0 to 800 mV (shown by the blue dashed lines) and a negative shift in υ(CO) above 800 mV (shown by the black dashed lines).

Similar potential dependences of CO have also been reported on the adsorbed CO onto CoPt nanoparticles.[314]

5.4.3 The level of electrochemical control during formic acid oxidation in the ATR-IR SEC cell

The electrochemical control of formic acid oxidation is through direct electron transfer between the working electrode and the catalyst adsorbed on the carbon surface. As the noble metal nanoparticles are already immobilised onto the carbon particle, they respond to the applied potential rapidly. This rapid response is proved by the synchronization of the infrared spectra and the cyclic voltammograms in terms of the CO building-up and stripping-off during formic acid oxidation.

5.4.4 The lack of formate and multi-bonded CO

Osawa *et al.* proposed that adsorbed formate is the active intermediate in the direct pathway of formic acid oxidation.[187] The asymmetric O-C-O stretch would be around 1640 cm^{-1}, but is invisible for adsorbed formate due to the surface selection rule, and the symmetric O-C-O stretch should be around 1340 cm^{-1}, as shown in Table 9.[315] However, the symmetric formate is still not observed in our ATR-IR SEC cell although the 1300 ± 50 cm^{-1} region is flat and free from interference from H_2SO_4 and Nafion, as shown in Figure 5-17. As for CO, another poisoning intermediate during formic acid oxidation, its different forms in terms of linear CO, bridging CO and multi-bonded CO (see Table 9) are observed by SEIRA.[187] However, in our ATR-IR SEC cell during formic acid oxidation, only linear CO is observed at lower potentials.

One explanation for the lack of formate and multi-bonded CO in our cell is that the sensitivity provided by our ATR-IR SEC technique is not as high as that in the SEIRAS as there is minimal surface enhancement effect compared with Pt on a flat, roughened gold surface. However, it should be noted that the formate pathway during formic acid oxidation is still controversial.[187,252,316,317] As demonstrated above, CO_2 is known as the final product of formic acid oxidation. Breiter and Beden *et al.* proposed that the adsorbed formate is actually formed as an intermediate when CO_2 is reduced to CO.[315,318-320] In contrast, Osawa *et al.* proposed that the formate is an active intermediate formed at a relatively higher potential than the potential at which CO is formed during HCOOH oxidation.[187] Breiter and Beden *et al.* also found that the multi-bonded CO is formed through the reduction of CO_2 with the adsorbed hydrogen on Pt and the adsorbed formate.[252,316,320,321] Notably, the findings of the multi-bonded CO and formate either by Osawa[187] or Beden[320] are all based on a stationary cell, and the sampling geometry of the latter is electrochemically modulated infrared spectroscopy (EMIRS) in which the electrolyte is a thin layer of solution and the product CO_2 cannot be effectively removed during the measurement. Therefore, the stationary cell or the thin layer electrolyte provides the possibility that CO_2 can build up near the catalyst surface and therefore form the multi-bonded CO and formate. However, our ATR-IR SEC cell is equipped with flow capability and therefore the final product CO_2 of formic acid oxidation is efficiently removed. This could also explain why multi-bonded CO and formate are not observed in our cell. Interestingly, one experiment was performed with a Pt@C/Nafion composite film which was incubated inside the cell for several hours. Then a spectrum was taken under stationary conditions before introducing the fuel and the bridge-bonded CO was observed, located at 1850 cm^{-1} (not shown). As described in Chapter 2, the Pt@C particle film was made with ethanol in order to disperse the Pt nanoparticles. The self-decomposition of ethanol could happen on the surface of Pt, and the product CO_2 can build up this time as the cell is stationary. Therefore, the CO_2 molecules can have time to generate the multi-bonded CO.

5.4.5 A versatile method for studying a variety of catalysts and the support effect

It is well established that the properties of a catalyst rely on many factors: composition, size, morphology and support.[161,311,322-324] As shown in Figure 5-19 and Figure 5-21, the adsorbed CO oxidation experiments were performed on Pd@C and Pt@C, respectively. Although Pt and Pd both belong to group VIII, the catalytic properties in terms of CO desorption are different, proved by the difference in the onset potential for CO oxidation in the cyclic voltammograms. In comparison with SEIRA which has very strict requirement for the making of the thin film,[187] the method for making the particle film (3-D particle network) in our ATR-IR SEC cell is very versatile and convenient. It applies not only to the single metal system like Pd@C and Pt@C but also to the bimetallic system like PtRu@C. It can readily be adopted to study catalyst particles with different sizes or morphologies. It can also be extended to investigate not only the carbon support but also other supports, such as TiO_2 which is widely used in the solar energy field.[325] Therefore, the ATR-IR SEC technique developed and described in this Chapter provides a very broad range of opportunities for studying a variety of catalysts and the support effect.

5.5 Conclusions

In summary, an *in-situ* ATR-IR SEC cell with flow capability has been developed. The exchange of electrolyte and access of gas to the catalyst have been proved to be efficient. Formic acid oxidation catalysed by carbon-supported metal nanoparticles including Pt, Pd and PtRu has been examined by *in-situ* infrared spectroelectrochemistry. Carbon monoxide as a poisoning intermediate adsorbed onto the surface of catalyst is monitored as a function of applied potential. As the catalyst nanoparticle is immobilised onto the carbon particle, direct electrochemical control is achieved, proved by the potential-dependent CO building-up and oxidising-off during formic acid oxidation.

It should be now possible for the catalyst to be extended to a protein molecule. As discussed in Chapter 1, in protein film electrochemistry, an aliquot of enzyme is spotted onto a PGE electrode and forms a monolayer or submonolayer. The properties of the enzyme can then be investigated by controlling the potential. It has also been shown that protein electrochemistry can be recorded for proteins on graphite particles immobilised on an electrode, similar to the Pt@C electrodes discussed in this Chapter.[326,327] Therefore, it should be possible to examine protein-adsorbed on graphite or carbon nanoparticles by this ATR-IR SEC technique. With the built-in flow capability, the enzyme can be further investigated with a controllable supply of substrates and inhibitors. In Chapter 6, I will examine how this ATR-IR SEC technique can be applied to study the regulatory hydrogenase from *Ralstonia eutropha*. Preliminary ATR-IR SEC experiments are reported for this enzyme trapped in a particle network electrode, but future work should allow this to be extended to immobilised proteins.

Chapter 6

Infrared Spectroelectrochemical Investigation of *Ralstonia eutropha* Regulatory Hydrogenase

6.1 Infrared spectroelectrochemistry for studying hydrogenases

6.1.1 Methods for applying infrared spectroelectrochemistry to hydrogenase enzymes

In Chapter 3 and 4, *Re* SH and RH have been investigated by protein film electrochemistry and O_2-induced inactive states have been observed. However, electrochemistry alone cannot provide the structural information with regard to the ligands at the active site of the hydrogenase. In Chapter 5, formic acid oxidation catalysed by noble metals adsorbed on carbon particles has been studied as a test system for the ATR-IR SEC cell. This Chapter describes application of this ATR-IR SEC technique at graphite electrodes to a hydrogenase enzyme, *Re* RH. Essentially, the infrared spectroelectrochemistry is providing electrochemical control of the redox level of the hydrogenase enzymes during infrared monitoring of active site states.

Moss *et al.* developed an IR-SEC transmission cell for studying the *in-situ* conformational changes in cytochrome *c* with a combination of infrared spectroscopy and electrochemistry.[328] Based on it, Albracht and De Lacey *et al.* further applied this cell for studying hydrogenase enzymes.[111] The working electrode in this system is a 6 μm-thick, 70% transmitting gold mesh. A Pt foil counter electrode and an Ag/AgCl reference electrode, together with the Au mesh complete the three electrode configuration. The electrochemistry takes place in a thin layer of solution typically composed of 10 ~ 25 μL of *ca.* 1 mM hydrogenase enzyme (*ca.* 10 ~ 20 nmol of enzyme is required at this concentration). The thin layer requirement is to minimise the huge absorbance arising from the water, meaning a limited pathlength for the infrared radiation is required. The thin layer electrochemistry setup is lacking efficient substrate supply and product removal which will greatly affect the redox states of the hydrogenase enzymes. In most cases, redox mediators are always present to accelerate the electron transfer between the Au mesh and the hydrogenase molecule as the hydrogenase molecule is *ca.* 5 nm in diameter and is slow to diffuse to the working electrode.[111,114] Another limitation arising from the thin layer configuration in the transmission cell is that a relatively high concentration of enzyme is required to observe the signal (CO and CN^- stretching), but in practice some hydrogenase enzymes cannot be concentrated to 1 mM without causing denaturation. So far this is the most well-established IR-SEC technique for studying hydrogenase enzymes. A wide range of hydrogenases have been investigated through this transmission approach, including *A. vinosum* MBH,[113] *D. gigas* NiFe hydrogenase,[111] *D. fructosovorans* NiFe hydrogenase[112] and *D. desulfuricans* FeFe hydrogenase.[329] The midpoint potential for a redox transition can be obtained by fitting the plot of the integrated intensity of the main band (CO) in the absolute spectra versus applied potentials to the Nernst equation and the number of electrons involved in this process can also be obtained. Furthermore, the reaction kinetics can also be examined by plotting a semilogarithimic plot of the integrated intensity of the CO vibration band as a function of time. It was found that the activation of a standard NiFe hydrogenase such as the *D. gigas* (Ni-A to Ni-SU) enzyme under a reducing environment (-500 mV) follows first-order kinetics, only dependent on the Ni-A concentration. The rate constant can be calculated from the slope of the fitted line. The situation is similar in the redox transition of anaerobic inactivation (Ni-SI to Ni-B), which is relatively slow compared to the reverse process and is a first-order reaction.[111] Furthermore, the activation energy for the redox transition can be obtained by plotting a semilogarithimic plot of the rate constant as a function of different temperatures.[111]

As discussed in earlier Chapters, Osawa *et al.* developed a new approach SEIRA (Surface Enhanced Infrared Reflection Absorption) by combining the direct electrochemical control and *in-situ* infrared spectroscopy within an ATR configuration to study thin layer rough metal electrodes.[187] Based on this technique, Hildebrandt and coworkers used a similar cell setup to study *Desulfovibrio vulgaris* Miyazaki F NiFe hydrogenase and *R. eutropha* MBH.[115-117] The metal electrode (gold in this case) is critical for the surface enhancement. A thin layer of Au was coated on an ATR prism and further modified with a self-assembled monolayer (SAM) of amino-terminated mercaptane. Then the covalent protein immobilisation onto the Au surface was achieved through EDC/NHS coupling (EDC: 1-ethyl-3-[3-(dimethylamino)propyl]carbodiimide hydrochloride; NHS: *N*-hydroxysuccinimide). The working electrode is the enzyme modified Au layer coated onto the prism. The reference and counter electrode are placed in the solution above the working electrode, allowing a conventional electrochemistry cell geometry and good solute access. The immobilisation of the hydrogenases (*Desulfovibrio vulgaris* Miyazaki F NiFe hydrogenase and *R. eutropha* MBH) clearly works as the CO and CN^- bands at the active site observed by this method are consistent with the findings from the Moss cell.[115,117] Under 'ideal' conditions, the advantage with this SEIRA set-up is the direct electrochemical control of the redox potential level. Furthermore, the immobilised enzyme can work under catalytic turnover conditions whereas the transmission cell with a thin layer solution is greatly limited by electron and H_2 availability. The orientation of the covalently bound protein should also be highly uniform in theory, determined by the ordered configuration of the self-assembled monolayer modified on Au surface. As this approach is not dependent on the mediator or the diffusion of the enzyme, this direct electrochemical control in theory allows rapid time-resolved spectra to be taken, in conjuction with the step-scan (miliseconds) and rapid-scan (seconds) techniques. However, in practice, only a small portion of the hydrogenase responds rapidly to potential control under H_2, and it takes several hours to observe complete potential-dependent inactivation, indicating the electronic contact between the Au and the immobilised enzyme is not uniformly efficient.[116] Furthermore, the disadvantages related to the use of an Au surface exist. There is a risk of denaturing of the enzyme on the Au surface. Furthermore, H_2 evolution is catalysed by Au (*ca.* -0.8 V at neutral pH; the lower the pH, the higher the H_2 evolution potential)[330] and hydrogenases may perturb the alkanethiol layer on Au (a desorption of thiol layer below around -0.4 V)[331] which is used to immobilise the hydrogenase enzyme via the functional groups.[332] A third drawback is that a very limited number of hydrogenase enzymes are suitable for the EDC/NHS coupling because this relies on a patch of negatively charged residue close to the distal FeS cluster.[332]

6.1.2 Towards an ATR-IR SEC method for studying hydrogenases at carbon electrode

Considering the advantages and disadvantages of the two infrared spectroelectrochemical techniques described above, this project has explored preliminary development of a new *in-situ* ATR-IR SEC method for investigating the redox states of metalloenzymes under catalytic turnover conditions at a graphite electrode.[326]

6.2 Infrared spectroelectrochemical results of *Re* RH

6.2.1 Chemistry in the ATR-IR SEC cell

In order to characterise the O_2-inactivated state of the RHstop found by protein film electrochemistry as described in Chapter 4, a novel ATR-IR SEC cell with a flow capability has been built up, as described in Chapter 5. The ultimate goal is a method for studying hydrogenases adsorbed on the carbon particle. However, in contrast to the carbon-supported noble metal nanoparticle network described in Chapter 5, the RHstop studied in this Chapter is not directly immobilised onto the carbon particle due to the low coverage of the enzyme on the particles. Instead, the enzyme is dispersed into a Nafion-phosphate mixture but with carbon black particles closely packed around to exchange electrons, and this enzyme/carbon particle composite network has a 3-D geometry, as shown schematically in Figure 6-1. The detailed preparation of the enzyme/carbon particle composite network is described in Chapter 2, and the ATR geometry and conventional three-electrode configuration in the cell are as described in Chapter 5.

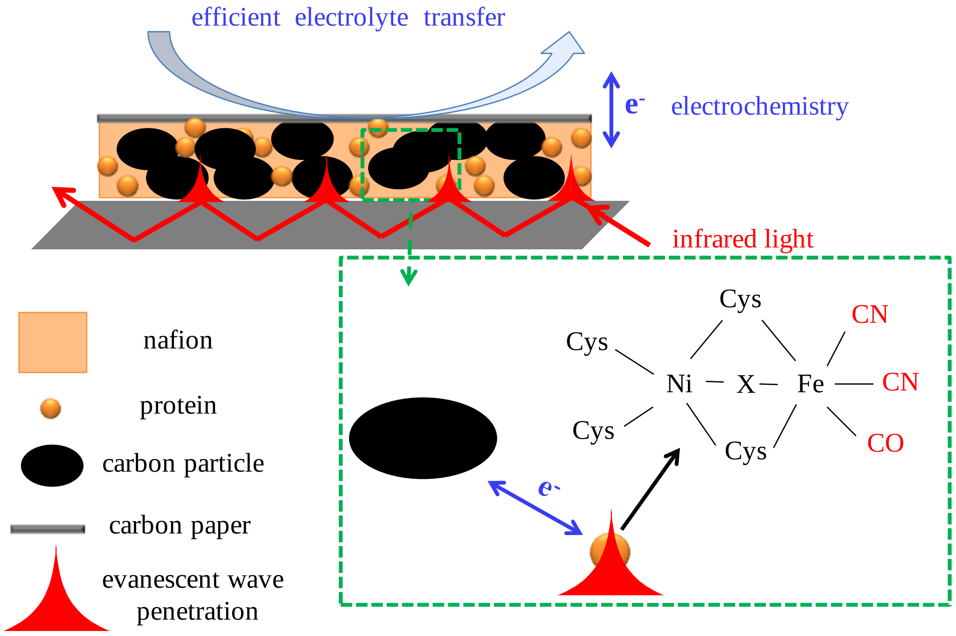

Figure 6-1. Chemistry at the interface of the enzyme/carbon particle composite network in the ATR-IR SEC cell.

Figure 6-1 depicts the configuration of the enzyme/carbon particle composite network in the ATR-IR SEC cell and the inset enlarges the infrared detection of CO and CN^- ligands coordinated to the Fe at the active site of the NiFe hydrogenase with electrochemical control. Unlike the direct potential control over formic acid oxidation catalysed by noble metals adsorbed on the carbon particles as described in Chapter 5, the electrochemical control level is adjusted for studying *Re* SH in this case, i.e., the potential is not directly applied on the enzyme. Although the carbon black particles are closely sitting around the enzyme molecules in the 3-D particle film, it still takes time for the protein to exchange electrons with the carbon particle due to slow diffusion of large enzyme molecules. Vibrations of the ligands (CO and CN^-) at the active site of the RHstop are infrared active and the corresponding infrared spectrum is very sensitive to changes in the redox state controlled by the applied potential or introduction of substrate (H_2) and inhibitors (CO and O_2).

6.2.2 IR spectrum of the RHstop without potential control

As-isolated RHstop

Figure 6-2 shows an ATR-IR spectrum of as-isolated RHstop in a network electrode as described above, processed against a spectrum of a water-filled cell with an unmodified prism. The enzyme electrode was prepared anaerobically inside the N_2-filled glove-box and mixed with Nafion, phosphate and carbon black particles, as described in Chapter 2. The carbon dioxide CO_2 bands are observed from CO_2 remaining in the sampling compartment, as the characteristic double peak around 2350 cm^{-1}. The Amide I and II bands of the RHstop are readily distinguished by their sharp peaks located at 1645 and 1543 cm^{-1}, which are related to the stretching of the C=O and a combination of N-H bending and C-N stretching arising from the peptide chain, respectively.[333] In protein-related infrared spectroscopy, the amide bands can be used as a marker to examine the presence of the enzyme. Therefore, it can be concluded from the obvious amide bands that the RHstop/carbon particle composite network is close to the Si prism in the ATR-IR SEC cell and the ligands (CO and CN^-) arising from the active site of the enzyme can be spectroscopically detected, as shown in the inset of Figure 6-2. The H_2O and Nafion-phosphate features are indicated by the grey boxes in Figure 6-2. As they are very strong and broad, it is not easy to detect other species which absorb in these regions. Fortunately, vibrational bands arising from CO and CN^- at NiFe hydrogenase active sites fall in the region between approximately 2150 and 1850 cm^{-1}. This region is relatively clean and flat, thereby providing the possibility to observe any tiny changes in the redox states of the active centre of the RHstop. In the inset, the stretching band of CO coordinated at the Fe site is centred at 1943 cm^{-1} whereas the stretching vibrations of CN^- ligands are located at 2080 cm^{-1} and 2072 cm^{-1}, respectively. The as-isolated state for RHstop is termed as Ni_a-S as it is active for H_2 oxidation even in its as-isolated form but silent in the EPR spectrum.[148] The infrared spectra of the as-isolated RHstop recorded in this ATR-IR SEC cell correspond well with the reported findings from experiments in a transmission cell, including the wavenumber (υ(CO): 1943 cm^{-1}, $\upsilon(CN^-)$:

2080 and 2072 cm^{-1}), the relative intensity and shape of the three bands.[148,246,334] The amount of the protein used in this ATR-IR SEC cell should be emphasised: as mentioned in Chapter 2, the overall quantity of the enzyme in a particle-Nafion network was around 1 nmol which is very promising for studies on low availability enzyme samples.

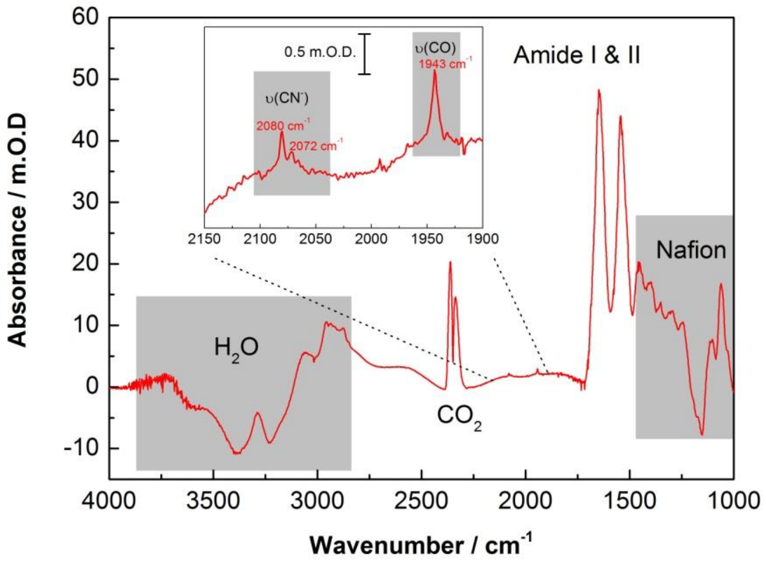

Figure 6-2. A spectrum of an as-isolated RHstop film recorded in the ATR-IR SEC cell. The inset is an enlargement of the CO and CN^- region in which the 1943 cm^{-1} peak corresponds to the vibration of the CO bound to the active site and the double peaks at 2080 cm^{-1} and 2072 cm^{-1} are arising from the two CN^- ligands. The grey squares are features of the water band and Nafion-phosphate which are the constituents of the enzyme network. The Amide I & II bands and the CO_2 bands are also indicated. Other conditions: the spectrum represents an average of 500 co-added scans recorded at a resolution of 2 cm^{-1} and is taken against a background of a water-filled cell with a ‘clean’ prism.

H_2-incubated RHstop

Although the RHstop is purified in air, it is active for H_2 oxidation even at its as-isolated state, as demonstrated in Chapter 4. In order to demonstrate spectroscopically that the RHstop is active and able to react with H_2, an experiment was designed to incubate the enzyme with H_2. The RHstop particle network was made inside the N_2-filled glove-box and further incubated with 1% H_2 buffer before the IR measurement. Compared to the as-isolated state as shown above, the H_2-incubated RHstop shows a different redox state as a dramatic shift in the wavenumber of CO is observed, as shown in Figure 6-3. Notably, the υ(CO) is centred at

1961 cm^{-1} even though the H_2 concentration is only 1% in N_2 whereas the υ(CO) is located at 1943 cm^{-1} in the as-isolated state. The CN^- bands are centred at 2083 and 2071 cm^{-1}, respectively. This H_2-incubated treatment induces a new state termed as Ni_a-C which is EPR-detectable and resembles the Ni-C state in other NiFe hydrogenases.[148] It is widely accepted that there is a bridging hydride between the Ni and Fe sites in the Ni-C state.[335] Four-pulse ESEEM (hyperfine sublevel correlation, HYSCORE) and pulse electron nuclear double resonance (ENDOR) spectroscopy measurements reported by Lubitz and co-workers on *Re* RH have confirmed that there is a hydride ion bridging the Ni and the Fe site.[43] As a new bond related to the bridging hydride H^- is formed, the electron density on the Fe site will correspondingly change. The shift of the υ(CO) to higher wavenumber indicates that the π-backbonding by accepting electrons from the metal Fe decreases. After H_2 incubation, the active site of RHstop should be more reduced than the isolated state, therefore, the π-backbonding from the metal to the CO ligand bound to Fe should increase, causing a lower υ(CO). This upward shift in υ(CO) can be explained by the fact that this transition Ni_a-S to Ni-C is a H^+ coupled step in which the oxidation state of Ni changes from +2 (EPR-silent) to +3 (EPR-active) and a bridging H^- is formed, indicating that the electron density on Fe should decrease as well. Thus a higher υ(CO) is observed in the Ni-C state. In contrast to CO which is a stronger π-acceptor and barely a σ-donor, the ligand CN^- is a stronger σ-donor but at the same time can also be a π-acceptor, therefore buffering the change in the wavenumber as these two effects have opposite contributions to the bond strength. This explains why the wavenumber of CN^- does not change as much as that of CO during the transition. In summary, the two reported states Ni_a-S and Ni-C of the RH are observed using this ATR-IR cell economically (around 1 nmol sample).

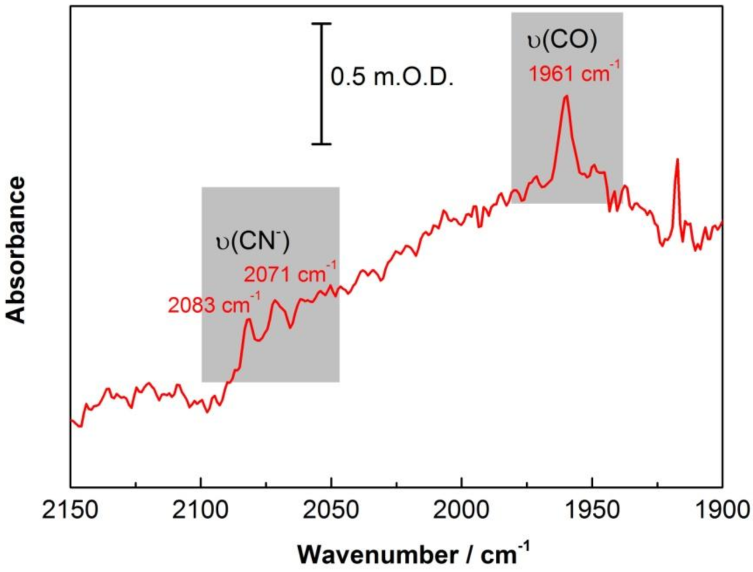

Figure 6-3. A spectrum of a H_2-incubated RHstop network recorded in the ATR-IR SEC cell. The CO and CN^- regions are marked by the grey boxes. Other conditions: the spectrum represents an average of 500 co-added scans recorded at a resolution of 2 cm^{-1} and is taken against a background of a water-filled cell with a 'clean' prism.

6.2.3 RHstop in the ATR-IR SEC cell with potential control

RHstop in the ATR-IR cell with potential control

Then electrochemical control was added, taking advantage of the widely dispersed carbon particles. Again, a RHstop/carbon particle network was made inside the N_2-filled glove-box anaerobically. Figure 6-4 shows the redox states of RHstop when applying different potentials. The working electrode was initially held at an oxidative potential +200 mV, as shown by the black line in Figure 6-4. The υ(CO) is centred at 1943 cm^{-1} and the other two CN^- peaks are located at 2080 and 2072 cm^{-1}, respectively. The state of the RHstop at +200 mV is the as-isolated Ni_a-S state, as shown in Figure 6-2. Then a reductive potential was applied at -500 mV as shown by the red line and the corresponding absorption peak of CO shifts significantly. The state of the RHstop at -500 mV is almost identical to the H_2-incubated state, as shown in Figure 6-3. When applying a low potential such as -500 mV, the RHstop should be capable of catalysing H^+ reduction at pH 6.0 proved by protein film electrochemistry (Chapter 4), with electrons passed through the dispersed carbon particles to the enzyme. Therefore, this electrochemical control is playing a similar role as the incubation with H_2. On the other hand, when applying a positive potential such as +200 mV, the working electrode is biased to accept the electrons from the enzyme through the carbon particles thus this oxidative potential is similar as exposure to O_2 (the RHstop is purified in air). The background spectrum was collected using a water-filled cell with an unmodified prism, therefore, the absolute spectra are shown here. Due to the slight difference in water environments experienced by an enzyme-particle-network modified prism and an unmodified one, the background in the informative infrared window for hydrogenases (2150-1900 cm^{-1}) is a little bumpy, but the absorption peaks of CO and CN^- are still obvious although no base-line correction is applied.

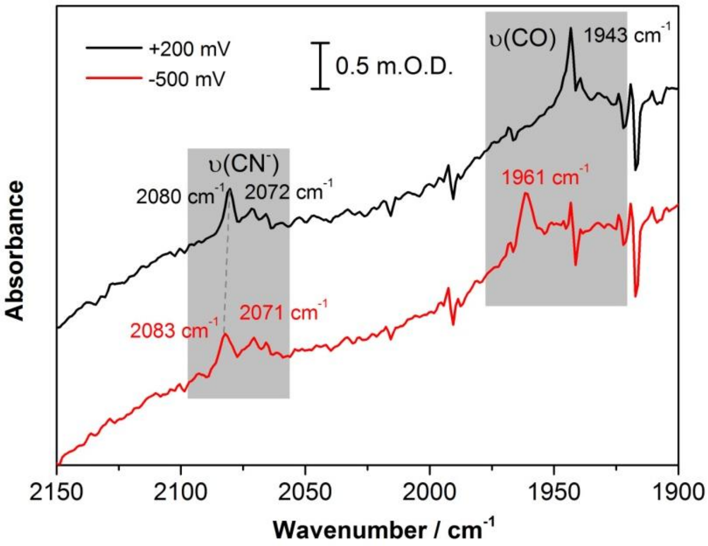

Figure 6-4. The absolute spectrum of a RHstop particle network in the ATR-IR SEC cell. The enzyme composite network was made inside the N_2-filled glove-box anaerobically. The black spectrum was collected while the potential was held at +200 mV at room temperature. The red spectrum was collected at -500 mV. Other conditions: the spectrum represents an average of 500 co-added scans recorded at a resolution of 2 cm^{-1} and is taken against a background of a water-filled cell with a 'clean' prism.

Response time to a potential step

An important question is how long the enzyme network takes to respond to a potential step. In order to examine the response time, an experiment was designed on RHstop by stepping down the potential from a high value (+200 mV) to a low value (-500 mV). The background spectrum was collected when the potential was held at +200 mV, and a difference spectrum was taken at 2 minutes after stepping down the potential to -500 mV, as shown on the left panel (black) in Figure 6-5. Clearly, the Ni-C population (υ(CO): 1961 cm^{-1}) in RHstop increases whereas the Ni$_a$-S (υ(CO): 1943 cm^{-1}) decreases, indicated by the black arrows. Then, a second spectrum was collected after holding at -500 mV for 7 minutes to examine whether there is further transformation from Ni$_a$-S to Ni-C. Only a slight increase in the 1961 cm^{-1} peak is observed, implying 90% of the transition is finished within around 5 min as it takes around 3 min to collect a spectrum (250 co-added scans at a resolution of 2 cm^{-1}). In the end, a third spectrum at 14 min (blue) was collected and no further transition is observed compared to the 7-min spectrum. Therefore, it takes around 10 min for complete conversion of the enzyme network in the ATR-IR cell in response to a potential step.

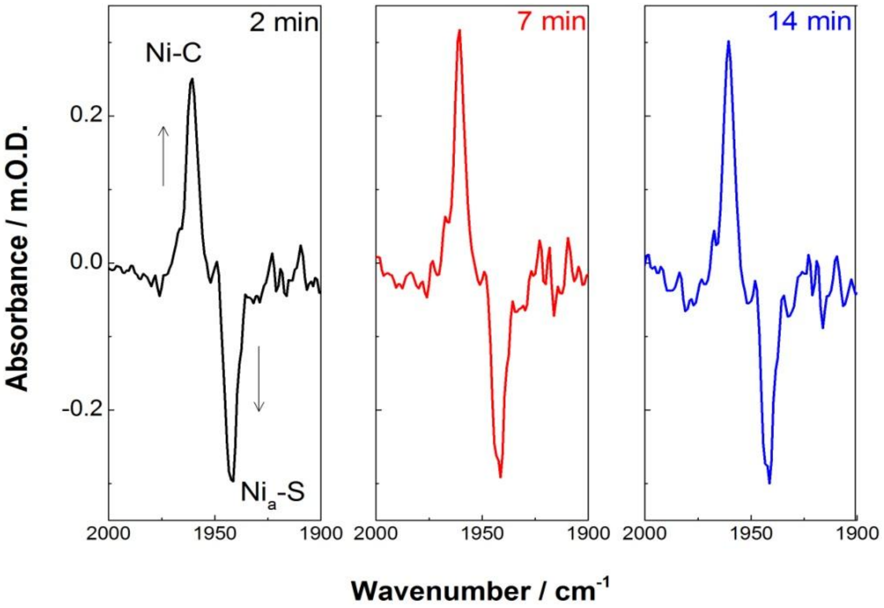

Figure 6-5. Difference infrared spectra of a RHstop particle network in the ATR-IR SEC cell. The film was made inside the N_2-filled glove-box anaerobically. The spectra were collected while the potential was held at -500 mV for different periods. The red spectrum was collected at -500 mV. Other conditions: the spectrum represents an average of 250 co-added scans recorded at a resolution of 2 cm^{-1} and is taken against a background of spectrum at +200 mV.

Redox titration of RHstop

A redox titration of the interconversion of Ni_a-S and Ni-C was performed as shown in Figure 6-6 by stepwise control of the applied potential. Figure 6-6(A) shows the process of stepping the potential from +200 mV to -500 mV and then back to +200 mV at a step of ±100 mV. Through applying reductive poises as shown by the black line in Figure 6-6(A), a difference spectrum is presented for the -500 mV shown by the black line in Figure 6-6(B), processed against the -200 mV spectrum. It clearly demonstrates the increase of the Ni-C state indicated by the corresponding 1961 cm^{-1} peak. On the reverse process, i.e., through applying the oxidative poises shown by the red trace in Panel A, a difference spectrum is shown by the red line in Panel B for the +200 mV spectrum, processed against the -500 mV one. It is clear that a population of the Ni_a-S state increases as the corresponding 1943 cm^{-1} peak goes upward. The whole experiment took *ca.* 6 hours as shown in Panel A, demonstrating the enzyme within the cell is still intact and active on the time scale of hours. The transformation from Ni_a-S to Ni-C or reverse is therefore reversible, as shown in Panel B.

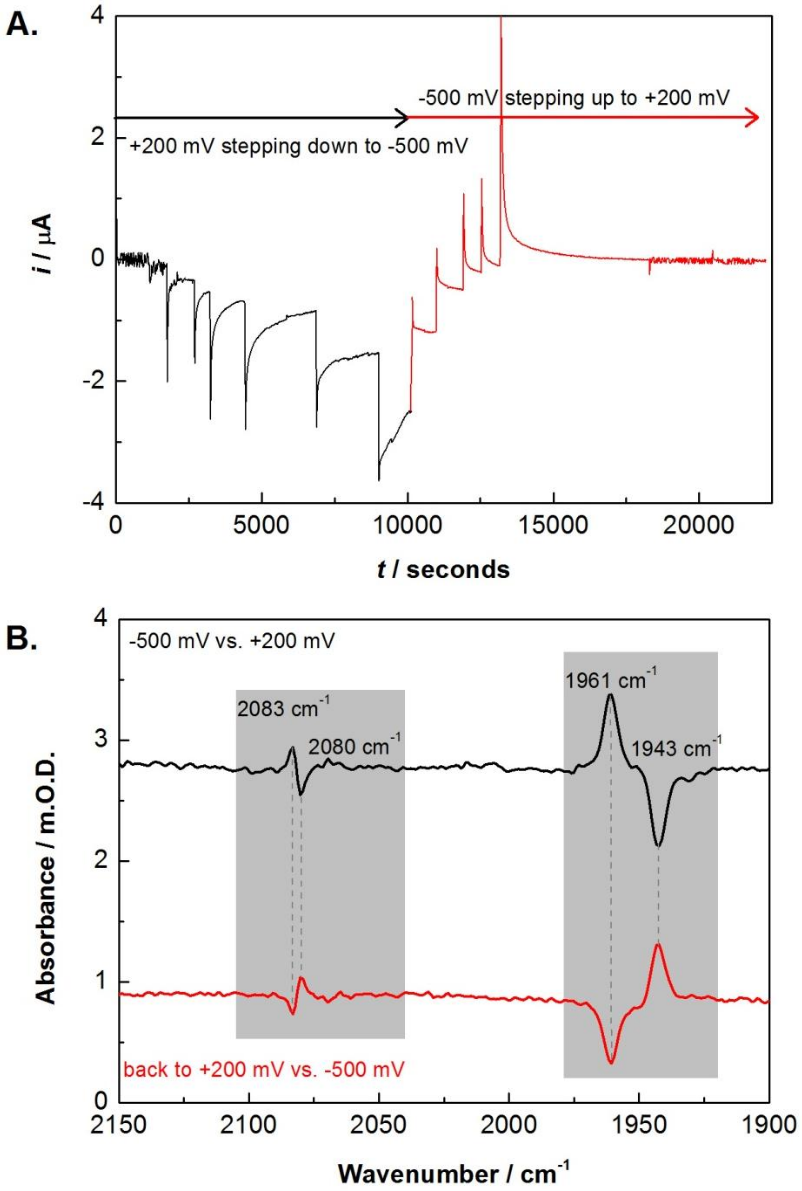

Figure 6-6. Infrared spectroelectrochemical investigation of a RHstop particle network in the ATR-IR SEC cell. The protein film was made inside the N_2-filled glove-box anaerobically. Panel A: The electrochemical control over the enzyme network through stepping the potential between +200 and -500 mV. The potential was initially set at +200 mV, then stepped down -500 mV (in black) and back to +200 mV (in red) at a step of ±100 mV. Panel B: The difference infrared spectrum of -500 mV vs. +200 mV (in black) and back to +200 mV vs. -500 mV (in red). The black line represents the spectrum taken at -500 mV, processed against the +200 mV, and the corresponding electrochemistry is shown in black in Panel A. The red line represents the spectrum was taken when the potential was stepped back to +200 mV as shown in the red line in Panel A, processed against the -500 mV spectrum. Each spectrum represents an average of 500 co-added scans recorded at a resolution of 2 cm^{-1}.

The ratio of Ni_a-S (black closed circles, indicated by the 1943 cm^{-1} band) and Ni-C (red closed squares, indicated by the 1961 cm^{-1} band) over the overall concentration of Ni_a-S and Ni-C is plotted as a function of applied potential, respectively, as shown in Figure 6-7. Furthermore, this plot can be fitted to the Nernst equation for a one-electron process, as shown in eqn [6-1]. The fitted black line represents the transformation from Ni_a-S to Ni-C when the potential is stepped down to lower values. No obvious changes happen until-200 mV is reached in the negative direction to observe Ni-C. In each step, the potential is set at the indicated value for 15 min before taking the spectrum which ensures that the equilibrium is reached. The red fitted line represents the transformation from Ni-C to Ni_a-S. The reappearance of Ni_a-S state starts after -500 mV. The midpoint potential ($E_m^{'}$) for the transformation Ni_a-S/Ni-C of -340 mV at pH 6.0 is obtained by fitting the data to Nernst equation.

$$E_1 = E_1^0 + \frac{RT}{nF}\ln\frac{[\mathrm{Ox}_1]}{[\mathrm{Red}_1]} \qquad [6\text{-}1]$$

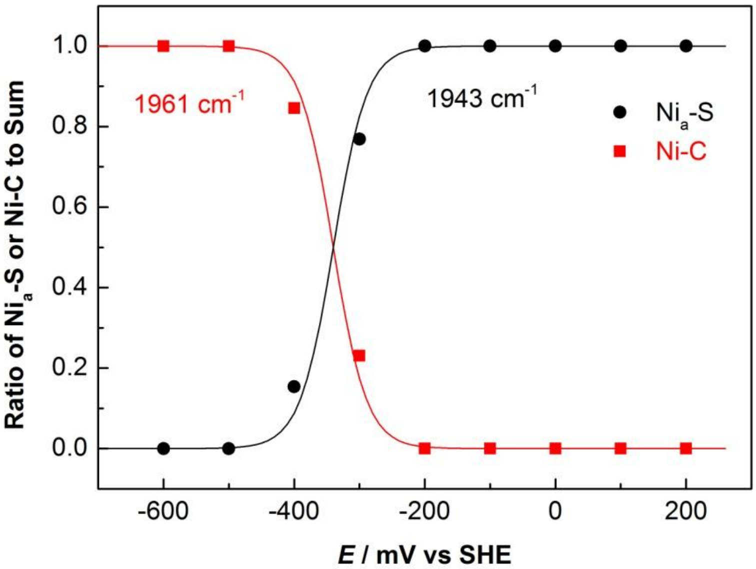

Figure 6-7. Redox titrations of the active site of RHstop by ATR-IR SEC: closed square, Ni-C signal, 1961 cm^{-1}; closed circles, Ni_a-S signal, 1943 cm^{-1}. Lines: fit to the data for a 1 e^- transformation with E_m = -340 mV.

6.2.4 RHstop in the ATR-IR SEC cell with flow and potential control

O_2 introduction under N_2

As demonstrated by protein film electrochemistry (Chapter 4), the as-isolated RHstop is active for H_2 oxidation even though it is purified in air. Therefore, a RHstop particle network was made anaerobically and 10% O_2 in N_2-saturated buffer was later flowed into the cell (with the aid of the pump as described in Chapter 5) to examine the reaction of the enzyme with O_2. A high potential (+200 mV) was held to avoid O_2 reduction at carbon particles. However, no new states occurred and only the Ni_a-S state was observed, implying that RHstop in the Ni_a-S state is not reacting with O_2. This finding is consistent with the electrochemical results. As the enzyme is purified in air, there is no reason for it to further react with O_2. As found by protein film electrochemistry, the condition for observing an O_2-inactivated state includes a H_2 environment which might be crucial for generating the O_2-inactive species.

RHstop under H_2 at +200 mV

A RHstop particle film was then made inside the N_2-filled glove-box anaerobically and incubated with a high concentration of H_2. A spectrum was collected when the potential was held at +200 mV, as shown in Figure 6-8. In comparison with the RHstop at +200 mV without H_2 which only shows the Ni_a-S state, the RHstop at +200 mV with H_2 around shows both states of Ni_a-S and Ni-C which are characteristic for the 1943 and 1961 cm^{-1} peaks in the IR spectra, respectively. The oxidative potential +200 mV in this case drives the RHstop into the Ni_a-S state as discussed for Figure 6-4. However, at the same time the H_2 molecules around the protein favour the transition to Ni-C state as demonstrated in Figure 6-3. The reason for the mixed states under this condition is possibly related to the configuration of the enzyme/carbon particle network. As shown in Figure 6-1, the enzyme is not directly anchored onto the surface of the carbon black particle which functions to enhance electrical contact between the carbon paper and the protein molecules. As the electrochemical control was not directly applied to the protein molecule, it took time to exchange electrons between the enzyme and the carbon paper, arising from slow diffusion of the hydrogenase molecule.

This experiment was designed initially for the O_2 inactivation measurement and a low concentration of O_2 was introduced with the aid of O_2-saturated buffer supplied to the uppersection of the cell via a peristaltic pump. However, no new states or change in the ratio of the two states (Ni-C and Ni_a-S) was observed. One possible explanation is that even though a new O_2-inactivated state was generated, it would be immediately reactivated by the H_2 molecule trapped in the enzyme particle network or by remaining active hydrogenase molecules. In order to minimise the H_2 effect as a reducing agent to activate the enzyme, 1% H_2 was used to incubate with the enzyme because H_2 is also a requirement for generating an O_2-inactive species found by electrochemistry. However, still no signs of O_2-inactive states were observed. The most likely possibility is that the O_2-inactivated state is a short-lived species, further implying that direct immobilisation of the enzyme onto the carbon particles is crucial for providing direct potential control to the enzyme and observing any short-lived species.

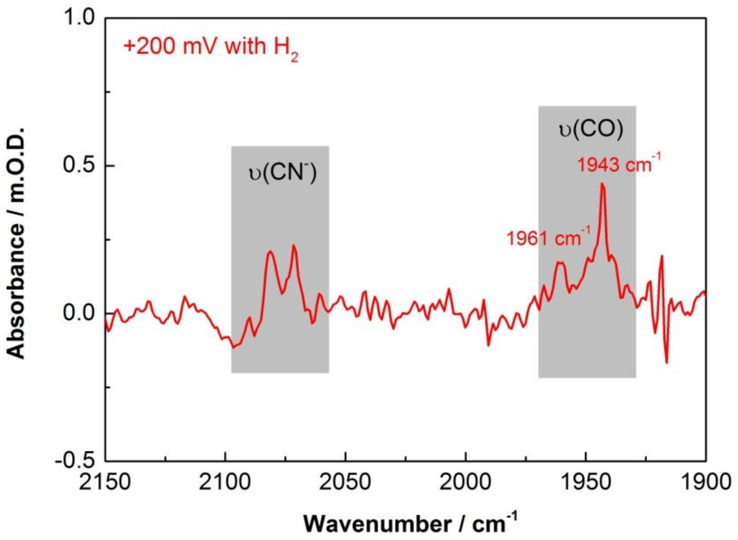

Figure 6-8. The absolute spectrum of a RHstop particle network in the ATR-IR SEC cell. The particle network was made inside the N_2-filled glove-box anaerobically and incubated with high concentration of H_2. The spectrum was collected while the potential was held at +200 mV at room temperature. Other conditions: the spectrum represents an average of 500 co-added scans recorded at a resolution of 2 cm^{-1} and is taken against a background of a water-filled cell with a 'clean' prism.

6.3 Discussion and Conclusions

6.3.1 Demonstration of an ATR-IR SEC method for studying proteins at a carbon electrode

All infrared spectroelectrochemistry reported so far for hydrogenase has been done at gold, as discussed in **Section 6.1**. This study shows that it is possible to use carbon particles as the working electrode and this doesn't have to slow down the response time to potential steps, as demonstrated by Figure 6-5. Furthermore, the enzyme remains catalytically active in the Nafion/carbon composite network on the time scale of at least 6 hours. It has been demonstrated that it is possible to control the redox level of the enzyme without mediators, as shown by the redox titration in Figure 6-6. In the absence of mediators, the enzyme must be exchanging electrons effectively with the widely dispersed carbon particles, and enzyme diffusion is reasonably rapid even in viscous Nafion: it typically takes 10 minutes to reach equilibrium following a potential step. It is still too slow to sustain rapid catalytic turnover, but does avoid need for a complex cocktail of mediators. Furthermore, this ATR-IR SEC cell is equipped with a flow capability, ensuring that substrate or inhibitor can be flowed in during an experiment which is not possible in thin layer transmission as in Moss cell. Carbon electrodes open up wider opportunities for future infrared spectroelectrochemistry as they can provide a wider potential range than Au because carbon is good down to -0.8 V, and is chemically inert (It is found that Au can react with CN^- that are important ligands bound to Fe at the active site of hydrogenases). Apart from the science advantages for studying hydrogenases with this ATR-IR cell, it also provides a relatively economic way because it has been demonstrated that even 1 nmol of protein works well.

6.3.2 Redox states of *Re* RH

Two states Ni-C and Ni_a-S are observed as in earlier spectroscopic studies. It is likely that other states (including O_2 and CO inhibited states, as detected by protein film electrochemistry in

Chapter 4) are generated during catalysis but are not long-lived enough to be seen. The redox titration has proved that the interconversion of these two states is achievable and reversible. The Ni$_a$-S species under N_2 failed to further react with O_2, as the enzyme is purified in air. However, experiments with H_2 also failed to reveal a new state (as detected by protein film electrochemistry in Chapter 4). This may be because the O_2-inactivated species is short-lived and the potential control over the enzyme is not direct, arising from the configuration of the enzyme (RHstop) in the composite network as shown in Figure 6-1. However, experiments shown in this Chapter give a useful evaluation about the amount of enzyme (1-2 nmol of RHstop) required to be observed spectroscopically through vibrations of CO and CN^- ligands at the active site. As described in Chapter 2, around 1.5 μL of 10 mg/mL carbon black (Vulcan XC72) is used to make this enzyme composite network. Due to the requirement of the penetration depth (see calculation in Chapter 2), the network cannot be too thick. A reported value of the BET (Brunauer-Emmet-Teller) surface area of Vulcan XC72 is *ca.* 250 m^2/g,[336] therefore the total surface area of the carbon particle sample used for making the composite network in this ATR-IR cell is calculated to be *ca.* 40 cm^2. Although the coverage of *Re* RH in this case is not known, the coverage of *Av* MBH adsorbed on a PGE electrode is estimated to be in the range of 3-12 pmol/cm^2.[337] As *Av* MBH is a hydrogenase that gives a relatively high coverage, 1 pmol/cm^2 is used to estimate the loading of *Re* RH achievable if directly adsorbed on carbon particles. Therefore, an amount of 40 pmol ($40\ cm^2 \times 1\ pmol/cm^2$) adsorbed RH is achievable in the SEC network. At least a 25-fold increase (1 nmol / 40 pmol) in enzyme loading is therefore required to get 1 nmol in the film if the enzyme is anchored onto the carbon particle directly. In order to achieve this goal, an increase in enzyme coverage or use of smaller carbon particles (the Vulcan XC72 carbon black is around 50 μm in diameter as described in Chapter 2) for enzyme immobilisation will be necessary.

6.3.3 Future work

Future work is now needed, beyond the scope of this study to develop methods for studying hydrogenases adsorbed directly on carbon particle electrodes (perhaps in nano size) and use them to characterise states of *Re* RH, especially to investigate the reaction of the enzyme with O_2 or CO under certain conditions. Furthermore, it would also be beneficial to apply similar methods for studying the SH because O_2 can inactivate the SH under certain conditions and it seems that more than one O_2-inactivated species is generated, as observed by protein film electrochemistry. This study has contributed preliminary developments in the area of SEC at carbon electrodes which should have wide applications in future studies of protein redox chemistry.

References

1. R. Cammack, M. Frey and R. Robson, *Hydrogen as a Fuel : Learning from Nature*, Taylor and Francis, London and New York, 2001.
2. N. Wilberg, *Inorganic Chemistry*, Academic Press, London, 2001.
3. K. Schutz, T. Happe, O. Troshina, P. Lindblad, E. Leitao, P. Oliveira and P. Tamagnini, *Planta*, 2004, **218**, 350-359.
4. M. L. Ghirardi, *Indian J. Biochem. Biophys.*, 2006, **43**, 201-210.
5. M. L. Ghirardi, M. C. Posewitz, P. C. Maness, A. Dubini, J. P. Yu and M. Seibert, *Annu. Rev. Plant Biol.*, 2007, **58**, 71-91.
6. R. Conrad, C. Erkel and W. Liesack, *Curr. Opin. Biotech.*, 2006, **17**, 262-267.
7. M. W. W. Adams, *Biochim. Biophys. Acta, Bioenerg.*, 1990, **1020**, 115-145.
8. D. R. Lovley, D. E. Holmes and K. P. Nevin, *Adv. Microb. Physiol.*, 2004, **49**, 219-286.
9. R. Knowles, *Microbiol. Rev.*, 1982, **46**, 43-70.
10. J. A. Cracknell, A. F. Wait, O. Lenz, B. Friedrich and F. A. Armstrong, *Proc. Natl. Acad. Sci. U. S. A.*, 2009, **106**, 20681-20686.
11. T. Burgdorf, O. Lenz, T. Buhrke, E. van der Linden, A. K. Jones, S. P. J. Albracht and B. Friedrich, *J. Mol. Microbiol. Biotechnol.*, 2005, **10**, 181-196.
12. R. Conrad, *Microbiol. Rev.*, 1996, **60**, 609-640.
13. D. R. Lovley, *Appl. Environ. Microbiol.*, 1985, **49**, 1530-1531.
14. H. D. Kluber, S. Lechner and R. Conrad, *FEMS Microbiol. Ecol.*, 1995, **16**, 167-175.
15. P. Constant, S. P. Chowdhury, L. Hesse, J. Pratscher and R. Conrad, *Appl. Environ. Microbiol.*, 2011, **77**, 6027-6035.
16. P. M. Vignais and B. Billoud, *Chem. Rev.*, 2007, **107**, 4206-4272.
17. L. F. Wu and M. A. Mandrand, *FEMS Microbiol. Rev.*, 1993, **104**, 243-270.
18. P. M. Vignais, B. Billoud and J. Meyer, *FEMS Microbiol. Rev.*, 2001, **25**, 455-501.
19. S. Shima and R. K. Thauer, *Chem. Rec.*, 2007, **7**, 37-46.
20. J. C. Fontecilla-Camps, A. Volbeda, C. Cavazza and Y. Nicolet, *Chem. Rev.*, 2007, **107**, 4273-4303.
21. C. S. A. Baltazar, M. C. Marques, C. M. Soares, A. M. De Lacey, I. A. C. Pereira and P. M. Matias, 2010, 948-962.
22. S. Shima, O. Pilak, S. Vogt, M. Schick, M. S. Stagni, W. Meyer-Klaucke, E. Warkentin, R. K. Thauer and U. Ermler, *Science*, 2008, **321**, 572-575.
23. A. L. De Lacey, V. M. Fernandez, M. Rousset and R. Cammack, *Chem. Rev.*, 2007, **107**, 4304-4330.
24. P. M. Vignais and A. Colbeau, *Curr. Issues Mol. Biol.*, 2004, **6**, 159-188.
25. A. Volbeda, M. H. Charon, C. Piras, E. C. Hatchikian, M. Frey and J. C. Fontecilla-Camps, *Nature*, 1995, **373**, 580-587.
26. A. Volbeda, E. Garcin, C. Piras, A. L. De Lacey, V. M. Fernandez, E. C. Hatchikian, M. Frey and J. C. FontecillaCamps, *J. Am. Chem. Soc.*, 1996, **118**, 12989-12996.

27. K. A. Bagley, C. J. Vangarderen, M. Chen, E. C. Duin, S. P. J. Albracht and W. H. Woodruff, *Biochemistry*, 1994, **33**, 9229-9236.
28. K. A. Bagley, E. C. Duin, W. Roseboom, S. P. J. Albracht and W. H. Woodruff, *Biochemistry*, 1995, **34**, 5527-5535.
29. R. P. Happe, W. Roseboom, A. J. Pierik, S. P. J. Albracht and K. A. Bagley, *Nature*, 1997, **385**, 126.
30. Y. Higuchi, T. Yagi and N. Yasuoka, *Structure*, 1997, **5**, 1671-1680.
31. Y. Montet, P. Amara, A. Volbeda, X. Vernede, E. C. Hatchikian, M. J. Field, M. Frey and J. C. FontecillaCamps, *Nat. Struct. Biol.*, 1997, **4**, 523-526.
32. P. M. Matias, C. M. Soares, L. M. Saraiva, R. Coelho, J. Morais, J. Le Gall and M. A. Carrondo, *J. Biol. Inorg. Chem.*, 2001, **6**, 63-81.
33. E. Garcin, X. Vernede, E. C. Hatchikian, A. Volbeda, M. Frey and J. C. Fontecilla-Camps, *Struct. Fold. Des.*, 1999, **7**, 557-566.
34. W. Lubitz, E. Reijerse and M. van Gastel, *Chem. Rev.*, 2007, **107**, 4331-4365.
35. Y. Higuchi, F. Toujou, K. Tsukamoto and T. Yagi, *J. Inorg. Biochem.*, 2000, **80**, 205-211.
36. Y. Higuchi, H. Ogata, K. Miki, N. Yasuoka and T. Yagi, *Struct. Fold. Des.*, 1999, **7**, 549-556.
37. C. Fichtner, C. Laurich, E. Bothe and W. Lubitz, *Biochemistry*, 2006, **45**, 9706-9716.
38. S. Foerster, M. Stein, M. Brecht, H. Ogata, Y. Higuchi and W. Lubitz, *J. Am. Chem. Soc.*, 2003, **125**, 83-93.
39. M. E. Pandelia, H. Ogata and W. Lubitz, *Chemphyschem*, 2010, **11**, 1127-1140.
40. P. W. Atkins, *Physical Chemistry*, Oxford University Press, Oxford, 2006.
41. M. Stein, E. van Lenthe, E. J. Baerends and W. Lubitz, *J. Am. Chem. Soc.*, 2001, **123**, 5839-5840.
42. C. Stadler, A. L. De Lacey, Y. Montet, A. Volbeda, J. C. Fontecilla-Camps, J. C. Conesa and V. M. Fernandez, *Inorg. Chem.*, 2002, **41**, 4424-4434.
43. M. Brecht, M. van Gastel, T. Buhrke, B. Friedrich and W. Lubitz, *J. Am. Chem. Soc.*, 2003, **125**, 13075-13083.
44. A. Volbeda, L. Martin, C. Cavazza, M. Matho, B. W. Faber, W. Roseboom, S. P. J. Albracht, E. Garcin, M. Rousset and J. C. Fontecilla-Camps, *J. Biol. Inorg. Chem.*, 2005, **10**, 239-249.
45. C. C. Page, C. C. Moser and P. L. Dutton, *Curr. Opin. Chem. Biol.*, 2003, **7**, 551-556.
46. D. Leys and N. S. Scrutton, *Curr. Opin. Struct. Biol.*, 2004, **14**, 642-647.
47. M. Teixeira, I. Moura, A. V. Xavier, J. J. G. Moura, J. Legall, D. V. Dervartanian, H. D. Peck and B. H. Huynh, *J. Biol. Chem.*, 1989, **264**, 16435-16450.
48. M. Rousset, Y. Montet, B. Guigliarelli, N. Forget, M. Asso, P. Bertrand, J. C. Fontecilla-Camps and E. C. Hatchikian, *Proc. Natl. Acad. Sci. U. S. A.*, 1998, **95**, 11625-11630.
49. R. Bingemann and A. Klein, *Eur. J. Biochem.*, 2000, **267**, 6612-6618.
50. S. Dementin, V. Belle, P. Bertrand, B. Guigliarelli, G. Adryanczyk-Perrier, A. L. De Lacey, V. M. Fernandez, M. Rousset and C. Leger, *J. Am. Chem. Soc.*, 2006, **128**, 5209-5218.
51. R. Cammack, V. M. Fernandez and E. C. Hatchikian, *Methods Enzymol.*, 1994, **243**, 43-68.
52. V. M. Fernandez, E. C. Hatchikian and R. Cammack, *Biochim. Biophys. Acta Prot. Struct. Mol. Enzym.*, 1985, **832**, 69-79.

53. K. Schneider and H. G. Schlegel, *Biochim. Biophys. Acta Protein Struct. Mol. Enzymol.*, 1976, **452**, 66-80.

54. F. A. Armstrong, H. A. O. Hill and N. J. Walton, *J. Electrochem. Soc.*, 1983, **130**, C117-C117.

55. K. A. Vincent, A. Parkin and F. A. Armstrong, *Chem. Rev.*, 2007, **107**, 4366-4413.

56. F. A. Armstrong and J. Hirst, *Proc. Natl. Acad. Sci. U. S. A.*, 2011, **108**, 14049-14054.

57. A. Parkin, J. Seravalli, K. A. Vincent, S. W. Ragsdale and F. A. Armstrong, *J. Am. Chem. Soc.*, 2007, **129**, 10328-10329.

58. Y. B. Zu, R. J. Shannon and J. Hirst, *J. Am. Chem. Soc.*, 2003, **125**, 6020-6021.

59. L. Dos Santos, V. Climent, C. F. Blanford and F. A. Armstrong, *Phys. Chem. Chem. Phys.*, 2010, **12**, 13962-13974.

60. V. Fourmond, B. Burlat, S. Dementin, M. Sabaty, P. Arnoux, E. Etienne, B. Guigliarelli, P. Bertrand, D. Pignol and C. Leger, *Biochemistry*, 2010, **49**, 2424-2432.

61. C. Leger, S. Dementin, P. Bertrand, M. Rousset and B. Guigliarelli, *J. Am. Chem. Soc.*, 2004, **126**, 12162-12172.

62. O. Lenz, M. Ludwig, J. A. Cracknell, K. A. Vincent and F. A. Armstrong, *J. Biol. Chem.*, 2009, **284**, 465-477.

63. K. S. Chen, J. Hirst, R. Camba, C. A. Bonagura, C. D. Stout, B. K. Burgess and F. A. Armstrong, *Nature*, 2000, **405**, 814-817.

64. A. K. Jones, S. E. Lamle, H. R. Pershad, K. A. Vincent, S. P. J. Albracht and F. A. Armstrong, *J. Am. Chem. Soc.*, 2003, **125**, 8505-8514.

65. S. E. Lamle, S. P. J. Albracht and F. A. Armstrong, *J. Am. Chem. Soc.*, 2004, **126**, 14899-14909.

66. S. E. Lamle, S. P. J. Albracht and F. A. Armstrong, *J. Am. Chem. Soc.*, 2005, **127**, 6595-6604.

67. C. Leger, F. Lederer, B. Guigliarelli and P. Bertrand, *J. Am. Chem. Soc.*, 2006, **128**, 180-187.

68. F. Leroux, S. Dementin, B. Burlatt, L. Cournac, A. Volbeda, S. Champ, L. Martin, B. Guigliarelli, P. Bertrand, J. Fontecilla-Camps, M. Rousset and C. Leger, *Proc. Natl. Acad. Sci. U. S. A.*, 2008, **105**, 11188-11193.

69. P. P. Liebgott, F. Leroux, B. Burlat, S. Dementin, C. Baffert, T. Lautier, V. Fourmond, P. Ceccaldi, C. Cavazza, I. Meynial-Salles, P. Soucaille, J. C. Fontecilla-Camps, B. Guigliarelli, P. Bertrand, M. Rousset and C. Leger, *Nat. Chem. Biol.*, 2010, **6**, 63-70.

70. A. J. Bard and L. R. Faulkner, *Electrochemical Methods : Fundamentals and Applications*, John Wiley & Sons, Inc., 2000.

71. S. Dementin, B. Burlat, V. Fourmond, F. Leroux, P. P. Liebgott, A. Abou Hamdan, C. Leger, M. Rousset, B. Guigliarelli and P. Bertrand, *J. Am. Chem. Soc.*, 2011, **133**, 10211-10221.

72. C. Leger, A. K. Jones, S. P. J. Albracht and F. A. Armstrong, *J. Phys. Chem. B*, 2002, **106**, 13058-13063.

73. T. Reda and J. Hirst, *J. Phys. Chem. B*, 2006, **110**, 1394-1404.

74. A. K. Jones, E. Sillery, S. P. J. Albracht and F. A. Armstrong, *Chem. Commun.*, 2002, 866-867.

75. K. A. Vincent, A. Parkin, O. Lenz, S. P. J. Albracht, J. C. Fontecilla-Camps, R. Cammack, B. Friedrich and F. A. Armstrong, *J. Am. Chem. Soc.*, 2005, **127**, 18179-18189.

76. J. A. Cracknell, B. Friedrich and F. A. Armstrong, *Chem. Commun.*, 2010, **46**, 8463-8465.
77. A. Parkin, C. Cavazza, J. C. Fontecilla-Camps and F. A. Armstrong, *J. Am. Chem. Soc.*, 2006, **128**, 16808-16815.
78. A. F. Wait, C. Brandmayr, S. T. Stripp, C. Cavazza, J. C. Fontecilla-Camps, T. Happe and F. A. Armstrong, *J. Am. Chem. Soc.*, 2011, **133**, 1282-1285.
79. K. A. Vincent, N. A. Belsey, W. Lubitz and F. A. Armstrong, *J. Am. Chem. Soc.*, 2006, **128**, 7448-7449.
80. G. Goldet, C. Brandmayr, S. T. Stripp, T. Happe, C. Cavazza, J. C. Fontecilla-Camps and F. A. Armstrong, *J. Am. Chem. Soc.*, 2009, **131**, 14979-14989.
81. C. Baffert, M. Demuez, L. Cournac, B. Burlat, B. Guigliarelli, P. Bertrand, L. Girbal and C. Leger, *Angew. Chem. Int. Ed.*, 2008, **47**, 2052-2054.
82. K. A. Vincent, J. A. Cracknell, O. Lenz, I. Zebger, B. Friedrich and F. A. Armstrong, *Proc. Natl. Acad. Sci. U. S. A.*, 2005, **102**, 16951-16954.
83. G. Goldet, A. F. Wait, J. A. Cracknell, K. A. Vincent, M. Ludwig, O. Lenz, B. Friedrich and F. A. Armstrong, 2008, **130**, 11106-11113.
84. A. Parkin, L. Bowman, M. M. Roessler, R. A. Davies, T. Palmer, F. A. Armstrong and F. Sargent, *FEBS Lett.*, 2011, **doi:10.1016/j.febslet.2011.07.044**, In press.
85. M. J. Lukey, A. Parkin, M. M. Roessler, B. J. Murphy, J. Harmer, T. Palmer, F. Sargent and F. A. Armstrong, *J. Biol. Chem.*, 2010, **285**, 3928-3938.
86. M. J. Lukey, M. M. Roessler, A. Parkin, R. M. Evans, R. A. Davies, O. Lenz, B. Friedrich, F. Sargent and F. A. Armstrong, *J. Am. Chem. Soc.*, 2011, **133**, 16881-16892.
87. M. E. Pandelia, V. Fourmond, P. Tron-Infossi, E. Lojou, P. Bertrand, C. Leger, M. T. Giudici-Orticoni and W. Lubitz, *J. Am. Chem. Soc.*, 2010, **132**, 6991-7004.
88. V. Fourmond, P. Infossi, M. T. Giudici-Orticoni, P. Bertrand and C. Leger, *J. Am. Chem. Soc.*, 2010, **132**, 4848-4857.
89. A. Parkin, G. Goldet, C. Cavazza, J. C. Fontecilla-Camps and F. A. Armstrong, 2008, **130**, 13410-13416.
90. C. L. McIntosh, F. Germer, R. Schulz, J. Appel and A. K. Jones, *J. Am. Chem. Soc.*, 2011, **133**, 11308-11319.
91. S. T. Stripp, G. Goldet, C. Brandmayr, O. Sanganas, K. A. Vincent, M. Haumann, F. A. Armstrong and T. Happe, *Proc. Natl. Acad. Sci. U. S. A.*, 2009, **106**, 17331-17336.
92. F. A. Armstrong, N. A. Belsey, J. A. Cracknell, G. Goldet, A. Parkin, E. Reisner, K. A. Vincent and A. F. Wait, *Chem. Soc. Rev.*, 2009, **38**, 36-51.
93. R. Cammack, D. Patil, R. Aguirre and E. C. Hatchikian, *FEBS Lett.*, 1982, **142**, 289-292.
94. J. M. C. C. Coremans, J. W. Vanderzwaan and S. P. J. Albracht, *Biochim. Biophys. Acta*, 1992, **1119**, 157-168.
95. L. M. Roberts and P. A. Lindahl, *J. Am. Chem. Soc.*, 1995, **117**, 2565-2572.
96. S. Kurkin, S. J. George, R. N. F. Thorneley and S. P. J. Albracht, *Biochemistry*, 2004, **43**, 6820-6831.

97. H. Ogata, P. Kellers and W. Lubitz, *J. Mol. Biol.*, 2010, **402**, 428-444.

98. J. W. Vanderzwaan, J. Coremans, E. C. M. Bouwens and S. P. J. Albracht, *Biochim. Biophys. Acta Protein Struct. Mol. Enzymol.*, 1990, **1041**, 101-110.

99. S. J. George, S. Kurkin, R. N. F. Thorneley and S. P. J. Albracht, *Biochemistry*, 2004, **43**, 6808-6819.

100. H. Ogata, S. Hirota, A. Nakahara, H. Komori, N. Shibata, T. Kato, K. Kano and Y. Higuchi, *Structure*, 2005, **13**, 1635-1642.

101. P. Soderhjelm and U. Ryde, *J. Mol. Struc.-Theochem*, 2006, **770**, 199-219.

102. M. Carepo, D. L. Tierney, C. D. Brondino, T. C. Yang, A. Pamplona, J. Telser, I. Moura, J. J. G. Moura and B. M. Hoffman, *J. Am. Chem. Soc.*, 2002, **124**, 281-286.

103. J. R. Pilbrow, *Transition Ion Electron Paramagnetic Resonance*, Clarendon, Oxford, 1990.

104. F. Dole, A. Fournel, V. Magro, E. C. Hatchikian, P. Bertrand and B. Guigliarelli, *Biochemistry*, 1997, **36**, 7847-7854.

105. J. E. Huyett, M. Carepo, A. Pamplona, R. Franco, I. Moura, J. J. G. Moura and B. M. Hoffman, *J. Am. Chem. Soc.*, 1997, **119**, 9291-9292.

106. M. Teixeira, I. Moura, A. V. Xavier, D. V. Dervartanian, J. Legall, H. D. Peck, B. H. Huynh and J. J. G. Moura, *Eur. J. Biochem.*, 1983, **130**, 481-484.

107. R. Cammack, D. S. Patil, E. C. Hatchikian and V. M. Fernandez, *Biochim. Biophys. Acta*, 1987, **912**, 98-109.

108. G. J. Kubas, *Chem. Rev.*, 2007, **107**, 4152-4205.

109. R. P. Happe, W. Roseboom and S. P. J. Albracht, *Eur. J. Biochem.*, 1999, **259**, 602-608.

110. L. M. Roberts and P. A. Lindahl, *Biochemistry*, 1994, **33**, 14339-14350.

111. A. L. De Lacey, E. C. Hatchikian, A. Volbeda, M. Frey, J. C. FontecillaCamps and V. M. Fernandez, *J. Am. Chem. Soc.*, 1997, **119**, 7181-7189.

112. A. L. De Lacey, C. Stadler, V. M. Fernandez, E. C. Hatchikian, H. J. Fan, S. H. Li and M. B. Hall, *J. Biol. Inorg. Chem.*, 2002, **7**, 318-326.

113. B. Bleijlevens, F. A. van Broekhuizen, A. L. De Lacey, W. Roseboom, V. M. Fernandez and S. P. J. Albracht, *J. Biol. Inorg. Chem.*, 2004, **9**, 743-752.

114. A. L. De Lacey, C. Gutierrez-Sanchez, V. M. Fernandez, I. Pacheco and I. A. C. Pereira, *J. Biol. Inorg. Chem.*, 2008, **13**, 1315-1320.

115. D. Millo, M.-E. Pandelia, T. Utesch, N. Wisitruangsakul, M. A. Mroginski, W. Lubitz, P. Hildebrandt and I. Zebger, *J. Phys. Chem. B*, 2009, **113**, 15344-15351.

116. D. Millo, P. Hildebrandt, M.-E. Pandelia, W. Lubitz and I. Zebger, *Angew. Chem. Int. Ed.*, 2011, **50**, 2632-2634.

117. N. Wisitruangsakul, O. Lenz, M. Ludwig, B. Friedrich, F. Lendzian, P. Hildebrandt and I. Zebger, *Angew. Chem. Int. Ed.*, 2009, **48**, 611-613.

118. S. Q. Niu, L. M. Thomson and M. B. Hall, *J. Am. Chem. Soc.*, 1999, **121**, 4000-4007.

119. H. Ogata, Y. Mizoguchi, N. Mizuno, K. Miki, S. Adachi, N. Yasuoka, T. Yagi, O. Yamauchi, S. Hirota and Y. Higuchi, *J. Am. Chem. Soc.*, 2002, **124**, 11628-11635.

120. M. E. Pandelia, H. Ogata, L. J. Currell, M. Flores and W. Lubitz, *Biochim. Biophys. Acta, Bioenerg.*, 2010, **1797**, 304-313.

121. M. Saggu, I. Zebger, M. Ludwig, O. Lenz, B. Friedrich, P. Hildebrandt and F. Lendzian, *J. Biol. Chem.*, 2009, **284**, 16264-16276.

122. M. E. Pandelia, P. Infossi, M. T. Giudici-Orticoni and W. Lubitz, *Biochemistry*, 2010, **49**, 8873-8881.

123. M. E. Pandelia, P. Infossi, M. Stein, M. T. Giudici-Orticoni and W. Lubitz, *Chem. Commun.*, 2011, **48**, 823-825.

124. K. A. Vincent, J. A. Cracknell, J. R. Clark, M. Ludwig, O. Lenz, B. Friedrich and F. A. Armstrong, *Chem. Commun.*, 2006, 5033-5035.

125. E. Reisner, D. J. Powell, C. Cavazza, J. C. Fontecilla-Camps and F. A. Armstrong, *J. Am. Chem. Soc.*, 2009, **131**, 18457-18466.

126. J. Cohen, K. Kim, M. Posewitz, M. L. Ghirardi, K. Schulten, M. Seibert and P. King, *Biochem. Soc. Trans.*, 2005, **33**, 80-82.

127. J. Cohen, K. Kim, P. King, M. Seibert and K. Schulten, *Structure*, 2005, **13**, 1321-1329.

128. A. Volbeda, Y. Montet, X. Vernede, E. C. Hatchikian and J. C. Fontecilla-Camps, *Int. J. Hydrogen Energy*, 2002, **27**, 1449-1461.

129. L. K. Black, C. L. Fu and R. J. Maier, *J. Bacteriol.*, 1994, **176**, 7102-7106.

130. L. Kleihues, O. Lenz, M. Bernhard, T. Buhrke and B. Friedrich, *J. Bacteriol.*, 2000, **182**, 2716-2724.

131. T. Buhrke, O. Lenz, N. Krauss and B. Friedrich, *J. Biol. Chem.*, 2005, **280**, 23791-23796.

132. S. Dementin, F. Leroux, L. Cournac, A. L. De Lacey, A. Volbeda, C. Leger, B. Burlat, N. Martinez, S. Champ, L. Martin, O. Sanganas, M. Haumann, V. M. Fernandez, B. Guigliarelli, J. C. Fontecilla-Camps and M. Rousset, *J. Am. Chem. Soc.*, 2009, **131**, 10156-10164.

133. P. P. Liebgott, A. L. De Lacey, B. Burlat, L. Cournac, P. Richaud, M. Brugna, V. M. Fernandez, B. Guigliarelli, M. Rousset, C. Leger and S. Dementin, *J. Am. Chem. Soc.*, 2011, **133**, 986-997.

134. J. Fritsch, P. Scheerer, S. Frielingsdorf, S. Kroschinsky, B. Friedrich, O. Lenz and C. M. T. Spahn, *Nature*, 2011, **479**, 249-252.

135. Y. Shomura, K.-S. Yoon, H. Nishihara and Y. Higuchi, *Nature*, 2011, **479**, 253-256.

136. K. Knuttel, K. Schneider, A. Erkens, W. Plass, A. Muller, E. Bill and A. X. Trautwein, *Bull. Pol. Acad. Sci. Chem.*, 1994, **42**, 495-511.

137. K. Schneider, D. S. Patil and R. Cammack, *Biochim. Biophys. Acta Protein Struct. Mol. Enzymol.*, 1983, **748**, 353-361.

138. J. W. Peters, M. H. B. Stowell, S. M. Soltis, M. G. Finnegan, M. K. Johnson and D. C. Rees, *Biochemistry*, 1997, **36**, 1181-1187.

139. M. E. Pandelia, W. Nitschke, P. Infossi, M. T. Giudici-Orticoni, E. Bill and W. Lubitz, *Proc. Natl. Acad. Sci. U. S. A.*, 2011, **108**, 6097-6102.

140. T. Happe and J. D. Naber, *Eur. J. Biochem.*, 1993, **214**, 475-481.

141. T. Goris, A. F. Wait, M. Saggu, J. Fritsch, N. Heidary, M. Stein, I. Zebger, F. Lendzian, F. A.

Armstrong, B. Friedrich and O. Lenz, *Nat. Chem. Biol.*, 2011, **7**, 310-U387.

142. M. Bernhard, B. Benelli, A. Hochkoeppler, D. Zannoni and B. Friedrich, *Eur. J. Biochem.*, 1997, **248**, 179-186.
143. R. O. Louro, T. Catarino, D. L. Turner, M. A. Picarra-Pereira, I. Pacheco, J. LeGall and A. V. Xavier, *Biochemistry*, 1998, **37**, 15808-15815.
144. O. Lenz, M. Ludwig, T. Schubert, I. Burstel, S. Ganskow, T. Goris, A. Schwarze and B. Friedrich, *Chemphyschem*, 2010, **11**, 1107-1119.
145. M. Horch, L. Lauterbach, O. Lenz, P. Hildebrandt and I. Zebger, *FEBS Lett.*, 2011.
146. O. Lenz and B. Friedrich, *Proc. Natl. Acad. Sci. U. S. A.*, 1998, **95**, 12474-12479.
147. L. Lauterbach, J. Liu, M. Horch, P. Hummel, A. Schwarze, M. Haumann, K. A. Vincent, O. Lenz and I. Zebger, *Eur. J. Inorg. Chem.*, 2011, 1067-1079.
148. A. J. Pierik, M. Schmelz, O. Lenz, B. Friedrich and S. P. Albracht, *FEBS Lett.*, 1998, **438**, 231-235.
149. M. Horch, L. Lauterbach, M. Saggu, P. Hildebrandt, F. Lendzian, R. Bittl, O. Lenz and I. Zebger, *Angew. Chem. Int. Ed.*, 2010, **49**, 8026-8029.
150. J. W. Peters, W. N. Lanzilotta, B. J. Lemon and L. C. Seefeldt, *Science*, 1998, **282**, 1853-1858.
151. T. B. Rauchfuss, *Science*, 2007, **316**, 553-554.
152. A. Le Goff, V. Artero, B. Jousselme, P. D. Tran, N. Guillet, R. Metaye, A. Fihri, S. Palacin and M. Fontecave, *Science*, 2009, **326**, 1384-1387.
153. C. Tard, X. M. Liu, S. K. Ibrahim, M. Bruschi, L. De Gioia, S. C. Davies, X. Yang, L. S. Wang, G. Sawers and C. J. Pickett, *Nature*, 2005, **433**, 610-613.
154. D. W. Mulder, E. S. Boyd, R. Sarma, R. K. Lange, J. A. Endrizzi, J. B. Broderick and J. W. Peters, *Nature*, 2011, **465**, 248-251.
155. M. Y. Darensbourg, E. J. Lyon and J. J. Smee, *Coord. Chem. Rev.*, 2000, **206**, 533-561.
156. A. C. Marr, D. J. E. Spencer and M. Schroder, *Coord. Chem. Rev.*, 2001, **219**, 1055-1074.
157. T. B. Rauchfuss, *Inorg. Chem.*, 2004, **43**, 14-26.
158. E. Bouwman and J. Reedijk, *Coord. Chem. Rev.*, 2005, **249**, 1555-1581.
159. X. M. Liu, S. K. Ibrahim, C. Tard and C. J. Pickett, *Coord. Chem. Rev.*, 2005, **249**, 1641-1652.
160. L. C. Sun, B. Akermark and S. Ott, *Coord. Chem. Rev.*, 2005, **249**, 1653-1663.
161. J. R. C. Salgado, F. Alcaide, G. Alvarez, L. Calvillo, M. J. Lazaro and E. Pastor, *J. Power Sources*, 2010, **195**, 4022-4029.
162. S. Wasmus and A. Kuver, *J. Electroanal. Chem.*, 1999, **461**, 14-31.
163. S. Rojas, F. J. Garcia-Garcia, S. Jaras, M. V. Martinez-Huerta, J. L. G. Fierro and M. Boutonnet, *Appl. Catal. A*, 2005, **285**, 24-35.
164. J. A. Cracknell, K. A. Vincent and F. A. Armstrong, *Chem. Rev.*, 2008, **108**, 2439-2461.
165. A. F. Wait, A. Parkin, G. M. Morley, L. dos Santos and F. A. Armstrong, *J. Phys. Chem. C*, 2010, **114**, 12003-12009.
166. E. Reisner, J. C. Fontecilla-Camps and F. A. Armstrong, *Chem. Commun.*, 2009, **46**, 550-552.
167. C. Tard and C. J. Pickett, *Chem. Rev.*, 2009, **109**, 2245-2274.
168. W. F. Liaw, C. H. Chen, G. H. Lee and S. M. Peng, *Organometallics*, 1998, **17**, 2370-2372.

169. A. M. Royer, T. B. Rauchfuss and S. R. Wilson, *Inorg. Chem.*, 2008, **47**, 395-397.
170. C. H. Lai, J. H. Reibenspies and M. Y. Darensbourg, *Angew. Chem. Int. Ed.*, 1996, **35**, 2390-2393.
171. S. C. Davies, D. J. Evans, D. L. Hughes, S. Longhurst and J. R. Sanders, *Chem. Commun.*, 1999, 1935-1936.
172. M. C. Smith, J. E. Barclay, S. P. Cramer, S. C. Davies, W. W. Gu, D. L. Hughes, S. Longhurst and D. J. Evans, *J. Chem. Soc., Dalton Trans.*, 2002, 2641-2647.
173. D. Sellmann, F. Geipel, F. Lauderbach and F. W. Heinemann, *Angew. Chem. Int. Ed.*, 2002, **114**, 654-656.
174. Y. Ohki, K. Yasumura, K. Kuge, S. Tanino, M. Ando, Z. L. Li and K. Tatsumi, *Proc. Natl. Acad. Sci. U. S. A.*, 2008, **105**, 7652-7657.
175. F. Gloaguen, J. D. Lawrence, T. B. Rauchfuss, M. Benard and M. M. Rohmer, *Inorg. Chem.*, 2002, **41**, 6573-6582.
176. F. J. Wang, M. Wang, X. Y. Liu, K. Jin, W. B. Donga and L. C. Sun, *Dalton Trans.*, 2007, 3812-3819.
177. M. L. Helm, M. P. Stewart, R. M. Bullock, M. R. DuBois and D. L. DuBois, *Science*, 2011, **333**, 863-866.
178. M. Frey, *ChemBioChem*, 2002, **3**, 153-160.
179. B. Payen, M. Segui, P. Monsan, K. Schneider, C. G. Friedrich and H. G. Schlegel, *Biotechnol. Lett.*, 1983, **5**, 463-468.
180. R. Mertens, L. Greiner, E. C. D. van den Ban, H. B. C. M. Haaker and A. Liese, *J. Mol. Catal. B*, 2003, **24-5**, 39-52.
181. R. Mertens and A. Liese, *Curr. Opin. Biotech.*, 2004, **15**, 343-348.
182. H. A. Reeve, L. Lauterbach, P. A. Ash, O. Lenz and K. A. Vincent, *Chem. Commun.*, 2011, **48**, 1589-1591.
183. A. Cornish-Bowden, *Fundamentals of Enzyme Kinetics*, Porland Press, 2004.
184. M. R. Wright, *Introduction to Chemical Kinetics*, Wiley, 2004.
185. D. Eisenberg and W. Kauzmann, *The Structure and Properties of Water*, Oxford University Press, London, 1969.
186. J. J. Max and C. Chapados, *J. Chem. Phys.*, 2009, **131**, 184505.
187. A. Miki, S. Ye and M. Osawa, *Chem. Commun.*, 2002, 1500-1501.
188. K. Nakamoto, *Infrared and Raman Spectra of Inorganic and Coordination Compounds*, Wiley, 2009.
189. L. H. Jones, R. S. McDowell and M. Goldblatt, *Inorg. Chem.*, 1969, **8**, 2349.
190. E. Bernhardt, B. Bley, R. Warchow, H. Willner, E. Bill, P. Kuhn, I. H. T. Shah, M. Bodenbinder, R. Brochler and F. Aubke, *J. Am. Chem. Soc.*, 1999, **121**, 7188-7200.
191. E. W. Abel, R. A. N. McLean, S. P. Tyfield, P. S. Braterman, A. P. Walker and P. J. Hendra, *J. Mol. Spectrosc.*, 1969, **30**, 29-50.
192. H. Stammreich, K. Kawai, Y. Tavares, P. Krumholz, J. Behmoiras and S. Bril, *J. Chem. Phys.*, 1960, **32**, 1482.

193. M. Bigorgne, *J. Organomet. Chem.*, 1970, **24**, 211-229.

194. C. Elschenbroich and A. Salzer, *Organometallics: A Concise Introduction*, VCH, Weinheim, 1992.

195. B. L. Mojet, S. D. Ebbesen and L. Lefferts, *Chem. Soc. Rev.*, 2010, **39**, 4635-4655.

196. M. F. Amr EI-Sayed and R. K. Sheline, *J. Inorg. Nucl. Chem.*, 1958, **6**, 187-193.

197. W. P. Griffith and G. T. Turner, *J. Chem. Soc. A* 1970, 858-862.

198. R. Sander, http://www.rolf-sander.net/henry/henry.pdf.

199. C. Massanz, S. Schmidt and B. Friedrich, *J. Bacteriol.*, 1998, **180**, 1023-1029.

200. M. M. Bradford, *Anal. Biochem.*, 1976, **72**, 248-254.

201. T. Burgdorf, E. van der Linden, M. Bernhard, Q. Y. Yin, J. W. Back, A. F. Hartog, A. O. Muijsers, C. G. de Koster, S. P. J. Albracht and B. Friedrich, *J. Bacteriol.*, 2005, **187**, 3122-3132.

202. T. Buhrke, O. Lenz, A. Porthun and B. Friedrich, *Mol. Microbiol.*, 2004, **51**, 1677-1689.

203. A. Sucheta, R. Cammack, J. Weiner and F. A. Armstrong, *Biochemistry*, 1993, **32**, 5455-5465.

204. K. Tedsree, C. W. A. Chan, S. Jones, Q. A. Cuan, W. K. Li, X. Q. Gong and S. C. E. Tsang, *Science*, 2011, **332**, 224-228.

205. M. Kuhn, A. Steinbuchel and H. G. Schlegel, *J. Bacteriol.*, 1984, **159**, 633-639.

206. K. Schneider, R. Cammack and H. G. Schlegel, *Eur. J. Biochem.*, 1984, **142**, 75-84.

207. D. Carrieri, K. Wawrousek, C. Eckert, J. Yu and P. C. Maness, *Bioresour. Technol.*, 2011, **102**, 8368-8377.

208. L. A. Sazanov and P. Hinchliffe, *Science*, 2006, **311**, 1430-1436.

209. S. P. J. Albracht and R. Hedderich, *FEBS Lett.*, 2000, **485**, 1-6.

210. L. Lauterbach, Z. Idris, K. A. Vincent and O. Lenz, *PloS one*, 2011, **6**, e25939.

211. H. X. Wang, C. Y. Ralston, D. S. Patil, R. M. Jones, W. Gu, M. Verhagen, M. Adams, P. Ge, C. Riordan, C. A. Marganian, P. Mascharak, J. Kovacs, C. G. Miller, T. J. Collins, S. Brooker, P. D. Croucher, K. Wang, E. I. Stiefel and S. P. Cramer, *J. Am. Chem. Soc.*, 2000, **122**, 10544-10552.

212. K. Schneider, R. Cammack, H. G. Schlegel and D. O. Hall, *Biochim. Biophys. Acta Protein Struct. Mol. Enzymol.*, 1979, **578**, 445-461.

213. E. Van der Linden, T. Burgdorf, M. Bernhard, B. Bleijlevens, B. Friedrich and S. P. J. Albracht, *J. Biol. Inorg. Chem.*, 2004, **9**, 616-626.

214. B. Bleijlevens, T. Buhrke, E. van der Linden, B. Friedrich and S. P. J. Albracht, *J. Biol. Chem.*, 2004, **279**, 46686-46691.

215. A. Erkens, K. Schneider and A. Mueller, *J. Biol. Inorg. Chem.*, 1996, **1**, 99-110.

216. E. van der Linden, T. Burgdorf, A. L. Lacey, T. Buhrke, M. Scholte, V. M. Fernandez, B. Friedrich and S. P. J. Albracht, *J. Biol. Inorg. Chem.*, 2006, **11**, 247-260.

217. F. Germer, I. Zebger, M. Saggu, F. Lendzian, R. Schulz and J. Appel, *J. Biol. Chem.*, 2009, **284**, 36462-36472.

218. A. Tran-Betcke, U. Warnecke, C. Boecker, C. Zaborosch and B. Friedrich, *J. Bacteriol.*, 1990, **172**, 2920-2929.

219. J. P. Whitehead, R. J. Gurbiel, C. Bagyinka, B. M. Hoffman and M. J. Maroney, *J. Am. Chem. Soc.*, 1993, **115**, 5629-5635.

220. Z. J. Gu, J. Dong, C. B. Allan, S. B. Choudhury, R. Franco, J. J. G. Moura, J. LeGall, A. E. Przybyla, W. Roseboom, S. P. J. Albracht, M. J. Axley, R. A. Scott and M. J. Maroney, *J. Am. Chem. Soc.*, 1996, **118**, 11155-11165.

221. G. Davidson, S. B. Choudhury, Z. J. Gu, K. Bose, W. Roseboom, S. P. J. Albracht and M. J. Maroney, *Biochemistry*, 2000, **39**, 7468-7479.

222. M. Haumann, A. Porthun, T. Buhrke, P. Liebisch, W. Meyer-Klaucke, B. Friedrich and H. Dau, *Biochemistry*, 2003, **42**, 11004-11015.

223. S. Maldonado, A. Lostao, M. P. Irun, J. Fernandez-Recio, C. Gustavo Genzor, E. Begona Gonzalez, J. A. Rubio, A. Luquita, F. Daoudi and J. Sancho, *Biochim.*, 1998, **80**, 813-820.

224. K. Schneider and H. G. Schlegel, *Biochem. Biophys. Res. Commun.*, 1978, **84**, 564-571.

225. S. P. J. Albracht, E. van der Linden and B. W. Faber, *Biochim. Biophys. Acta, Bioenerg.*, 2003, **1557**, 41-49.

226. E. van der Linden, B. W. Faber, B. Bleijlevens, T. Burgdorf, M. Bernhard, B. Friedrich and S. P. J. Albracht, *Eur. J. Biochem.*, 2004, **271**, 801-808.

227. J. M. Berrisford and L. A. Sazanov, *J. Biol. Chem.*, 2009, **284**, 29773-29783.

228. S. Ghisla and V. Massey, *Eur. J. Biochem.*, 1989, **181**, 1-17.

229. K. Schneider, H. G. Schlegel and K. Jochim, *Eur. J. Biochem.*, 1984, **138**, 533-541.

230. W. Johanssen, H. Gerberding, M. Rohde, C. Zaborosch and F. Mayer, *Arch. Microbiol.*, 1991, **155**, 303-308.

231. S. E. Lamle, K. A. Vincent, L. M. Halliwell, S. P. J. Albracht and F. A. Armstrong, *Dalton Trans.*, 2003, 4152-4157.

232. M. Brugna-Guiral, P. Tron, W. Nitschke, K. O. Stetter, B. Burlat, B. Guigliarelli, M. Bruschi and M. T. Giudici-Orticoni, *Extremophiles*, 2003, **7**, 145-157.

233. F. A. Armstrong, A. K. Jones, S. E. Lamle, H. R. Pershad, K. A. Vincent and S. P. J. Albracht, *J. Am. Chem. Soc.*, 2003, **125**, 8505-8514.

234. L. Lauterbach, *Personal communication*.

235. L. Brennan, D. L. Turner, A. C. Messias, M. L. Teodoro, J. LeGall, H. Santos and A. V. Xavier, *J. Mol. Biol.*, 2000, **298**, 61-82.

236. G. Fritz, D. Griesshaber, O. Seth and P. M. H. Kroneck, *Biochemistry*, 2001, **40**, 1317-1324.

237. F. M. A. Valente, A. S. F. Oliveira, N. Gnadt, I. Pacheco, A. V. Coelho, A. V. Xavier, M. Teixeira, C. M. Soares and I. A. C. Pereira, *J. Biol. Inorg. Chem.*, 2005, **10**, 667-682.

238. U. Wissenbach, A. Kroger and G. Unden, *Arch. Microbiol.*, 1990, **154**, 60-66.

239. D. J. Richardson, *Microbiol.*, 2000, **146**, 551-571.

240. M. C. Marques, R. Coelho, A. L. De Lacey, I. A. C. Pereira and P. M. Matias, *J. Mol. Biol.*, 2010, **396**, 893-907.

241. M. Y. Darensbourg and W. Weigand, *Eur. J. Inorg. Chem.*, 2011, 994-1004.

242. B. Friedrich, T. Buhrke, T. Burgdorf and O. Lenz, *Biochem. Soc. Trans.*, 2005, **33**, 97-101.

243. O. Lenz, A. Strack, A. Tran-Betcke and B. Friedrich, *J. Bacteriol.*, 1997, **179**, 1655-1663.

244. G. Winter, T. Buhrke, K. Jones Anne and B. Friedrich, *Arch. Microbiol.*, 2004, **182**, 138-146.

245. O. Lenz, M. Bernhard, T. Buhrke, E. Schwartz and B. Friedrich, *J. Mol. Microbiol. Biotechnol.*, 2002, **4**, 255-262.

246. M. Bernhard, T. Buhrke, B. Bleijlevens, A. L. De Lacey, V. M. Fernandez, S. P. J. Albracht and B. Friedrich, *J. Biol. Chem.*, 2001, **276**, 15592-15597.

247. T. Buhrke, S. Loescher, O. Lenz, E. Schlodder, I. Zebger, L. K. Andersen, P. Hildebrandt, W. Meyer-Klaucke, H. Dau, B. Friedrich and M. Haumann, *J. Biol. Chem.*, 2005, **280**, 19488-19495.

248. P. Wardman, *Free. Radical. Res. Com.*, 1991, **14**, 57-67.

249. F. A. Armstrong, J. A. Cracknell, A. F. Wait, O. Lenz and B. Friedrich, *Proc. Natl. Acad. Sci. U. S. A.*, 2009, **106**, 20681-20686.

250. D. Lide, *CRC Handbook of Chemistry and Physics*, CRC Press, 1997.

251. R. G. Keefe, M. J. Axley and A. L. Harabin, *Arch. Biochem. Biophys.*, 1995, **317**, 449-456.

252. B. Beden, A. Bewick and C. Lamy, *J. Electroanal. Chem.*, 1983, **148**, 147-160.

253. B. Lim, M. Jiang, P. H. C. Camargo, E. C. Cho, J. Tao, X. Lu, Y. Zhu and Y. Xia, *Science*, 2009, **324**, 1302-1305.

254. H. S. Liu, C. J. Song, L. Zhang, J. J. Zhang, H. J. Wang and D. P. Wilkinson, *J. Power Sources*, 2006, **155**, 95-110.

255. H. F. Oetjen, V. M. Schmidt, U. Stimming and F. Trila, *J. Electrochem. Soc.*, 1996, **143**, 3838-3842.

256. C. Rice, R. I. Ha, R. I. Masel, P. Waszczuk, A. Wieckowski and T. Barnard, *J. Power Sources*, 2002, **111**, 83-89.

257. A. S. Arico, S. Srinivasan and V. Antonucci, *Fuel Cells*, 2001, **1**, 133-161.

258. H. A. Gasteiger, S. S. Kocha, B. Sompalli and F. T. Wagner, *Appl. Catal. B Environ.*, 2005, **56**, 9-35.

259. T. E. Springer, T. A. Zawodzinski and S. Gottesfeld, *J. Electrochem. Soc.*, 1991, **138**, 2334-2342.

260. H. P. Liang, H. M. Zhang, J. S. Hu, Y. G. Guo, L. J. Wan and C. L. Bai, *Angew. Chem. Int. Ed.*, 2004, **43**, 1540-1543.

261. S. H. Joo, S. J. Choi, I. Oh, J. Kwak, Z. Liu, O. Terasaki and R. Ryoo, *Nature*, 2001, **412**, 169-172.

262. Z. L. Liu, X. Y. Ling, X. D. Su and J. Y. Lee, *J. Phys. Chem. B*, 2004, **108**, 8234-8240.

263. M. K. Min, J. H. Cho, K. W. Cho and H. Kim, *Electrochim. Acta*, 2000, **45**, 4211-4217.

264. W. J. Zhou, Z. H. Zhou, S. Q. Song, W. Z. Li, G. Q. Sun, P. Tsiakaras and Q. Xin, *Appl. Catal. B-Environ*, 2003, **46**, 273-285.

265. P. J. Ferreira, G. J. la O, Y. Shao-Horn, D. Morgan, R. Makharia, S. Kocha and H. A. Gasteiger, *J. Electroanal. Chem.*, 2005, **152**, A2256-A2271.

266. E. S. Steigerwalt, G. A. Deluga, D. E. Cliffel and C. M. Lukehart, *J. Phys. Chem. B*, 2001, **105**, 8097-8101.

267. E. S. Steigerwalt, G. A. Deluga and C. M. Lukehart, *J. Phys. Chem. B*, 2002, **106**, 760-766.

268. M. C. Daniel and D. Astruc, *Chem. Rev.*, 2004, **104**, 293-346.

269. A. Chen and P. Holt-Hindle, *Chem. Rev.*, 2010, **110**, 3767-3804.

270. K. L. Oura, V. G.; Saranin, A. A.; Zotov, A. V.; Katayama, M.; Yates, J. T., *Surface Science: An Introduction*, Springer-Verlag, Berlin, 2003.

271. H. N. Dinh, X. M. Ren, F. H. Garzon, P. Zelenay and S. Gottesfeld, *J. Electroanal. Chem.*, 2000, **491**, 222-233.

272. T. J. Schmidt, M. Noeske, H. A. Gasteiger, R. J. Behm, P. Britz and H. Bonnemann, *J. Electrochem. Soc.*, 1998, **145**, 925-931.

273. U. A. Paulus, U. Endruschat, G. J. Feldmeyer, T. J. Schmidt, H. Bonnemann and R. J. Behm, *J. Catal.*, 2000, **195**, 383-393.

274. C. Rice, S. Ha, R. I. Masel and A. Wieckowski, *J. Power Sources*, 2003, **115**, 229-235.

275. S. Ha, R. Larsen and R. I. Masel, *J. Power Sources*, 2005, **144**, 28-34.

276. A. Capon and R. Parsons, *J. Electroanal. Chem.*, 1973, **44**, 239-254.

277. H. Okamoto, W. Kon and Y. Mukouyama, *J. Phys. Chem. B*, 2005, **109**, 15659-15666.

278. H. Okamoto, W. Kon and Y. Mukouyama, *J. Phys. Chem. B*, 2004, **108**, 4432-4438.

279. A. Capon and R. Parsons, *J. Electroanal. Chem.*, 1973, **44**, 1-7.

280. A. Capon and R. Parsons, *J. Electroanal. Chem.*, 1973, **45**, 205-231.

281. A. Capon and R. Parsons, *J. Electroanal. Chem.*, 1975, **65**, 285-305.

282. Y. X. Chen, M. Heinen, Z. Jusys and R. J. Behm, *Langmuir*, 2006, **22**, 10399-10408.

283. S. C. Chang, L. W. H. Leung and M. J. Weaver, *J. Phys. Chem.*, 1990, **94**, 6013-6021.

284. K. Kunimatsu, *J. Electroanal. Chem.*, 1986, **213**, 149-157.

285. K. Kunimatsu and H. Kita, *J. Electroanal. Chem.*, 1987, **218**, 155-172.

286. S. G. Sun, J. Clavilier and A. Bewick, *J. Electroanal. Chem.*, 1988, **240**, 147-159.

287. L. Lefferts, B. L. Mojet and S. D. Ebbesen, *Chem. Soc. Rev.*, 2010, **39**, 4643-4655.

288. T. Iwasita and F. C. Nart, *Prog. Surf. Sci.*, 1997, **55**, 271-340.

289. S. Kinugasa, K. Tanabe and T. Tamura, *Spectral Database for Orgainic Compounds SDBS*, 2011.

290. N. R. Avery, *Appl. Surf. Sci.*, 1982, **11-2**, 774-783.

291. K. Kunimatsu, B. Bae, K. Miyatake, H. Uchida and M. Watanabe, *J. Phys. Chem. B*, 2011, **115**, 4315-4321.

292. R. C. Alkire, D. M. Kolb, J. Lipkowski and P. Ross, *Diffraction and Spectroscopic Methods in Electrochemistry*, Wiley-VCH, Weiheim, 2006.

293. M. Osawa, *Bull. Chem. Soc. Jpn.*, 1997, **70**, 2861-2880.

294. M. Osawa, *Top. Appl. Phys.*, 2001, **81**, 163-186.

295. M. Osawa, K. Ataka, K. Yoshii and Y. Nishikawa, *Appl. Spectrosc.*, 1993, **47**, 1497-1502.

296. G. T. Merklin and P. R. Griffths, *Langmuir*, 1997, **13**, 6159-6193.

297. Y. G. Yan, Q. X. Li, S. J. Huo, M. Ma, W. B. Cai and M. Osawa, *J. Phys. Chem. B*, 2005, **109**, 7900-7906.

298. F. Maillard, E. R. Savinova, P. A. Simonov, V. I. Zaikovskii and U. Stimming, *J. Phys. Chem. B*, 2004, **108**, 17893-17904.

299. M. Arenz, K. J. J. Mayrhofer, V. Stamenkovic, B. B. Blizanac, T. Tomoyuki, P. N. Ross and N. M. Markovic, *J. Am. Chem. Soc.*, 2005, **127**, 6819-6829.

300. S. Park, A. Wieckowski and M. J. Weaver, *J. Am. Chem. Soc.*, 2003, **125**, 2282-2290.

301. V. Stamenkovic, M. Arenz, P. N. Ross and N. M. Markovic, *J. Phys. Chem. B*, 2004, **108**, 17915-

17920.

302. E. R. Savinova, F. Hahn and N. Alonso-Vante, *J. Phys. Chem. C*, 2008, **112**, 18521-18530.
303. W. Chen, S. G. Sun, Z. Y. Zhou and S. P. Chen, *J. Phys. Chem. B*, 2003, **107**, 9808-9812.
304. H. Cherdron, L. Hohr and W. Kern, *Makromol. Chem.*, 1962, **52**, 48-58.
305. H. Li, G. Sun, Q. Jiang, M. Zhu, S. Sun and Q. Xin, *Electrochem. Commun.*, 2007, **9**, 1410-1415.
306. Y. Zhu, Y. Kang, Z. Zou, Q. Zhou, J. Zheng, B. Xia and H. Yang, *Electrochem. Commun.*, 2008, **10**, 802-805.
307. H. Miyake, T. Okada, G. Samjeske and M. Osawa, *Phys. Chem. Chem. Phys.*, 2008, **10**, 3662-3669.
308. M. V. Mirkin, D. P. Zhan and J. Velmurugan, *J. Am. Chem. Soc.*, 2009, **131**, 14756-14760.
309. K. Ataka, T. Yotsuyanagi and M. Osawa, *J. Phys. Chem.*, 1996, **100**, 10664-10672.
310. M. Osawa, M. Tsushima, H. Mogami, G. Samjeske and A. Yamakata, *J. Phys. Chem. C*, 2008, **112**, 4248-4256.
311. H. A. Gasteiger, N. Markovic, P. N. Ross and E. J. Cairns, *J. Phys. Chem.*, 1994, **98**, 617-625.
312. J. W. Russell, J. Overend, K. Scanlon, M. Severson and A. Bewick, *J. Phys. Chem.*, 1982, **86**, 3066-3068.
313. J. Y. Wang, H. X. Zhang, K. Jiang and W. B. Cai, *J. Am. Chem. Soc.*, 2011, **133**, 14876-14879.
314. Q. S. Chen, S. G. Sun, Z. Y. Zhou, Y. X. Chen and S. B. Deng, *Phys. Chem. Chem. Phys.*, 2008, **10**, 3645-3654.
315. B. A. Sexton, *Appl. Phys. A Mater Sci. Process.*, 1981, **26**, 1-18.
316. B. Beden, A. Bewick and C. Lamy, *J. Electroanal. Chem.*, 1983, **150**, 505-511.
317. A. Cuesta, G. Cabello, C. Gutierrez and M. Osawa, *Phys. Chem. Chem. Phys.*, 2011, **13**, 20091-20095.
318. M. W. Breter, *Electrochim. Acta*, 1967, **12**, 1213.
319. M. W. Breter, *J. Electroanal. Chem.* , 1979, **101**, 329.
320. B. Beden, A. Bewick, M. Razaq and J. Weber, *J. Electroanal. Chem.*, 1982, **139**, 203-206.
321. B. Beden, A. Bewick, K. Kunimatsu and C. Lamy, *J. Electroanal. Chem.*, 1982, **142**, 345-356.
322. Z. F. Liu, M. Shamsuzzoha, E. T. Ada, W. M. Reichert and D. E. Nikles, *J. Power Sources*, 2007, **164**, 472-480.
323. S. A. Lee, K. W. Park, J. H. Choi, B. K. Kwon and Y. E. Sung, *J. Electrochem. Soc.*, 2002, **149**, A1299-A1304.
324. B. R. Cuenya, *Thin Solid Films*, 2010, **518**, 3127-3150.
325. A. L. Linsebigler, G. Q. Lu and J. T. Yates, *Chem. Rev.*, 1995, **95**, 735-758.
326. A. J. Healy, H. A. Reeve and K. A. Vincent, *Faraday Discuss.*, 2011, **148**, 345-357.
327. A. J. Healy, H. A. Reeve, A. Parkin and K. A. Vincent, *Electrochim. Acta*, 2011, **56**, 10786-10790.
328. D. Moss, E. Nabedryk, J. Breton and W. Mantele, *Eur. J. Biochem.*, 1990, **187**, 565-572.
329. W. Roseboom, A. L. De Lacey, V. M. Fernandez, E. C. Hatchikian and S. P. J. Albracht, *J. Biol. Inorg. Chem.*, 2006, **11**, 102-118.
330. M. Diaz, M. S. Martin-Gonzalez and J. L. Costa-Kramer, *Surf. Sci.*, 2010, **604**, 1420-1424.
331. F. A. Armstrong, N. L. Barlow, P. L. Burn, K. R. Hoke, L. J. C. Jeuken, C. Shenton and G. R.

Webster, *Chem. Commun.*, 2004, 316-317.

332. O. Rudiger, J. M. Abad, E. C. Hatchikian, V. M. Fernandez and A. L. De Lacey, *J. Am. Chem. Soc.*, 2005, **127**, 16008-16009.
333. F. Siebert and P. Hildebrandt, *Vibrational Spectroscopy in Life Sciences*, Wiley, Weinheim, Germany, 2008.
334. O. Lenz, I. Zebger, J. Hamann, P. Hildebrandt and B. Friedrich, *FEBS Lett.*, 2007, **581**, 3322-3326.
335. F. Dole, M. Medina, C. More, R. Cammack, P. Bertrand and B. Guigliarelli, *Biochemistry*, 1996, **35**, 16399-16406.
336. M. Carmo, A. R. Dos Santos, J. G. R. Poco and M. Linardi, *J. Power Sources*, 2007, **173**, 860-866.
337. H. R. Pershad, J. L. C. Duff, H. A. Heering, E. C. Duin, S. P. J. Albracht and F. A. Armstrong, *Biochemistry*, 1999, **38**, 8992-8999.